Surface Modified Cellulose Nanomaterials : A Source of Non-Spherical Nanoparticles for Drug Delivery

Author:
Khine, Yee Yee

Publication Date:
2021

DOI:
https://doi.org/10.26190/unsworks/2241

Surface Modified Cellulose Nanomaterials: A Source of Non-Spherical Nanoparticles for Drug Delivery

Yee Yee Khine

A thesis submitted in fulfilment of the requirements for the degree of

Doctor of Philosophy

Centre for Advanced Macromolecular Design

School of Chemistry

Faculty of Science

The University of New South Wales, Australia

June 2020

Thesis/Dissertation Sheet

Surname/Family Name	:	**Khine**
Given Name/s	:	**Yee Yee**
Abbreviation for degree as give in the University calendar	:	**PhD**
Faculty	:	**Science**
School	:	**Chemistry**
Thesis Title	:	**Surface Modified Cellulose Nanomaterials: A source of Non-spherical Nanoparticles for Drug Delivery**

Abstract 350 words maximum: (PLEASE TYPE)

Cellulose nanomaterials are excellent carriers to deliver therapeutics as they are biocompatible and have a desirable non-spherical shape. However, these materials display low solubility in aqueous media and need to be modified with water-soluble polymers to achieve high colloidal stability. A critical challenge is to perform efficient surface modification without disrupting the original properties of cellulose. In this study, we modified TEMPO-oxidized cellulose nanofibers bearing carboxylic acid moieties (CNFs) by two different routes: nitrile imine/mediated tetrazole/carboxylic acid ligation (NICAL), and three-component Passerini reaction. The advantage of these reactions is the direct functionalization of CNFs under ambient conditions in aqueous media so that additional modification or solvent exchange process prior to surface grafting can be avoided. The NICAL reaction was performed under UV irradiation at λ = 326 nm for 10 hr, resulting in the self-fluorescent polymer grafted CNFs. On the other hand, Passerini reaction is regarded as an effective functionalization approach, which can be carried out in the presence of three components: an acid, an aldehyde and an isocyanide under mild reaction conditions, with a yield of 36 % grafting efficiency within 30 min. In this thesis, reversible addition-fragmentation chain transfer (RAFT) polymerization was employed to generate polymers with functional end groups. At last, the cellulose-based nanomaterials with covalently tethered functional polymer chains on the surface ($PHEA_{37\text{-}Cy5}$-$PDMAEA_{12}$)-*g*-CNFs were designed to bind and release immunostimulator/chemokines (MIP-1α). The drug carriers were non-toxic against MCF-7 cancer cell lines and successfully up-taken by *in vitro* (both 2D and 3D) cancer cell models. The physical, chemical and biological properties of nanoparticles were performed by a variety of characterization techniques including FT-IR, TGA, UV-Vis, XRD, LSCM, and flow cytometry.

ORIGINALITY STATEMENT

'I hereby declare that this submission is my own work and to the best of my knowledge it contains no materials previously published or written by another person, or substantial proportions of material which have been accepted for the award of any other degree or diploma at UNSW or any other educational institution, except where due acknowledgement is made in the thesis. Any contribution made to the research by others, with whom I have worked at UNSW or elsewhere, is explicitly acknowledged in the thesis. I also declare that the intellectual content of this thesis is the product of my own work, except to the extent that assistance from others in the project's design and conception or in style, presentation and linguistic expression is acknowledged.'

Signed ……

Date ……**26 / 06/ 2020**……

COPYRIGHT STATEMENT

Signed .....

Date ..... **26 / 06/ 2020**.....

AUTHENTICITY STATEMENT

'I certify that the Library deposit digital copy is a direct equivalent of the final officially approved version of my thesis. No emendation of content has occurred and if there are any minor variations in formatting, they are the result of the conversion to digital format.'

Signed .....

Date ..... **26 / 06/ 2020**.....

INCLUSION OF PUBLICATIONS STATEMENT

UNSW is supportive of candidates publishing their research results during their candidature as detailed in the UNSW Thesis Examination Procedure.

Publications can be used in their thesis in lieu of a Chapter if:

- The candidate contributed greater than 50% of the content in the publication and is the "primary author", ie. the candidate was responsible primarily for the planning, execution and preparation of the work for publication
- The candidate has approval to include the publication in their thesis in lieu of a Chapter from their supervisor and Postgraduate Coordinator.
- The publication is not subject to any obligations or contractual agreements with a third party that would constrain its inclusion in the thesis

Please indicate whether this thesis contains published material or not:

☐ This thesis contains no publications, either published or submitted for publication

(if this box is checked, you may delete all the material on page 2)

☐ Some of the work described in this thesis has been published and it has been documented in the relevant Chapters with acknowledgement

(if this box is checked, you may delete all the material on page 2)

☒ This thesis has publications (either published or submitted for publication) incorporated into it in lieu of a chapter and the details are presented below

CANDIDATE'S DECLARATION

I declare that:

- I have complied with the UNSW Thesis Examination Procedure
- where I have used a publication in lieu of a Chapter, the listed publication(s) below meet(s) the requirements to be included in the thesis.

Candidate's Name	Signature	Date (dd/mm/yy)
Yee Yee Khine		**26 / 06/ 2020**

POSTGRADUATE COORDINATOR'S DECLARATION *To only be filled in where publications are used in lieu of Chapters*

I declare that:

- the information below is accurate
- where listed publication(s) have been used in lieu of Chapter(s), their use complies with the UNSW Thesis Examination Procedure
- the minimum requirements for the format of the thesis have been met.

PGC's Name	PGC's Signature	Date (dd/mm/yy)
Prof. Naresh Kumar		

For each publication incorporated into the thesis in lieu of a Chapter, provide all of the requested details and signatures required

Details of publication #1:
Full title: Surface modified Cellulose Nanomaterials: A Source of Non-Spherical Nanoparticles for Drug Delivery
Authors: Yee Yee Khine, Martina H. Stenzel
Journal or book name: Materials Horizons
Volume/page numbers: -
Date accepted/ published: Accepted on 21 February 2020, Published on 22 February 2020

Status	*Published*		*Accepted and In press*		*In progress (submitted)*	
		X				

The Candidate's Contribution to the Work
Primary investigator and author

Location of the work in the thesis and/or how the work is incorporated in the thesis:
CHAPTER - 2

PRIMARY SUPERVISOR'S DECLARATION
I declare that:

- the information above is accurate
- this has been discussed with the PGC and it is agreed that this publication can be included in this thesis in lieu of a Chapter
- All of the co-authors of the publication have reviewed the above information and have agreed to its veracity by signing a 'Co-Author Authorisation' form.

Primary Supervisor's name	Primary Supervisor's signature	Date (dd/mm/yy)
Prof. Martina H. Stenzel		**26/ 06/ 2020**

Details of publication #2:
Full title: Photo-Induced Modification of Nanocellulose: The Design of Self-Fluorescent Drug Carriers
Authors: Yee Yee Khine, Rhiannon Batchelor, Radhika Raveendran, Martina H. Stenzel
Journal or book name: Macromolecular Rapid Communications
Volume/page numbers: Volume 41, Article number 1900499
Date accepted/ published: Accepted on 2 November 2019, Published on 18 November 2019

Status	*Published*	***X***	*Accepted and In press*		*In progress (submitted)*	

The Candidate's Contribution to the Work
Primary investigator and author

Location of the work in the thesis and/or how the work is incorporated in the thesis:
CHAPTER – 4

PRIMARY SUPERVISOR'S DECLARATION
I declare that:

- the information above is accurate
- this has been discussed with the PGC and it is agreed that this publication can be included in this thesis in lieu of a Chapter
- All of the co-authors of the publication have reviewed the above information and have agreed to its veracity by signing a 'Co-Author Authorisation' form.

Primary Supervisor's name	**Primary Supervisor's signature**	**Date (dd/mm/yy)**
Prof. Martina H. Stenzel		**26/ 06/ 2020**

Details of publication #3:
Full title: Covalent Tethering of Temperature Responsive PNIPAm onto TEMPO-Oxidized Cellulose Nanofibrils via Three-Component Passerini Reaction
Authors: Yee Yee Khine, Sylvia Ganda and Martina H. Stenzel
Journal or book name: ACS Macro Letters
Volume/page numbers: Volume 7, Page 412-418
Date accepted/ published: Accepted on 8 March 2018, Published on 15 March 2018

Status	*Published*	***X***	*Accepted and In press*		*In progress (submitted)*	

The Candidate's Contribution to the Work
Primary investigator and author

Location of the work in the thesis and/or how the work is incorporated in the thesis:
CHAPTER – 5

PRIMARY SUPERVISOR'S DECLARATION
I declare that:

- the information above is accurate
- this has been discussed with the PGC and it is agreed that this publication can be included in this thesis in lieu of a Chapter
- All of the co-authors of the publication have reviewed the above information and have agreed to its veracity by signing a 'Co-Author Authorisation' form.

Primary Supervisor's name	**Primary Supervisor's signature**	**Date (dd/mm/yy)**
Prof. Martina H. Stenzel		**26/ 06/ 2020**

Add additional boxes if required

ACKNOWLEDGEMENTS

I am feeling obliged in taking opportunity to sincerely thank to all people who have been always helping and encouraging me throughout my PhD journey. Without their help, the completion of this thesis would not have been possible.

First and foremost, my absolute gratitude goes to my beloved supervisor, Scientia Prof. Martina H. Stenzel for her continuous support and guidance during my research studies. I had a chance to know her as the lecturer during my Master by coursework study; Since then, she brought me until the end of PhD with all financial, physical, and mental supports. Also, her unique qualities of life including kind-heartedness, enthusiasm, being wise and immense knowledge always make me proud of being one of her students. My very strong thanks also go to my dear collaborators: Prof. Dr. Michael A. R. Meier at the School of Chemistry (KIT, Germany), and Dr. Maté Biro at the School of Medical Science (UNSW, Australia) for giving me the precious opportunity to work in (as a visiting PhD student) or visit their labs.

In addition, I would like to express my sincere gratitude to my undergraduate supervisor, Daw Si Si Win, who firstly introduced me to the polymer chemistry. Besides my supervisors, my sincere thanks also go to my mentor, Prof. Yanyan Jiang for her assistance and insightful comments in the beginning of my research life. I like to express my deep appreciation to Dr. Aydan Dag, who treats me like her biological sister and always ready to answer all my questions related to experimental works. In addition, I am eager to thank Dr. Robert Chapman and Dr. Hongxu Lu, for their endless help, and efficient lab management. I also like to convey my thanks to UNSW staffs from nuclear magnetic resonance (NMR) facility, electron microscope unit (EMU) and bioanalytical mass spectrometry facility (BMSF).

My deepest appreciations go to all my amazing friends (names are just in the alphabetical order): Dr. Fumi Ishizuka, Dr. Jeaniffer Yap, Dr. Mingxia Lu, Marzieh Monfared, Nidhi Joshi, Dr. Noor Nik Hadzir (Awin), Dr. Rhiannon Batchelor, Dr. Radhika Raveendran, Sylvia Ganda, Steph Xu, Sandy Wong and Dr. Sri Agustina for always understanding and helping me during my difficult time. It was my great pleasure to work in the good environment with nice colleagues (names are just in the alphabetical order): Dr. Alberto Piloni, Ahmed Mustafa, Dr. Ben Kent, Dr. Cheng

Cao, Daniele Melodia, Dr. Fan Chen (Charles), Guannan Wang, Dr. Haiwang Lai, Henry Foster, Dr. Janina Noy, Johnny Lim, Jordan Lovegrove, Lin Zhang, Dr. Manuela Callari, Dr. Mitchell Nothling, Russul Mahmood, Rebecca Lai, Shegufta Farazi, Yiping Wang, Yimeng Li, Zihao Li (Alvin) and all others in the group including visiting PhD students: Kamilia Henni, Dr. Malgorzata Burek (Gosia), Mehwish Abid, Maximiliane Frölich, and so on. I also thanks to all my close friends from my home country, Myanmar, for their kindness, friendship, and the warmth. I especially like to send my gratitude to Mitch, Radhika, Rhiannon, Sandy, and Steph for proofreading my thesis.

I am very grateful to the AVSS (Australian Visa and Student Service, Myanmar) for firstly introducing me to study in Australia and the University of New South Wales (UNSW) for kindly providing me the University International Postgraduate Award (UIPA) for undertaking 3.5 years of PhD program. This financial support gave me the life-changing experiences as a doctoral student.

Special thanks are owed to my family: my parents and all my siblings, who have supported me throughout my years of education, both morally and financially. Without their unparalleled love, help and support, this journey would not have been possible. I am always grateful to my brother, Mr. Thet Zawmyintoo, who sacrificed most of his precious time to give me the opportunities and invaluable experiences that have made me who I am now. My family is a hidden strength behind every success that I have achieved.

ABSTRACT

Cellulose nanomaterials are excellent carriers to deliver therapeutics as they are biocompatible and have a desirable non-spherical shape. However, these materials display low solubility in aqueous media and need to be modified with water-soluble polymers to achieve high colloidal stability. A critical challenge is to perform efficient surface modification without disrupting the original properties of cellulose. In this study, we modified TEMPO-oxidized cellulose nanofibers bearing carboxylic acid moieties (CNFs) by two different routes: nitrile imine/mediated tetrazole/carboxylic acid ligation (NICAL), and three-component Passerini reaction. The advantage of these reactions is the direct functionalization of CNFs under ambient conditions in aqueous media so that additional modification or solvent exchange process prior to surface grafting can be avoided. The NICAL reaction was performed under UV irradiation at λ = 326 nm for 10 hr, resulting in the self-fluorescent polymer grafted CNFs. On the other hand, Passerini reaction is regarded as an effective functionalization approach, which can be carried out in the presence of three components: an acid, an aldehyde and an isocyanide under mild reaction conditions, with a yield of 36 % grafting efficiency within 30 min. In this thesis, reversible addition-fragmentation chain transfer (RAFT) polymerization was employed to generate polymers with functional end groups. At last, the cellulose-based nanomaterials with covalently tethered functional polymer chains on the surface ($PHEA_{37\text{-}Cy5}$-$PDMAEA_{12}$)-*g*-CNFs were designed to bind and release immunostimulator/chemokines (MIP-1α). The drug carriers were non-toxic against MCF-7 cancer cell lines and successfully up-taken by *in vitro* (both 2D and 3D) cancer cell models. The physical, chemical and biological properties of nanoparticles were performed by a variety of characterization techniques including FT-IR, TGA, UV-Vis, XRD, LSCM, and flow cytometry.

List of Publications

List of publication included in the thesis:

Chapter 2

1. **Khine, Y. Y.**; Stenzel, M. H., Surface modified cellulose nanomaterials: a source of non-spherical nanoparticles for drug delivery. *Mater Horiz* **2020**.

Chapter 4

2. **Khine, Y. Y.**; Batchelor, R.; Raveendran, R.; Stenzel, M. H., Photo-Induced Modification of Nanocellulose: The Design of Self-Fluorescent Drug Carriers. *Macromol Rapid Commun* **2020,** *41* (1), 1900499.

Chapter 5

3. **Khine, Y. Y.**; Ganda, S.; Stenzel, M. H., Covalent tethering of temperature responsive PNIPAm onto TEMPO-oxidized cellulose nanofibrils *via* three-component passerini reaction. *ACS Macro Lett* **2018,** *7* (4), 412-418.

List of publication not included in the thesis:

1. Lu, M.; **Khine, Y. Y.**; Chen, F.; Cao, C.; Garvey, C. J.; Lu, H.; Stenzel, M. H., Sugar Concentration and Arrangement on the Surface of Glycopolymer Micelles Affect the Interaction with Cancer Cells. *Biomacromolecules* **2018,** *20* (1), 273-284.

2. Lu, M.; Henry, C. E.; Lai, H.; **Khine, Y. Y.**; Ford, C. E.; Stenzel, M. H., A new 3D organotypic model of ovarian cancer to help evaluate the antimetastatic activity of RAPTA-C conjugated micelles. *Biomater Sci* **2019,** *7* (4), 1652-1660.

3. Cao, C.; Zhao, J.; Chen, F.; Lu, M.; **Khine, Y. Y.**; Macmillan, A.; Garvey, C. J.; Stenzel, M. H., Drug-Induced Morphology Transition of Self-Assembled Glycopolymers: Insight into the Drug–Polymer Interaction. *Chem Mater* **2018,** *30* (15), 5227-5236.

Conference Presentations

2019 – The 16th Pacific Polymer Conference (PPC 16) - Singapore

Poster Presentation: Covalent Tethering of Temperature Responsive PNIPAm onto TEMPO-Oxidized Cellulose Nanofibrils *via* Three-Component Passerini Reaction

2018 – World Polymer Congress (Macro 2018) – Cairns, Australia

Oral Presentation: Covalent Tethering of Temperature Responsive PNIPAm onto TEMPO-Oxidized Cellulose Nanofibrils *via* Three-Component Passerini Reaction

2017 – CAMD China-Australia Polymer Symposium CACAPS – Sydney, Australia

Poster Presentation: Covalent Tethering of Temperature Responsive PNIPAm onto TEMPO-Oxidized Cellulose Nanofibrils *via* Three-Component Passerini Reaction

Abbreviations

AA	Acrylic acid
A549	Adenocarcinomic human alveolar basal epithelial cell line
AEM	2-Aminoethylmethacrylate
AEMA	*N*-(2-aminoethylmethacrylamide)
AFM	Atomic force microscopy
AIBN	Azobisisobutyronitrile
AKD	Alkyl ketene dimer
ALB	Albumin
ALP	Alkaline phosphatise
ALT	Alanine aminotransferase
ARGET	Activators regenerated by electron transfer
AST	Aspartate aminotransferase
ATRP	Atom transfer radical polymerization
ATP	Adenosine 5´-triphophate
a.t.	Ambient temperature
BA	Butyl acrylate
B16-F10	Metastatic mouse melanoma cell line
BASO	Basophil count
Bpy	2,2´-bipyridine
BC	Bacterial cellulose
BCA	Bicinchoninic acid
BCNW	Bacterial cellulose nanowhiskers
β-CD	Beta-cyclodextrin
bEnd.3	Mouse brain cell line derived from BALB/c mice
BSA	Bovine serum albumin
BSPA	3-Benzylsulfanylthiocarbonylsulfanylpropionic acid
BUN	Urea nitrogen
C6	Rat brain tumour cell line
Caco-2	Human epithelial cell line
$CDCl_3$	Deuterated chloroform
CHO-K1	Chinese hamster ovary cell line

CHOL	Cholesterol
CHNP	Chitosan nanoparticles
CI	Crystallinity index
CIP	Ciprofloxacin
CNFs	Cellulose nanofibers
COS7	Fibroblast-like cell line
CPADB	4-Cyano-4-(phenylcarbonothioylthio)pentanoic acid
CREAT	Creatinine
CRP	Controlled radical polymerization
CSIRO	Australian commonwealth scientific and industrial research organisation
CTA	Chain transfer agent
CTAB	Cetyl trimethylammonium bromide
CTAC	Cetyl trimethylammonium chloride
CTMAB	Cetyl trimethylammonium bromide
CT imagine	Computerized tomography
3D	Three-dimensional
DA	Diels-Alder reactions
DBTRG-05MG	Human glioma cell line
DCM	Dichloromethane
DDMAT	*S*-Dodecyl-*S*′-(α,α′-dimethyl-α′′-acetic acid)trithiocarbonate
DEGMA	Di(ethylene glycol) methyl ether methacrylate
DLS	Dynamic light scattering
DMA	*N*,*N*-dimethyl acrylamide
DMAE	2-Dimethylaminoethanol
DMAEMA	*N*,*N*-Dimethylaminoethyl methacrylate
DMEM	Dulbecco's Modified Eagle's Medium
DMF	*N*,*N*-dimethylformamide
DMSO	Dimethyl sulfoxide
DMSO-d_6	Deuterated dimethyl sulfoxide
DNA	Deoxyribonuclei acid
D_2O	Deuterium oxide
DOX.HCl	Doxorubicin hydrochloride

DP_n	Degree of polymerization
DTPA	Diethylenetriaminepentaacetic acid
DTX	Docetaxel
DU-145	Prostatic cancer cells
EANI	4-Ethoxy-9-allyl-1,8-naphthalimide
ECTTP	2-((Ethoxycarbonothioyl)thio)propanoic acid
EO	Ethylene oxide
EOSIN	Eosinophil count
EPR	Enhanced permeation and retention
EtOAc	Ethyl acetate
ETOP	Etoposide
FACS	Fluorescence-activated cell sorting
FBS	Fetal bovine serum
Fe_3O_4	Iron(II,III) oxide
FFA	Free fatty acid
FFF-MALS	Field flow fraction-multi angle light scattering
FT-IR	Fourier transform infrared
GlU	Glucose
H4	Human neuroglioma cell line
HaCaT	Immortal human keratinocyte cell line
hASC	Human adipose mesenchymal stem cell line
HBMEC	Human brain microvascular endothelial cell line
HCAEC	Human coronary artery endothelial cells
HCL	Hydrochloric acid
HCT	Hematocrit
HCT-116	Human colorectal carcinoma cell line
HDL	Cholesterol and high-density lipoprotein
HDQ	Hydroquinone
Hela	Immortal human cell line
HEK293	Human embryonic kidney cell line
HepG2	Human liver carcinoma cell line
HEYA8	Human ovarian cancer cell line
hFOB1.19	Human bone derived osteoblasts

HGB	Hemoglobin
HMTETA	1,1,4,7,10,10-Hexamethyltriethylenetetramine
HL-7702	Human hepatocyte cell line
HSA	Human serum albumin
H_2SO_4	Sulfuric acid
HT-29	Human colorectal adenocarcinoma cell line
HUVEC	Human umbilical vein endothelial cell
IC_{50}	The half maximal inhibitory concentration
IL-1β	Interleukin 1 beta
ISO	International organization for standardization
i.v	Intravenous injection
J774	Mouse macrophage cell line
KB	Human epithelial carcinoma cell line
KOH	Potassium hydroxide
KU-7	bladder cancer cell line
LA	Latic acid
LbL	Layer-by-layer
L929	Normal mouse fibroblasts cell line
LCST	Lower critical solution temperature
LDH	Lactate dehydrogenase assay
LDL	Cholesterol and low-density lipoprotein
LiCl	Lithium chloride
LUS	Luteoloside
LUT	Luteolin
LYM	Lymphocyte count
LYS	Lysozyme
M_n	Number average molecular weight
M_w	Weight average molecular weight
MA	Maleic anhydride
MA	Methyl acrylate
MAA	Methacrylic acid
MCCs	Microcrystalline cellulose
MCF-7	Michigan Cancer Foundation-7 (breast cancer cell line)

MCF-10A	Human breast epithelial cell line
MCHC	Mean corpuscular hemaglobin concentration
MCV	Mean corpuscular volume
MDA-MB-231	Epithelial, human breast cancer cell line
MDCK	Madin-Darby Canine kidney cell line
MEOH	Methanol
MEO_2MA	Di(ethylene glycol)methyl ether methacrylate
MePEG	Methyl-polyethylene glycol
METAC	[2-(Methacryloyloxy)ethyl]trimethylammonium chloride
Me_6TREN	Tris(2-(dimethylamino)ethyl) amine
MIP-1α	Immune chemokines/recombinant murine (CCL3)
MMA	Methylmethacrylate
MMAZO	6-[4-(4-methoxyphenylazo)phenoxy] hexyl methacrylate
MONO	Monocyte count
MPS	Mononuclear phagocyte system
MPV	Mean platelet volume
MTT	(3-[4, 5-dimethylthiazol-2-yl]-2,5-diphenyl tetrazolium bromide)
MTS	(3-(4,5-dimethylthiazol-2-yl)-5-(3-carboxymethoxyphenyl)-2-(4-sulfophenyl)-2H-tetrazolium)
MTX	Methotrexate
NaBr	Sodium bromide
$NaIO_4$	Sodium metaperiodate
NaOCl	Sodium hypochlorite
NCI H 460	Human lung cancer cell line
NHS	*N*-hydroxysuccinimide
NICAL	Nitrile imine-carboxylic acid ligation
NIH3T3	Murine fibroblast cell line
NIPA	*N*-isopropylacrylamide
NITEC	Nitrile imine-mediated tetrazole-ene cycloaddition
NMR	Nuclear magnetic resonance
NMP	Nitroxide-mediated polymerization
NpMA	Naphthyl methacrylate
NPs	Nanoparticles

NVCL	*N*-vinylcaprolactam
OEGMA	Oligo(ethylene glycol) methyl ether methacrylate
OMRP	Organometallic-mediated radical polymerization
PAA	Poly(acrylic acid)
PAEM	Poly(2-aminoethylmethacrylate)
PAEMA	*N*-(2-aminoethylmethacrylamide)
PC-3	Prostatic cancer cell line
PCL	Poly(ε-caprolactone)
PDMAEA	Poly(2-(dimethylamino)ethyl acrylate)
PDMAEMA	Poly(2-(dimethylamino)ethyl methacrylate)
PDMAPMAm	Poly(dimethylaminopropyl methacrylamide)
PDLLA	poly-DL-lactide
pDNA	Plasmid DNA
PEEP	Poly(ethyl ethylene phosphate)
PEG	Polyethylene glycol
PEG-PGlu	Poly(ethylene)glycol-poly(glutamicacid)
PEI	Polyethylenimine
PHEA	Poly(2-hydroxyethyl acrylate)
PMDETA	*N*,*N*,*N*′,*N*″,*N*″-Pentamethyldiethylenetriamine
PMMA	Poly(methyl methacrylate)
PMN	Neutrophil count
PLA	Poly(lactic acid)
PLT	Platelet count
PO	Propylene oxide
POX	Poly(2-ethyl-2-oxazoline)
PPEGEEMA	Poly(poly(ethylene glycol)ethyl ether methacrylate)
PPy	Polypyrrole
PTX	Paclitaxel
PVCL	Poly(*N*-vinylcaprolactam)
RAFT	Reversible addition-fragmentation chain transfer
RAW264.7	Macrophage cell
RBC	Red blood cell count
RB-NHS	NHS-modified rhodamine B ester

RDRP	Reversible deactivation radical polymerization
RES	Reticuloendothelial system
RGD	Arginylglycyl aspartic acid
RNA	Ribonuclei acid
ROS	Reactive oxygen species
4-SS	Sodium 4-vinylbenzenesulfonate
SANS	Small-angle neutron scattering
SAXS	Small-angle X-ray scattering
SBAM	Soybeanamide methacrylate
SEM	Scanning electron microscopy
SRB	Sulforhodamine B
3T3	Fibroblast cell line
TA-DA	Tannic acid and decylamine
TAEA	Tris(2-aminoethyl)amine
TBIL	Bilirubin
TBTG	S-(thiobenzoylthioglycolic) acid
TCA	Trichloroacetic acid
TEER	Trans-epithelial electrical resistance
TEM	Transmission electron microscopy
Temp.	Temperature
TEMPO	2,2,6,6-Tetramethylpiperidine-1-oxyl
TET	Tetracycline
TGA	Thermogravimetric analysis
THF	Tetrahydrofuran
THP-1	Human leukemic cell line
TP	Protein
TRIG	Triglycerides
U87MG	Human-derived glioblastoma cell line
US	United States
VAc	Vinyl acetate
WBC	White blood cell
XPS	X-ray photoelectron spectroscopy
ZnO	Zinc oxide

Table of Content

CHAPTER - 1

Introduction, Objectives

&

Outline of the Thesis

1.1. Introduction

Since ancient times, the medicinal products derived from natural resources such as plants, animals, and microorganisms have been widely used against various diseases including cancer, diabetes, and inflammation. The favourable reputation of natural products is due to their remarkable characteristics such as low toxicity and side effects, reasonable price, desirable chemical and biological properties.[1] However, the application of large sized materials in drug delivery encounters major challenges including poor aqueous dispersion, poor bioavailability, poor absorption in the body and, recognition and clearance by the body immune system. Nano based drug delivery systems have emerged as an interesting tool in advanced medicine to alleviate all these critical issues.[2, 3] Nanomaterials can be distinguished as materials with sizes ranged between 1 and 100 nm, enabling them to circulate more freely in the human body as compared to larger materials.[2] Moreover, nanoparticles can be specially designed according to our needs to deliver therapeutics into targeted sites with enhanced efficacy and reduced toxicity compared to conventional drugs.[4] Hence, we herein are interested in the application of plant-derived natural products, more specifically cellulose, as a nano drug carrier. The focus of this work is to generate cellulose-based nanomaterials which are suitable for drug delivery application.

1.2. Objectives

This thesis involves three main objectives:

1. The first is to investigate the efficient surface modification techniques to covalently tether the synthesized polymer chains onto cellulose nanomaterials under mild reaction conditions. From this study, it was expected to produce the functional cellulose nanofibers with unique properties which are suitable for drug delivery applications.
2. The second is to understand the chemical, physical and biological properties of designed polymer-grafted cellulose nanomaterials as drug delivery system.

3. The third is to extend the application of cellulose for cancer immunotherapy by designing the functional cellulose nanomaterials for the delivery of immune stimulators (MIP-1α).

1.3. Outline of the Thesis

This thesis extensively discusses the literature review, and our attempts for the application of cellulose nanomaterials as drug delivery system.

1. **Chapter 2** of this thesis provides context for the aims by reviewing the current literature on the fibrillation techniques to produce cellulose nanomaterials, followed by the surface modification of CNFs with small molecules or polymer chains for their use in biomedical applications, especially in drug delivery. Subsequently, Reversible addition-fragmentation chain transfer (RAFT), is presented as it has been employed for the synthesis of all polymer chains in the thesis.
2. **Chapter 3** focuses on the synthesis of cellulose nanofibrils (CNFs) from microcrystalline cellulose (MCCs) *via* mechanically assisted TEMPO-mediated oxidation and analytical techniques that were applied in the thesis were discussed.
3. **Chapter 4** describes the attempt to synthesize self-fluorescent CNFs by attaching synthetic polymer chains *via* photo-induced nitrile imine-carboxylic acid ligation (NICAL) reaction. The resulting fluorescence property helps to monitor the uptake of designed nanoparticles in breast cancer cell line (MCF-7). The drug loading experiment indicates that the higher drug loading is more efficient in inhibiting the proliferation of cancer cells.
4. **Chapter 5** investigates an alternative approach called Passerini reaction for tethering PNIPAm onto CNFs under ambient conditions. The results indicate that this technique efficiently generates functional CNFs with thermo-sensitivity and colloidal stability without disrupting the original properties of CNFs.
5. **Chapter 6** discusses the design of cellulose-based nanomaterials for binding and release of chemokines (MIP-1α) for cancer immunotherapy. The designed drug-loaded nanoparticles possess *in vitro* stability, low cytotoxicity, and relatively high uptake into both 2D and 3D cell culture models.
6. **Chapter 7** provides the conclusion and recommendations for future works.

CHAPTER - 2

Literature Review

https://doi.org/10.1039/C9MH01727E

Table of Content

2.1. Non-Spherical Nanoparticles as Drug Carriers

Nanoparticles are widely investigated as way to enhance the delivery of drugs. The success is evident by the number of nanoformulations currently on the market and in clinical trials.[5, 6] This field is dominated by nanoparticles developed for the treatment of cancer, but also nanomedicines for other diseases are under development.[5] A large variety of different nanoparticles are available as drug carriers - ranging from dendrimers, micelles to liposomes and many others. It is noticeable though that most nanocarriers discussed in literature are spherical, although in recent years there is more and more interest in non-spherical nanoparticles for nanomedicine as they were found to have superior properties.[7] To understand this, it is important to look at the journey of drug carriers when entering the blood stream. In the body, the nanoparticle may undergo elimination by the reticuloendothelial system (RES), also coined mononuclear phagocytic system (MPS), or renal clearance. Both will limit the circulation time of the nanoparticle before it can reach the tumour. The blood circulation time is initially determined by the size of the nanoparticle. Particles with 100 nm in diameter reported to have the lowest clearance and highest tumour accumulations in some studies.[8] Crucial is also the surface chemistry as this will determine how nanoparticles interact with blood proteins. The resulting protein corona influences the surface structure and ultimately the fate of the nanoparticles.[9] Elongated nanoparticles were found to have prolonged circulation times as they can align in the blood stream and alter the interaction with phagocytes.[10] If nanoparticles manage to evade elimination in the blood, the next step is extravasation, the transition from the blood stream to the tumour tissue.[8] This process is often enhanced by leaky vasculature, which coincides with the sluggish lymphatic drainage of the tumour. This process, coined by Maeda is enhanced permeation and retention (EPR) effect,[11] is often cited as the main motivation for nanomedicine. Extravasation is enhanced with smaller nanoparticles,[8, 12] but simulations have shown that non-spherical nanoparticles with high aspect ratio should have better extravasation.[13] Cylindrical nanoparticles prepared from carbon

nanotubes,[14] iron oxide[15, 16] and polymers[17] displayed prolonged circulation and retention time compared to their spherical counterparts. These particles enable a greater flow through the vascular pore as the elongated nanoparticle can align favourably with the blood stream through the pore while not interacting with the pore as such.[13] Once the nanoparticles reached the tumour tissue, the nanoparticles need to enter the cells to unload their drugs. Again, non-spherical particles behave differently to spherical particles although there are a range of conflicting reports in regards to which shape if superior. [7, 18] Reduced uptake of rod-like nanoparticles compared to spherical ones was observed with gold nanoparticles, [19, 20]self-assembled poly(acrylic acid)-*b*-polystyrene,[21] latex nanoparticles,[22] polyelectrolyte-based hydrogel[23] and self-assembled rods[24] from glycopolymers and others.[25] Cylindrical bacteria such as *E. coli* use their shape to reduce uptake by phagocytosis allowing them to evade immune response.[26-28] In contrast, other studies reported on the enhanced uptake of elongated shapes compared to spherical nanoparticles.[15, 16, 29-31] The difficulty to draw a clear conclusion may stem from the various factors affecting cell uptake, which ranges from properties such as size, surface chemistry to surface charge and the cell line chosen.[25] Non-spherical nanoparticles have additional parameters to consider such as the aspect ratio of the nanoparticles, [32] the flexibility and ability to bend.[33]

The cellular uptake of non-spherical nanoparticles is influenced by the orientation of the rods in relation to the cell surface (**Figure 2.1a**). The internalization of nanoparticles was reported to be enhanced when the tangent angle (Ω) (**Figure 2.1a**) is smaller than 45°, thus below of the value of spherical particles. Internalization of the particles can be inhibited at Ω > 45° because the nanoparticle can only spread on the cell surface but cannot be internalized.[34] The perpendicular entry mechanism of non-spherical nanoparticles suggests that hard nanoparticle that can maintain the shape in this position, as it would be the case with cellulose nanomaterials, would be advantageous. Hard non-spherical particles have indeed displayed better cellular uptake than soft particles.[33] Non-spherical nanoparticles with targeting ligands can

furthermore optimize receptor-mediated endocytosis as the elongated shape allows large amounts of their binding sites to interact with the target cell receptors (**Figure 2.1b**).[18] Moreover, sharp-shaped nanoparticles not only have high tendencies to penetrate the endosomal membrane but also localize in the cytoplasm limiting the chance of nanoparticles to be excreted *via* exocytosis.[35]

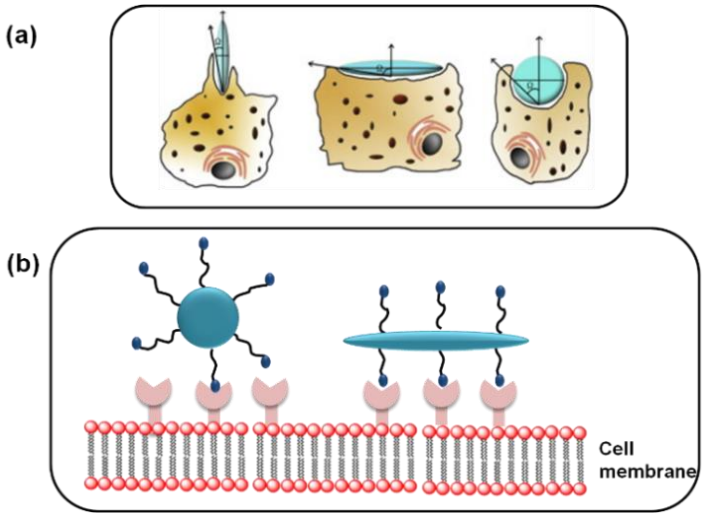

Figure 2.1. (a) The effect of particle shape on cellular uptake,[34] and **(b)** the interaction of spherical and elongated nanoparticles with cell receptors.

Considering the prolonged circulation time and the unusual cell uptake of non-spherical nanoparticles, a case can be made for their use as drug carriers. Non-spherical nanoparticles can be generated with a range of techniques. Inorganic nanoparticles such as gold rods are easily obtained by adjusting the conditions during the gold nanoparticle formation. Rods based on organic materials such as polymers can be obtained by the self-assembly of block copolymers, the use of crystalline block copolymers or by the synthesis of graft polymers.[36] Whoever worked with these approaches knows that some of them are difficult to reproduce and upscale to kilogram amounts. While these approaches have a lot of merits, we propose the use of cellulose nanomaterials as a source of a non-spherical scaffold. In the following, we will introduce the readers to cellulose nanomaterials and the opportunities to use these materials as non-spherical drug delivery carriers. This includes a detailed discussion on the surface functionalization, which is necessary to generate nanoparticles with high stability in blood.

2.2. Cellulose Nanomaterials

Significant progress has been made in recent years in the applications of natural polymers, including collagen, starch, alginate, gelatin, chitosan, elastin, and cellulose as promising biomaterials owing to their low cost, renewable and bio-degradable characteristics.[37] Among all, cellulose nanomaterials have attracted a great deal of scientific and technological interest owning to their outstanding chemical, mechanical, structural and biological properties.[38]

Cellulose is a fibrous, tough and water-insoluble substance, which can in theory be isolated from any plant including flax (retted), flax (unretted), hemp, jute, kenaf, ramie, bagasse, soft wood, hard wood, cotton, sisal, wheat, bamboo and coconut (coir).[39-41] Plant cellulose is mainly assembled into long microfibrils on the inner surface of the primary cell wall, which is embedded in a hydrated matrix of hemicellulose, pectin, proteins, fats, waxes and minerals.[39, 42, 43] These microfibrils (with diameter approximately 2 - 20 μm and length in the range of 100 - 40,000 nm depending on the origin) consist of approximately 36 individual cellulose molecular chains with 5 – 50 nm in diameter. An individual cellulose fibril contains water-insoluble and linear polysaccharides with several hundreds to many thousands of β-1,4-anhydro- D-glucopyranose units joined by β- D-(1 → 4) glycosidic linkages. Each unit has three hydroxyl groups on carbon position 2, 3, and 6 (C2, C3 and C6) with the primary hydroxyl group on C6 being much more reactive than the other two.[44] Cellulose chains interact with each other through inter- and intra-molecular hydrogen bonds, where intermolecular hydrogen bonding occurs between the hydrogen at the C6 position and oxygen at the C3 position as well as the hydrogen at the C2 position and oxygen at the C6 position. In contrast, intramolecular hydrogen bonding occurs between the hydrogen at the C2 and the adjacent oxygen at the C6 position as well as the OH group at the C3 position and the hemiacetal oxygen belonging to the adjacent glucose unit (**Figure 2.2**).[45] Cellulose consists of both crystalline (highly ordered) and amorphous (disordered) domains in varying proportions, depending on the sources of plant species. The mechanical property of cellulose depends on both crystallinity

and type of cellulose present. Amongst several types of cellulose, type I is native cellulose and possesses better mechanical properties, whereas other types (II, III, IV and V) can be obtained by degeneration or alkali treatment of native cellulose. Nishiyama *et al.* expanded the understanding on the crystallinity of cellulose and observed that the crystalline structure of native cellulose is a mixture of two crystal allomorphs: namely cellulose I_α and I_β.[46-48]

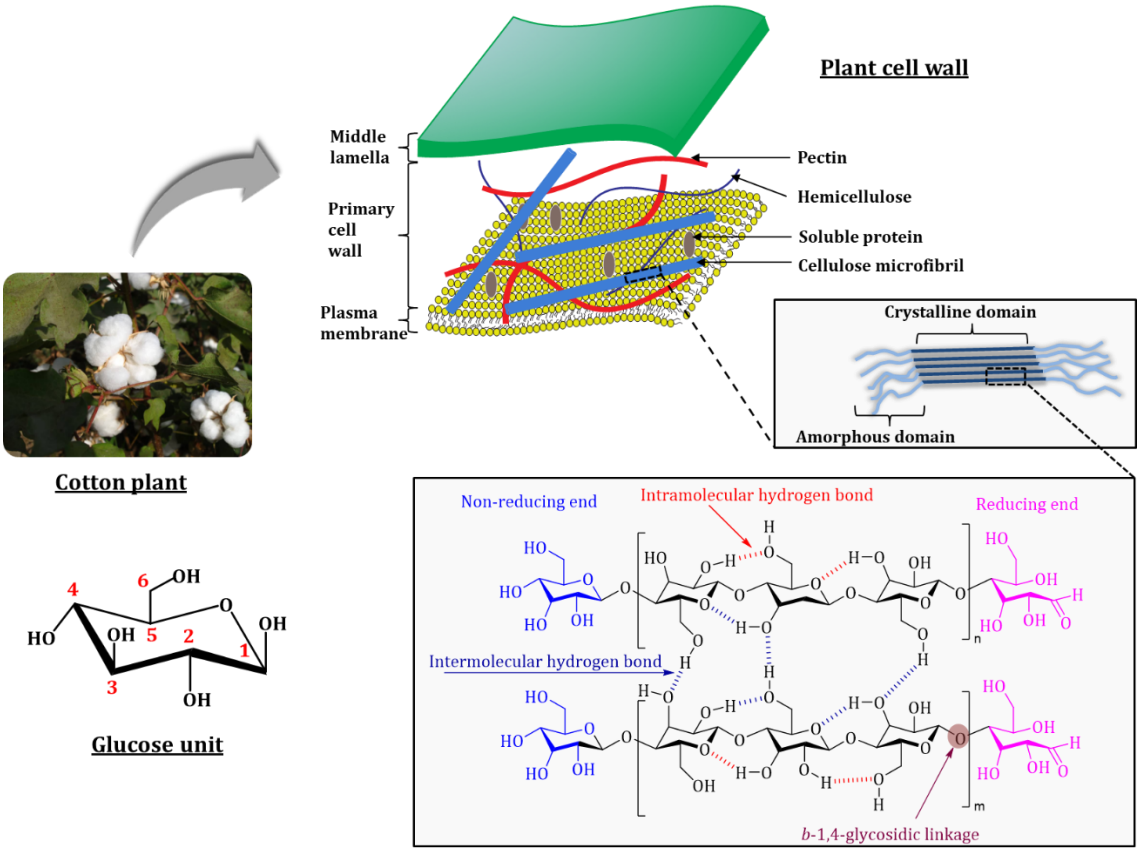

Figure 2.2. Illustrated diagram of cellulose production from cotton plant, and the structure presenting the arrangement between individual fibers.[49]

The amount of these phases can vary depending on the origin of cellulose.[46] I_α can be found in some algae and bacterial cellulose, while I_β can be found in higher plants such as cotton and wood.[48] Preparation of cellulose nanomaterials involve the disintegration of native cellulose from a large unit (μm) to a small unit (nm), mainly by destroying inter- and intra-molecular hydrogen bonds between individual chains. Depending on the source of cellulose and the employed extraction conditions, cellulose nanomaterials have been

divided into three main categories: (a) cellulose nanocrystals (CNCs), (b) cellulose nanofibrils (CNFs), which is also known as nanofibrillated cellulose, and (c) bacterial cellulose (BC).[45]

2.2.1. Cellulose nanocrystals (CNCs)

When native cellulose is treated with acid, the fibres will start to break down into rod-like fragments. Acid hydrolysis is commonly carried out using predominantly sulfuric acid (H_2SO_4) or hydrochloric acid (HCl) under aqueous condition at high temperatures.[50-53] This technique results in the formation of cellulose nanomaterials with high crystallinity as acid breaks down the amorphous region of the native cellulose, which is more susceptible to acidic treatment than the crystalline regions.

The general procedure of acid hydrolysis to yield individual cellulose involves the treatment of cellulose with acids under constant stirring at high temperature, followed by dilution in water to quench the reaction, centrifugation, washing with water (or) dialysis against water to remove residual acid, and finally mechanical treatment like homogenization or sonication.[54-56] The obtained CNCs have a cross section of 5 - 12 nm and are usually 100 - 200 nm in length.[54, 57] CNCs treated with HCl[58] have low colloidal stability as a result of the abundance of hydroxyl groups on the surface.[52] Hydrolysis using H_2SO_4 is in contrast often preferred as it introduces a small amount of negatively charged sulfate groups ($-SO_3^-$) on the surface of CNCs, [59] which contributes to the high dispersibility in aqueous media due to the electrostatic repulsion, although this often lowers the thermal stability. [60] Some recent strategies including $FeCl_3$-catalyzed formic acid hydrolysis,[61] metal-salt based HCl hydrolysis,[53] phosphotungstic acid based hydrolysis[62] and pressurized heating in a stainless steel vessel[63] were found to enhance the properties such as the morphology, crystallinity, and thermal stability of the CNCs.[51, 61, 64-66] **Table 2.1** summarizes CNCs from various sources and prepared *via* different isolation conditions.

Table 2.1. Reaction conditions of acid hydrolysis, the final properties, and the yields of produced CNCs.

Source	Main component for hydrolysis	Reaction temperature (°C)	Reaction time	Catalyst	Size		CI[b] (%)	Yield (%)	Ref.
					Diameter (nm)	Length (nm)			
Eucalyptus	Formic acid (88 wt %)	90	12 hr	$FeCl_3$	11	141	79	24.2	[61]
Cotton	Sulfuric acid (64 wt %)	45	45 min	-	7	128			[55]
Bamboo	Phosphotungstic acid (12.5 wt %)	90	≈ 8 - 9 hr	-	25 - 50	200 - 300	79.6	88	[32]
				-	23 ± 10	245 ± 24	89.4	85	
				$FeCl_3$	10 ± 3	168 ± 25	92.3	73	
Microcrystalline cellulose	Hydrochloric acid (4 M)	110	3 hr	$AlCl_3$	14 ± 7	190 ± 17	91.8	77	[53]
				$CuCl_2$	18 ± 9	208 ± 23	91.5	78	
				$MnCl_2$	20 ± 7	221 ± 21	91.0	80	
Microcrystalline cellulose	Pressurized hot water (20.3 MPa)	120	1 hr	-	55 ± 20	242 ± 98	79.0	21.9	[63]
Ferula gummosa	Sulfuric acid (64 wt %)	45	2 hr	-	20 - 60 nm round shape		-	-	[67]
Hardwood	Sulfuric acid (64 wt %)	50	50 min	-	171 ± 41	14.9 ± 3.5	54.9	20	[68]

Source	Main component for hydrolysis	Reaction temperature (°C)	Reaction time	Catalyst	Size		CI[b] (%)	Yield (%)	Ref.
					Diameter (nm)	Length (nm)			
Softwood	Sulfuric acid (64 wt %)	50	50 min	-	179 ± 43	16.9 ± 4.5	58.0	20.5	[68]
Cotton	Sulfuric acid (64 wt %)	50	50 min	-	278 ± 68	33.0 ± 3.38	65.1	33.4	[68]
Cattail fibers	Sulfuric acid (64 wt %)	50	50 min	-	249 ± 65	18.7 ± 4.5	54.1	17	[68]
Red algae	Sulfuric acid (64 wt %)	50	50 min	-	432 ± 87	28.6 ± 6.5	62.8	20.5	[68]
Cassava root[a]	Sulfuric acid (30 wt %)	60	30 min	-	400 ± 31	5.4 ± 1.3	56	55	[69]
Rice straw	Sulfuric acid (64 wt %)	50	75 min	-	130 - 650	12 - 20	66.3	64	[70]
Wheat straw	Sulfuric acid (64 wt %)	50	75 min	-	120 - 600	15 - 20	71.0	75	[70]
Barley straw	Sulfuric acid (64 wt %)	50	75 min	-	160 - 800	10 - 25	63.4	69	[70]

a) many acid concentrations and reaction times were tested, only one example is given here, b) crystallinity index

2.2.2. Cellulose nanofibers (CNFs)

Cellulose nanofibers (CNFs), which contain both amorphous and crystalline parts, can be isolated by chemical treatment, especially by TEMPO-mediated oxidation, which is effective in the production of CNFs with a high surface content of carboxylates. The catalytic oxidation using stable nitroxyl radicals such as 2,2,6,6-tetramethylpiperidine-1-oxyl (TEMPO), assisted by sodium hypochlorite (NaOCl) and sodium bromide (NaBr), is highly selective for primary alcohols. A significant increase in the water-solubility of the oxidized cellulose nanomaterials was observed owing to the presence of carboxyl groups that imparted negative charges to the surfaces depending on the pH value and thus induce electrostatic stabilization.[71] The advantage of TEMPO-mediated oxidation is its green and facile process, cost-effectiveness, its selectivity to primary alcohols, the high yield of the final product while maintaining crystallinity, morphological stability and high aqueous dispersibility.[64, 72] CNFs, which are prepared *via* TEMPO-mediated oxidation followed by a mechanical treatment, can be obtained with approximately 7 nm in diameter with high aqueous dispersibility and relatively high crystallinity (56 %).[73-75] Titration of the obtained CNFs revealed a carboxylate group density of approximately 1.6 mmol of groups per gram of oxidized-CNFs.[73, 74] However, the amount of carboxylate groups, the degree of polymerization and the yield of CNFs are highly dependent on the concentration of NaOCl added and the strength of mechanical treatment.[76] Visanko and co-workers proposed oxidation using periodate as an alternative approach. Unlike TEMPO-oxidation, this reaction oxidizes the hydroxyl groups of cellulose at position 2 and 3 and cleaves the C2-C3 bond to form aldehyde groups.[77, 78] The most notable feature of this technique is that the formation of dialdehyde cellulose is devoid of significant side reactions.[77] The reaction is conducted using lithium chloride (LiCl)-assisted sodium metaperiodate ($NaIO_4$) oxidation at an elevated temperature of 75 °C (**Figure 2.3**).

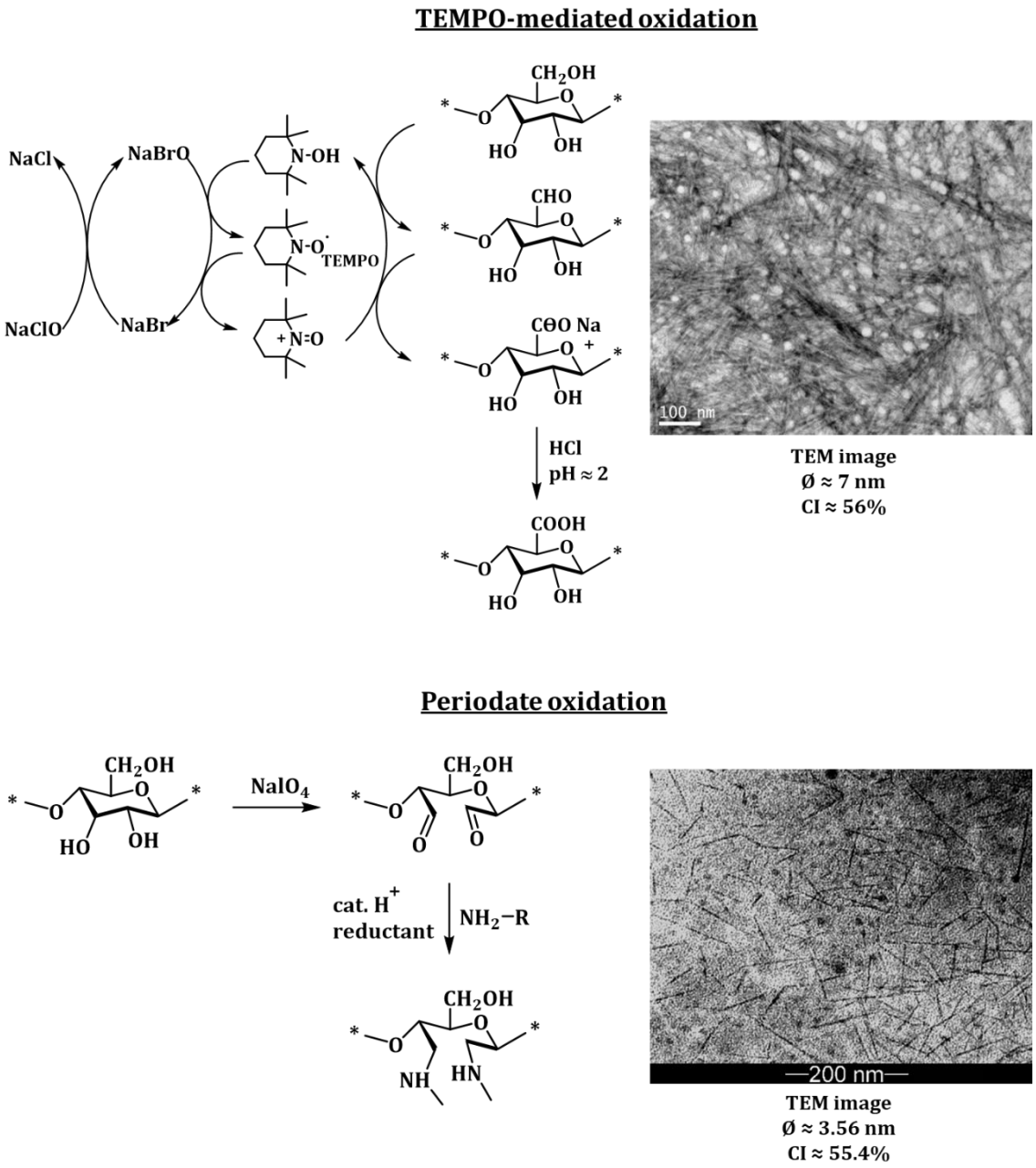

Figure 2.3. Schematic illustration for the preparation of CNFs *via* two different oxidation methods: TEMPO-mediated oxidation and periodate oxidation.[73, 77] Both techniques were assisted by mechanical treatment. TEM images are reprinted with permission from (ref. [73, 77]). Copyright (2014, 2018), American Chemical Society.

2.2.3. Bacterial cellulose (BC)

Bacterial cellulose (BC), a promising natural polymer synthesized by bacteria, has the same molecular formula as plant-derived cellulose, but with better properties including higher purity and higher water retaining capacity. Some bacterial species that can extracellularly produce cellulose include Gram-positive bacteria such as *Sarcina ventriculi* and Gram-negative bacteria such as *Acetobacter*, *Aerobacter*, *Gluconacetobacter xylinus*, *Rhizobium*, *Salmonella*, *Alcaligenes*, *Azotobacter*, *Achromobacter*, *Agrobacterium* and *Pseudomonas*. Among the mentioned species, *Gluconacetobacter*, *Agrobacter* and *Sarcina* are the most studied sources of cellulose. The synthesis of BC can be effectively performed in both synthetic and non-synthetic media through oxidative fermentation at a pH range of 3 – 7 within a temperature between 25 and 30 °C, using saccharides as a carbon source. The biosynthesis of BC consists of a complex process, but in general, the bacterial species firstly produce 1,4-β-glucan chains in the body and extrude them outside the cell through tiny pores, allowing them to self-assemble into microfibrillar structure. The readers are referred to the review article published by UI-Islam *et al.* for detail synthetic strategies for BC.[79] The formed microfibrils from each synthetic site further aggregate to form cellulose ribbons in the growth medium. The formed ribbons generate a pellicle, which allows bacteria float at the air-liquid interface where the oxygen is readily supplied. The BC production yield can be affected by the several parameters including culture methods, bacterial strains, fermentative media, carbon sources, and growth conditions. **Table 2.2** summarises the recent investigations on main factors which can be altered to achieve high yield of BC.

Table 2.2. Production of BC by using different carbon sources, fermentative media, and cultivation conditions.

Bacterial Name	Carbon Sources	Fermentative Medium	Concentration of carbon source (%, w/v)	Cultivation Conditions	Yield ($g\ L^{-1}$)	Year	Ref.
Komagataeibacter xylinus K2G30 (UMCC 2756)	Mannitol, xylitol and glucose	GY broth	1.5 (Mannitol) 5 (Glucose) 5 (Xylitol)	Static, 9 days, 28 °C	8.77 ± 0.04 (Mannitol) 6.17 ± 0.02 (Glucose) 1.36 ± 0.05 (Xylitol)	2019	[80]
Komagataeibacter rhaeticus PG2	Fructose, lactose, xylose, sucrose, galactose, mannitol, sorbitol and glycerol	Hestrin–Schramm (HS) liquid media	2	Static, 15 days, 28 °C	~ 6.9 (Glycerol) ~ 4.05 (Glucose) ~ 1.65 to 3.41 (Sorbitol and Mannitol) ~ poor yield (others)	2018	[81]
Komagataeibacter xylinus B-12068	Maltose, mannitol, sucrose, and galactose	Hestrin-Schramm (HS) agar medium	2	Static, 7 days, 30 °C	~ 2.2 (Glucose) ~ 1.6 (Sucrose) ~ 1.4 (Galactose) ~ 0.1 – 0.2 (Maltose and Mannitol)	2018	[82]
Komagataeibacter medellinensis	Glucose, fructose, and sucrose	Standard Hestrin-Schramm medium	2	Static, 8 days, 28 °C	2.80 (Glucose) 1.68 (Sucrose) 0.38 (Fructose)	2017	[83]
Gluconacetobacter xylinus (PTCC 1734, A2 and S)	Glucose, fructose, sucrose, mannitol, food-grade sucrose, glycerol, whey and starch	Hestrin-Shramm medium		Static, 20 days, 28 °C		2016	[84]

Bacterial Name	Carbon Sources	Fermentative Medium	Concentration of carbon source (%, w/v)	Cultivation Conditions	Yield ($g\ L^{-1}$)	Year	Ref.
Gluconacetobacter xylinus (PTCC 1734)	syrup, glucose, mannitol, sucrose, and food-grade sucrose	Hestrin–Schramm	2	150 rpm, 7 days, 28 °C	~ 1.4 (Mannitol) ~ 0.7 (Food-grade sucrose) ~ 1.45 (Sucrose) ~ 1.15 (Date syrup) ~ 0.85 (Glucose)	2015	[85]
		Yamanaka	5		~ 1.05 (Mannitol) ~ 1.1 (Food-grade sucrose) ~ 1.5 (Sucrose) ~ 0.65 (Date syrup) ~ 0.7 (Glucose)		
		Zhou	4		~ 1.85 (Mannitol) ~ 1.15 (Food-grade sucrose) ~ 1.65 (Sucrose) ~ 0.9 (Date syrup) ~ 1 (Glucose)		

2.3. From Cellulose Nanomaterials to Nanomedicine

Cellulose-based nanomaterials are now widely applied for biomedical application[86-88] such as medical implants,[89] tissue engineering,[90, 91] drug delivery,[92] wound healing,[93] and other medical applications. Some products based on cellulose nanomaterials have even made it into clinical trials.[86] In most applications, cellulose nanomaterials are used predominantly as structural materials to enhance the physico-chemical properties of the large-scale bulk materials[86] such as hydrogels.[94]

The field of drug delivery using cellulose nanomaterials is currently dominated by cellulose-based nanocomposites that are processed into films, foams, hydrogels and large scale materials.[88] Applications include wound healing where the high surface area of cellulose nanomaterials was seen as advantageous for increased drug loading together with the enhanced stiffening of the materials. For example, a nanocomposite based on cellulose nanomaterials and poly(ethyleneimine) PEI was used to deliver pDNA and curcumin. After electrospinning, the fibres were employed to treat burns and the experiments using animals showed improved wound healing.[95] A related nanocomposite based on CNCs, gelatin, collagen and curcumin showed antimicrobial activity, which helped prevent infections during wound healing.[96] Fischer and co-workers designed an antimicrobial dressing based on octenidine by blending cellulose nanomaterials of bacterial origin with the commercial polymer Poloxamer.[97] Bacterial cellulose was also found to be a suitable support for zinc oxide (ZnO)-filled nanocomposite with antibacterial activity.[98] While these materials prevented infection during wound healing, strategies were explored to enhance the wound healing process. This was accomplished by soaking sutures made from cellulose nanomaterials with human adipose mesenchymal stem cells (hASC).[99] Next to wound healing materials, other areas that benefit from cellulose nanomaterials is the treatment of cancer. A CNCs-xanthan hydrogel was loaded with 5-flurouracil, which was slowly released from the matrix.[100] Long-term antibiotic release was achieved by preparing composite nanofibers: poly(lactic)acid

(PLA)/CNCs/polyethylene glycol (PEG), loaded with tetracycline hydrochloride.[101] Many of these examples used plant-derived cellulose nanomaterials, but also drug-filled membranes and hydrogels prepared from bacterial cellulose nanomaterials are frequently described.[102-104]

The overview on cellulose-based drug delivery system based on large scale materials (fibres, hydrogels, membranes) was kept brief here. The reader is referred to review articles on the use of cellulose nanomaterials in a biomedical setting.[86-88] Grassi and co-workers discussed cellulose materials from the viewpoint of the medical application.[86] In contrast, Khademhosseini and co-workers focused on hydrogels, foams and films for biomedical application in relation to the type of cellulose-based nanomaterials such as CNCs, BC and CNFs.[88] Sotudeh- Gharebagh discussed the preparation of nanoparticles, tablets, hydrogels, and aerogels for drug delivery,[105] while Fischer and co-workers focussed specifically on BC as carrier for therapeutic drugs.[106] In many cases, cellulose nanomaterials were not functionalized and used as prepared as the existing surface functionality is sufficient to adsorb the drugs and to create stable composites. There is however no review available that discusses cellulose nanomaterials for i.v. applications. As this material has only limited water-solubility, i.v. applications require the modification of the surface, often with polymers, in order to ensure high colloidal stability in the blood and good protein repellency.

Many of the reported drug delivery applications are topical treatments, but it is well-known that cellulose-based materials can be used for oral administration. Cellulose has been used for a long time to enhance the delivery of drugs. It is widely used in tablets in the form of microcrystalline cellulose.[107] However, the control of the rate of tablet disintegration and drug release is limited, which is the result of a relatively small surface area compared to the bulk of insoluble microcrystalline cellulose combined with weak drug adsorption and limited drug loading capacity. Cellulose nanomaterials in contrast have higher surface areas and can therefore adsorb higher amounts of drugs. Moreover, cellulose nanomaterials have mucoadhesive properties

making these materials ideal for oral delivery. An aerogel loaded with bendamustine hydrochloride was administered orally resulting in a blood concentration of the drug that was superior to the marketed formulation.[108]

At this point in time, it seems that cellulose nanomaterials do not cause any harmful effect and can most likely be used as safe drug carriers. As engineered fibres can potentially be toxic such as in the case of carbon nanotubes,[109] it is understandable that there is caution around the field of nanomaterials.[110, 111 112] Studies on rats that inhaled cellulose dust showed signs of fibrosing granulomatous pulmonary disease. When the same material was incubated with blood cells, evidence of damages induced by radical formation was visible.[113] However, the study used cellulose material on the larger scale, which was often observed to be cleared very slowly from the lungs. CNFs ranging from approximately 3 to 23 μm were barely cleared from rat lungs within a time frame of 400 days.[114] The toxicity and biodurability of cellulose are also crucial as it is the starting material for the preparation of cellulose nanomaterials and the researchers in the lab are exposed to potential dangers when inhaling the raw materials.[115] There is enough concern about long-term damages to the lungs that the US Occupational Safety and Health Administration has put a maximum exposure limit on cotton dust.[116] However, it needs to be considered that these studies use microcrystalline cellulose, but it seems that also inhaled cellulose nanomaterials may cause an inflammatory response in the lungs and change in the alveolar macrophages.[117]

Cellulose nanomaterials have been employed in various cytotoxicity studies, which explored the inhibition of cell proliferation. Various studies have examined the cytotoxicity of cellulose nanomaterials *in vitro* using different cell lines, a variety of incubation times (hours to days), and various assay methods (**Table 2.3**). There is an agreement that cellulose nanomaterials are non-toxic to cells; however, several studies have revealed that the cytotoxicity can be affected by several parameters including the structure, preparation procedure, surface chemistry and cell types. For instance, Alexandrescu *et al.* investigated the cytotoxicity of CNFs with thin, dense, open or porous

structures, respectively, and reported that none of them did induce toxic effects on the tested fibroblast cells (3T3 cells).[118] Ideally, the materials should not only inhibit cell proliferation, but also be devoid of interfering with cell functions and activities. The same authors observed that cellulose-based nanomaterials did not change the mitochondrial activity and the DNA proliferation during direct and indirect contacts between materials and the 3T3 cells.[118] Moreover, recent studies found that cellulose nanomaterials (both CNCs and CNFs) extracted *via* different techniques such as acid hydrolysis and TEMPO-oxidation did not exert acute toxic effects on various cell lines including human dermal fibroblasts,[119, 120] monocyte (white blood cells),[120] murine fibrosarcoma cells (L929),[121, 122] Hela cells,[122] adenocarcinomic human alveolar basal epithelial cells (A549),[123] immortal human keratinocyte cells (HaCaT)[124] and human prostatic carcinoma cells (PC-3)[124] (**Table 2.3**). However, the same samples have a slight cytotoxic effect against human monocytic (THP-1) and breast cancer (MCF-7) cell lines even at the working concentration of 300 μg mL^{-1} (**Table 2.3**). Tibolla *et al.* found dose-dependent cytotoxic effects of cellulose nanomaterials extracted from banana peels using combined chemical (sulfuric acid hydrolysis) and mechanical treatments. The group concluded that the fibrillated CNFs with diameter between 2.89 to 4.65 nm did not reduce the viability of the human colon carcinoma (Caco-2) cell line at low concentrations (50 – 500 μg mL^{-1}), but caused significant cell death at concentrations above 1000 μg mL^{-1} after 24 hr of incubation.[125] In this case, the preparation process of cellulose nanomaterials such as the acid concentration used and the purification procedure was evaluated. With increasing acid concentration, the CNCs were found to increase in toxicity, albeit not significantly. However, cellulose nanomaterials prepared with high acid concentrations in the absence of any mechanical agitation was found to be non-toxic. In another study, cellulose nanomaterials with different amounts of carboxylate groups on the surface was incubated with four different cell lines (MDCK, HeLa, Caco-2, J774).[126] Now it is evident that a more negative surface charge will enhance toxicity although some cells such as MDCK are more sensitive than Caco-2.

It seems that toxicity can be influenced by many parameters such as the type of mechanical processing, the acid concentration during hydrolysis, the source of cellulose materials, end-product impurities during purification process and/or aspect ratio. In general, materials are considered to be safe when their toxicity is below the limit of 70 % as defined by ISO standard.[127] Moreover, the cytotoxicity of cellulose nanomaterials also depend on the tested cell types (**Table 2.3**), but overall there is little evidence that cellulose nanomaterials are cytotoxic. For example, several studies demonstrated the safety of BC regarding its potential use in biomedical applications. The cytotoxicity studies of pure BC and BC composites have been conducted with many other cell lines including HaCaT, L929 and HT-29, showing excellent biocompatibility with no sign of toxicity.[128-130] The recent study evaluated the haemocompatibility (haemolysis and thrombogenicity) and acute and sub-chronic immune responses to three-dimensional (3D) BC biomaterials *via ex vivo* and *in vivo* analyses. The results demonstrated that 3D BC exhibited haemocompatible behaviour and a mild acute inflammatory response but did not elicit foreign body reaction and chronic inflammation.[131] Moreover, the cytotoxicity of CNCs against nine different cell lines (HBMEC, bEnd.3, RAW 264.7, MCF-10A, MDA-MB-231, MDA-MB-468, KB, PC-3 and C6) was measured using two different assays and showed no effects at concentrations up to 50 μg mL^{-1}.[132-134] However, there is evidence that toxicity is cell type specific as incubation of various cellulose nanomaterials with THP-1 cells displayed some cytotoxicity, cellular damage and inflammatory responses, while A549 cells were more resilient.[135]

However, it needs to be considered that low cytotoxicity as measured with standard assays does not mean that the material is safe. More detailed studies that monitor the effect of the material on cell processes are necessary. CNCs incubated with unpolarized and polarized macrophages were readily taken up by the cells and showed only minimal cell proliferation inhibition.[117] However, the presence of CNCs led to a burst of cytokines and changes in the phagocytic activity of the macrophages. This could mean that after exposure to CNCs, the ability of macrophages to respond to infections is hampered.

An interesting observation was made when testing the cytotoxicity on *E.coli* as sonication, which led to better dispersity, enhanced the toxicity.[136] Sonication can help disaggregate CNCs and therefore makes the nanoparticles smaller, this potentially enhances cellular uptake. It was also observed that the surface charge has an effect on the toxicity, although the surface charge itself did not affect the membrane integrity.[126] Indeed, an increased negative charge density, here carboxylates, was observed to lead to higher cell uptake. [126] Enhanced accumulation of cellulose nanomaterials inside the cells may explain in parts why negative charged nanoparticles display enhanced toxicities.

While cellulose is widely used in oral delivery and deemed to be safe, the small size of cellulose nanomaterials may lead to different effects. A recent study explored the effects of ingested CNFs (diameter ≈ 25 nm and 50 nm) and CNCs (diameter ≈ 25 nm and 50 nm) derived from softwood bleached kraft fibres on cell layer integrity, cytotoxicity and oxidative stress by using triculture model in transwell inserts that include enterocytes, goblet cells and M-cells to mimic the intestinal epithelium. The *in vitro* experiments, performed by using trans-epithelial electrical resistance (TEER) measurements, lactate dehydrogenase (LDH) assay, and a fluorometric assay, show that no significant changes in monolayer integrity, cytotoxicity and reactive oxygen species (ROS) production were observed after incubating the cells with ingested cellulose nanomaterials at the working concentration of 0.75 and 1.5 % w/w (**Figure 2.4**).

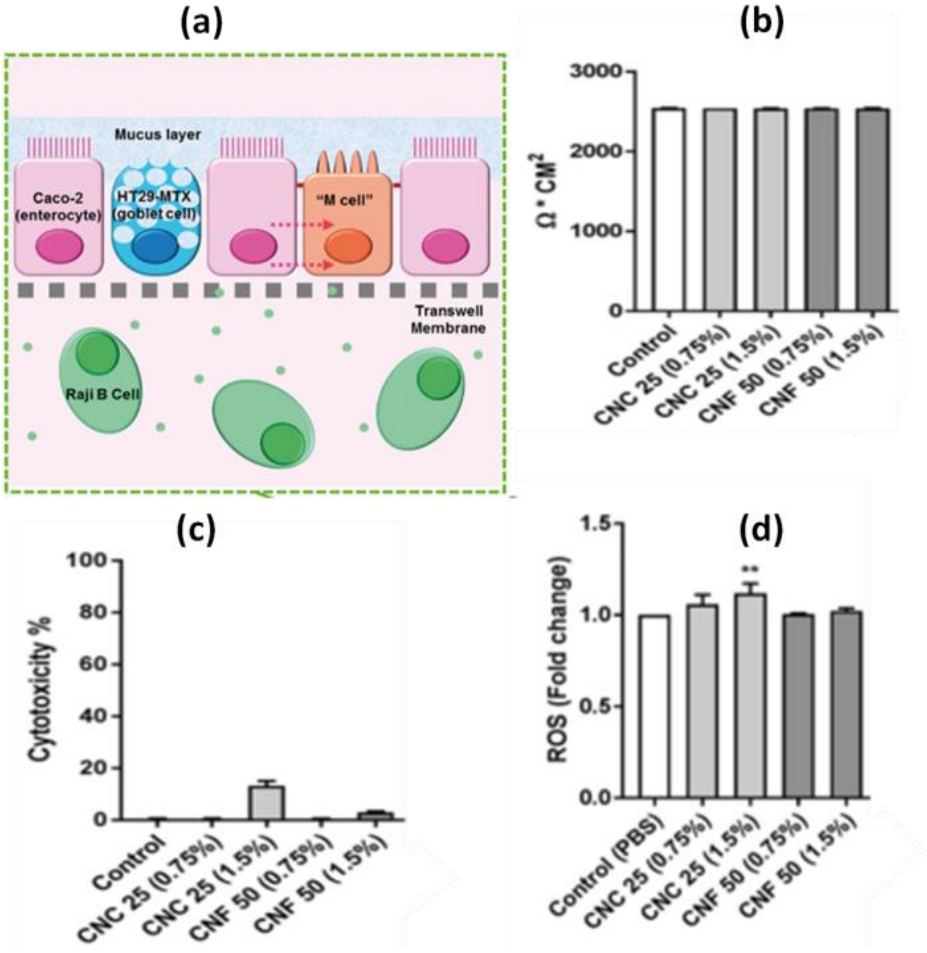

Figure 2.4. (a) Triculture cell model, **(b)** TEER measurements used for cell integrity analysis, **(c)** cell viability (%) analysis from LDH assay after 24 hours of exposure to test materials at specific concentration, **(d)** ROS generation (fold change from control) after 24 hr of exposure to nanomaterials. Reprinted with permission from (ref.[137]). Copyright 2019, Royal Society of Chemistry.

There is only a limited amount of biodistribution studies available. One study on rats using spherical cellulose nanomaterials isolated from *Ferula gummosa* found significant accumulation in the kidney, which may raise concerns. [67] However, the authors used round nanoparticles with sizes of 20 - 60 nm, which may behave differently to the typical cellulose nanomaterials with high aspect ratio. A biodistribution study of cellulose nanomaterials with 200 nm in length and negative surface charges as a result of the acidic treatment of the cellulose with H_2SO_4 found that the CNCs were cleared by the liver and kidney within seven days.[138] However, some accumulation was found in the spleen. Interesting here was that there was a temporal enrichment of cellulose

nanomaterials in the bone, which the authors thought was due to binding with Ca^{2+}. Overall, the mice tolerated the CNCs treatment well.[138] An *in vivo* study with non-spherical CNFs using rats could not find any indication of significant toxicity. Here, rats were ingested with CNFs (diameter ≈ 50 nm) during a five-week study (**Figure 2.5**). The rats showed insignificant weight reduction as well as no differences in blood counts, including total white blood cells, neutrophils, lymphocytes, monocytes, eosinophils, basophils and red blood cells.[139] Similarly, no substantial impacts on hemoglobin concentration, hematocrit, mean corpuscular volume, mean corpuscular hemoglobin, mean corpuscular hemoglobin concentration, platelet count or mean platelet volume were measured after CNFs exposure compared to the control.[139] Also, the treated CNFs did not alter the amount of serum markers (total cholesterol, high density lipoprotein, low density lipoprotein, free fatty acid), markers of hepatic function (alanine amino transaminase, aspartate amino transaminase, alkaline phosphatase, total protein and albumin), markers of renal function (total bilirubin, creatinine) or electrolytes (sodium, potassium, chloride).[139] In the case of white blood cell counts, these results are in contrast to the earlier findings by Yanamala *et al.*. Here, pharyngeal aspiration exposure of wood pulp-derived CNCs (diameter = 88.4 ± 9.8 nm, 200 μg $mouse^{-1}$) caused a significant increase in white blood cells. This might be due to the different exposure route, tested animal model and the properties of cellulose nanomaterials.[140]

These results are highly encouraging as cellulose nanomaterials seemed to be non-toxic against many cell lines, have low environmental risk[141] and have limited toxicities *in vivo*[138, 142] although it has been proposed that the amount of data available so far is not sufficient to draw concrete conclusions.[142] It can so far be concluded that cellulose nanomaterials could be suitable carriers for drug delivery. With lengths between 100 - 500 nm, the size is suitable to circulate in the blood stream for an extended period of time and to display high cellular uptake.[34, 143-146]

Table 2.3. *In vitro* cytotoxic effects of cellulose nanomaterials based on sources, diameter, incubation time, concentration and so on.

Sources	Type of cellulose nanomaterials	Diameter (nm)	Cell type	Assay	Incubation time (hr)	Concentration	Cell viability	Main outcomes	year	Ref.
Picea abies	CNFs	10 - 70 (AFM)	L929	MTT	48	1 mg mL^{-1}	Non-toxic	-	2015	[147]
Wood pulp	CNCs	10 - 20	Hela, L929	MTT	48	1 mg mL^{-1}	Non-toxic	-	2015	[122]
Softwood cellulose pulp	CNCs, oxidized with different COOH content	100 (TEM)	MDCK, HeLa, Caco-2, J774	MTS, LDH	24	300 µg mL^{-1}	20 - 100%	Toxicity depends on cell lines and surface charge	2015	[126]
Wood	CNCs	20 (TEM)	A549 THP-1	Alamar blue	72	300 µg mL^{-1}	Non-toxic ≈ 60 %	Cell viability depends on cell types	2016	[135]
Wood	CNFs	50 (TEM)	A549 THP-1	Alamar blue	72	300 µg mL^{-1}	Non-toxic ≈ 80 %	Cell viability depends on cell types	2016	[135]

Sources	Type of cellulose nanomaterials	Diameter (nm)	Cell type	Assay	Incubation time (hr)	Concentration	Cell viability	Main outcomes	year	Ref.
Soft wood	CNFs	≈ 200 (AFM)	HaCaT, PC-3	MTT	24	10 % v/v	Non-toxic	-	2019	[124]
Ferula gummosa	CNCs	20 - 60 (SEM) Spherical shape	A549	MTT	24	250 µg mL^{-1}	≈ 50 %	-	2019	[67]
Wood pulp	CNCs	100 - 500	*Escherichia coli* strain 652T7	Bioluminescence	3	300 µg mL^{-1}	≈ 90 %	Higher concentration displays antimicrobial activity Sonication enhances toxicity	2016	[136]

AFM: atomic force microscopy, A549: adenocarcinomic human alveolar basal epithelial cell line, Caco-2: human epithelial cell line, CNFs: cellulose nanofibers, CNCs: cellulose nanocrystals, HaCaT: immortal human keratinocyte cell line , Hela: human cell line, , J774: mouse macrophage cell line, LDH: lactate dehydrogenase assay, L929: murine fibroblast cell line, MTT: (3-[4, 5-dimethylthiazol-2-yl]-2, 5 diphenyl tetrazolium bromide) assay, MDCK: Madin-Darby Canine kidney cell line, MTS: (3-(4, 5-dimethylthiazol-2-yl)-5-(3-carboxymethoxyphenyl)-2-(4-sulfophenyl)-2H-tetrazolium, inner salt) assay, PC-3: human prostatic carcinoma cell line, TEM: transmission electron microscopy, THP-1: human leukemic cell line, SEM: scanning electron microscopy

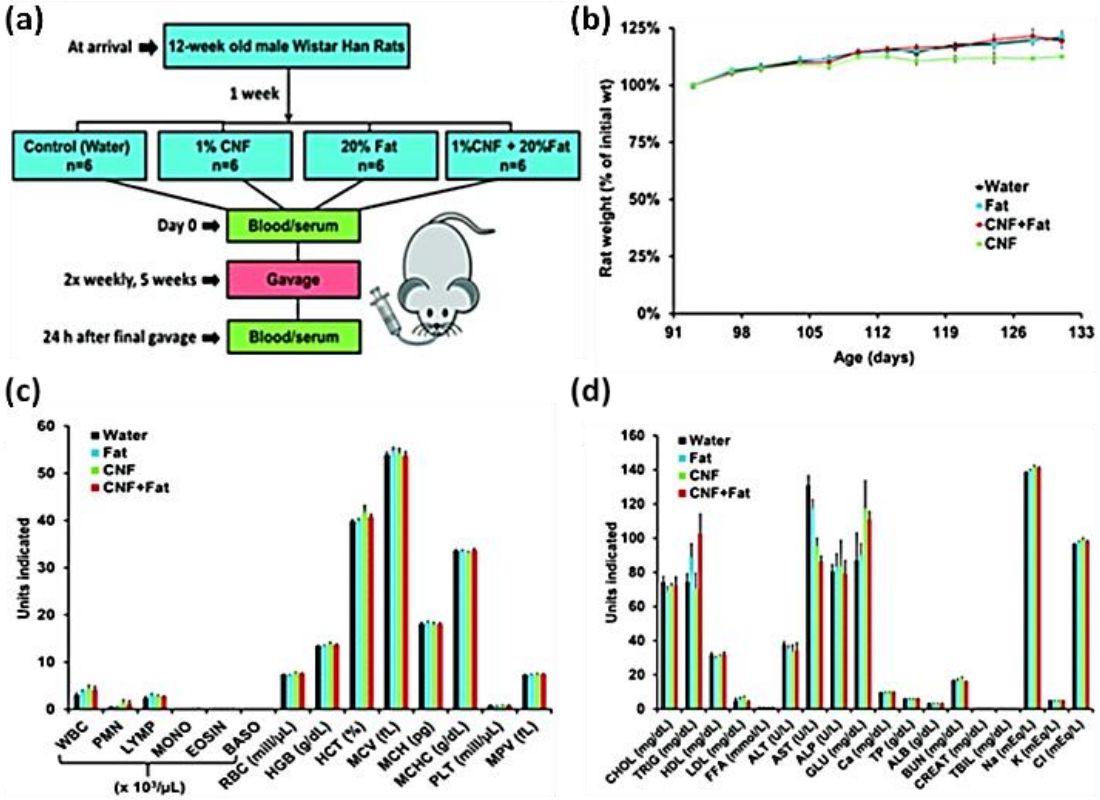

Figure 2.5. *In vivo* cytotoxicity of cellulose nanomaterials in Wistar Han rats: **(a)**the experimental design, **(b)** analysis on the weight change of rats over time, **(c)** changes on blood cell counts and hematological parameters, **(d)** changes in serum markers after exposure with nanomaterials. Reprinted with permission from (ref.[137]). Copyright 2019, Royal Society of Chemistry.

ALB: albumin, ALT: alanine aminotransferase, AST: aspartate aminotransferase, ALP: alkaline phosphatise, BUN: urea nitrogen, BASO: basophil count, CREAT: creatinine, CHOL: cholesterol, total, Ca: calcium, CNFs: cellulose nanofibers, Cl: chloride, EOSIN: eosinophil count, FFA: free fatty acid, GLU: glucose, HDL: cholesterol and high density lipoprotein, HGB: hemoglobin concentration, HCT: hematocrit, K: potassium, LDL: cholesterol and low density lipoprotein, LYM: lymphocyte count, MPV: mean platelet volume, MCHC: mean corpuscular hemoglobin concentration, MONO: monocyte count, MCH: mean corpuscular haemoglobin, MCV: mean corpuscular volume, Na: sodium, PMN: neutrophil count, RBC: red blood cell count, PLT: platelet count, TRIG: triglycerides, TP: protein, TBIL: bilirubin, WBC: white blood cell

Cellulose nanomaterials have the desirable non-spherical shape that may enhance circulation time. As discussed above, non-spherical nanoparticles can be difficult to be produced on a large scale while cellulose nanomaterials can be obtained easily on a kilogram scale. Prerequisite is that enough cellulose raw material is available as a new supplier might lead to slightly different morphologies. A further advantage is that cellulose nanomaterials have high concentrations of functional groups on the surface making it suitable to attach drugs or targeting ligands.

So, what are the challenges? Cellulose nanomaterials by themselves have low water solubility and low stability in various buffer solutions. Although variation in pH values can help to disperse the material, scattering analysis reveals the tendency of cellulose nanomaterials to aggregate. The colloidal instability can be made worse when drugs are attached, which are exposed on the surface, altering solubility.

The key to a successful drug delivery system is the functionalization of the surface to achieve the following outcomes.

- High colloidal stability in the blood stream: This can be achieved attaching either water-soluble polymers or highly charged functional groups.
- Low protein adsorption: The key here is to carefully fine-tune polymer grafting density, the length of the attached polymer and the surface charge as this will influence the amount of proteins attached, the type of proteins and ultimately the fate of the nanoparticle
- Suitable matrix for drug entrapment: The surface of cellulose nanomaterials may have an abundance of functional groups, but these are not suitable to bind hydrophobic drugs or biologics. Surface modification, most promisingly with polymers, can create a matrix that binds drugs chemically or physically resulting in high drug loading content.

Understanding the chemistry of surface modification of cellulose nanomaterials is therefore a crucial parameter. There are several review papers focusing on the surface functionalization of cellulose nanomaterials to tune the mechanical and physical properties of the material.[60, 148, 149] This review in contrast will focus on current advances in surface modification techniques that can be employed to design efficient water-soluble cellulose-based nanovehicles for drug delivery. Surface modification is necessary not only to improve the properties of cellulose nanomaterials but also to bind and release of drugs that cannot easily be bound to the surface, such as hydrophobic and non-charged drugs.

2.4. Surface Modification of Cellulose Nanomaterials

In the following, various reactions are introduced that allow modification of cellulose nanomaterials either directly by using the existing hydroxyl or carboxylic acid groups on the surfaces or indirectly by using techniques that require pre-treatment of cellulose nanomaterials to attach the appropriate functionalities, which can either be controlling agents for polymers (see paragraph below), fluorophores,[150, 151] or simply to modify the surface charge.

2.4.1. Direct surface modification

Reactions with hydroxyl groups

The abundance of hydroxyl groups can be directly used to modify the surface (**Figure 2.6**). Widely explored is esterification using acyl chloride in the presence of pyridine to remove the generated HCl, as the maintenance of a high pH value is crucial to prevent the acidic hydrolysis of cellulose.[152-155] Esters can also be generated using the highly reactive alkyl ketene dimer (AKD)[65] or by solvent-free esterification reactions,[156, 157] Other techniques include the nucleophilic reaction between epoxides and the hydroxyl groups of cellulose nanomaterials results in the formation of stable ether groups[158] as well as silylation.[159-164] [165] Also the formation of urethanes and thiourethanes is possible as the surface bound hydroxyl groups react quickly with isocyanates.[166-171] The reaction with isocyanates seems less important for drug delivery purposes, but conjugation of fluorescent dyes using thioisocyanates is commonly used to create fluorescent cellulose nanomaterials that can be tracked in a biological experiment such as demonstrated using Rhodamine B isothiocyanate.[151] These reactions are often carried out in aqueous solutions at a controlled pH value. Finally, the reaction with dyes such as 5-(4,6-dichlorotriazinyl) aminofluorescein is a popular way to label cellulose nanomaterials with a fluorophore as the dye is commercially available and can be directly reacted with the hydroxyl groups on CNCs.[151, 172]

Surface modification of cellulose nanomaterials			Ref.
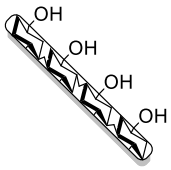	Ester	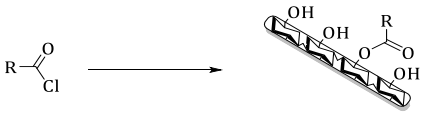	153, 157, 173 156, 157, 152-154, 155, 65
	Ether	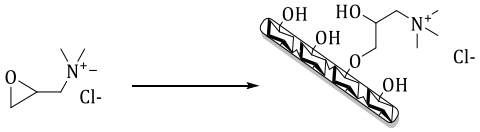	158
	Silane	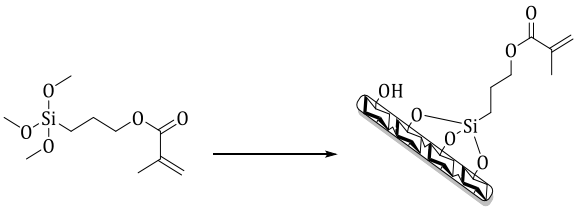	159-165
	Urethane/ thiourethane	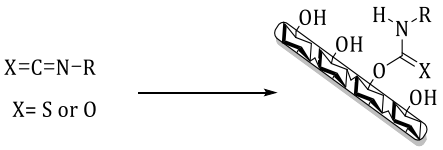	151, 167-169
	Triazine derivatives	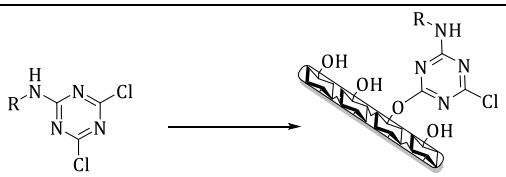	151, 172
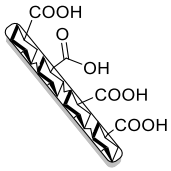	Amide	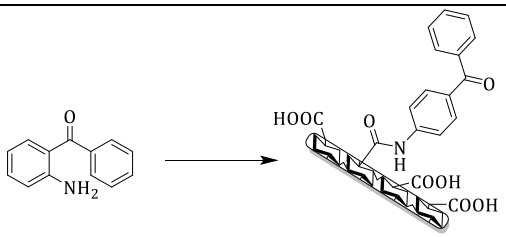	174, 175, 176
	Hydrazide	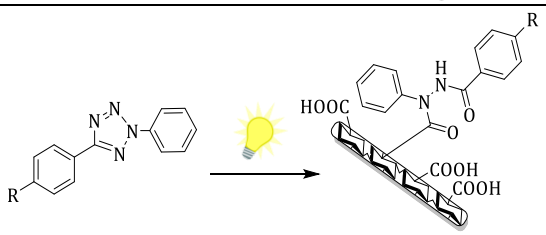	177
	Passerini Product	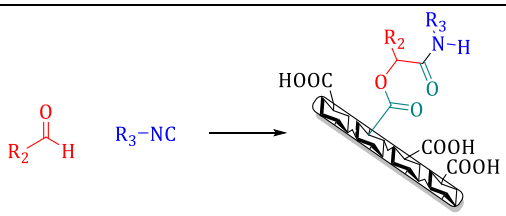	73
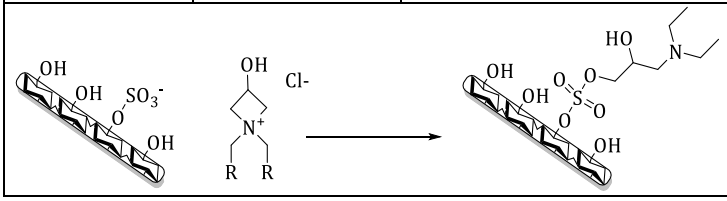			178

Figure 2.6. Summary of coupling reactions carried out directly onto CNCs, CNFs and CNCs with residual sulfate groups without prior modification.

Reactions with carboxylic acid groups

Owing to the wealth of accessible carboxylic acid groups on TEMPO-oxidized cellulose nanomaterials, amidation reaction is well explored to functionalize the surfaces of cellulose nanomaterials (**Figure 2.6**). This reaction is typically facilitated by the addition of a coupling agents.[175, 176] Amidation is often employed to attach fluorophores to TEMPO-oxidized cellulose nanomaterials such as in the case of the reaction with Lissamine rhodamine B ethylenediamine.[151] Occasionally it is deemed necessary to generate activated esters as intermediate, for example in the form of *N*-hydroxysuccinimide (NHS).[174, 179, 180] The nitrile imine carboxylic acid ligation (NICAL), which uses tetrazoles, can directly be employed to functionalize TEMPO-oxidized cellulose nanomaterials without the recourse of an additional functionalization step.[177, 181] Advantage is the formation of fluorescent benzohydrazide that can be used to monitor the interaction with cells. Highly efficient are multicomponent reactions such as Passerini or Ugi reaction that react directly with carboxylic acid.[182] So far, only Passerini reaction has been used to modify cellulose nanomaterials with polymers, which is discussed below.[73] Cellulose nanomaterials isolated by sulfuric acid treatment can moreover be directly reacted using azetidinium salt.[178]

2.4.2. Indirect surface modification requiring pre-modification

The reactions described in this part require the functionalization of cellulose nanomaterials first using any of the reactions described above. Reasons to undergo two-step process may be the enhanced activity of the newly introduced functional group, which is often the case when the new functionality allows click reactions. Two-step processes also allow the introduction of a variety of functional groups allowing the conjugation of a multitude of different molecules such as different dyes.

Amide. Depending on the isolation process of cellulose nanomaterials, carboxylate functionalities may be absent. In that case, the surface can be

modified with amine groups, followed by the coupling reaction between amines and for example activated esters such as the NHS-esters. Navarro and co-workers successfully synthesized fluorescently labelled CNFs by attaching NHS-modified rhodamine B ester (RB-NHS) on the surface of cellulose nanomaterials, which were modified with amines in a prior step (amine-CNFs) (**Figure 2.7**).[183] This technique has been indeed frequently employed to attach fluorescent dye onto cellulose nanomaterials. The amine was introduced *via* epoxide chemistry followed by reaction with isothiocyanates.[150, 184]

Alkyne-Azide click reaction. Prerequisite is the introduction of an alkyne functionality on the surface. This can be accomplished by reacting 1-azido-2,3-epoxypropane with the hydroxyl groups of CNFs at ambient temperature.[185] Alternatively, propargylic groups are introduced by reacting with propargylamine **(Figure 2.7)**,[186, 187] or propargyl-modified 4,6-dichloro-1,3,5-triazine[188] The efficient copper-catalysed click reaction allows now the attachment of various groups including gold nanoparticle carrying dendrimers[186] and β-cyclodextrin.[189] This avenue was explored to react cellulose nanomaterials with poly(ε-caprolactone) PCL[190] and poly(ethyl ethylene phosphate) (PEEP).[122]

Diels-Alder cycloaddition. The attraction of Diels-Alder (DA) reactions lies not only in its efficiency, but also the orthogonality in the presence of other groups.[191-193] Navarro and co-workers aimed at modifying the CNFs with maleimide moiety as depicted in **Figure 2.7 and 2.8**, which can be further modified with functional molecules *via* thiol-Michael click reaction. Subsequent conjugation of different dyes allowed monitoring the labelled CNFs in a biological setting.[153]

Photo-Thiol-Ene or -Yne reaction. These radical reactions were predominantly used to prepare surface modified cellulose nanomaterials for nanocomposites,[155, 165, 194] but this reaction is barely explored to generate water-soluble cellulose-based drug carriers.

Light-Driven Nitrile Imine Mediated Tetrazole-Ene Cycloaddition (NITEC) reaction. The NITEC, which is related to the above discussed NICAL reaction, is a promising light-induced ligation reaction, which involves non-activated alkenes as reaction partners.[195] One of the most attractive properties of the NITEC reaction is the strong fluorescence of the resulting pyrazoline cycloadducts with variable emissions in the region of 487 - 538 nm, depending on the structure of alkene.[196] This allows the design of cellulose nanomaterials with in-build fluorescence, ready for direct monitoring of the material in a biological setting.[175, 197] However, this feature has not yet been explored to generate water-soluble cellulose nanomaterials, but has been tested in the preparation of fluorescent hydrogels containing cellulose nanomaterials.[175, 197]

Thiol-Michael click reaction. In contrast to the radical photo-catalysed thiol-ene or thiol-yne reaction, the thiol-Michael reaction is a nucleophilic reaction.[198] Among all approaches, the reaction with maleimides with thiols is one of the most widely used pathways to functionalize biomolecules *via* thiol-Michael addition. As maleimides can also be used in Diels-Alder reactions, this functional group can be purposed for two separate reactions. This idea was successfully pursued when functionalizing cellulose nanomaterials using Diels-Alder cycloaddition and thiol-Michael reaction at the same time to synthesis multicolour fluorescent cellulose nanofibrils. The authors confirmed the successful attachment of two fluorescent dyes on the surface of CNFs *via* fluorescence spectroscopy, which showed the emission band at 530 nm for the fluorescein dye (excitation = 510 nm) and 406 nm for the coumarin dye (excitation =327 nm) (**Figure 2.8**).[153]

Surface modification of cellulose nanomaterials	Ref.
Amine-maleimide coupling reaction 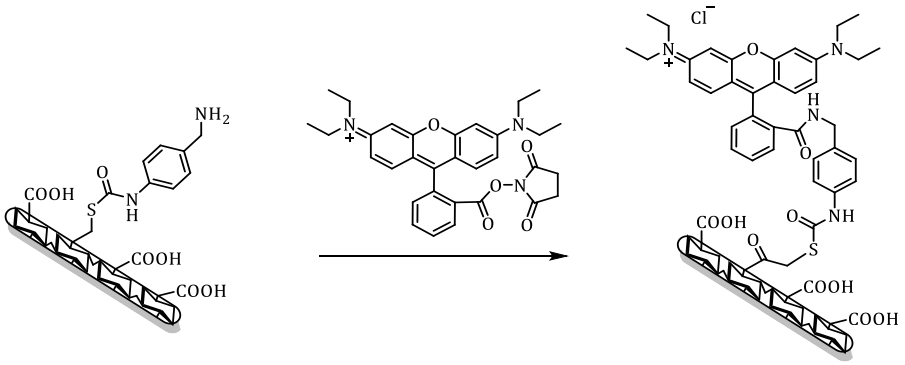	183
Azide-alkyne click chemistry 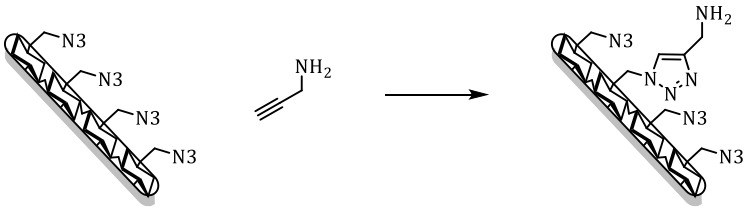	186, 199
Diel-Alder cycloaddition 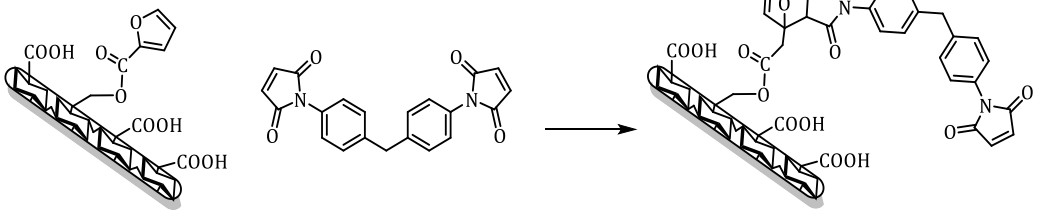	153, 191
Thiol-ene reaction under UV irradiation 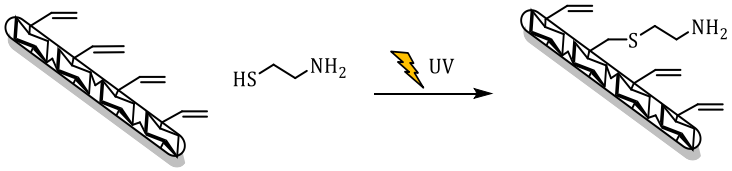	165
Photo-induced thiol-yne reaction 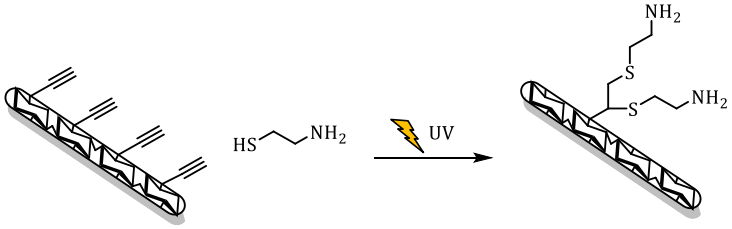	194

Figure 2.7. Surface modifications requiring premodification of cellulose nanomaterials.

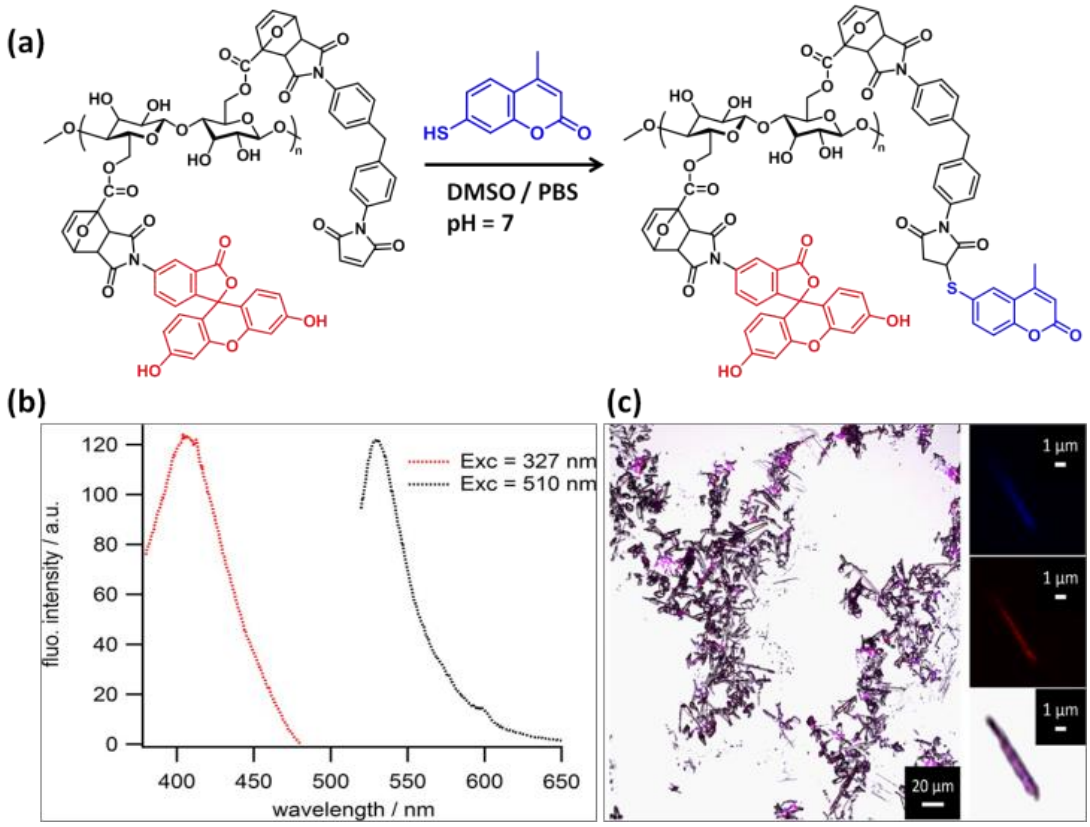

Figure 2.8. (a) Schematic illustration of the synthesis of CNFs modified with two fluorescent probes, **(b)** fluorescence emission spectra of modified CNFs with multicolour fluorescent properties, and **(c)** the overlay confocal scanning laser microscopy imaging of fluorescein/coumarin-labelled CNFs (coumarin, blue colour, excitation wavelength 405 nm and fluorescein, red colour, excitation 540 nm).[200] The pictures are reprinted with permission from (ref. [200]). Copyright 2015, American Chemical Society.

2.4.3. Isotropically modified cellulose nanomaterials: Selective grafting on end groups

Polysaccharides such as cellulose, including cellulose nanomaterials, can be selectively modified at the end group only as the hemiacetal end functionality can react with amines under ring-opening reaction or the group can be oxidized to the carboxylic acid (**Figure 2.9**).[201] This approach makes it possible to bind the cylinder-shaped cellulose nanomaterials to a surface by the base only as it has been done with CNCs modified with thiols at the reducing end.[201] This opened the pathway to some unusual structures as the endfunctional cellulose nanomaterials can be attached to various scaffold. Villares *et*

al. attached biotin by oxidation of the reducing end functionality and subsequent amidation. Incubation with streptavidin that has four binding sites for biotin led to 4-arm star shaped cellulose nanomaterials (**Figure 2.9** picture).[202] The presence of aldehyde groups can also be used to react with dyes such as Alexa Fluor 633 hydrazide.[138] The final fluorescent conjugate was used to measure the *in vivo* distribution of CNCs.

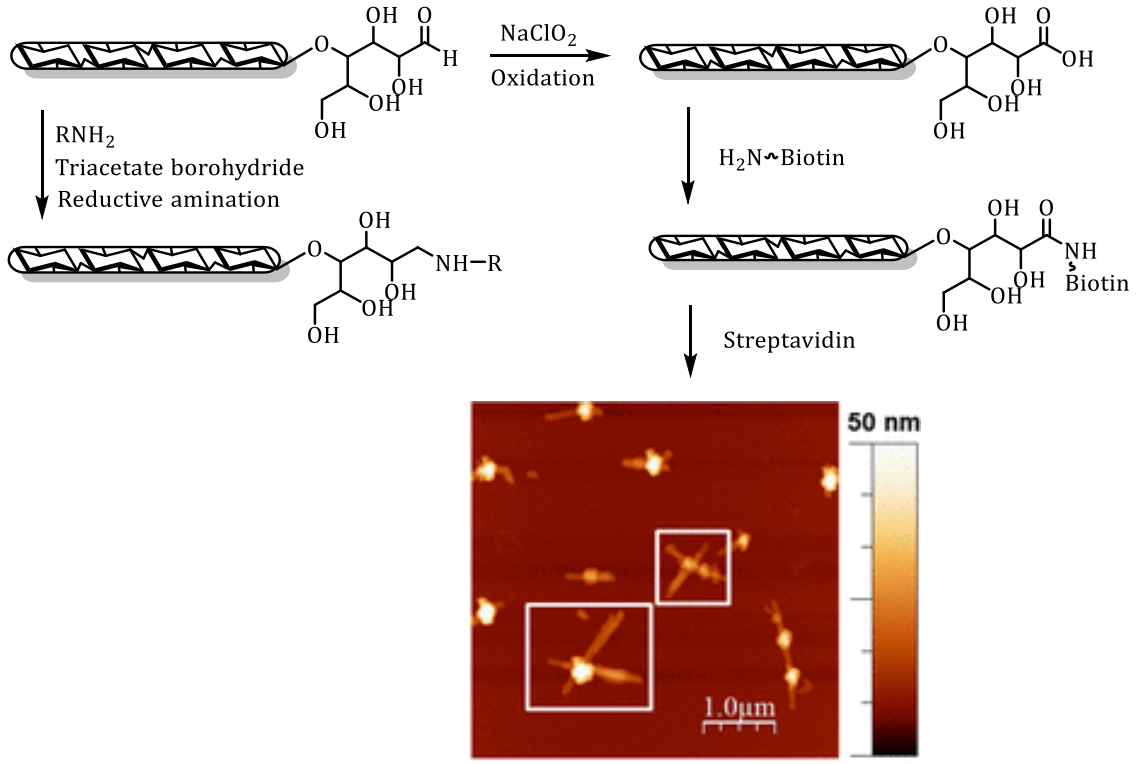

Figure 2.9. Selective reaction at the reducing end to introduce functionalities for either binding to surfaces or to streptavidin (picture insert).[202] The picture is reprinted with permission from (ref. [202]). Copyright 2018, American Chemical Society.

2.4.4. Toxicity of cellulose nanomaterials modified with small functional groups

The initial studies on unmodified cellulose nanomaterials suggest that there is limited toxicity exerted by the material.[203, 204] However, modification with small molecules will now change the surface properties and thus alter the toxicity.

In general, modification of the surface with neutral molecules does so far not cause any toxicity issues. Coating with lignin, which has an abundance of phenolic hydroxyl groups, on CNCs and CNFs seems to slightly increase the cytotoxicity towards A549 and THP-1 cells.[135] These two cell lines were chosen as they are the first exposure to nanoparticles when inhaled. However, the effect of coating on membrane integrity and other cellular function was negligible. It was noted that the type of scaffold had a larger effect as CNCs behaved differently to CNFs.[135]

Another neutral conjugate with plenty hydroxyl groups is cyclodextrin. Cyclodextrin is widely used to enhance the solubility of drugs and was therefore attached to cellulose nanomaterials as a potential host. The presence of cyclodextrin on the surface of CNCs did not alter the cell proliferation of J774A.1 and MCF-7 cells.[205] The material also did not noticeably increases the intracellular inflammatory response.[206] In this study, the materials were exposed to a human monocyte cell line (THP-1) and a mouse macrophage-like cell line (J774A.1). The authors found that there is little increase in IL-1β secretion or the production of reactive oxygen species and they concluded that the material is non-immunogenic.[206]

A photoluminescent hybrid material was obtained by attaching amino-containing carbon quantum dots to the surfaces of TEMPO-oxidized cellulose nanomaterials.[207] The materials were found to be non-toxic to HeLa cells, but displayed some toxicity when RAW 264.7 macrophage cells and concentrations higher than 500 μg mL^{-1} were used. Interestingly, TEMPO-oxidized cellulose nanomaterials were slightly more toxic than the modified one.[207]

Unlike neutral surfaces, it is feasible to think that the attachment of amino groups, which would form potentially toxic cationic charges, should inhibit cell proliferation. Indeed, there are visible toxic effects on J774A.1 and MCF-7 cells after the surfaces of cellulose nanomaterials were modified with primary amines. While there was no toxicity measured after 24 hr of incubation, even low concentrations of 10 μg mL^{-1} caused cell death after 48 hr.[205]

This contrasts the observation made after attaching tris(2-aminoethyl)amine to cellulose nanomaterials as there was no cytotoxicity against MCF-7 cells and limited hemolytic activity.[208] In contrast, attachment of negative charged molecules seems to cause limited toxicity. Surface modification with phosphoric acid led not only to a more negative surface charge, but also to better cellular uptake by osteoblasts, which contrasted with the native CNCs that showed no uptake even after 24 hr. This study also showed how subtle changes to the surface can affect biological outcomes. Conjugation with fluorescent dye increased the hydrophobicity, which led to aggregation and consequently different biological behaviour. There was no evidence of any cytotoxic behaviour according to the MTT assay.[209]

The limited amount of experiments carried out so far highlight that surface modification might not have a huge effect on toxicity, which was also confirmed using *in vivo* models. An embryonic zebrafish model was used to test the toxicity of various cellulose nanomaterials. CNCs, fibrillated from various sources (cotton, kraft pulp or wood pulp) with different surface properties ranging from neutral, cationic and anionic functionalities were found to have low toxicity independent from the surface modification.[121] It appeared however that longer crystals displayed slightly higher toxicity.[121]

2.5. Surface Functionalization of Cellulose Nanomaterials with Water-Soluble Polymers

Surface grafting of polymer chains has been considered as the most effective and versatile method to achieve high stability in solution since interfacial properties can be tuned by the nature of the polymers.[149] Polymer-modified cellulose nanomaterials are either obtained using "grafting onto" and "grafting from" methods.[149] These techniques are well established for cellulose materials, but they are now increasingly applied to graft polymers onto cellulose nanomaterials.

Many reactions between polymer chains and cellulose nanomaterials are not for the purpose to generate soluble polymer wrapped cellulose nanoentities, but to create nanocomposites where the purpose of the cellulose-based nanomaterials is the reinforcement of the polymer material. Examples include the reaction of cellulose nanomaterials with isocyanates modified polymers,[210] the Diels-Alder reaction between cellulose nanomaterials and polymers modified with maleimide and furan, respectively, [192, 211] the reaction between polyethylene amine, epoxides and cellulose,[212] transamidation reactions with polyamides,[208] or the formation of vitrimer composites by reacting epoxides with CNFs.[213] The reader is referred to review articles on the design of nanocomposites of polymers and cellulose nanomaterials[214-216] or cellulose nanomaterials in polymer hydrogels.[94]

Due to the existence of anions on the surface, CNCs can be modified with polymers *via* electrostatic interaction. This approach can form strong physical bonds and was often used to form advanced cellulose nanomaterials.[217] Worth mentioning here is the possibility to coat CNCs with polydopamine (PDA)[218, 219] with the aim to reinforce the PDA material,[218, 219] but also to create well-dispersed nanosized cellulose materials.[220] Conducting CNCs was formed by polymerizing pyrrole in the presence of cellulose nanomaterials creating a conducting layer of polypyrrole (PPy).[221] Similarly, CNCs soaked in Fe(III) ions can initiate the polymerization of rhodamine.[222] Moreover, silica nanorods were obtained by condensation of tetraethyl orthosilicate onto

CNFs.[223] The focus here is the modification of cellulose nanomaterials with hydrophilic polymers that can assist with the solubility of the nanocarriers in aqueous solution.

2.5.1. "Grafting-to" approach

The tethering of polymer chains to a specific surface can be performed *via* chemical or physical attachment although physical attachment is not discussed here. Grafting onto permits the synthesis of well-defined polymer chains with a specific molecular weight and narrow polydispersity prior to the attachment on the surface, thus giving the opportunity to form functionalized cellulose nanomaterials with tailored polymer chains. However, the major limitation is the low grafting density of this approach. The focus of this review is the chemical modification of the surfaces of cellulose nanomaterials with water-soluble polymers to make them suitable for drug delivery purposes. Notable is the reaction between TEMPO-oxidized cellulose nanomaterials (CNFs) and amino-terminated polymers such as PEG[224] or the thermo-responsive statistical copolymers of ethylene oxide (EO) and propylene oxide (PO).[225] Alternatively, PEG was attached by epoxide-ring opening polymerization.[226] The resulting PEG grafted CNCs were stable in aqueous solution, but, once concentrated, formed a chiral nematic phase (**Figure 2.10**).

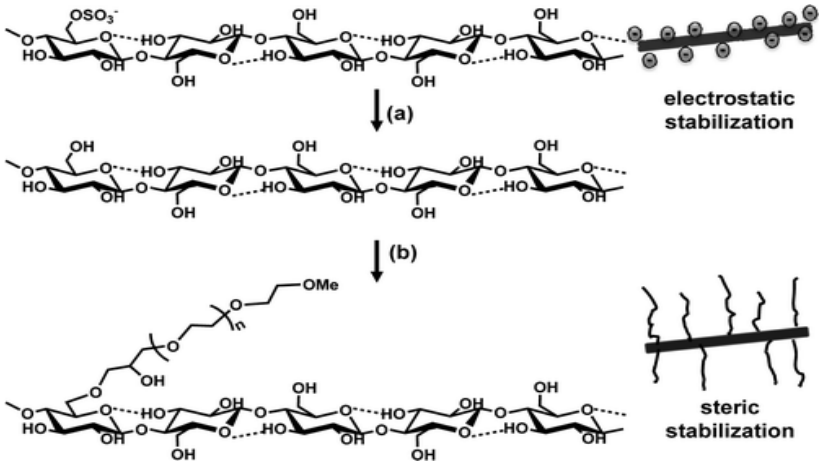

Figure 2.10. PEO-grafting strategy: **(a)** desulfation reaction, followed by **(b)** grafting with PEO epoxide under alkaline reaction conditions.[226]

Click reactions is the first consideration when looking for efficient grafting strategies to attach polymers on surfaces. This avenue was indeed explored when attaching the water-soluble poly(ethyl ethylene phosphate) (PEEP), that carries a propargyl end functionality, to azide modified cellulose nanomaterials.[122] This material was subsequently used to deliver drugs.

Modification of cellulose nanomaterials with aldehyde functionalities enables the reaction with polymers that carry hydrazine as the end group forming fluorescent bisaryl hydrazones as connection between cellulose nanomaterials and polymer chains.[227] The aldehyde functionality was introduced by reacting CNCs with epichlorohydrin and the product subsequently reacted with 4-formylbenzamide. Meanwhile, the water-soluble polymer depicted in **Figure 2.11** was prepared by ring-opening polymerization and a series of end group and side-group modifications to introduce metal chelators. The coupling reaction can be easily monitored as the bisaryl hydrazones is fluorescent, which can be used to count the tethered polymers. [227]

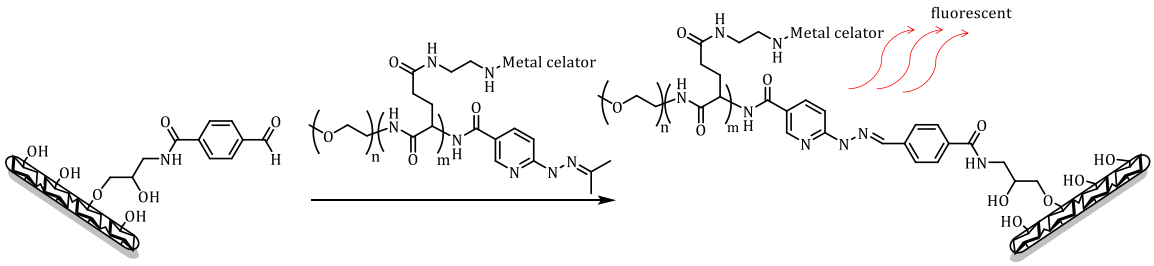

Figure 2.11. Grafting of polymers onto aldehyde-modified cellulose nanomaterials by hydrazone formation.[227]

A grafting technique that is orthogonal to many functional groups and can be carried out in water is the NICAL reaction. Modification of TEMPO-oxidized CNFs by the UV-triggered reaction between tetrazoles and carboxylic acids can create polymer-coated fluorescent cellulose nanoparticles, thanks to the formed benzohydrazide. Tetrazole-functional polymers are obtained during RAFT polymerization in the presence of RAFT agents derivatised with tetrazoles. This approach is suitable for the attachment of various polymers and can be carried out in aqueous solution but has so far only been demonstrated using the water-soluble poly(2-hydroxyethyl) acrylate PHEA (**Figure 2.12**).

With the occurrence of the UV-catalysed reaction, the solution turned fluorescent, which allowed direct monitoring of the cellulose nanomaterials after incubation with cancer cells.[181]

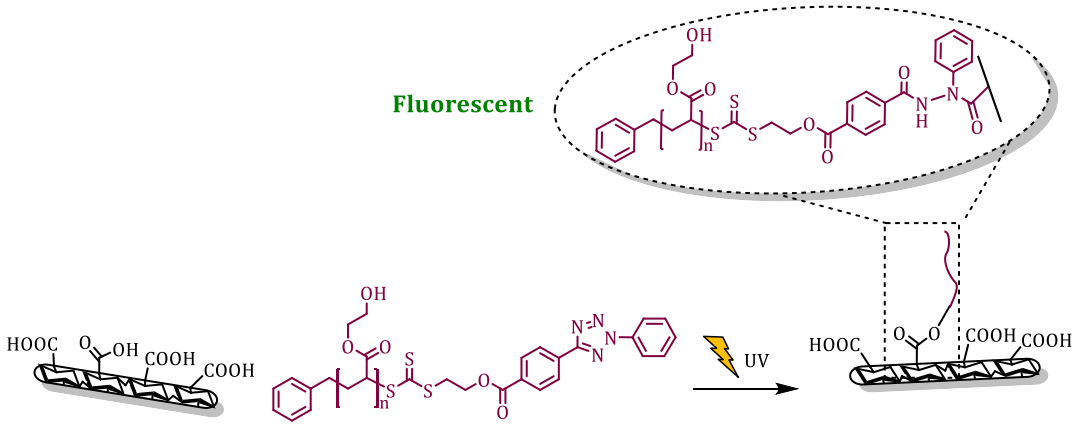

Figure 2.12. General synthetic routes for the synthesis of self-fluorescent PHEA-*g*-CNFs *via* Tetrazole-Acid click chemistry under UV irradiation at ambient temperature.

Another efficient way of modifying cellulose nanomaterials with polymers in aqueous solution is the Passerini reaction, an isocyanide-based multicomponent reaction (MCRs),[228] in which three molecules react in one-pot (**Figure 2.13**).[229, 230] As the TEMPO-oxidized CNFs are already bearing carboxylic acid moieties, polymers with either aldehyde or isocyanide end functionalities are required. Polymers with aldehyde functionality are readily available as the design of acetal-based RAFT agents, the protected version of aldehydes, has already been described in literature[231, 232] (**Figure 2.13**). In our opinion, we found that this reaction results in the best surface coverage displaying the highest stability in serum.

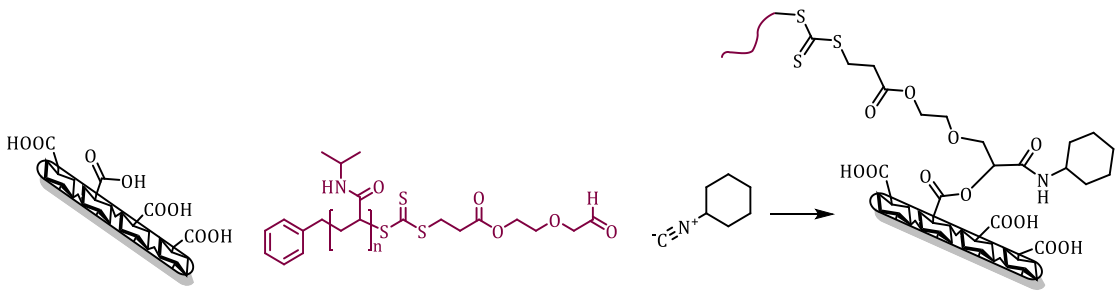

Figure 2.13. Synthesis of PNIPAm-grafted cellulose nanomaterials *via* three component Passerini reaction.

2.5.2. "Grafting from" approach

In the graft copolymerization approach, which is a surface-initiated polymerization, the growth of polymer chains occurs from the immobilized initiator or controlling agent attached to the surface of cellulose.[233] Examples of widely used "grafting from" technique includes (i) ring-opening polymerization and (ii) controlled radical polymerization (or) reversible deactivation radical polymerizations (RDRPs).[234-238] The main advantage of this strategy is the high grafting densities as the polymers grow now often at similar rates from the surface, which contrasts the grafting to strategy where long polymers have to be tethered on the surface, a process that is entropically less likely.[239] Disadvantage of the grafting from strategy is often the uncertainty if the polymer grows in a controlled manner as analysis of molecular weight and molecular weight distribution is difficult.

Ring-opening polymerization

Ring-opening polymerization from cellulose-based materials is well established and the approach has been reviewed earlier.[240] The attraction lies in the abundance of hydroxyl groups that are able to initiate the ring-opening process once activated by catalysts such as Tin(II) 2-ethylhexanoate ($Sn(Oct)_2$) (**Figure 2.14**). This approach has been described to polymerize monomers such as ε-caprolatone (ε-CL), [241-243] lactide (LA) [244-253] or *p*-dioxanone[242, 254-256], but the resulting polymer-grafted CNCs are insoluble in water. A notable exception is the design of poly(2-ethyl-2-oxazoline) POX that was obtained by cationic ring opening polymerization of 2-ethyl-2-oxazoline (**Figure 2.14**). CNCs were modified with tosyl chloride, which served as the initiator for the subsequent polymerization. The resulting POX-*g*-CNCs could be hydrolysed in acidic conditions creating cellulose nanomaterials with grafted poly(ethylene imine).[257] The reader is referred to a review article that details various polymerization conditions for ring-opening polymerization from cellulose nanomaterials.[258] As side reactions that may lead to crosslinking should be absent as long as the polymerization is well-controlled, ring-opening

polymerizations are suitable to generate discrete soluble nano-objects for drug delivery.

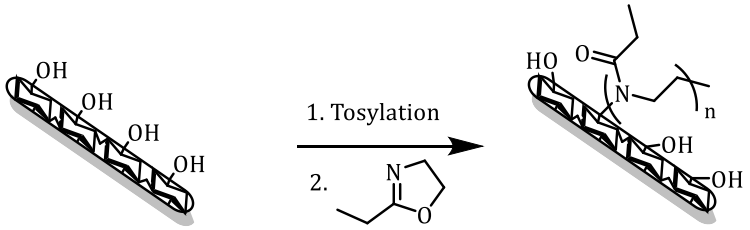

Figure 2.14. Ring-opening polymerization of 2-ethyl-2-oxazoline from the surfaces of cellulose nanomaterials.

Surface-initiated free radical polymerization (SI-FRP)

A simple way to graft polymers on the surface is by the surface-initiated free radical polymerization of vinyl monomers. The underpinning idea is the formation of radicals by H-abstraction, which is triggered by a radical initiator such as potassium persulfate (**Figure 2.15**). The surface bound radical can then initiate the free radical polymerization yielding cellulose nanomaterials with grafted chains. As this technique forms free polymers in parallel to surface-bound polymers and the radical termination reaction may lead to crosslinking, SI-FRP is not the best choice for the synthesis of dispersible and defined polymer-wrapped cellulose nanomaterials. However, it is possible to generate nanoparticles when the polymerization is carried out in a water in oil emulsion system. In this scenario, cellulose nanomaterials can take on the role of the emulsion stabilizer[259] including Pickering emulsions.[260] This approach was however more commonly used to design hydrogels filled with cellulose nanomaterials[261, 262] for water detection,[261] as protein adsorbent,[263] or for wound dressing.[264]

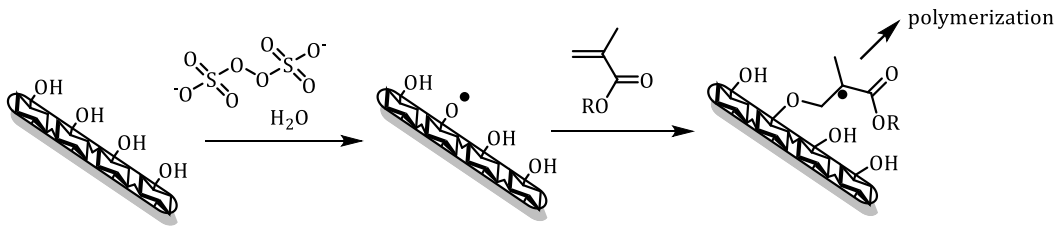

Figure 2.15. Mechanism of Surface-initiated free radical polymerization (SI-FRP) from the surfaces of cellulose nanomaterials.

Radicals can be generated on the surface by means of other techniques such as molybdenum hexacarbonyl-catalysed polymerization.[265] A prerequisite is the immobilization of trichloroacetyl groups onto cellulose nanomaterials, which are activated by the release of carbon monoxide and the homolytic cleavage of the C-Cl bond. Polymerization of low bio-fouling 2-methacryloyloxyethyl phosphorylcholine and stearyl methacrylate was then carried out in ethanol at refluxing.[266]

Grafting through free radical polymerization (SI-FRP)

The immobilization of vinyl functionalities on the surfaces of cellulose nanomaterials, as it can be accomplished by reaction with γ-methacryloxypropyl trimethoxy silane (**Figure 2.6**),[162, 163] is an efficient way to yield highly crosslinked nanocomposites, but this technique is less suitable to obtain dispersible products.

Cerium-initiated radical polymerization

Cerium (IV) ions have the ability to coordinate with the hydroxyl groups on cellulose material and generate radicals in the subsequent oxidation step. Similar to SI-FRP, the radical can initiate the polymerization. As this is again a free radical process, crosslinking by bimolecular radical termination could theoretically occur, but the termination of the polymerization is more likely the result of a redox reaction with excess Ce(IV) making this technique more suitable to generate soluble polymer-grafted cellulose nano-objects.[267-271 272]

Surface-Initiated Controlled Radical Polymerization (SI-CRP)

Controlled radical polymerization (CRP), also known as reversible deactivation radical polymerizations (RDRPs), encompasses reversible addition-fragmentation chain transfer (RAFT) polymerization, atom transfer radical polymerization (ATRP), nitroxide-mediated polymerization (NMP) and

organometallic-mediated radical polymerization (OMRP) among others. The clear advantage is that the molecular weight of synthesized polymer is well-controlled due to the equilibrium between active and dormant state, making SI-CRP the method of choice for polymer-grafted cellulose nanomaterials for drug delivery applications.

Reversible Addition-Fragmentation Chain Transfer (RAFT)/Xanthates (MADIX) polymerization

RAFT polymerization has been successfully employed to synthesize polymer-grafted cellulose nanomaterials. What distinguishes RAFT polymerization from all other CRP methods is the capability of polymerizing a wide range of monomers including charged monomers (anionic, cationic and zwitterionic) without polluting the product with metal catalysts.[273] The RAFT agent can be conjugated either by its radical leaving group 'R' or the stabilizing group 'Z', which has implications on the outcomes.[274, 275] The detail mechanism of RAFT polymerization is discussed in **Section 2.8**. Related to the RAFT process is the macromolecular design *via* the interchange of xanthates (MADIX), which follows the same reaction mechanism but a different CTA (chain transfer agent) is employed.[276] In MADIX, the stabilizing group contains a xanthate functionality (**Figure 2.16**). A range of monomers has been polymerized from the surfaces of cellulose nanomaterials *via* surface-initiated RAFT polymerization in the presence of free CTA (**Table 2.4**). The characteristics of grafted polymers can be determined by analysing the free polymer chains present in the reaction.

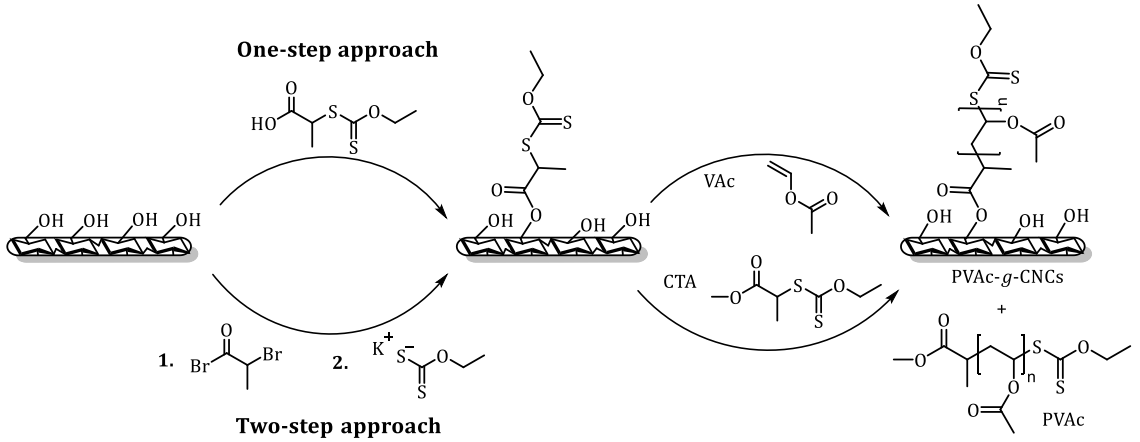

Figure 2.16. Schematic illustration of CTA agent immobilization on cellulose nanomaterials and polymerization of vinyl acetate monomer as an example.[277]

Table 2.4. Summary of RAFT polymerizations with RAFT agent tethered to the surface.

	Type of polymerization (CTA or initiator)	Monomer	Temp. (°C)	Solvent	Year [Ref.]
RAFT R-group	CPADB	MMA	70	THF	2016[278]
MADIX/RAFT R-group	ECTTP	VAc	60	EtOAc	2016[277]
RAFT R-group	DDMAT	AA, NIPAm	70	1,4-dioxane	2014[279] 2018[280]
RAFT R-group	TBTG	AA, NIPAm	70	DMF	2017[281]

AA: acrylic acid, CPADB: 4-cyano-4-(phenylcarbonothioylthio)pentanoic acid, DDMAT: S-Dodecyl-S′-(α,α′-dimethyl-α′′-acetic acid)trithiocarbonate, ECTTP: 2-((ethoxycarbonothioyl)thio)propanoic acid, EtOAc: ethyl acetate, TBTG: S-(thiobenzoylthioglycolic) acid, DMF: N,N-dimethylformamide, NIPAm: N-isopropylacrylamide, THF: tetrahydrofuran, Temp.: Temperature, VAc: vinyl acetate,

In order to generate well-defined polymer-grafted cellulose nanomaterials, it is crucial to introduce sacrificial RAFT agent (**Figure 2.16**).[277] Poly(acrylic acid) PAA and poly(*N*-isopropylacrylamide) PNIPAm were grafted by Zeinali *et al*.,[279] who later cleaved the polymers from the surface for further analysis. They compared the free PAA and PNIPAm polymers in solution, which are the result of polymerization with the sacrificial RAFT agent, with the one that was recovered from the surface. The molecular weight of the

polymers on the surface was in good agreement with the one in solutions showing that the "grafting from" process is indeed well-controlled. The authors dispersed the polymer-grafted CNCs in aqueous solution resulting in discrete soluble crystals with a hydrodynamic diameter of at least 200 nm depending on the conditions. The nano-objects displayed pH and thermo-responsive behaviours.[280]

RAFT polymers were also grafted on cellulose nanomaterials by a combination of cerium-initiated free radical polymerization and RAFT polymerization. Cellulose nanomaterials were mixed with water-soluble poly(acryl amide) macroRAFT agent and additional monomer, followed by the addition of cerium ammonium nitrate. This triggered the formation of radicals on the surface, initiating the polymerization of the monomer.[282, 283]

Another variation is the attachment of radical initiator to the surface. The resulting surface functionalized cellulose nanoparticles were then mixed with *S*,*S*′-bis(α,α′-dimethyl-α″-acetic acid)-trithiocarbonate as RAFT agent and the monomer poly(ethylene glycol)ethyl ether methacrylate.[284] This polymerization was combined with atom transfer radical polymerization (ATRP) to generate cellulose nanomaterials with two different water-soluble surface bound polymers, suitable to trap drugs.[284]

Atom Transfer Radical Polymerization (ATRP)

Atom transfer radical polymerization (ATRP) is another powerful strategy to prepare multifunctional cellulose nanoparticles with high degree of polymer grafting. In order to perform the ATRP polymerization from cellulose nanomaterials, reactive groups (hydroxyl or carboxyl groups) present on the surface of CNCs are firstly modified with a well-known ATRP initiators, usually α-bromoisobutyryl bromide, and then polymer chains are grown directly from the surface (**Figure 2.17**) (**Table 2.5**).[285-290] Importance is the addition of sacrificial initiator in the solution. Similar to the RAFT process, the sacrificial initiator can prevent loss of initiating site and contribute to the control of the molecular weight of the grafted chains. A convenient feature is also

that the free polymer can be easily analysed, and conclusion can be drawn in regard to the length of the grafted chains. It is widely assumed that surface bound polymers are similar in size to free polymers. While this may often be the case,[291] it has been shown that surface bound polymer can have higher[292] or lower dispersity[293] than the polymer in solution. This means that the analysis of free polymer in solution does not replace the analysis of surface bound polymer, which needs to be cleaved for further characterization. Interesting is that the charge of cellulose surface can influence the rate of reaction as it was shown using partly sulfonated surfaces. Zoppe *et al.* observed that electrostatic interactions between the negatively charged cellulose nanomaterials and the catalyst can enhance the initiator efficiency.[294] Although ATRP on cellulose nanomaterials was initially carried out in non-polar or aprotic solvents, the use of water as polymerization media presented a significant step forward. Aqueous solution not only facilitated the dispersibility of the hydrophilic cellulose nanomaterial, but the polymerization was often observed to be significantly faster. For this process, a new mechanism was proposed in literature, which outlines the disproportionation of CuX into Cu^0 and CuX_2. The high activity was assigned to nascent Cu^0, which led to the use of copper wire as catalysts while the amount of CuX could be reduced to a minimum making this process more biofriendly. A very convenient further development is the generation of CuX species in situ. In the AGET ATRP approach for surface grafting of cellulose nanoparticles, the initiator is mixed with CuX_2, which is subsequently reduced to CuX. A further development in grafting brushes from the surfaces is photo-initiated ATRP, which was introduced by Hatton *et al.* on CNCs.[285] Similar to traditional ATRP, α-bromoisobutyryl bromide was immobilized on CNCs *via* esterification reaction. The polymerization proceeded under UV irradiation ($\lambda_{max} \approx 360$ nm with an intensity of approximately 40 mW cm^{-2}) at ambient temperature for 90 min under argon atmosphere (**Figure 2.17**). The main benefit of this technique is the high monomer conversion of around 90 % within 90 min and the low copper catalyst concentration.[285] The reader is referred to a recent summary that outlines the history of ATRP.[295]

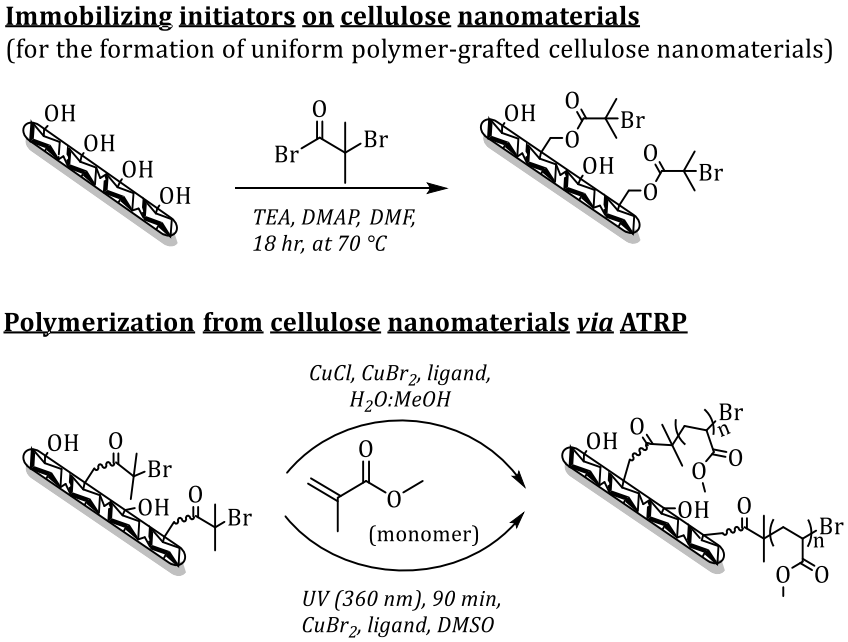

Figure 2.17. Schematic illustration for the synthesis of polymer-grafted cellulose nanomaterials *via* surface-initiated atom transfer radical polymerization (ATRP).[285]

Using various variations of ATRP (**Table 2.5**) a range of monomers could be grafted from the surface. Hydrophobic monomers such as styrene,[296, 297] MMA/BA,[298] or MA[299] the azo-monomer 6-[4-(4-methoxyphenylazo)phenoxy] hexyl methacrylate,[300] or fatty acids derived monomers[301] were grafted to generate composites.

However, most polymer-grafted CNCs that were synthesized by ATRP were designed to generate discrete cellulose nano-objects that are dispersible in aqueous conditions (**Table 2.5**). A range of stimuli-responsive polymers have been grafted from the surfaces of cellulose nanomaterials including thermo-responsive polymers. Leading this field is the design of PNIPAm-grafted cellulose nanomaterials.[290, 292, 293, 302, 303] The possibility to use these materials in a biological setting was demonstrated by Chen *et al.* who employed these materials as injectable embolization agent.[303] The cloud point can be tuned by co-polymerization[304, 305] or alternatively other thermo-responsive polymers can be used such as poly(*N*-vinylcaprolactam) (PVCL).[306]

Table 2.5. Summary of previous works on grafting polymers to the surface of cellulose nanomaterials by ATRP.

Type	catalyst	Temp. (°C)	Reaction time (hr)	Monomer (solvent)	[Year] Ref.
ATRP	HMTETA: CuBr= 1: 1	110	12	Styrene (bulk)	2008[296]
ATRP	HMTETA: CuBr= 1: 1	90	24	MMAZO (chlorobenzene)	2008[300]
ATRP	PMDETA: CuBr = 1: 1	100	-	Styrene (anisol)	2009[297]
ATRP	HMTETA: CuBr= 1: 1	55	12	DMAEMA (methanol)	2009[291]
ATRP	PMDETA: CuBr = 1: 1	75	-	*t*BA (DMF)	2011[307]
ATRP	HMTETA: CuBr= 1: 1	70	3	DMAEMA/ NpMA (DMF)	2014[308]
ATRP	HMTETA: CuBr= 1: 1	70	4	DMAEMA (DMF)	2014[309]
ATRP	PMDETA: CuBr = 1: 1	70	-	*t*BA (DMF)	2016[310]
ATRP	PMDETA: CuBr = 1: 1	70	24	Styrene (anisol)	2016[288]
ATRP	Me_6TREN: CuBr= 1: 1	90	12	SBAM (DMF)	2016[301]
ATRP	PMDETA: CuBr = 1: 1	80	-	MMA/ BA	2016[298]
ATRP	2,2-dipyridal: CuBr= 2: 1	45	24	DEGMA/ OEGMA (DMF)	2016[304]
ATRP	PMDETA: CuBr = 1: 1	a.t.	8	DEGMA/ OEGMA (DMF)	2017[305]
ATRP	PMDETA: CuBr = 1: 1	75	12	NVCL (DMF)	2017[306]
ATRP	MDETA: CuCl= 1.5: 1	70	1	DMAEMA/ PMDETA (DMF)	2018[311]
SET-LRP	PMDETA: CuBr = 1: 1/ PMDETA: $CuBr_2$ = 1: 0.6	a.t.	24	NIPAm (water/ methanol)	2010[292] 2014[302] 2014[303]
SET-LRP	PMDETA: CuBr = 1: 1	a.t.	2	METAC, 4-SS, NIPAm (water/ methanol)	2017[290]
SET-LRP	PDMDETA: CuBr= 1: 1	a.t.	24	AEM/ AEMA (water/ methanol)	2015[312]
Cu(0) SET-LRP	Me_6TREN: $CuBr_2$= 2: 1 Cu-wire	25	-	MA (DMSO)	2015[299]
Cu(0) SET-LRP	HMTETA: $CuBr_{2=}$ 110: 1/ Cu-wire	60	24	DMAEMA/ DEAEMA (methanol/ small amount of DMF)	2017[313]
AGET-ATRP	PMDETA: $CuBr_2$= 2: 1 L-ascorbic acid	a.t.	8	NIPAM/ EANI (water/ methanol)	2015[293]
AGET-ATRP	PMDETA:CuCl:$CuBr_2$=2: 0.3: 1	a.t.	-	DMA (water)	2016[294]

Type	catalyst	Temp. (°C)	Reaction time (hr)	Monomer (solvent)	[Year] Ref.
AGET-ATRP	PMDETA: $CuBr_2$= 2: 1 CuBr	60	24	DMAEMA	2019[314]
AGET-ATRP	PMDETA: $CuBr_2$= 2: 1 CuBr	60	24	DMAEMA	2019[314]
ARGET-ATRP	Bpy: $CuBr_2$= 2: 1 L-ascorbic acid	30	2	MMA/ OEGMA (water)	2019[315]
Photo-ATRP	Me_6TREN: $CuBr_2$= 1: 1 λ= 360 nm, ≈ 40mW cm^{-2}	a.t.	1.5	MA (DMSO)	2017[285]
ATRP and RAFT	BPy: CuBr= 2: 1	25	-	DMAEMA(water/ methanol)	2016[284]

AEM: 2-aminoethylmethacrylate, a.t.: ambient temperature, AEMA: N-(2-aminoethylmethacrylamide), Bpy: 2,2'-bipyridine, DMA: N,N-dimethyl acrylamide, DMAEMA: N,N- dimethylaminoethyl methacrylate, DEGMA: diethylene glycol mono-methyl ether methacrylate, EANI: 4-ethoxy-9-allyl-1,8-naphthalimide, HMTETA: 1,1,4,7,10,10-hexamethyltriethylenetetramine, MA: methyl acrylate, METAC: [2-(methacryloyloxy)ethyl]trimethylammonium chloride, Me_6TREN: tris (2-(dimethylamino)ethyl) amine, MMAZO: 6-[4-(4-methoxyphenylazo)phenoxy] hexyl methacrylate, NIPAm: NpMA: naphthyl methacrylate, N-isopropylacrylamide, NVCL: N-vinylcaprolactam, OEGMA: oligoethylene glycol mono-methyl ether methacrylate, PMDETA N,N,N′,N″,N″-pentamethyldiethylenetriamine, SBAM: soybeanamide methacrylate, 4-SS: sodium 4-vinylbenzenesulfonate

Cellulose nanomaterials were often used as a scaffold to grow polyelectrolyte brushes. Poly(acrylic acid) brushes were obtained by grafting *tert*-butyl acrylate (*t*BA), followed by deprotection.[307, 310] The resulting anionic cellulose-based brushes can now interlink with cationic polymers *via* electrostatic interaction.[310] More common is however grafting of cationic polymers, in particular poly(*N,N*- dimethylaminoethyl methacrylate) (PDMAEMA),[291, 308, 309, 311, 313, 314] These polymers can be permanently quaternized and subsequently used to bind viruses such as the cowpea chlorotic mottle virus.[309]

Nitroxide-mediated polymerization (NMP)

To our knowledge, so far only two reports describe the use of nitroxide-mediated polymerization (NMP) to graft PMA and PMMA,[316] or

poly(dimethylaminoethyl methacrylate) (PDMAEMA), poly(diethylaminoethyl methacrylate) (PDEAEMA) and poly(dimethylaminopropyl methacrylamide) (PDMAPMAm) from the surface of cellulose nanomaterials.[317]

Grafting on the reactive end groups

As it is possible to selectively functionalize the reactive end group only, polymers can be grafted onto or grown from the reducing end. Zoppe *et al.* have developed a water-tolerant synthetic protocol for the preparation of CNCs with end-tethered polymer chains. The hemiacetal end group, which is in equilibrium with the aldehyde functionality, was first oxidized to carboxylic acid, which was then modified with an ATRP initiator (**Figure 2.18**), followed by polymerization.[318] Although this pathway was prone to side reactions, this approach opens up new opportunities to create hierarchical structures.[319]

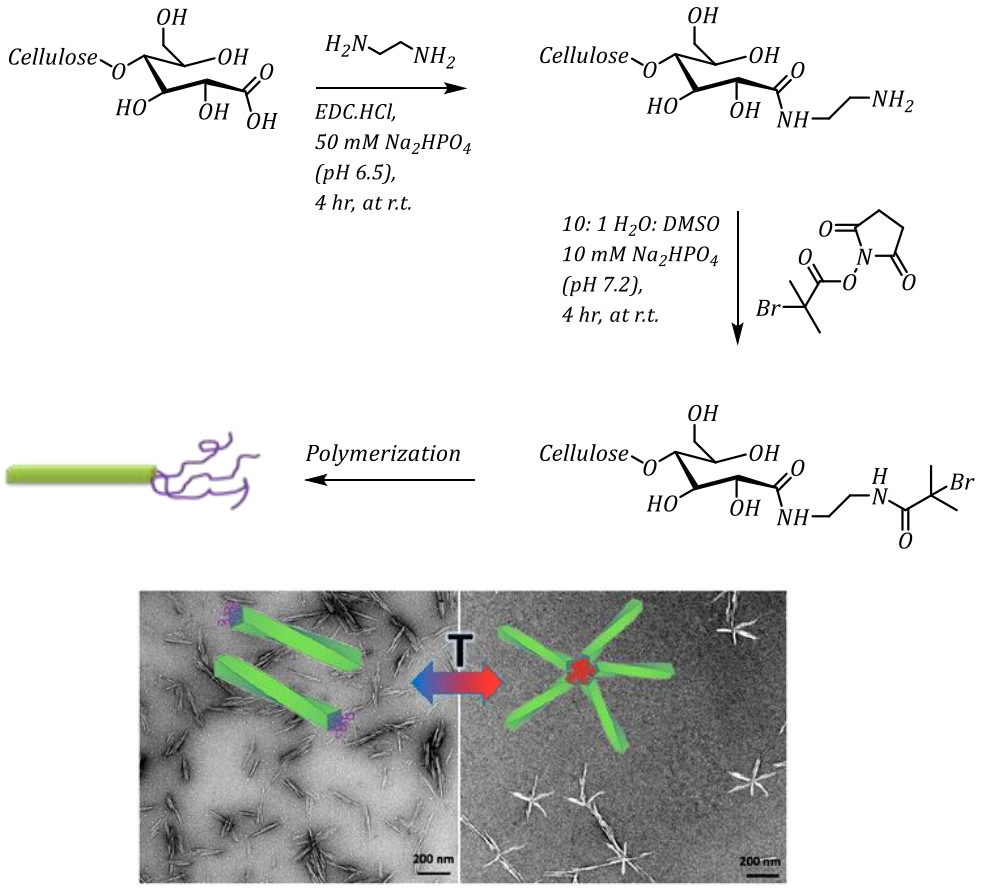

Figure 2.18. Modification of reducing end groups with polymers enabling self-assembly into large hierarchical structures.[319] The picture is reprinted with permission from (ref. [319]). Copyright 2019, American Chemical Society.

2.5.3. Toxicity of cellulose nanomaterials modified with polymers

The toxicity of polymer-grafted cellulose nanomaterials was often studied together with the drug loaded carriers in order to identify if the toxicity is the result of drug loading or polymer coating, which is discussed below. In most cases, polymer-coated cellulose nanomaterials do not induce any cytotoxicity due to the biocompatibility of chosen polymers. For example, coating with poly(ethylene glycol) PEG does not induce any toxicity on the ovarian cancer cell line HEYA8 cells within the concentrations measured.[177] Similar results were obtained with grafted poly(ethyl ethylene phosphate) (PEEP), which was non-toxic to the cervical cancer cell line (HeLa) and murine fibroblast cell line (L929), [122] and grafted poly(2-hydroxyethyl) acrylate (PHEA), which did not cause any cytotoxicity in MCF-7 cells. [181]

An important study on the toxicity of polymer-grafted cellulose nanomaterials was carried out by Ferraz *et al*. [120] The authors coated the cellulose nanomaterials with the conducting poly(polypyrrole) (PPy) and investigated the material *in vitro* and *in vivo*. It was found that the non-toxicity was strongly dependent on the purification technique as well as the age of the material. Intensive rinsing is required to obtain a biocompatible material. Moreover, aging had a negative effect on the toxicity. [120]

The non-toxicity of neutral polymers contrasts the results found with cationic polymers. Positively charged grafted poly[*N*-(3-aminopropyl)methacrylamide] was indeed found to induce toxicity against J774A.1 and MCF-7 after 48 hr of incubation. However, when compared to CNCs that were modified with 1,4-butylene diamine only, the polymer coated CNCs were significantly less toxic than CNCs modified with low molecular weight amino groups only, which were found to be toxic at low concentrations already.[205] In contrast, cellulose nanomaterials grafted with poly(2-aminoethylmethacrylate) (PAEM) or poly(*N*-(2-aminoethylmethacrylamide)) (PAEMA) have only limited toxicity despite a high positive surface charge.[312] For comparison, grafting of PNIPAm in the same system did not cause any toxicity issues. [205] Cationic polymers are often used to condense nucleic acid drugs. The gold standard of

gene delivery, poly(ethylene imine) (PEI), is efficient, but it is known to cause toxicity. However, it was found that PEI on the surface of cellulose nanomaterials, condensed with DNA, displayed lower toxicities on L929, in fact no toxicity within the concentration range, compared to the free PEI-DNA complex.[320] It should nevertheless be assumed that coating of cationic polymers will erase toxicity of the normally toxic polymer. Poly(2-(dimethylamino)ethyl methacrylate) (PDMAEMA) of different lengths was grafted onto cellulose nanomaterials by ATRP.[321] The authors found that longer PDMAEMA displayed higher toxicity on the fibroblast-like cell line COS7 and the human liver carcinoma cell line HepG2, but the polymer had overall lower toxicities than PEI.[321] The toxicity of cationic polymers can be reduced by co-grafting of PDMAEMA with poly(poly(ethylene glycol)ethyl ether methacrylate) (PPEGEEMA).[284] Again, longer PDMAEMA had a negative effect on the cell viability. Reducing the concentration of cationic groups can also be beneficial on the biocompatibility as it was shown with cellulose nanomaterials grafted with poly(2-oxazoline) that carried a positive end functionality.[322] The polymers were found to be non-toxic to concentrations up to 25 μg mL^{-1}, which is however within the low concentration range.

Beyond the cell death, cellulose nanomaterials wrapped in cationic polymers can potentially display immunogenicity. Therefore, poly(aminoethyl methacrylate) (PAEM) was compared to poly(aminoethyl methacrylamide) (PAEMA) and it was found that only PAEMA induced significant IL-1β secretion, a sign of proinflammatory response, in mouse macrophage cell lines (J774A.1). This was caused by the release of reactive oxygen species (ROS) from the mitochondria, which then triggered an increase in extracellular adenosine 5´-triphosphate (ATP).[323]

2.5.4. Cellulose nanomaterials as water soluble drug carriers

Nano-sized drug carriers modified with small functional molecules

Owing to the large surface areas and negative charges (in case of TEMPO-oxidized cellulose), large amounts of drugs can be loaded onto cellulose nanomaterials. However, also other strategies are available as depicted in **Figure 2.19** and summarized in **Table 2.6.**

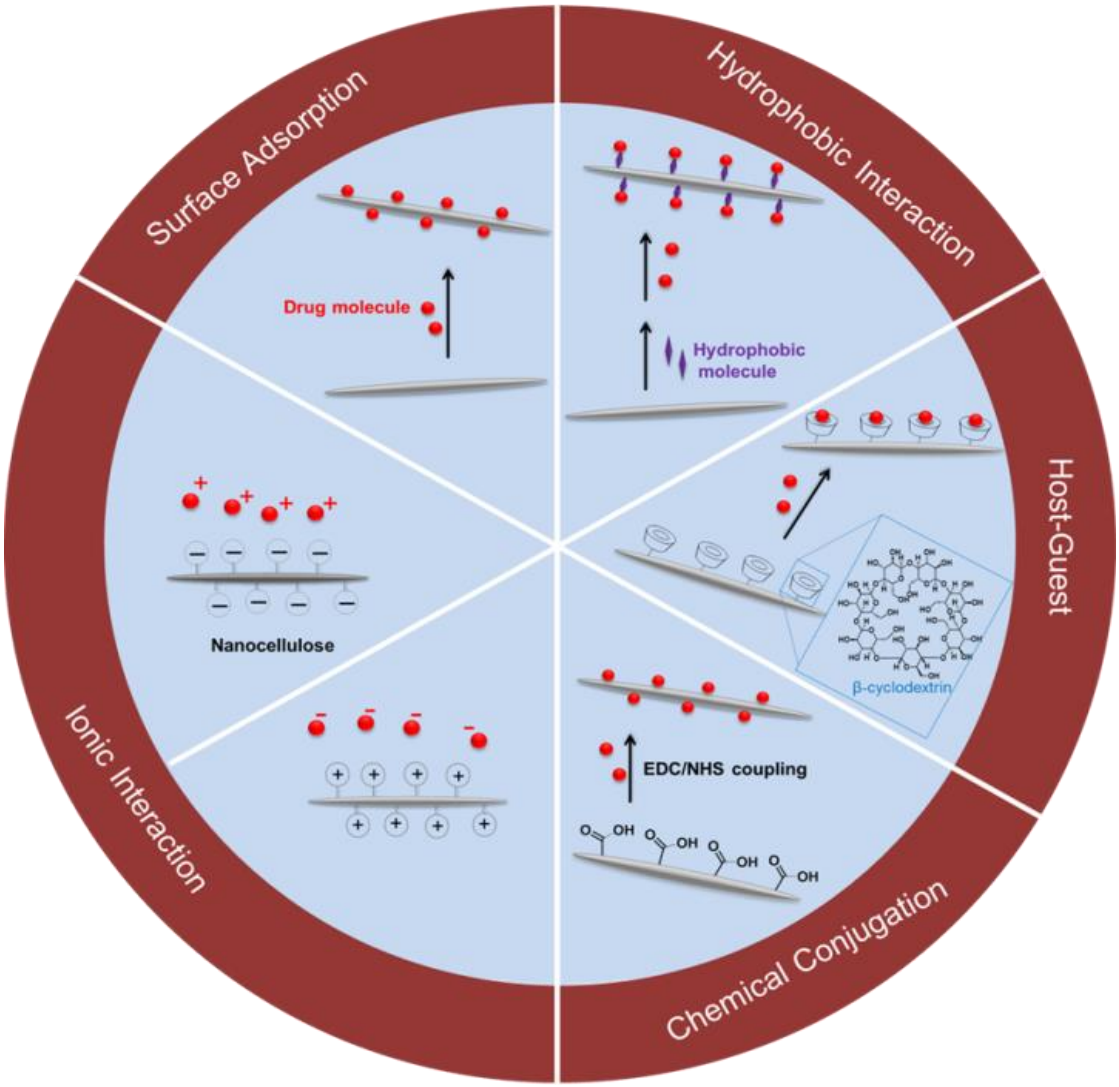

Figure 2.19. Drug binding onto cellulose nanomaterials *via* five main routes: hydrophobic interaction, ionic interaction, surface adsorption, host guest and chemical conjugation.

Table 2.6. Summary of various approaches for the delivery of drugs using cellulose nanomaterials.

Source of cellulose	Formulation	Therapeutic Molecule	Responsiveness and linkage	Drug Loading technique	Loading efficiency (DLE)	Tested cell line	*In vitro* Cytotoxicity	Published year	Ref.
Microcrystalline cellulose	CNCs	HDQ	-	Adsorption	30 %	-	-	2015	[324]
Wood	CNCs	Metformin	-	Electrostatic interaction	Around 10 %	B16-F10 L929	IC_{50} = 17.6 mg ml^{-1} Non-toxic	2017	[325]
Wood	CNCs	DOX, TET	-	Electrostatic interaction	65 % (DOX) 48 % (TET)	KU-7	N/A	2011	[326]
Microcrystalline cellulose	CNC-TAEA:	MTX, Fe_3O_4 NPs	-	Electrostatic interaction	91.2 %	MCF-7	$IC_{50} \approx 100$ - 150 mg L^{-1}	2017	[208]
Wood	CNCs-CTAB	PTX, DTX, ETOP	-	Hydrophobic interaction	90 % (PTX) 90 % (DTX) 48 % (ETOP)	KU-7	-	2011	[326]
Microcrystalline cellulose	TEMPO-CNCs-CTAC	Curcumin	-	Hydrophobic interaction	N/A	-	-	2018	[327]
Microcrystalline cellulose	CNCs-CTMAB	LUT, LUS	-	Hydrophobic interaction	The loading content: 12.9 ± 1.5 9 mg g^{-1} for LUT and 56.9 ± 0.9 mg g^{-1} for LUS	-	-	2016	[328]
Kenaf (*Hibiscus cannabinus*) bast fibers	CNCs-CTAB	Curcumin	-	Hydrophobic interaction	80 % - 96 %	-	-	2017	[329]

Source of cellulose	Formulation	Therapeutic Molecule	Responsiveness and linkage	Drug Loading technique	Loading efficiency (DLE)	Tested cell line	*In vitro* Cytotoxicity	Published year	Ref.
Oil palm empty fruit bunch	CNCs-TA-DA	Curcumin	-	Hydrophobic interaction	95 % - 99 %	-	-	2019	[330]
Filter paper	CNCs	Peptide chlorotoxin	Ester	Esterification	Conjugation is quantitative	U87MG, MCF-7	-	2018	[331]
Wood pulp	CNCs-oxidized to aldehyde	3-Aminopropylphosphonic acid or sodium alendronate	Amide	Schiff-base and reduction	N/A	hFOB1.19 osteoblast	Non-toxic	2017	[209]
Wood pulp	CNCs-MA	Tosufloxacintosilate (TFLX)	-Enzymatic cleavage -L-leucine linker	Amidation	99.84 %	-	-	2018	[332]
-	CNCs-NH_2	DOX.HCl	-pH-Responsive - *cis*-Aconitylamide linkage	Amidation	8 %	HL-7702, NCI H 460, KB, MCF-7	IC_{50} = 3.10 mg L^{-1}	2018	[218]
Dried leaves of bamboo	CNCs	Native proteins (BSA (or) HSA)	-	Physical adsorption	40 ± 2 %, 36 ± 1 %	Endothelial cells (HUVEC, HCAEC)	Non-toxic	2017	[333]
				Amidation	54 ± 2 %, 46 ± 3 %				

Source of cellulose	Formulation	Therapeutic Molecule	Responsiveness and linkage	Drug Loading technique	Loading efficiency (DLE)	Tested cell line	*In vitro* Cytotoxicity	Published year	Ref.
Medical absorbent hydrophilic cotton	CNCs-(β-CD)	Curcumin	Electrostatic binding of β-CD	Host-guest	8 % - 10 %	PC-3	7.5 µM (48 hr)	2016	334
						DU-145	5.5 µM (48 hr)		
						HT-29	4.5 µM (48 hr)		
Cotton	CNCs-(β-CD)	Chalcones	Electrostatic binding of β-CD	Host-guest	Loading ratio (w/w): 23.3 %	HT-29	4.5 ± 0.5 µM	2019	335
						HCT-116	8.9 ± 1.0 µM		
						PC-3	6.3 ± 1.5 µM		
						DU-145	7.9 ± 0.4 µM		
G. xylinus bacterial strain	CNCs-(β-CD)	CIP, PTX, DOX	Chemical binding of β-CD	Host-guest	~ 80 % (CIP) ~ 50 % (PTX) ~ 70 % (DOX)	*E.coli*		2019	336

BSA: bovine serum albumin, B16-F10: metastatic mouse melanoma cell line, (β-CD): β-cyclodextrin, CIP: ciprofloxacin, CNCs: cellulose nanocrystals, CTAB: cetyl trimethylammonium bromide, CTAC: cetyl trimethylammonium chloride, CTMAB: cetyltrimethylammonium bromide, DTX: docetaxel, DOX: doxorubicin, DU-145: prostatic cancer cells, ETOP: etoposide, Fe_3O_4: iron(II,III) oxide, HUVEC: human umbilical vein endothelial cell*, HCAEC: human coronary artery endothelial cells, , hFOB1.19: human bone derived osteoblasts, HL-7702: human hepatocyte cell line, HT-29: colorectal cancer cells, HCT-116: colorectal cancer cells, HDQ: hydroquinone, HSA: human serum albumin, IC_{50}: the half maximal inhibitory concentration, KB: human epithelial carcinoma cell line, KU-7: bladder cancer cell line, LUT: luteolin, LUS: luteoloside, L929: normal mouse fibroblasts cell line, MTX: methotrexate, MA: maleic anhydride, MCF-7: Michigan Cancer Foundation-7* (*breast cancer cell line), NCI H 460: human large cell lung cancer cell line, NPs: nanoparticles, PTX: paclitaxel, PC-3: prostatic cancer cel*ls*, TAEA: tris(2-aminoethyl)amine, TET: tetracycline, TA-DA: tannic acid-decylamine, TFLX: tosufloxacintosilate, U87MG: human-derived glioblastoma cell line*

Surface adsorption

The easiest way is to adsorb drugs to the surface. This was explored for the delivery of hydroquinone (HDQ) from CNCs to the skin in order to cure hyperpigmentation.[324] In this experiment, the drug was adsorbed onto the surface by simply mixing drug molecules and sulfuric acid-hydrolysed CNCs in distilled water with the attachment of HDQ being confirmed by FT-IR peaks.[324] The final product was dispersible in water and had a hydrodynamic diameter of D_h= 310 nm.

Electrostatic interaction

Charged drugs can be attached by electrostatic interactions such as the cationic drug metformin,[325] doxorubicin (DOX), [326] and tetracycline (TET). [326] The cellulose nanomaterials are loaded with the drugs by mixing drugs and carriers at set pH values until all drug is immobilized on the carrier. Jackson *et al.* compared binding of these charged drugs to other neutral drugs such as paclitaxel and found that non-charged drugs have only limited adsorption.[326] The drug loaded CNCs were effectively taken up by KU-7 bladder cancer cells, but no cytotoxicity was measured.

In order to deliver negatively charged drugs such as methotrexate (MTX), it is necessary to functionalize the surface with cationic groups such as tris(2-aminoethyl)amine.[208] After loading of Fe_2O_3 nanoparticles onto CNCs, the drug loaded carriers were incubated with MCF-7 breast cancer cells. MTX delivered on quaternized CNCs was found to be more efficient than free MTX. [208] The resulting particles were soluble in water, but DLS analysis suggested some aggregation. Interestingly, the final structures were spherical since the preparation process destroyed the fibre structure of cellulose nanomaterials.

Hydrophobic interaction

To accommodate hydrophobic drugs that do not display high adsorption or electrostatic binding, hydrophobic pockets need to be created. This can

be carried out by attaching positively charged cetyl trimethylammonium bromide (CTAB), a surfactant molecule, by electrostatic binding by incubating the cellulose nanomaterials in the presence of sodium chloride solution and CTAB. It was now possible to load a range of hydrophobic anti-cancer drugs like docetaxel and etoposide. To load the drug, the purified CTAB-CNCs were incubated with the drug dissolved in minimal amount of either DMSO or Me-PEG-*b*-PDLLA diblock copolymer. Drug loading of up to 90 % was achieved with DTX, whereas the loading efficiency of ETOP was only 48 %. The drug loading efficiency was strongly dependent on the concentration in the stock solution and the authors carried out a systematic study in that regard. The CTAB-CNCs-fluorescein nanocomplexes were incubated with KU-7 bladder cancer cells and observed to translocate into cells efficiently.[326]

Hydrophobic interaction approach has then been used to deliver further drugs such as luteolin (LUT) and luteoloside (LUS). Cetyltrimethylammonium bromide (CTMAB) was electrostatically bound to the surface of CNCs with excess sulfate groups. After loading the two hydrophobic drugs, the release was monitored showing a slightly higher release over 24 hr at pH 7.4 than pH 6.4. This was explained by the fact that the drugs are slightly acidic and they will be protonated at lower pH values.[328]

Curcumin was loaded at a relatively high amounts using similar drug carriers obtained by modifying the surface of TEMPO-oxidized cellulose nanomaterials with the surfactant CTAC (cetyl trimethylammonium chloride).[327] Instead of carboxylated surfaces, CNCs obtained directly from the sulphuric acid treatment can be used as the abundances of sulfate groups can bind large amounts of CTAB (cetyl trimethylammonium bromide). Loading of curcumin was overall very high (90 %), but it was found that the drug loading efficiency slightly decreased at high CTAB modification. [329] It was noted that CTAB surface modification led to more hydrophobic surfaces which may have lower the drug loading efficiency. The low dispersibility can be improved by conjugating a mixture of tannic acid (TA) and decylamine (DA) with the aim to load curcumin. The final product was soluble in water and could be used as

drug carrier.[337] The drug loading efficiency was very high, but no biological evaluation has been performed.

Host-guest chemistry

Some drugs are neither ionic, hydrophobic and they cannot be conjugated to the surface without losing activity. Here, indirect binding using cyclodextrins can help. Ntoutoume *et al.* immobilized cationic β-cyclodextrin (β-CD) to the surface of CNCs *via* electrostatic interaction to host curcumin as guest. The activity of curcumin against colorectal and prostatic cancer cell lines was noticeably enhanced when delivered in this complex.[334] This approach was also used to deliver other drugs such as chalcones. [335] Encapsulation into β-CD enhanced the solubility of chalcones and subsequently led to increased drug activity.

Instead of binding cyclodextrin *via* electrostatic interactions, the host can be conjugated to the surface using epichlorohydrin[338] or acrylamidomethyl cyclodextrin[339] by modifying the cyclodextrin with citric anhydride, followed by the reaction with cellulose nanomaterials. The antibiotic ciprofloxacin (CIP) and anticancer drugs doxorubicin (DOX) and paclitaxel (PTX) were subsequently used for loading.[336]

Conjugation of drugs, fluorophores and targeting ligands

Chemical conjugation can often be a better means of immobilizing drugs while ensuring slow release. The peptide chlorotoxin, which interacts with MMP-2 inside cells, was bound to the surface of CNCs by activating the peptide drug using NHS esters. The negatively charged CNCs were taken up by U87MG and MCF-7. As U87MG has higher MMP-2 concentrations, the nanocarriers were found to be more efficient.[331] Another example for chemical conjugation is the reaction with 3-aminopropylphosphonic acid or sodium alendronate, which are bisphosphonates that are used to treat bone diseases. Cellulose nanomaterials initially oxidized to aldehydes using periodide,

followed by the reaction with the amino groups to yield negatively charged soluble nanoparticles that can be internalized by osteoblast.[209] Finally, conjugation of proteins to surfaces is an established procedure that has also been employed to immobilize proteins such as bovine serum albumin (BSA) onto cellulose nanomaterials. In this case, the authors chose a combination of chemical conjugation and physical attachment. Slow and sustained release of proteins was measured with the released proteins maintaining their structural integrity. [333] These protein coated CNCs were observed to trigger a higher *in vitro* cholesterol efflux compared to free proteins.

The advantage of chemical attachment is the ability to decide when the drug is released. The linker between cellulose nanomaterials and drugs could be responsive to the presence of certain enzymes or to acidic environments. Enzymatic cleavage of the drugs was demonstrated using a L-leucin linker. To couple tosufloxacin tosilate on TEMPO-oxidized cellulose nanomaterials, Tang *et al.*, pretreated CNCs with L-leucin linkers to generate reactive amino acid functionalized CNCs. After conjugating the drug tosufloxacin-tosilate, a drug carrier for colon diseases was created in which the drug could be released enzymatically by lysozyme, but not by pepsin.[332]

A pH-responsive linker was created with a *cis*-aconityl-amide linkage. Cellulose nanomaterials initially modified with amino groups and reacted with *cis*-aconitic acid and subsequently lined with DOX. The conjugation efficiency was sufficient, but not high and it was proposed that the heterogenous reaction conditions play a role. In the final drug, the drug is released more efficiently at low pH values.[218]

The multitude of functional groups on the surface of CNCs does not only enable the attachments of dyes, but also that of targeting ligands. This has been demonstrated using folic acid, which significantly enhanced the cellular association of CNCs with the folic acid receptor positive cell lines DBTRG-05MG, H4, and C6 cells[340] and KB and MDA-MB-468.[341] Alternatively, the peptide RGD was conjugated to the surface of CNCs, which also hosts layers of PEI

and pDNA. An enhanced uptake by integrin overexpressing NIH3T3 cells was reported.[342]

In all these cases, it was crucial to monitor the uptake of cellulose nanomaterials. This was often accomplished by attaching fluorophores onto the surface,[153, 183, 188, 327] but similar chemistries can be employed to conjugate amino-functionalized carbon quantum dots to generate photoluminescent CNCs, which can be easily imaged during cell uptake studies.[207]

Nano-sized cellulose drug carriers modified with polymers

A variety of techniques have already been established to coat polymers onto the surfaces to design polymer-wrapped cellulose nanomaterials that display high stability and high drug loading. However, the amount of reports using polymers to enhance the stability of the cellulose-based nano drug carriers is rather limited. To our knowledge, the first two reports where polymer coated CNCs were used as drug carriers appeared in 2015 (**Table 2.7**).[122, 321]

It is noticeable that so far drugs were only bound by electrostatic interactions although polymers can provide build-in functionalities that allow chemical conjugation of drugs. This has only been realized yet by the attachment of a metal chelator.[227] The protein-repellent PEG based polymers, depicted in **Figure 2.11**, which carried diethylenetriaminepentaacetic acid (DTPA) as chelating groups to bind metal complexes were grafted onto CNCs.[227] The grafting process onto the aldehyde containing CNCs was monitored online as the newly formed hydrazone had a UV-Vis absorbance at 354 nm, which allowed quantifying the amounts of polymers attached to CNCs. The non-toxic carriers were now able to penetrate human ovarian cancer cell line (HEYA8) cultured in 3D spheroid models. This example shows the various advantages of polymers as they did not only convey colloidal stability, but they can bind compounds in a permanent manner preventing leaching. While this can be done without polymers as well, modification of cellulose nanomaterials alters the surface characteristics and may lead to precipitation.

In the following, the various cases of electrostatic binding are discussed. Positively charged drugs can be immobilized directly on the surface of the negatively charged cellulose nanomaterials. This is possible as polymer grafting is never so dense that all surface functionalities have been connected to a polymer (**Figure 2.20a**).[122] Other drugs such as nucleic acid requires the presence of cationic polymers. This can be accomplished by introducing cationic groups along the water-soluble polymers (**Figure 2.20b**)[343], by grafting cationic polymers (**Figure 2.20c**)[344] or by coating the negatively charged cellulose nanomaterials with positively charged polymers creating a layer-by layer assembly[320].

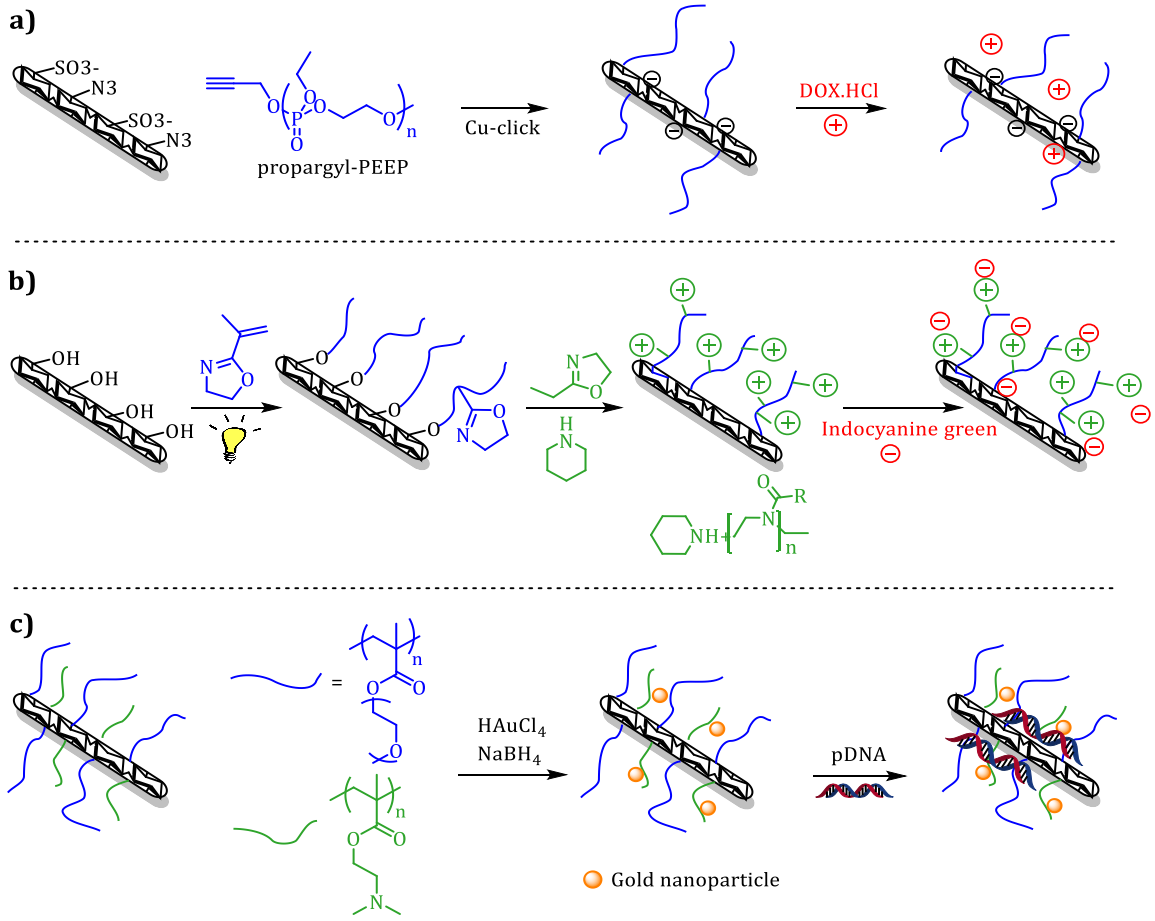

Figure 2.20. Strategies to deliver drugs with polymer coated CNCs.[122,343-344]

Electrostatic binding of positively charged drugs onto cellulose nanomaterials

In this scenario, the positively charged drugs are usually bound directly to the surfaces of cellulose nanomaterials by electrostatic interaction. The purpose of the attachment of polymer chains is then mainly to ensure high water-solubility and to control protein binding. One of the first such protein-repellent coatings used in cellulose nanomaterials-based drug delivery was poly(ethyl ethylene phosphate) (PEEP), which was obtained by ring-opening polymerization with propargyl alcohol as the initiator and clicked onto azide functionalized surfaces. As the chosen CNCs still carried sulfates, excess negative charges were available to bind doxorubicin, which showed an accelerated release profile at pH 5 compared to pH 7. The drug carriers were readily taken up by HeLa cells and the activity of the drugs inside the cell was comparable to that of the free drugs, although the toxicity was slightly lower.[122]

Attachment of polymer with a tetrazole end functionality to TEMPO-oxidized cellulose nanomaterials as shown in **Figure 2.12** creates CNCs-based fluorescent drug carriers that can be directly monitored in cell uptake studies with MCF-7 breast cancer cells. The drug carriers were loaded with various amounts of doxorubicin *via* electrostatic interaction resulting in drug carriers where the toxicity of the drug increased with increasing drug loading.[181]

In both these cases, the electrostatically bound drugs would slowly detach from the drug carriers, often triggered by concentration gradients or changes in ionic strength. To achieve better control over the drug release, Li *et al.* have reacted DOX with *cis*-aconitic anhydride to create now negatively charged drugs that are wrapped into a layer of PEI around CNCs.[345] The advantage of this approach is now the triggered release of drugs at low pH values instead of a gradual release. Once the nanocarrier can be found inside the endosomes, the *cis*-aconityl functionalities cleaves, reverting the drugs to their positively charged origins. The cationic drugs in the positively charged PEI matrix are then quickly pushed out. [345] In this case, the surfaces were in addition decorated with folic acid moieties to enhance cellular uptake and targeting.

Electrostatic binding of negatively charged drugs onto cellulose nanomaterials

While positively charged drugs can be loaded easily onto the surfaces of the often negatively charged cellulose nanomaterials, anionic drugs can only be electrostatically bound by positive charges. Attachment of cationic polymers can now easily offer a solution as it was shown by grafting poly(2-methyl-2-oxazoline) with a cationic end group to CNCs (**Figure 2.14**).[322] Poly(2-isopropenyl-2-oxazoline) was grafted by UV-induced photopolymerization and was subsequently used as initiator for the living cationic ring-opening polymerization of 2-alkyl-2-oxazoline. The polymerization was terminated with piperidine creating a positive charge at the end of each grafted polymer. The negatively charged indocyanine green molecules, which are used for NIR imaging and phototherapy, were loaded onto cellulose nanomaterials. The polymer-grafted cellulose nanomaterials were able to protect indocyanine green from photobleaching. After taken up by HeLa cells, the delivered indocyanine green introduced cytotoxicity, but only after laser irradiation at 808 nm.[322]

Other important negatively charged therapeutics are nucleic acid drugs such as small interfering RNAs (siRNAs) or plasmid DNA (pDNA), which also require a cationic matrix to efficiently bind the drug molecules. The negatively charged DNA can be assembled with negatively charged cellulose nanomaterials and the positively charged polyethylene imine (PEI), which is widely used for DNA delivery, using a layer-by-layer approach. Cellulose nanomaterials were coated with either linear or branched PEI, respectively, followed by coating with DNA. Depending on the type of PEI and the concentrations of DNA, nanoparticles with hydrodynamic diameters starting from 200 nm were created and tested with CHO-K1 cells. Branched PEI was associated with better DNA compaction, higher zetapotential, better transfection efficiency and overall better performance compared to linear PEI.[320]

Alternatively, the polymers can be grafted onto the surfaces of cellulose nanomaterials in order to create more permanent linkages. Binding PEI *via* reductive amination converted the negatively charged TEMPO-oxidized

CNFs to stable nanocarriers with sufficient positive charges, which were able to complex siRNA. The resulting complex with a hydrodynamic diameter of 280 nm was able to deliver the payload safely into C2C12 and induce apoptosis.[346]

Covalent binding of positively charged polymers can introduce an element of control as the chemical attachment point can be designed in a way that it can again be cleaved. This was achieved by immobilization of an ATRP initiator, which was bound to the surfaces by a disulphide bridge.[321] Once the drug carriers have been taken up by cells and are located within the reductive environment of the cell, the disulphide bond is reduced, the polymer is cleaved from the surface (**Figure 2.21**).

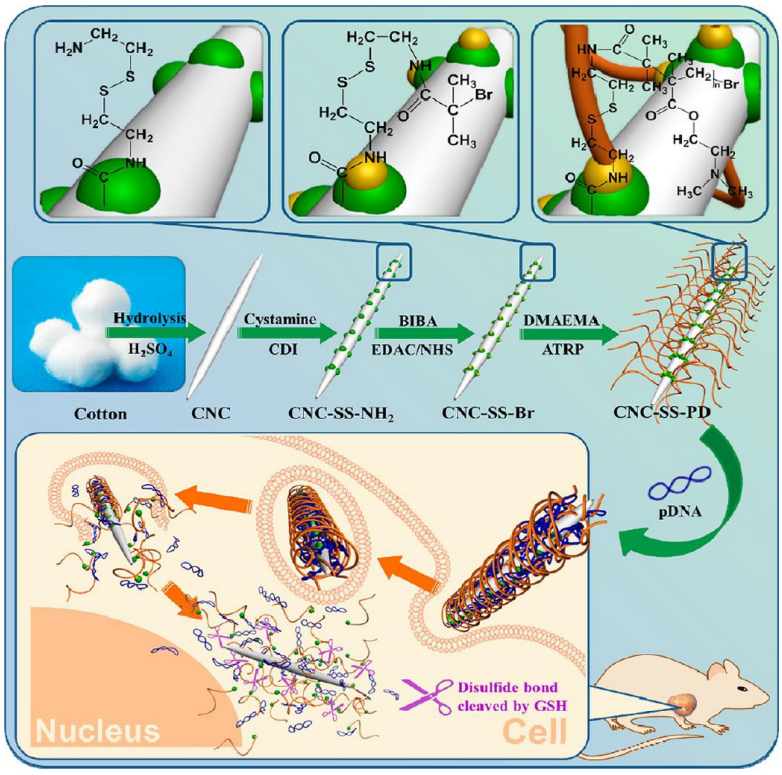

Figure 2.21. Schematic diagram illustrating the preparation of CNC-graft-PDMAEMA (CNC-SS-PD) *via* ATRP and the resultant gene delivery process.[321]

The presence of charges on the surface can result in the quick formation of a protein corona. To combat this, coating with neutral polymers such as PEG can significantly reduce protein binding. This was achieved by grafting two different polymers with a combined RAFT-ATRP approach to the

surfaces of cellulose nanomaterials (**Figure 2.20c**).[284] One polymer, Poly(poly(ethylene glycol) ethyl ether methacrylate) (PPEGEEMA), was able to shield the charges while the cationic poly(2-(dimethylamino)ethyl methacrylate) (PDMAEMA) acted as ligand for the in-situ formation of gold nanoparticles for CT-imaging and was able to bind DNA. HepG2 and HEK293 cell lines confirmed the successful transfection, but it was also interesting to note that the presence of PPEGEEMA did not have any substantial effects *in vitro* as the CNCs grafted with PDMAEMA acted in a similar way.[284]

Table 2.7. Summary of various approaches for the delivery of drugs using cellulose nanomaterials.

Source of cellulose	Formulation	Therapeutic Molecule	Responsiveness and linkage	Drug Loading technique	Drug Loading efficiency (DLE) or content (DLC)	Tested cell line	*In vitro* Cytotoxicity	Published year	Ref.
Cotton wool	CNCs-PDMAEMA	pDNA	-Redox-responsive disulfide linkage	Electrostatic interaction	-	HepG2		2015	[321]
Cotton wool	CNCs-PPEGEEMA/ PDMAEMA	pDNA, Au NPs	-	Electrostatic interaction	Various NPs ratio	HepG2, HEK293	Transfection efficiency dependent on length of PDMAEMA	2016	[284]
Medical absorbent hydrophilic cotton	CNCs-PEI	siRNA	-	Electrostatic interaction	Complete binding	Murine C2C12 myoblast	Significant cell death after 48 hr	2017	[346]
Komagataeibacter xylinus	BCNW-PEI	pDNA	-	Electrostatic interaction	-	L929	Non-toxic	2018	[320]
Cotton wool	CNCs- POX (bottle brush)	indocyanine green (ICG)	-	Electrostatic interaction	DLC = 8 wt %	HeLa	≈ 23 % - ≈ 66 % of cell death	2017	[322]

Source of cellulose	Formulation	Therapeutic Molecule	Responsiveness and linkage	Drug Loading technique	Drug Loading efficiency (DLE) or content (DLC)	Tested cell line	*In vitro* Cytotoxicity	Published year	Ref.
Wood pulp	CNCs-PEEP	DOX.HCl	-	Electrostatic interaction	27 %	HeLa	IC_{50} = 9.95 mg L^{-1}	2015	[122]
Bamboo	CNFs-PHEA	DOX.HCl	-	Electrostatic interaction	DLE = 70 - 90%	MCF-7	IC_{50} = 36 nM	2019	[181]
-	CNCs-PEI/folic acid	DOX.HCl	-pH-responsive *cis*-aconityl-amide linkage	Electrostatic-interaction-based LbL assembly method	19.4 %	MCF-7	IC_{50} = 0.12 ± 0.10 µmol L^{-1}	2019	[345]
Wood pulp	CNCs-PEG-PGlu	metal-chelator DTPA	-	Metal complex	-	HEYA8	-	2016	[227]

BCNW: bacterial cellulose nanowhiskers, CTAB: cetyl trimethylammonium bromide, DTPA: diethylenetriaminepentaacetic acid, DOX.HCl: doxorubicin hydrochloride, HepG2: human liver carcinoma cell line, HEYA8: human ovarian cancer cell line, L929: mouse fibroblasts, LbL: layer-by-layer, LYS: Lysozyme, NPs: nanoparticles, PEEP: poly(ethyl ethylene phosphate); PEG-PGlu: poly(ethylene)glycol-poly(glutamicacid), POX: poly(2-alkyl-2-oxazoline), PEI: poly(ethylene imine), PPEGEEMA: poly(poly(ethylene glycol) ethyl ether; PDMAEMA: poly(2-(dimethylamino)ethyl methacrylate

2.6. Characterization of Modified Cellulose Nanomaterials to Understand the Physico-Chemical Properties of the Drug Carrier

In this review, I discussed the feasibility and opportunities of cellulose nanomaterials as nano-size drug carriers, where the drug is delivered on discrete nanocrystals that are stable in aqueous solution. Unmodified CNCs are typically not soluble in aqueous solution and TEMPO oxidation only helps the water dispersibility when the surface is ionized in alkaline solutions. While the researcher can choose from many methods to attach small molecules to the surface for enhanced colloidal stability, nothing improves the stability of cellulose nanomaterials in water like a well-defined dense polymer brush. Blood circulation, cell uptake and tumour extravasation are all dependent on the physico-chemical properties of the nanoparticles. Detailed characterization of cellulose nanomaterials is therefore essential.

Composition and surface grafting density

The number of grafted polymers will not only determine the stability in biological media, but also affect the fate of the nanoparticles in the body. It is well-known that the density of polymer on the coated surface will influence binding of blood proteins, which can ultimately alter the fate of the material. It is therefore essential to quantify the amount of polymer in order to understand the biological activity. Grafting polymers or low molecular weight compounds is usually quickly confirmed by FT-IR analysis,[73, 347, 348] but X-ray photoelectron spectroscopy (XPS) [156, 349] and nuclear magnetic resonance (NMR), in particular solid state NMR[348] can provide more quantitative information. Thermal analysis is usually used for nanocomposites, but it can be useful to determine the composition of polymer-grafted cellulose nanomaterials and can be used to determine the grafting density when the molecular weight of the grafted polymer is known.[73] Occasionally, the grafting strategy itself enables direct quantification of the amount of attached functional groups as the occurring reaction will lead to a functional group that can be analysed by spectroscopy such as the product obtained from the reaction with tetrazoles[175] or

the formation of bisaryl hydrazones.[227] Moreover, the grafting density of fluorescent or UV-Vis active polymers can be quantified after grafting to the surfaces of cellulose nanomaterials.[73] It is worth to note that there is also a possibility of unspecific polymer binding on cellulose nanomaterials *via* physical adsorption.[73] Although the CNCs may appear intact under the microscope, it is possible that the crystallinity suffered. The crystallinity index (CI) of cellulose nanomaterials can be analysed *via* solid-state ^{13}C nuclear magnetic resonance (NMR) as crystalline and amorphous carbons can be distinguished by their slightly different shifts.[348] More common is the analysis *via* X-ray powder diffraction (XRD) revealing peaks at around 2 theta (Θ) 15°, 17.2° and 22.2°, indicating the crystal structure of cellulose nanomaterials.[350]

Shape

One of the motivations to use cellulose nanomaterials as drug carriers is the non-spherical shape as it was proposed by some literatures that this will extend circulation time. The surface-modified cellulose nanomaterials can initially be characterized using microscopy techniques such as transmission electron microscopy (TEM),[73, 351] scanning electron microscopy (SEM)[351] or cryo-scanning electron microscopy (Cryo-SEM), and atomic force microscopy (AFM) [73, 351] to provide initial feedback if surface modification led to the disintegration of the cellulose nanomaterials compared to the unmodified product. These techniques can be used to reveal chirality and contour length of cellulose nanomaterials.[351]

However, the aspect ratio is also crucial as this will determine cellular uptake and blood circulation time. It needs to be considered that CNCs can have a broad size distribution with the single clusters varying in lengths. Although microscopy analysis can provide an initial assessment of the polydispersity of the sample, the size distribution in solution can be assessed by field flow fraction-multi angle light scattering (FFF-MALS).[352, 353]

Behaviour in aqueous solution: Size and stability

For the purpose of drug delivery, the size, stability and morphology in aqueous solution are essential. Blood circulation, extravasation and cell

uptake are all dependent on the size and agglomeration of modified cellulose nanomaterials, limiting their uses in drug delivery applications. While cryo-TEM can reveal the morphology in solution, dynamic light scattering (DLS) is a frequently applied technique to measure the hydrodynamic diameter.[225, 279, 280, 294, 309] However, due to the high aspect ratio of cellulose nanomaterials, the obtained numbers are somehow meaningless, but they can provide information on colloidal stability over time and can offer some indication on whether discrete nano-object are present or if there is a tendency to aggregate. DLS can also provide an initial assessment if proteins are bound as it will be able to detect the formation of large protein coronas. I recommend that protein coating should moreover be studied with more sophisticated techniques such as QCM-D (Quartz crystal microbalance with dissipation monitoring). It is possible to obtain the lengths of cellulose nanomaterials by DLS in reasonably good agreement with TEM analysis by elucidating rotational and translational diffusion coefficients from the DLS experiment.[354] More information can be obtained by small-angle neutron scattering (SANS) and small-angle X-ray scattering (SAXS), which can provide precise information on the cross-section of the cellulose nanomaterials.[354] A simple way of determining the widths of cellulose nanomaterials is from turbidity measurements using light scattering.[355] This technique provides good estimates when compared to the results obtained from AFM studies. Isogai and co-workers have developed further techniques to understand the size of cellulose nanomaterials – length and diameter – in more detail.[356] They found that the intrinsic viscosity [η] is a direct measure of the aspect ratio. CNCs with high aspect ratios was found to be more flexible resulting in an increase of viscosity.[356] Finally, analysis of the surface charge is essential, which can easily be obtained by zeta potential measurements.[357] It is proposed that cationic nanoparticles have a higher cellular uptake while neutral and negatively charged polymers seemed to have better penetration into tumour.[358] However, in recent years, researchers have come to the realization that it is not due to the charges on the surface, but the effect of this charges have on protein binding. Again, analysis of the protein corona is essential.

2.7. Future Prospects, Major Challenges and Possible Alleviation Strategies

Cellulose nanomaterials have gained increasing interest as suitable candidates for drug delivery applications owing to their inherent attributes: non-toxicity, biocompatibility, good mechanical properties, high surface area-to-volume ratio, ideal size and shape for high cell internalization, and multi-functionality to be compatible with the biological environment.

Although much progress has been made on the development of cellulose-based nano drug delivery system in the form of cross-linked hydrogel or aerogel, the application of cellulose nanomaterials as drug carriers for intravascular administration is still in its infancy. To design efficient cellulose-based nano drug carriers for the *i.v.* route, the drug carrier needs to be able to address a range of challenges known in the delivery of free drugs such as (i) the low solubility of drug molecules and their accumulation in undesired sites, (ii) the fast clearance from the blood stream by mononuclear phagocyte system (MPS)[145, 359] and (iii) renal filtration and urinary excretion[360].

Encapsulation of therapeutics (e.g., small drug molecules, proteins, DNA, etc.) onto cellulose nanomaterials can overcome the first challenge by improving the solubility and facilitating the entry into the target cell resulting in the reduction of off-target effect. However, the limitation is that attaching small molecules directly on the surface of cellulose nanomaterials contributes sometimes to lower water-dispersibility; therefore, surface modification techniques need to be explored to design cellulose nanocarriers with high colloidal stability not only in water, but also in buffer, in cell growth media and in physiological conditions. Another challenge that needs to be addressed is that the drug encapsulated nanomaterials can be sequestrated from the blood stream by MPS, which is a network of immune cells located mainly in the liver, spleen and lymph nodes.[145, 359, 361] However, the sequestration can also be the result of the adsorption of plasma proteins including serum albumin onto the surface of circulating cellulose nanoparticles once injected into the blood-stream.[362] As the majority of the proteins display negatively charges, they can

be repulsed by negatively charges on the surfaces of cellulose nanomaterials. However, at the same time, this can attract the adsorption of cationic proteins which leads to the formation of proteolytic enzymes. This activates the C3 protein (an important protein in the body), which can bind to the surface of nanoparticles by transesterification. As a result, the nanoparticles coated with C3 proteins are quickly recognised and digested by the phagocytic cells that have C3 receptors on their surfaces.[363] This problem can be alleviated by coating the surface with anti-fouling polymers, especially poly(ethylene glycol) (PEG), to reduce protein adsorption in the biological medium.[145]

The drug carriers can also be eliminated from the body *via* renal filtration and urinary excretion. As the nanoparticles smaller than 5.5 nm have a higher tendency to be rapidly cleared from the body, toxicity and biological activities of nanoparticles are minimized.[360] This can be easily overcome by manipulating the surface chemistry of cellulose nanomaterials. The multitude of available reactions for surface functionalization can pave the way for cellulose nanomaterials to become a promising drug carrier: longer circulation time in the bloodstream, minimum side effects to healthy cells, increased toxicity to infected cells, enhanced cellular uptake by incorporation of active targeting moieties, and successful accumulation of therapeutics specifically at diseased sites.

In the end, the key is the tailored surface modification of cellulose nanomaterials. Although cellulose nanomaterials already have high surface functionalities, these groups are not enough to obtain colloidal stability in water. However, in the last few years, a multitude of surface functionalization techniques was explored to alter the surface structure without losing the structural integrity. As a result, cellulose nanomaterials that are stable against aggregation are now available. Moreover, polymers can enhance these effects while introducing stimuli-responsive features. A fully functioning synthetic toolset is now available to create cellulose nanomaterials with any desirable features including high drug loading and potentially, although not yet tested, low protein adsorption.

2.8. Polymerization Technique Used in The Thesis

A range of polymers mentioned throughout the thesis were synthesized by using reversible addition-fragmentation chain transfer (RAFT) polymerization. The major advantage of the application of RAFT polymerization is its feasibility to introduce typical functional groups at the end of polymer chains,[364] which in turn can be employed to modify cellulose nanomaterials. The mechanistic aspect of the process and the selection of the appropriate RAFT agent for the monomers to be polymerized are reviewed in the following section.

2.8.1. Reversible Addition-Fragmentation Chain Transfer (RAFT) Polymerization

The RAFT process was firstly reported by Australian Commonwealth Scientific and Industrial Research Organisation (CSIRO) as a versatile living or controlled radical polymerization in 1998.[365] The living character of the polymerization is maintained by thiocarbonylthio compounds, the so-called RAFT agents which behave as chain transfer agents.[366] The RAFT mechanism is generally based on the equilibrium between activation-deactivation process as depicted in **Figure 2.22 a**. In step I (the initiation step), the radical (I•) from an azo or peroxy intiator such as Azobisisobutyronitrile (AIBN) adds to the monomer (M) to form a propagating oligomer chain (Pn•). In step (II), the propagating oligomeric radical (Pn•) adds to the sulfur-carbon double bond (C=S) of the initial RAFT agent (1), resulting in a carbon-centered intermediated radical (2). The benefit of the RAFT process is that the generated RAFT radical limits the irreversible termination reaction between propagating species. In this case, the addition of primary initiator-derived radicals to the initial RAFT agent is negligible but it can occur with a high concentration of initiator, impacting the kinetics in the early phase of the RAFT process. As it is reversible, the intermediate radical (2) returns to the initial state resulting in a propagating radical (Pn•) and the RAFT agent, while it (2) may also fragment into a reinitiating radical species (R•) and an oligomeric RAFT agent or macro-CTA (a dormant chain) (3). The generated reinitiating radical (R•) reacts with monomers to start a new polymer chain (Pm•) (step III), which will again react with the macro-CTA (Step IV). In this

process, the polymerization can be controlled by the macro-CTA once the initial RAFT agent is completely consumed.[367] A rapid equilibrium between the dormant species (3) and the active propagating radicals (Pn• and Pm•) enable all living chains to grow simultaneously with equal chain length. The termination by radical-radical reaction (Step V) are often inevitable in a radical polymerization process.[366, 368, 369]

A wide range of monomers including acrylates, acrylamides, methacrylates, methacrylamides, styrene derivatives and vinyl esters can be polymerised *via* the RAFT process. However, the RAFT agent needs to be chosen carefully for the successful polymerization to achieve a pre-chosen molecular weight and low molecular weight distribution (dispersity) (**Figure 2.22 b**).[366, 370] A RAFT agent involves Z group and R group, in which Z is a stable group that modifies the reactivity of the C=S bond and derives adduct radial, while R is a leaving group (**Figure 2.22 a, b**). As mentioned above, the radical R• generated from R group must efficiently reinitiate polymerization to undertake the chain transfer process. Furthermore, the RAFT technique allows the synthesis of polymers with complex architectures which include block, random (statistical), gradient, star, comb, brush, hyperbranched, and network copolymers.[371] Also it opens up the opportunity to synthesize a wide range of polymers with a rich variety of functionality and architecture in controlled manner for their use in biomedical applications.[370, 371]

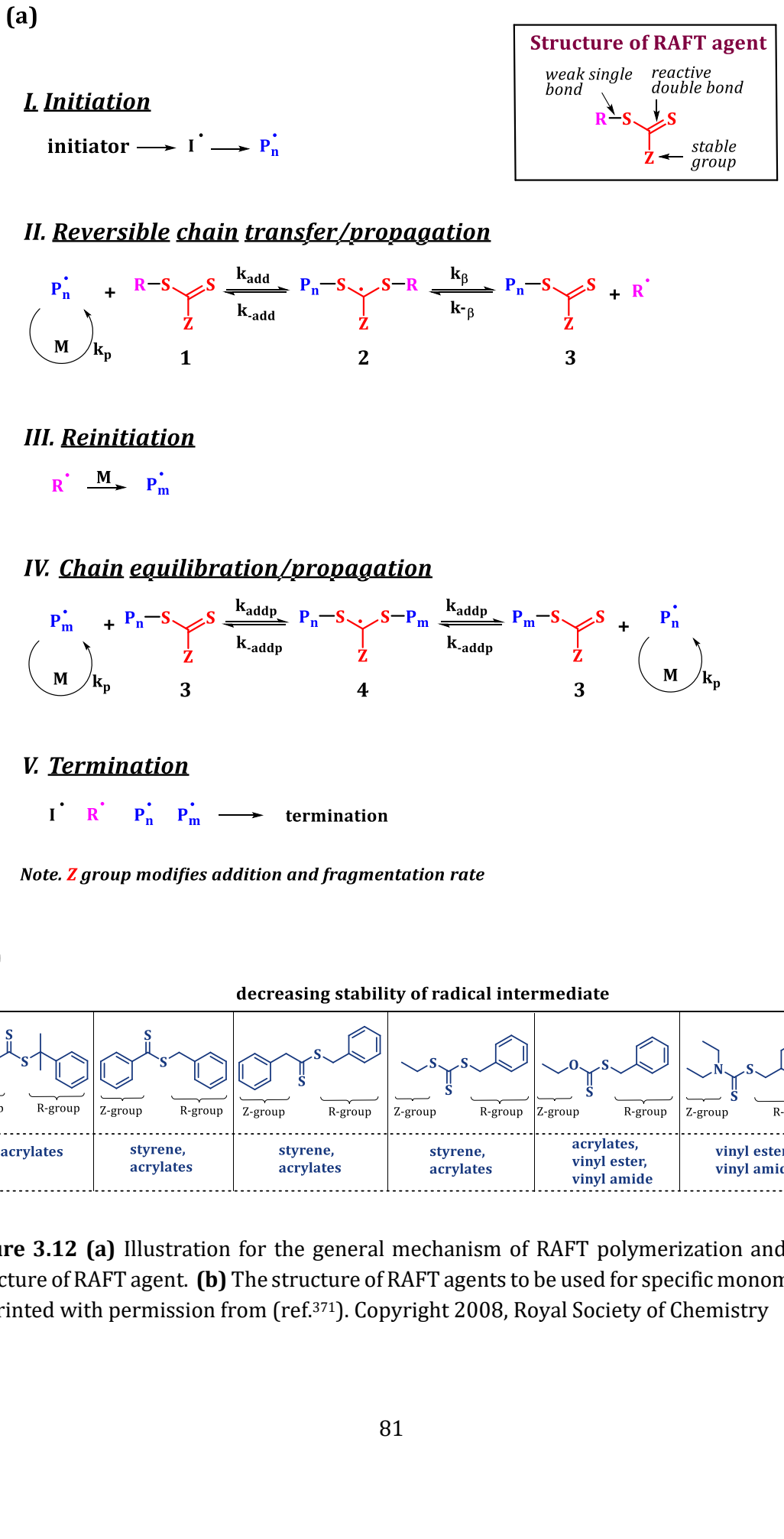

Figure 3.12 (a) Illustration for the general mechanism of RAFT polymerization and the structure of RAFT agent. **(b)** The structure of RAFT agents to be used for specific monomers. Reprinted with permission from (ref.[371]). Copyright 2008, Royal Society of Chemistry

CHAPTER - 3

Synthesis of Cellulose Nanofibers (CNFs)

&

Analytical Techniques of the Thesis

Table of Content

3.1. Overview

Plant-derived native cellulose was converted to individual fibrils *via* mechanically assisted 2,2,6,6,-tetramethylpiperidine-1-oxyl radical (TEMPO)-mediated oxidation. The electrostatic repulsion between TEMPO-oxidized cellulose fibrils (CNFs) resulted in a transparent dispersion in water with 7 nm in width and narrow particle size distribution based on the analyses *via* DLS and TEM. The carboxylate groups ($-COO^-$) on CNFs were then converted to acid (-COOH) moieties under HCl treatment (pH ≈ 2), as a requirement for further surface modifications. The chemical and physical properties of CNFs: acid (-COOH) contents ≈ 1.65 mmol g^{-1}, pKa = 5.22, crystallinity = 56 %, reversible aggregation behaviour, initial decomposition temperature = 252 °C and existence of reducing aldehyde groups, were confirmed *via* a potentiometric acid-base titration, FT-IR, XRD, DLS, TGA and BCA assay.

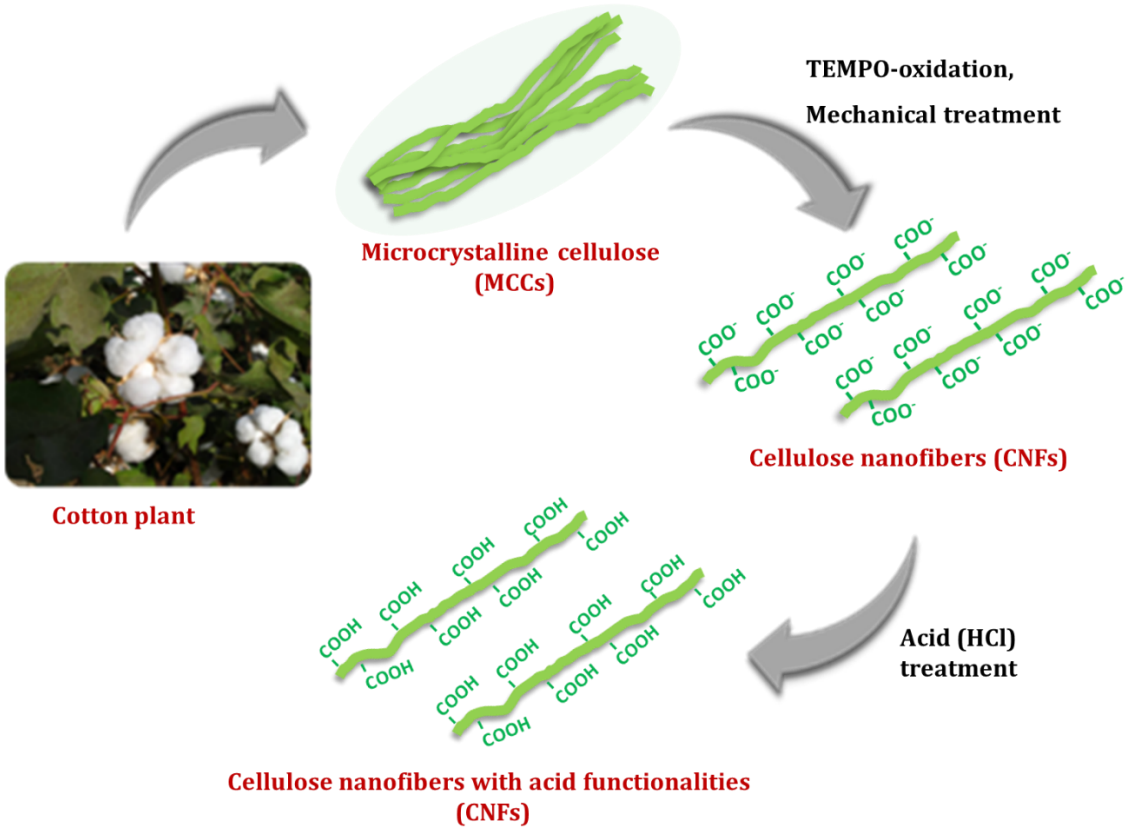

Scheme 3.1. Overall scheme for the synthesis of cellulose nanofibers (CNFs) with carboxylic acid functionalities.

3.2. Introduction

Cellulose, the most adwbundant natural biopolymer on earth, has attracted attention as a novel material for biomedical applications due to its unique properties: biocompatibility, biodegradability, and low cytotoxicity. In particular, cellulose nanomaterials isolated by the chemical or mechanical treatment of native cellulose, either as cellulose nanofibers (CNFs) or cellulose nanocrystals (CNCs), are attractive for material design due to their nano-sized dimensions.[61, 66, 372, 373] CNCs are commonly obtained by acid hydrolysis using sulphuric acid (H_2SO_4) or hydrochloric acid (HCl) under aqueous conditions at high temperature. This technique results in nano-sized cellulose with high crystallinity by removing acid-sensitive amorphous region of the native cellulose as discussed in **Chapter 2**. However, the properties of the resulting product highly depend not only on the lignocellulose source but also on the preparation conditions such as the nature of the acid, the reaction temperature, and the reaction time. For instance, excessive acidic conditions may lead to the dramatic decrease in the yield as well cellulose chains are degraded into individual glucose units. In addition to this, CNCs prepared *via* HCl hydrolysis tend to aggregate even in water due to the lack of surface charges that play a crucial role for the efficient fibrillation by electrostatic repulsion. Another alternative way of fibrillation to achieve cellulose nanomaterials in the form of CNFs is mechanical treatments by using a high-pressure homogenizer or high-pressure ultrasonication. However, cellulose fibrils in plant cell walls are tightly hooked to one another by inter- and intramolecular hydrogen bonding.[374] Thus, it is difficult to individualize cellulose fibrils only by mechanical treatment. Also, it was reported that the bundles of cellulose remain in the resulting product even after mechanical treatment.[375, 376] Therefore, to obtain individualized nanofibrils without significant aggregation, surface modifications of cellulose fibrils are required before mechanical disintegration.

During the last decade, efforts have been made to prepare cellulose nanomaterials from plant-derived cellulose by TEMPO-NaBr-NaOCl treatments followed by mechanical fibrillation. TEMPO stands for 2,2,6,6,-tetramethylpiperidine-1-oxyl radical and the main objective is the regioselective conversion of primary hydroxyl groups on the cellulose chains to charged carboxyl entities, while the secondary hydroxyls remain unaffected.[74, 377] The presence of ions on the surface makes it

possible to loosen the adhesion between cellulose chains *via* electrostatic repulsions.[378] The complete fibrillation of cellulose nanomaterials which have high aqueous dispersibility can be achieved by mechanical treatment of the oxidized cellulose/water slurries. This technique has been highly interesting due to their mild reaction conditions to individualize fibers of 3 – 4 nm in width while maintaining their fibrous morphologies and crystallinities.[379] Moreover, the existence of carboxyl groups allows for the subsequent modification of cellulose nanomaterials with polymers to ensure aqueous dispersibility under acidic conditions for the purpose its applications in drug delivery. In this research, we tend to fibrillate native cellulose obtained from cotton linters to nanofibers (CNFs) *via* mechanically assisted TEMPO-oxidation, followed by the formation of free acid (-COOH) functionalities by acid treatment. The general scheme is shown in **Scheme 3.2**. The structure and general surface chemistry of oxidized fibers were characterized *via* TEM, DLS, a potentiometric acid-base titration, FT-IR and XRD.

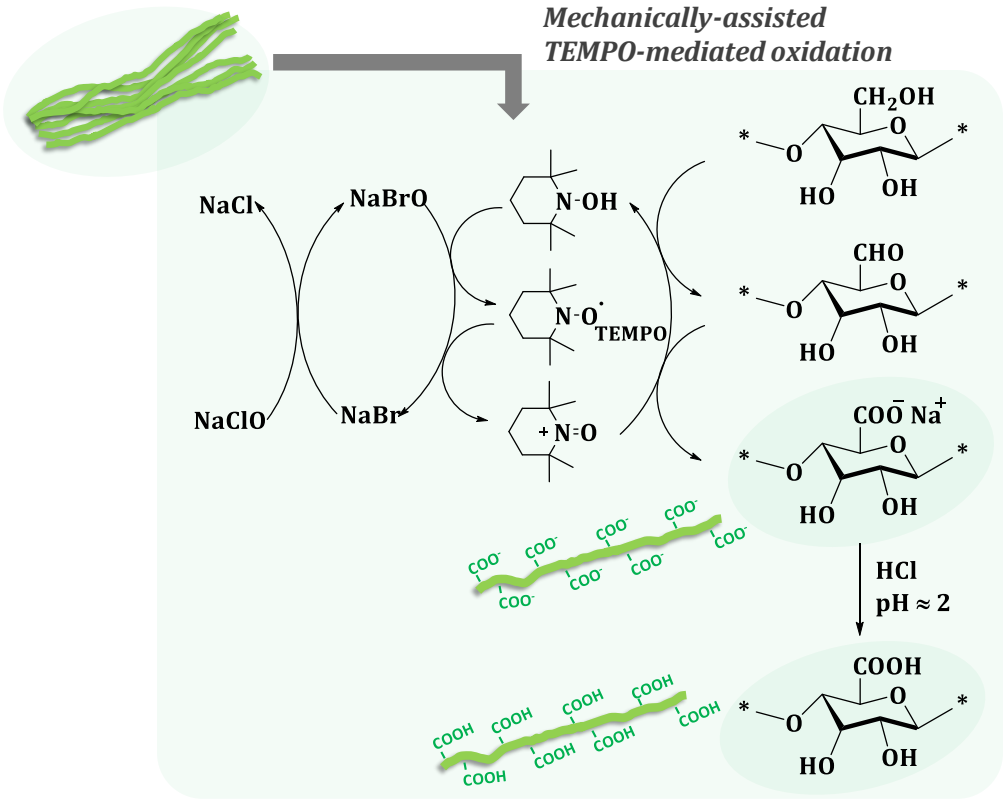

Scheme 3.2. Schematic illustration for the synthesis of cellulose nanofibers (CNFs) *via* mechanically assisted TEMPO-mediated oxidation under mild reaction conditions.

3.3. Results and Discussions

3.3.1. Fibrillation of cellulose *via* mechanically assisted TEMPO-mediated oxidation

This research mainly focuses on the fibrillation of cellulose *via* TEMPO-mediated oxidation which introduces ionic charges on the surface of fibrils. The charges on the surface can then separate individual fibers *via* electrostatic repulsion. This process containing TEMPO-NaOCl-NaBr selectively oxidises C6 primary hydroxyl groups of glucosyl units to sodium carboxylates under mild reaction conditions in aqueous media. During the reaction, the primary oxidizer (NaOCl) is consumed, while the pH value of the solution decreases, which can be monitored during the reaction. This was studied by suspending 0.5 g of microcrystalline cellulose in 200 mL of aqueous media containing 0.04 g of TEMPO, 0.2 g of NaBr, and 7.5 mL of 12 % NaOCl. The pH value was measured over 5 hr in which the pH level of the suspension decreased from approximately 12.25 to around 9.00. The reduced pH value during the 5 hr of oxidation is an indication of the formation of carboxyl groups (**Figure 3.1**).

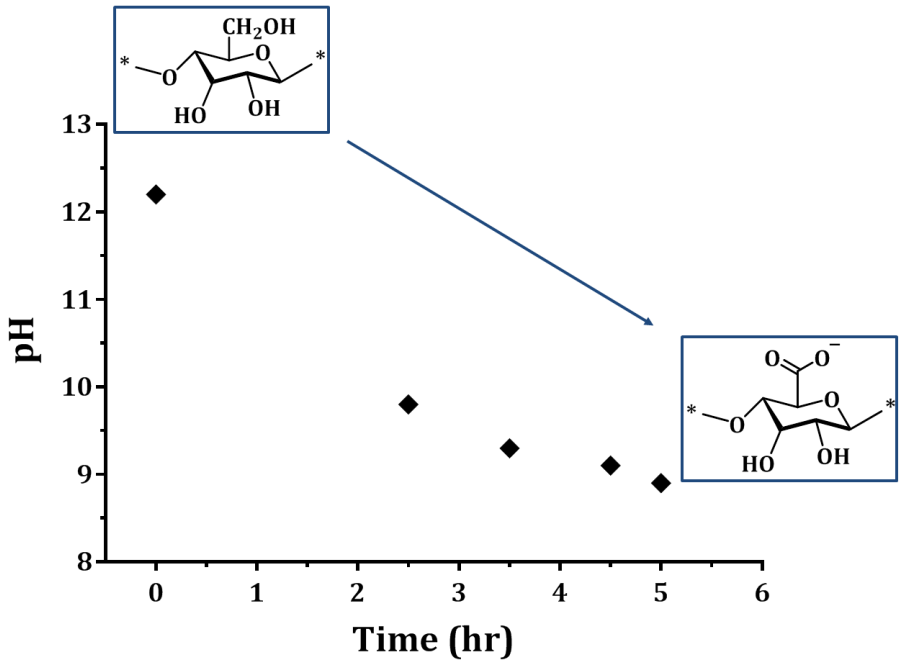

Figure 3.1. pH changes during TEMPO-mediated oxidation for the formation of nanofibrils (CNFs) from microcrystalline cellulose (MCCs).

Nevertheless, it was expected that the pH value would decrease below 9 if the reaction proceeded further. However, this was not attempted as the pH value of the suspension during oxidation reaction need to be maintained in the range between 10 and 11 in order to avoid any side reactions on the secondary hydroxyl groups on the surface of fibrils. In addition to this, maintaining the pH adjustment will lead to more efficient oxidation to form sodium carboxylates on the surface of fibrils.

Therefore, the reaction was further improved by using the TEMPO-oxidation condition according to the synthesis procedure mentioned in **Section 3.5.1**. During the oxidation process, the pH level was continuously monitored and maintained between 10 and 11. When no more pH changes were observed, which indicates no more consumption of NaOCl, the reaction was left stirring for 26 hr to ensure that surface oxidation was completed.

After stopping the reaction and dialysing against water to remove the excess of unreacted reactants, the fibrillated nanofibers were obtained; however, some aggregates were still clearly visible as shown in **Figure 3.2**. Deaggregation was achieved by further mechanical treatment using a high intensity ultrasonicator. The solid content of the suspension was adjusted to 0.1 % - 0.2 % for efficient fibrillation and 50 mL of suspension was treated for 15 min, at 30 % intensity. As expected, the dispersibility of the oxidized cellulose with sodium carboxylate groups ($-COO^-$) was significantly improved after mechanical treatment as shown in the recorded pictures in **Figure 3.2**. If there were some contaminations, the CNFs suspension can be simply centrifuged several times at 8000 rpm for 10 min to remove precipitated large particles and any impurities. The pure cellulose fibers (CNFs) remained in the supernatant. As an alternative, the large impurities can be removed by filtration. The formation of individualized cellulose nanofibers (CNFs) was confirmed by visual examination of the clear dispersion of the cellulose suspension after TEMPO-mediated oxidation and ultrasonic treatment.

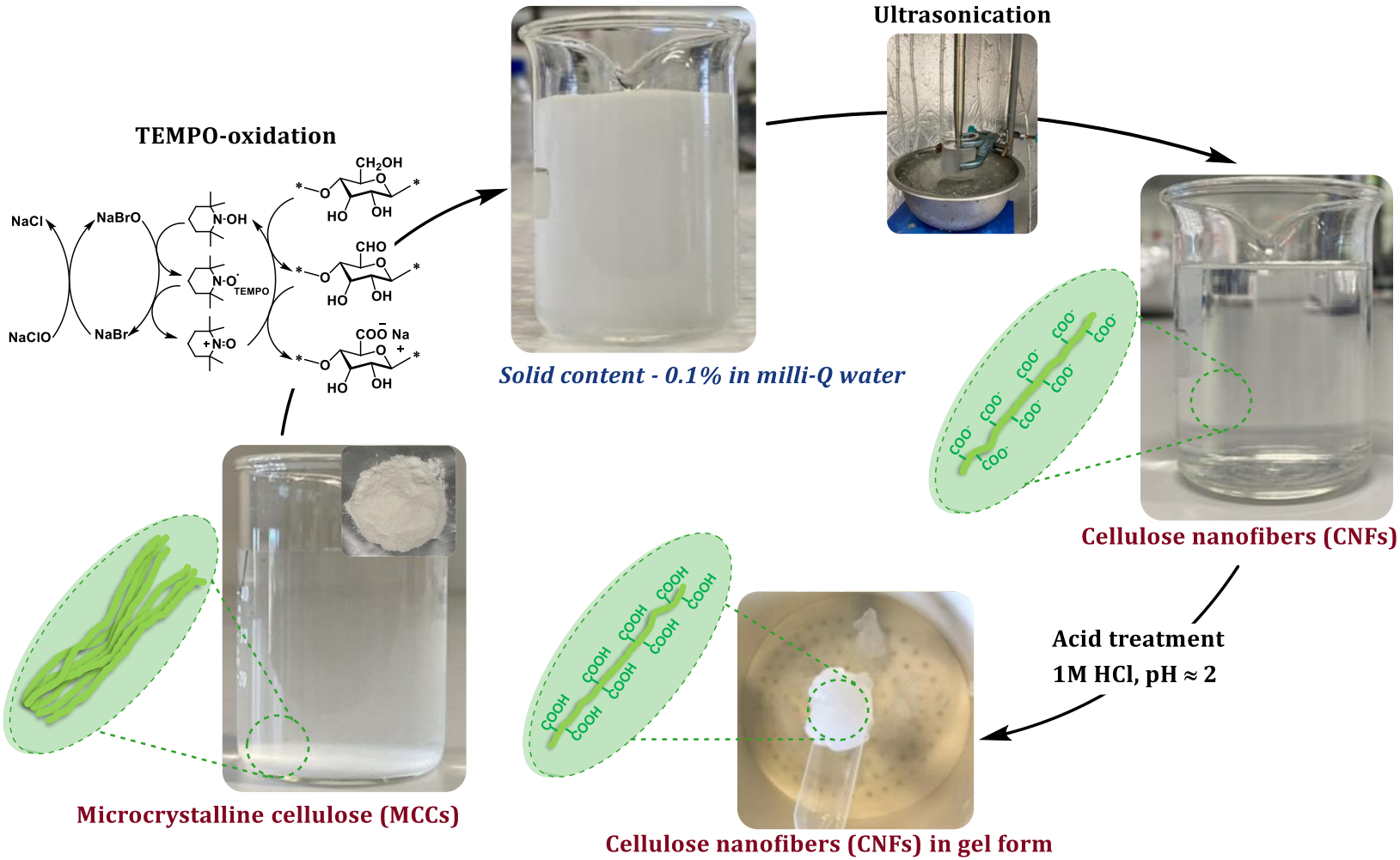

Figure 3.2. Recorded suspensions of MCCs and fibrillated CNFs *via* mechanically assisted TEMPO-mediated oxidation. The same solid content (0.1 % in milli-Q water) was used for all samples to compare their dispersibility.

3.3.2. Morphological study of mechanically assisted TEMPO-oxidized cellulose nanofibers (CNFs)

The morphological study of fibrillated CNFs was performed by TEM after negative staining by uranyl acetate (UA). The diameter of nano-sized fibers was measured to be approximately 7 nm, fragmented from a bundle of MCCs with the diameter approximately 170 nm (**Figure 3.3**). The widths of single fibers obtained from TEM characterization are almost in agreement with the findings in literature.[380, 381] Moreover, the individualized fibers were observed as very long rod-like fibers with varying degrees of entanglement. However, their web-like structure made it difficult to clearly reveal the length of single fiber at any TEM magnifications and it could be assumed to be a several micrometer.[382] Nevertheless, these findings confirm the fact that the TEMPO-mediated oxidation is mild enough to preserve the size and shape of fibrillated nanofibers.

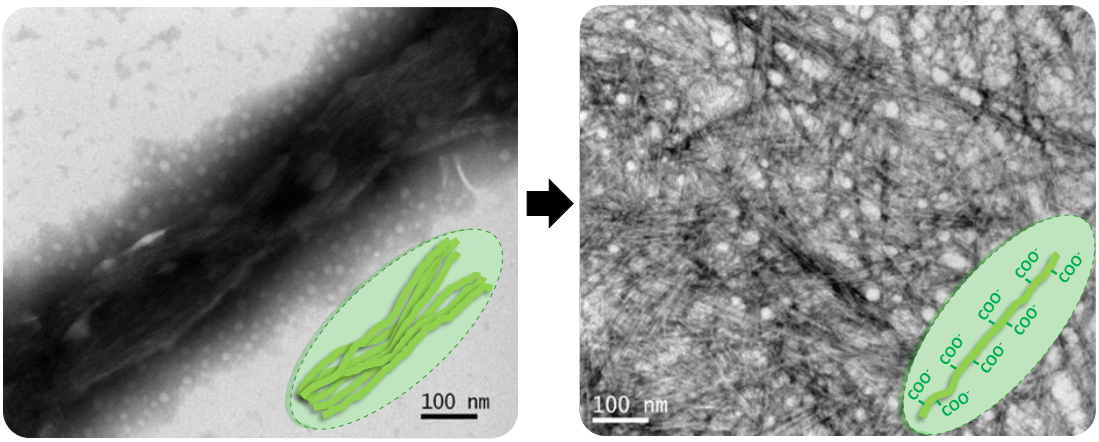

Figure 3.3. Transmission electron micrographs of MCCs (**left**) and CNFs after mechanically assisted TEMPO-mediated oxidation (**right**). 0.1 % CNFs dispersion in milli-Q water.

Moreover, dynamic light scattering (DLS) technique was employed to measure the hydrodynamic diameter distribution of nanofibrillated cellulose present in the suspension. In this analysis, it is recommended to use low concentration of CNFs (even less than 0.1 % solid content in most cases) to efficiently determine the statically average dimensions of individual cellulose nanomaterials. The statistical distribution as illustrated in **Figure 3.4** clearly confirms the existence of cellulose nanomaterials with the diameter of 126.3 nm and narrow dispersity (PDI = 0.216) in

the suspension. Here, the CNFs as rod-like particles may rotate in two dimensions: the lateral dimension ranging from 5 to 20 nm, and the longitudinal dimension ranging from 100 nm to 500 nm in general for TEMPO-oxidized CNFs.[383]

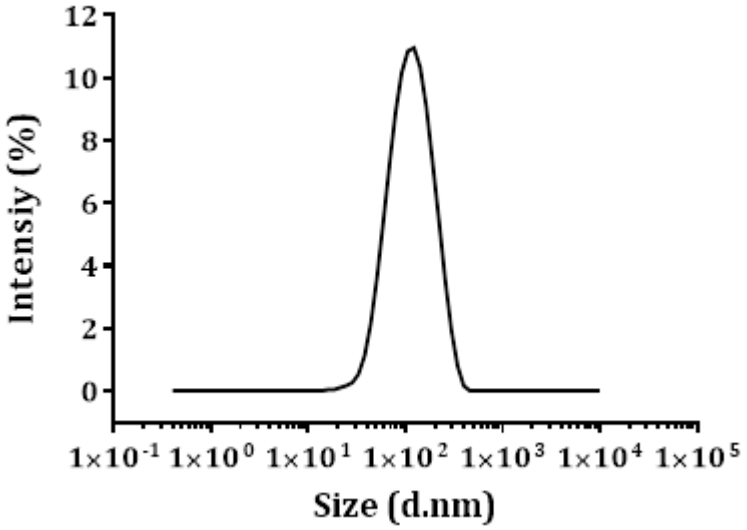

Figure 3.4. Particle size distribution of CNFs (-COO^-) obtained from DLS studies. Concentration = 1 mg mL^{-1} in milli-Q water.

Acid treatment of mechanically assisted TEMPO-oxidized CNFs

After generating oxidised CNFs with the desirable morphology, diameter and size distribution; the particle dispersion was neutralised using 1 M HCl for 30 min at room temperature. The purpose of this experiment is to learn more about the amount of carboxylate groups on the surface of CNFs, but also to understand how the dispersibility changes at different degrees of ionization. Once the carboxylate is protonated at low pH, the particles tend to aggregate into gel as the repulsive forces are now absent. This CNFs gel was subsequently collected by washing with water and centrifugation until the supernatant reached neutral pH indicating the complete removal of excess HCl. It is important to note that the incomplete removal of HCl may result in the collecting product as thick gel which was found not to be suitable for further functionalization as the gel could not be resuspended well in aqueous media. Also, direct use of the thick gel for further surface modification was not possible as the reactant cannot penetrate the gel enough to react with the CNFs surface. Therefore, the samples were washed with water several times in this work to

generate a less viscous gel. Depending on the preference of the experiments, the thickness of CNFs gel may be varied.

There are two things to consider when storing CNFs gel.

- Firstly, the obtained CNFs gel needs to be stored in the fridge at 4 °C to prevent growth of fungi. It is not recommended to store the gel in the freezer as it can damage the gel.
- Secondly, CNFs gel should not be dried as drying will give rise to irreversible aggregation. When water is removed from the gel, hydrogen bonding will result in strong interactions of the fibers and therefore aggregation; consequently, these aggregates are difficult to redisperse. The aggregation is worse if the organic solvent is removed from CNFs gel as it may result in irreversible assembles into a rigid plastic-like material.

Infrared analysis of oxidized CNFs and degree of carboxylation

As mentioned earlier, the presence of carboxylic acid in the protonated state is essential for some surface modification reactions. The degree of protonation at different pH values was therefore monitored by FT-IR and quantified by pH titration. The IR spectra of MCCs and oxidized CNFs before and after acid treatment are depicted in **Figure 3.5**. The characteristic peaks of unoxidized cellulose (MCCs), such as C-O-C stretching of pyranose ring skeleton at 1054 cm^{-1}, C-H stretching at 2898 cm^{-1}, hydrogen bonded O-H stretching at 3338 cm^{-1} are present in all samples and not influenced by TEMPO-mediated oxidation (**Figure 3.5a**). Upon oxidation of hydroxymethyl groups on the surface, a new band at 1604 cm^{-1} which corresponds to the C=O stretching vibration of sodium carboxylate groups ($-COO^-$) was observed (**Figure 3.5b**). Moreover, the IR spectrum confirms the presence of free carboxyl (C=O) groups at low pH values, which appear at an absorption band at 1724 cm^{-1} after protonation at pH ≈ 2, affirming the existence of free acid groups on the surface of CNFs (**Figure 3.5c**). Based on the findings from FT-IR, it could be concluded that the primary hydroxyl groups of glucose units on the surface of cellulose were successfully converted into carboxylic acid moieties under mild reaction conditions.

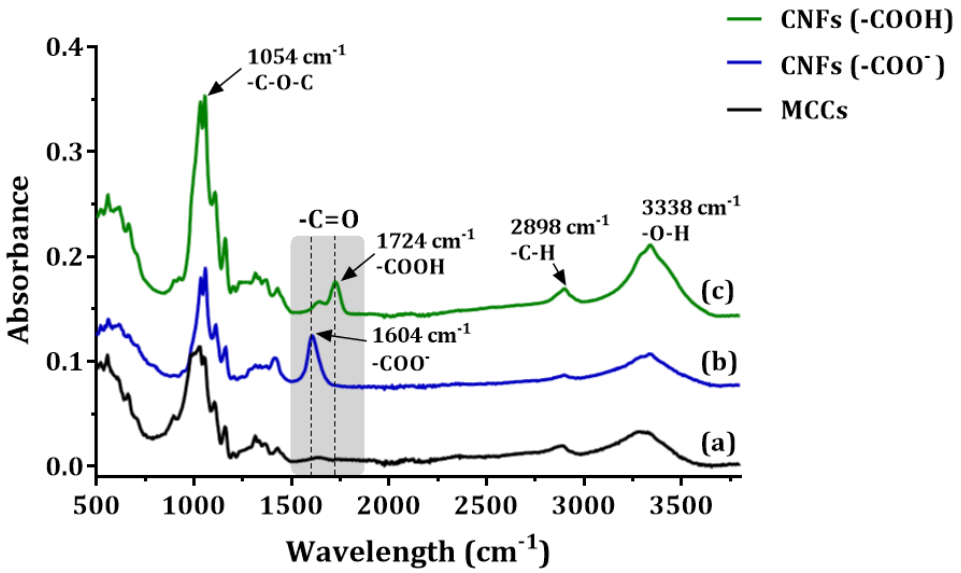

Figure 3.5. FT-IR spectra of untreated (MCCs) and TEMPO-oxidized cellulose samples.

The degree of carboxylation or the amount of carboxyl groups on the surface was determined by titration using 0.1 M NaOH. The pH value was recorded every time after the addition of 5 µL of NaOH solution into the dispersion containing 10 mg of dried CNFs bearing carboxylic acid groups in milli-Q water. The amount of carboxylate groups determined by titration amounted to around 1.65 mmol acid groups per g of CNFs and the pKa value was calculated to be 5.22 (**Figure 3.6**).

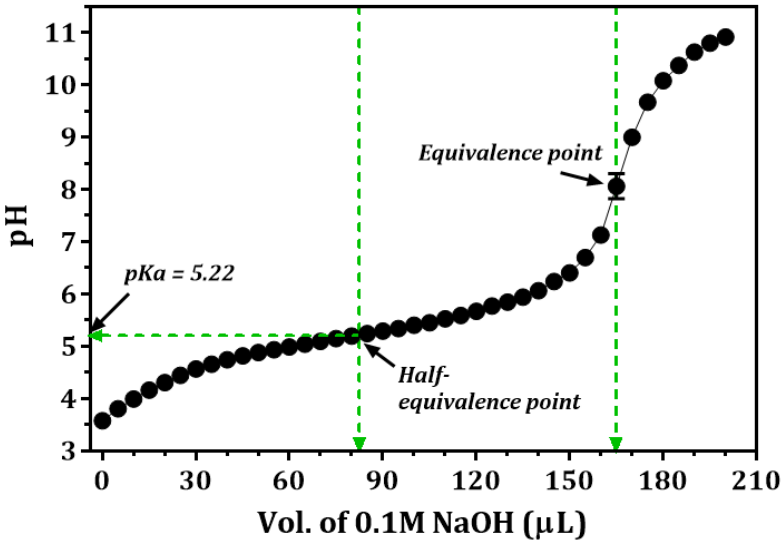

Figure 3.6. Titration curve of CNFs after acid treatment (moles of COOH = 1.65 mmol g^{-1} of CNFs, pKa = 5.22).

Dispersibility and aggregation of CNFs at different pH levels

For the investigation on the dispersibility changes of CNFs in aqueous media, 10 mg of freeze-dried CNFs was suspended in milli-Q water and the desired pH value was obtained by adding 0.1 M NaOH. Here, the freeze-dried CNFs were used to clearly visualize the aggregation-disaggregation behaviour. The visual differences in the dispersibility of CNFs suspension at different pH values is depicted in **Figure 3.7**. Depending on the pH value of the solution, the CNFs are now well dispersed in the aqueous solution. Even at low pH values, which correspond to a fully protonated state, the solution is stable, yet cloudy. The entanglement was obviously decreased at pH 6 with some aggregation occurring in the dispersion. The higher formation of ions above pH 7 improved the fiber dispersibility and resulted in clear dispersion at pH 11 as a consequence of efficient electrostatic repulsion.

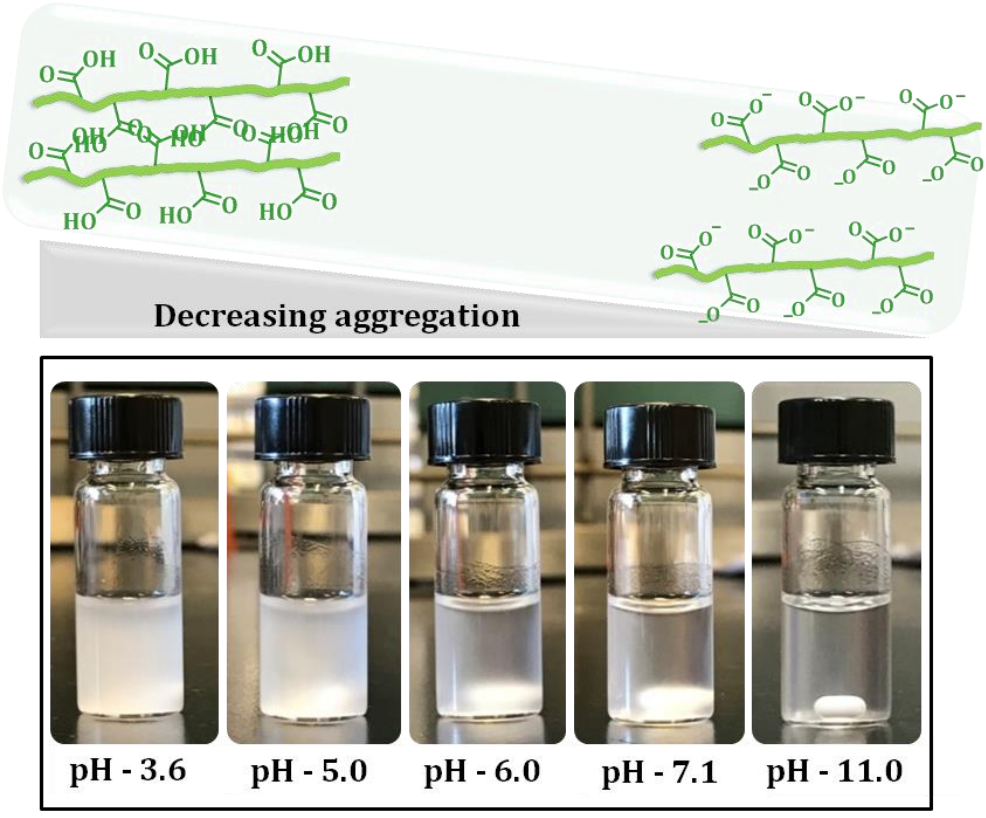

Figure 3.7. The visual records of the aqueous dispersibility of fibrils upon pH changes. The dispersion was stirred for a few seconds during each pH adjustment.

In addition to this, the degree of aggregation at different pH levels was monitored using DLS. It was observed that the fibrils aggregated below pH 3-4 but

tended to disassemble at higher pH values above the pKa value of the material. The process of aggregation and disaggregation with changing pH value was found to be reversible according to DLS results (**Figure 3.8**).

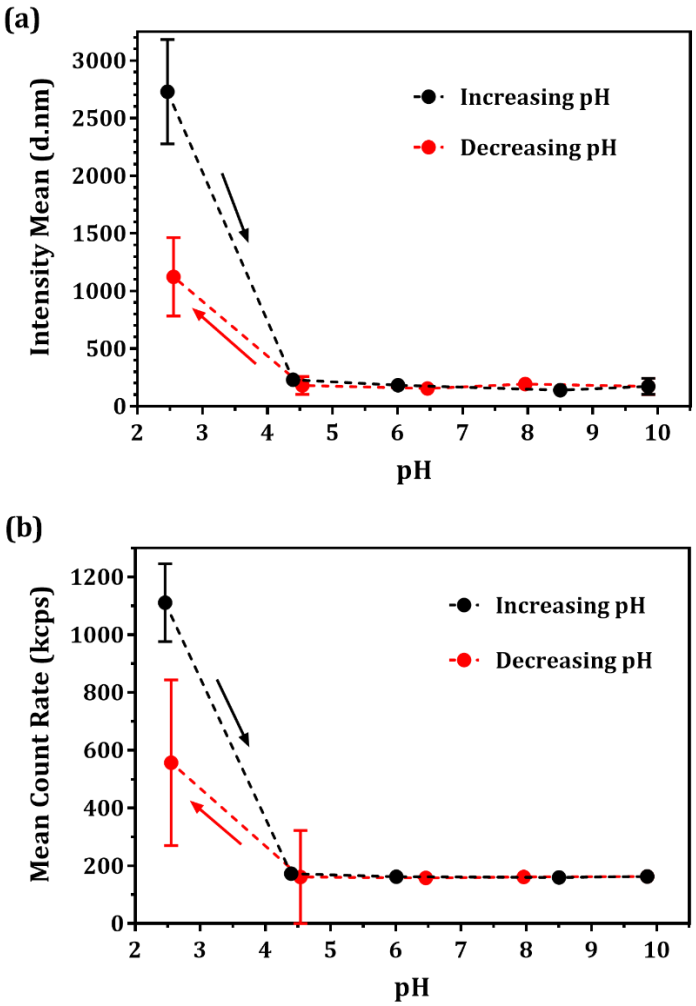

Figure 3.8. Investigation on the aggregation of CNFs bearing acid groups and their reversible behaviour in aqueous media at different pH levels. The graphs are illustrated in two ways: **(a)** intensity mean *vs* pH and **(b)** mean count rate *vs* pH.

Crystallinity of cellulose nanofibers (CNFs)

The crystallinity index (CI) of CNFs can be analysed *via* solid state ^{13}C nuclear magnetic resonance (NMR) and X-ray diffraction (XRD). In this research, XRD technique was employed to investigate the crystalline structure of cellulose nanofibrils obtained *via* mechanically assisted TEMPO-mediated oxidation, followed by acid treatment. According to the spectra depicted in **Figure 3.9**, the fibrils were

crystalline in nature as evidenced by the peaks at 2θ = 17.91° (1 1 0), 26.59° (2 0 0), and 40.87°, which is in agreement with the findings in literature.[74, 350] The crystallinity index (CI) of the cellulose was calculated by comparing the intensity of the (2 0 0) peak (I_{200}, 2θ = 26.59°) and the intensity between the (2 0 0) and (1 1 0) peaks (I_{AM}, 2θ = 21.98°).[350, 377] The equation is shown below.

$$\text{CI (\%)} = \frac{I_{200}\text{-}I_{AM}}{I_{200}} \times 100$$

The result shows that the crystalline structure of cellulose remained intact after the fibrillation process due to the achievement of relatively high crystallinity (56 %) (**Figure 3.9**).

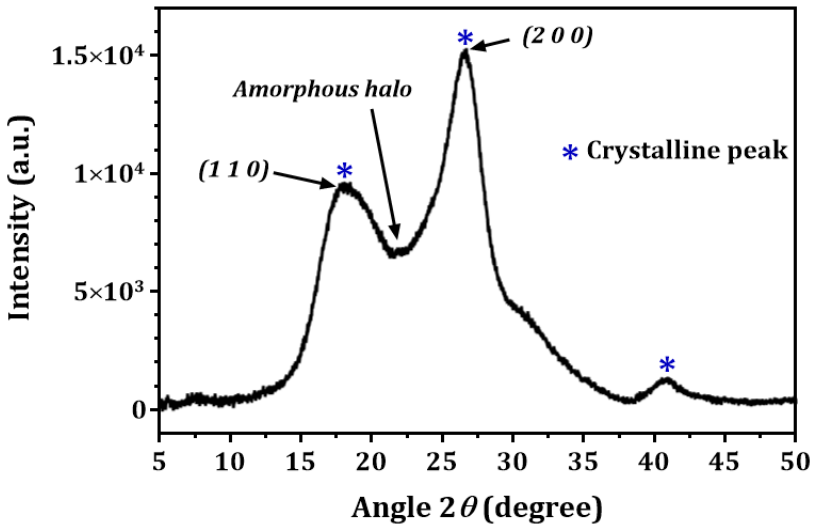

Figure 3.9. XRD spectra of CNFs after mechanically assisted TEMPO-mediated oxidation, followed by acid treatment. XRD data was collected using CoKα radiation.

Thermal properties of cellulose nanofibers (CNFs)

The thermal properties of unfibrillated (MCCs) and fibrillated cellulose (CNFs) were determined *via* thermogravimetric analysis (TGA) using dry samples. TGA, which was run at a heating rate of 20 °C min^{-1} in air, allows the study of the decomposition differences between cellulose samples by showing the residual mass (mass %) as a function of the temperature. In all cases, the initial weight loss at 25 – 100 °C is due to the evaporation of absorbed moisture in the material or low molecular weight compounds remaining from the fibrillation procedure.[74, 384, 385] The

initial decomposition of cellulose decreased from 303 to 252 °C after fibrillation as a result of the formation of nanosized particles from big bundles (**Figure 3.10**).

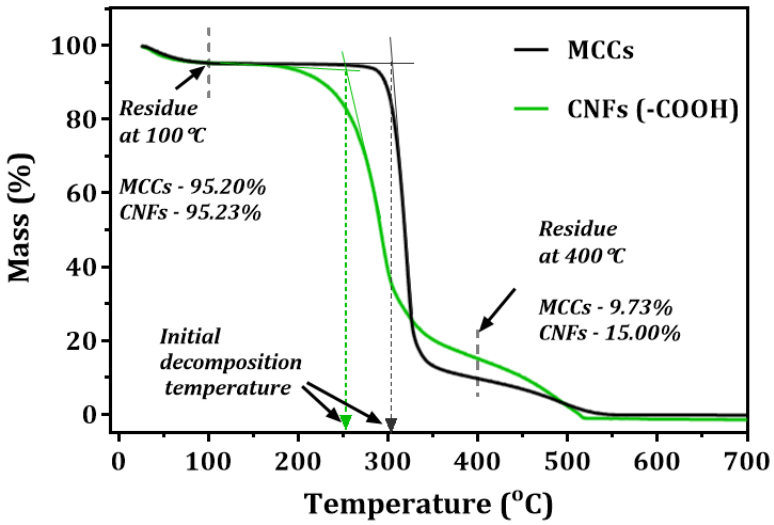

Figure 3.10. Thermal analyses of cellulose before and after fibrillation *via* mechanically assisted TEMPO-mediated oxidation, followed by acid treatment.

Investigation on the existence of reducing end aldehyde groups

According to the structure of fibrillated cellulose (CNFs), each fibril contains one end of the chain with a free hemiacetal or aldehyde group at C1 position, which is thus called a reducing end functionality (**Scheme 3.3, step 1**). Aldehydes are one of the active reducing groups which can reduce a variety of metal ions including Cu(II), Pt(II), Ag(I), Hg(I) and Au(III) to their zero-valent forms in mild alkaline conditions.[386, 387] In this study, we visually confirmed the existence of reducing end by using bicinchoninic acid (BCA) assay. BCA assay depends on the reduction of Cu^{2+} to Cu^{+}, which can be fulfilled by the aldehyde reducing end of CNFs, under alkaline conditions. When the Cu^{+} is detected by the reaction with BCA, the solution turns to an intense purple colour with an absorbance maximum at 562 nm. The proposed general mechanism of the assay is illustrated in **Scheme 3.3**. The sample preparation includes two steps: (1) mixing BCA reagents A and B at a ratio of 50: 1, followed by dispersing 200 µL of mixture into a 96 well-plate, and (2) Addition of 25 µL of sample solution to each well and incubating the plate for 30 min at 60 °C.

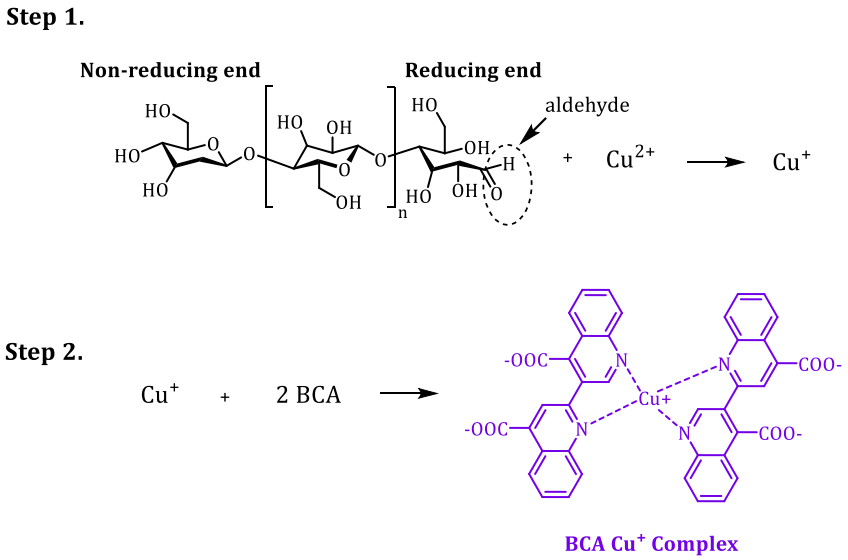

Scheme 3.3. The proposed general mechanism of BCA assay for the analysis of reducing aldehyde end groups of CNFs.

As a production of Cu^{+} is a function of the existence of aldehydes, we performed the analysis by simply mixing the BCA reagents with CNFs at different concentrations: 25 µg mL^{-1}, 50 µg mL^{-1} and 100 µg mL^{-1} which were dispersed in PBS (pH 7.4). After incubating the mixture for 30 min at 60 °C, the development of pale purple colour was observed, in which the most concentrated CNFs (100 µg mL^{-1}) resulted in a darker colour, indicating the larger amount of aldehyde moieties. As shown in **Figure 3.11**, the intense colour was observed for all sample mixtures after incubating for 8 days at room temperature. The results were compared with BCA control, where the colour by contrast did not turn purple even after several days. In summary, the BCA assay here provides more information about the structure of CNFs related to the presence of reducing aldehyde end groups.

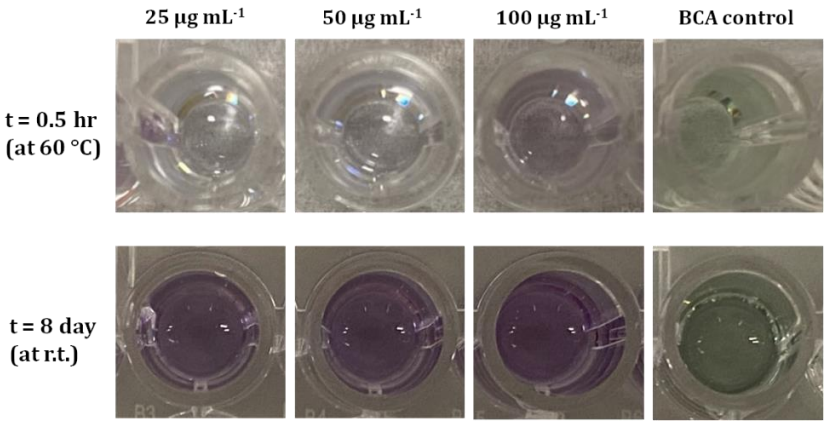

Figure 3.11. Investigation on the existence of reducing aldehyde end groups *via* bicinchoninic acid (BCA) assay.

3.4. Conclusions

In this chapter, plant-derived cellulose was efficiently fibrillated *via* mechanically assisted TEMPO-mediated oxidation. By this technique, oxidation to primary hydroxyl groups on the surface was performed under mild reaction condition and ultrasonication was employed to achieve more efficient disintegration of cellulose. The formation of negative charges on the surface as a consequence of oxidation allowed the cellulose fibrils apart from each other *via* electrostatic repulsion and resulted in the individual fibers with the diameter of 7 nm according to the TEM characterization. HCl treatment was further employed in order to achieve the acid functionalities on the surface, which were essential for further surface modification reactions that will be mentioned in following chapters. The final CNFs gel contained acid (-COOH) groups corresponding to around 1.65 mmol g^{-1} of dry cellulose and possessed the pKa of 5.22. The analysis of the acid groups was replicated three times and the average result was calculated. The chemical and morphological properties of fibrillated cellulose were performed by using a few techniques including DLS, FT-IR, XRD, TGA and BCA assay. The final product (CNFs) with the 56 % crystallinity and 252 °C of degradation temperature was aimed to be used for further experiments, specifically for surface modification with functional polymers to achieve more stable and versatile CNFs for biological applications.

3.5. Materials of the Thesis

Microcrystalline cellulose (MCCs, Sigma-Aldrich), 2,2,6,6-tetramethyl-1-piperidinyloxy (TEMPO, Sigma-Aldrich, 98 %), sodium bromide (NaBr, Sigma-Aldrich, ≥ 99 %), sodium hypochlorite solution (NaOCl, Sigma-Aldrich, 8 – 12.5 % available chlorine), sodium hydroxide (NaOH, Sigma-Aldrich, ≥ 97 %), hydrochloric acid (HCl, Sigma-Aldrich, 32 %), ethanol (95 %), potassium hydroxide (KOH, Sigma-Aldrich, 85 %), *N*-isopropylacrylamide (NIPAm, Sigma-Aldrich, 97 %) ethylene glycol (Sigma-Aldrich, 99.8 %), bromoacetaldehyde dimethyl acetal (Sigma-Aldrich, 97 %), chloroform (Sigma-Aldrich, ≥ 99.5 %), magnesium sulfate ($MgSO_4$, Sigma-Aldrich, ≥ 99.5 %), deuterated chloroform ($CDCl_3$, Sigma-Aldrich, 100%), deuterium oxide (D_2O, Sigma-Aldrich), dimethyl sulfoxide-d_6 (DMSO-d_6, Sigma-Aldrich, 100%), dichloromethane (DCM, Sigma-Aldrich), anhydrous dichloromethane (DCM, Sigma-Aldrich, ≥ 99.8 %), *N*-(3-dimethylaminopropyl)-*N*′-ethylcarbodiimide hydrochloride (EDC.HCl, Sigma-Aldrich), *N*,*N*′-dicyclohexylcarbodiimide (DCC, Sigma-Aldrich, 99 %), 4-(dimethylamino)pyridine (DMAP, Sigma-Aldrich, ≥ 99 %), hexane (Sigma-Aldrich, 95 %), ethyl acetate (Sigma-Aldrich), *N*,*N*-dimethylformamide (DMF, Sigma-Aldrich), anhydrous *N*,*N*-dimethylformamide (DMF, Sigma-Aldrich, 99.8 %), methanol, tetrahydrofuran (THF, Sigma-Aldrich), cyclohexyl isocyanide (Sigma-Aldrich, 98 %), methacrylic acid (Sigma-Aldrich, 99%), 2-mercaptoethanol (Sigma-Aldrich), potassium phosphate tribasic (K_3PO_4, Sigma-Aldrich), acetone (Sigma-Aldrich, ≥ 99.5 %), carbon disulfide (CS_2, Sigma-Aldrich, ≥ 99.9 %), benzyl bromide (Sigma-Aldrich, ≥ 98 %), potassium bromide (KBr, Sigma-Aldrich), cyclohexane (VWR International), 2-hydroxyethyl acrylate (HEA, Sigma-Aldrich), 2-(dimethylamino) ethyl acrylate (DMAEA, Sigma-Aldrich), doxorubicin hydrochloride (DOX.HCl, Sigma-Aldrich), 1-amino-3,3-diethoxypropane (Sigma-Aldrich, ≥ 97 %), 2,3,3-trimethyl-3*H*-indole (Sigma-Aldrich, 98 %), 6-bromohexanoic acid (Sigma-Aldrich, 97 %), potassium iodide (Ajax Finechem Pty Ltd), acetonitrile (Chem-Supply Pty. Ltd.), malonaldehyde bis(phenylimine) monohydrochloride (Sigma-Aldrich, 97 %), 1,2,3,3-tetramethyl-3*H*-indolium iodide (Sigma-Aldrich, 98 %), pyridine (Chem-Supply Pty. Ltd.), trichloroacetic acid (Sigma-Aldrich, 99 %), acetic acid (Chem-Supply Pty. Ltd.), recombinant murine MIP-1α (CCL3) (PeproTech), dulbecco's modified eagle's medium (DMEM power, Sigma-Aldrich), Penicillin and streptomycin (Sigma-Aldrich),

Trypsin/EDTA (Sigma-Aldrich), Glutamax (Life technologies), and Fetal bovine serum (Interpath Services) were used without purification. Azobisisobutyronitrile (AIBN) was purified by recrystallization in methanol.

3.6. Experimental Procedure

3.6.1. Synthesis of CNFs *via* TEMPO-mediated oxidation

Commercially available microcrystalline cellulose extracted from cotton linters (MCCs, 2 g) was suspended in 200 mL of milli-Q water and stirred at room temperature for 10 min. 2,2,6,6-Tetramethyl-1-piperidinyloxy (TEMPO, 0.035 g) and sodium bromide (NaBr, 0.58 g) were then added to the cellulose suspension. Once TEMPO was completely dissolved, 8 mL of sodium hypochlorite (NaOCl, 8 – 12.5 % available chlorine) was added dropwise. Through the reaction, the pH of the suspension was adjusted to between 10 and 11 by adding 0.5 M NaOH. The pH of the suspension was monitored by using a bench-top pH meter. Once the yellow colour of NaOCl disappeared, indicating the complete consumption of it during reaction, more NaOCl solution was gradually added until the final volume reached 23 mL. After stirring at room temperature for 26 hr, the reaction was stopped by adding 3 mL of ethanol. The obtained cellulose suspension carrying sodium carboxylate groups (CNFs-COO^-) was then dialysed against milli-Q water using 6 – 8 kDa MWCO membrane. After 3 days, the suspension was diluted by milli-Q water until the solid content reached approximately 0.1 % (w/v), and then it was mechanically treated by ultrasonication for 15 min using BRANSON solid/liquid digital ultrasonicator (450, amplitude = 30 % at room temperature and 50 mL of suspension was ultrasonicated each time). The amplitude and ultrasonication time may be increased depending on the efficiency of ultrasonicator. Finally, the acid groups on the surface of cellulose nanomaterials were obtained by treating CNFs (-COO^-) with 1 M HCl (pH ≈ 2) for 30 min (**Scheme 3.4**). The resulting gel-like product was collected by the cycle of washing and centrifugation in milli-Q water for 6 times (8000 rpm, 10 min) until the supernatant reached neutral for complete removal of excess HCl. The obtained CNFs gel was then stored at 4 °C.

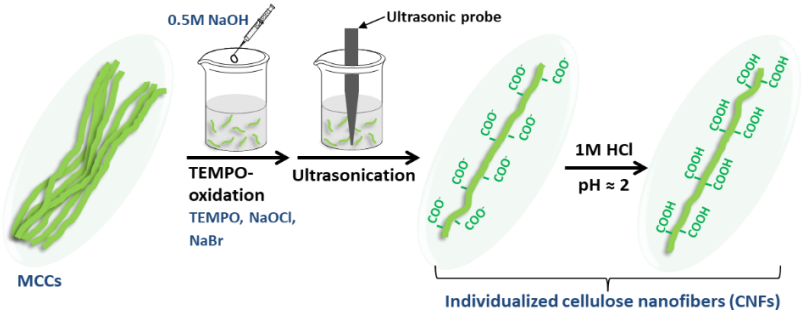

Scheme 3.4. Synthesis process of CNFs bearing carboxylic acid moieties.

3.7. Analytical Techniques of the Thesis

Size Exclusion Chromatography (SEC)

Size exclusion chromatography is a commonly used chromatography technique designed for the determination of the size of polymer chains. In this research, the molecular weight and molecular weight distribution of synthesized polymers were characterized *via* two SEC instruments equipped with a Shimadzu modular system.

SEC (eluent dimethylacetamide) is equipped with a DGU-12A degasser, a LC-20AT pump, a SIL-20A HT automatic injector, a RID-10A refractive index detector and a CTO-10A *VP* column oven. The instrument is also equipped with a PhenomenexPhenogel 5.0 μm bead-size guard column (50 × 7.5 mm), followed by a set of linear Phenomenex columns (10^5, 10^4, 10^3, and 10^2 Å). *N,N*-Dimethylacetamide (DMAc, 0.05% w/v BHT, 0.03% w/v LiBr) with a flow rate of 1 mL min^{-1} was used as the continuous phase at 50 °C. The system was calibrated based on commercially available linear poly(methyl methacrylate) (PMMA) standards (0.2 – 1000 kDa) with narrow molecular weight distributions.

SEC (eluent dimethylformamide) is also performed in Shimadzu modular system, comprising a SIL-10AD automatic injector, LC-10AT pump, CTO-10A oven, 5.0 μm bead guard column (50 × 7.8 mm) followed by four 300 mm × 7.8 mm linear columns (Phenomenex) with 500, 10^3, 10^4, 10^5 Å pore size and 5 μm particle size. *N,N*-dimethylformamide (DMF, HPLC grade, 0.05 % w/v of 2,6-dibutyl-4-methylphenol and 0.03 % w/v of LiBr) with a flow rate of 1 mL min^{-1} was used as the continuous phase at 50 °C. The instrument is also equipped with a refractive index detector (Shimadzu RID-10A). The system was calibrated based on commercially available linear poly(methyl methacrylate) (PMMA) standards (0.5 – 1000 kDa) with narrow molecular weight distributions.

Nuclear Magnetic Resonance (NMR) Spectroscopy

NMR spectra were recorded by using either a Bruker Avance III HD 300 MHz (Gyro, equipped with a BACS-60 sample changer and BBFO probe) or a Bruker Avance III HD 400 MHz (Rabi, equipped with a 60 bay sample changer and BBFO z-

gradient probe) instrument. Samples were dissolved and analysed in deuterated chloroform ($CDCl_3$), deuterium oxide (D_2O) or dimethyl sulfoxide-d_6 (DMSO-d_6). NMR spectra were processed by using either Bruker Topspin 4.0.6 software or MestReNova.

Fluorescence Spectroscopy

Fluorescence measurements of polymer-grafted CNFs were performed on a Cary Eclipse fluorescence spectrophotometer at room temperature. The excitation and emission wavelengths of PHEA-grafted CNFs prepared *via* photo-induced tetrazole/carboxylic acid click chemistry were approximately (380 – 390 nm) and (490 - 520 nm) respectively. The excitation and emission wavelengths of $PHEA_{Cy5}$-grafted CNFs *via* Passerini reaction were approximately 641 nm and 675 nm respectively. The concentration of polymer-grafted CNFs for analysis was between 1 and 2 mg mL^{-1} in milli-Q water. The obtained data were plotted in GraphPad Prism 7.03.

Ultraviolet-Visible (UV-Vis) Spectroscopy

Cary 50 Bio UV-visible spectrophotometer (Varian Australia Pty Ltd) was used to obtain the spectra of polymers and polymer-grafted CNFs. The spectra were recorded in the range from 200 to 800 nm in DMSO or milli-Q water. Blank CNFs dispersion in water was taken as baseline when measuring the amount of polymer on functionalized CNFs. The concentration of polymer-grafted CNFs for UV-Vis analysis was between 1 and 2 mg mL^{-1} in milli-Q water.

Transmission Electron Microscopy (TEM)

The TEM micrographs were obtained by using JEOL 1400 transmission electron microscope at accelerating voltages up to 120 kV. Samples were prepared by placing a drop of particle solution (less than 1 mg mL^{-1} concentration) on a formvar-coated copper grid for 1 - 3 min. Then the excess sample was removed by using filter paper. The samples were then dried overnight, followed by negative staining with uranyl acetate (UA, 2% aqueous solution). The staining was performed by leaving the sample grids under UA droplet for 2 min. The excess UA was wiped out by filter paper and washed with water by tapping the grid on the water droplet and dried

with filter paper. Then the sample grids were dried overnight at 30 °C overnight before characterization.

Atomic Force Microscopy (AFM)

The surface characteristics and the morphological stability of CNFs were determined by atomic force microscopy. Sample preparation for the analysis was as followed: a drop of diluted (less than 1 mg mL^{-1}) CNFs dispersion was placed on a clean mica plate and dried overnight at 30 °C. Then the samples were submitted to Bruker Dimension ICON SPM equipped with a proprietary ScanAsyst® image optimization technology in order to record the images in the range of 0.5 and 1 μm. The scanned images were processed using NanoScope Analysis (version 1.7).

Dynamic Light Scattering (DLS)

The diameter and size distribution of CNFs and polymer-modified CNFs were determined by using Malvern Zetaplus particle size analyser (laser angle = 173°) at a sample concentration of less than 1 mg mL^{-1} in milli-Q water. The typical concentration of CNFs for size and surface charge (zeta potential) analysis was approximately 100 μg mL^{-1}. Three measurements were recorded for each sample to determine the standard deviation. The obtained results were then processed by using GraphPad Prism 7.03.

Fourier Transform Infrared (FT-IR) Spectroscopy

The FT-IR spectra of polymers, CNFs and grafted CNFs were determined by portable ALPHA FT-IR spectrometer (Bruker Corporation, Germany). Spectra for each freeze-dried sample were obtained in the range from 400 to 4000 cm^{-1} with a spectral resolution of 4 cm^{-1}. Thirty-two scans were acquired for each sample at ambient temperature. The obtained spectra were processed by using GraphPad Prism 7.03.

X-Ray Diffraction (XRD)

The physical properties (crystallinity, CI) of CNFs before and after polymer grafting were measured *via* X-ray diffractometer (XRD, PANalytical Xpert Multipurpose X-ray Diffraction System). The system was used CoKα radiation generated at 45 kV and 40 mA. The scattering angle (2θ) was in the range of 5 to 65 degree in 0.026-degree steps. The beam mass was 10 mm and divergent slit was ½ degree. The CI was calculated according to the method reported by Park *et al.* in 2010.[388] The data were plotted by using GraphPad Prism 7.03.

Thermogravimetric Analysis (TGA)

Thermal stability of MCCs, CNFs and polymer-grafted CNFs were carried out by using thermogravimetric analysis (TGA) (TGA Q 5000 TA). The thermograms were performed from room temperature to 700 °C at a heating rate of 20 °C min^{-1} under air. The mass of sample powder submitted to the instrument was between 2 and 10 mg. The obtained data were processed *via* TA Universal Analysis and plotted by using GraphPad Prism 7.03.

Turbidity Study

The lower critical solution temperature (LCST) phenomena of the PNIPAm-grafted CNFs were observed by using Cary 300 Scan ultraviolet-visible (UV-Vis) spectrophotometer equipped with a temperature controller (Varian Australia Pty Ltd). Concentrated sample solution (10 mg mL^{-1} in milli-Q water) was prepared for the analysis starting from a temperature range of 25 to 40 °C. The wavelength was set at 563 nm and the heating rate at 1 °C min^{-1} was applied for all analyses.

Determination of the density of carboxylic acid groups (-COOH) on CNFs

The density of free carboxyl groups (-COOH) on the surface of CNFs after protonation at pH ≈ 2 was determined by using bench-top pH meter. Sample solutions were prepared by dispersing 10 mg of protonated freeze-dried CNFs in 2 mL of milli-Q water and stirred continuously during analysis. Three sample solutions were prepared and analysed to determine the standard errors.

CHAPTER - 4

Photo-Induced Modification of CNFs:

The Design

of

Self-Fluorescent Drug Carriers

https://doi.org/10.1002/marc.201900499
CNFs = Cellulose Nanofibers

Table of Content

4.1. Overview

In this study, we modified TEMPO-oxidized cellulose nanofibers bearing carboxylic acid moieties (CNFs) by nitrile imine-mediated tetrazole/ carboxylic acid ligation (NICAL). The advantage of this reaction is that CNFs do not need to be modified further and the polymer with tetrazole end-functionalities can be directly clicked onto the CNFs forming fluorescent functional groups. Poly(2-hydroxyethyl acrylate) with a molecular weight of M_n= 22600 g mol^{-1} and a tetrazole end-functionality was prepared using RAFT polymerization. The polymer was mixed with CNFs and after irradiation at λ = 326 nm for 10 hr, fluorescent PHEA-*g*-CNFs were obtained. The modified CNFs were found to disperse well in aqueous media and had only limited albumin binding. The uptake of these nanoparticles by MCF-7 breast cancer cell lines can now be monitored by fluorescent microscopy without further modification with fluorescent molecule. Excess negative charged carboxylic groups of CNFs allowed doxorubicin loading by electrostatic interactions at various drug loading capacities from 1.7 to 14.9 weight %. Higher drug loading was more efficient in inhibiting the cell proliferation highlighting the effect of drug loading on toxicity.

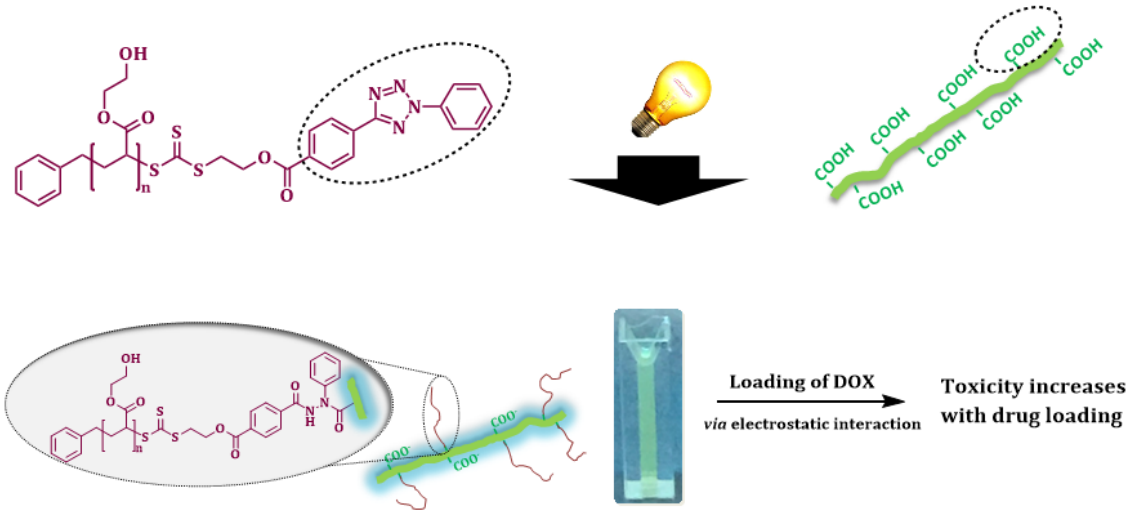

Scheme 4.1. Synthesis of self-fluorescent cellulose-based nanocarriers for loading and release of doxorubicin (DOX).

4.2. Introduction

Cellulose nanomaterials have been attracted great attentions for their use in biomedicine due to their surface chemistry and nano-sized dimensions.[61, 66, 372, 373] Specifically, the abundance of functional groups on the surface, after acidic or alkaline treatment,[62] has made cellulose nanomaterials appealing for drug delivery applications.[389, 390] The multitude of both hydroxyl and carboxyl groups[73] allows subsequent modification of the surface of cellulose nanomaterials with polymers to ensure high drug loading and compatibility with the biological environment. Jackson and co-workers used CNCs as excipients to deliver anticancer therapeutics in a controlled manner. In this work, the anionic property of CNCs was used as an advantage to bind cationic drugs, such as tetracycline and doxorubicin, by electrostatic interaction with high binding efficiency.[391]

One of the challenges in the use of cellulose nanomaterials for drug delivery is the often-weak dispersibility caused by the strong inter-and intra-molecular hydrogen bonding. This limitation can be addressed by attaching hydrophilic polymer chains onto cellulose nanomaterials using esterification, etherification, amidation or various click reactions. [224, 392, 393] Alternatively, polymers can be grown from the surface of cellulose nanomaterials using reversible deactivation radical polymerization (RDRP) techniques by the immobilization of the initiating or controlling agents. The resulting polymers often show high dispersibility in water making these composites ideal drug carriers that can deliver various drugs such as metal-based drugs, DNA and low molecular weight drugs.[122, 284, 322] Most polymer grafting strategies require an organic solvent or pre-treatment of the cellulose nanomaterials with functional groups. Also, the resulting polymer-grafted cellulose nanomaterials require further functionalization with fluorescent dyes to be able to follow the pathway of the nanoparticles in a biological setting. Self-fluorescent cellulose nanomaterials were recently introduced by Hoenders *et al.* who synthesized transparent cellulose nanomaterial surfaces *via* photo-induced nitrile imine-mediated tetrazole/ene cycloaddition (NITEC) reaction.[175] In this paper, cellulose nanomaterials were first modified with tetrazole functionalities *via* an amidation reaction, followed by covalent tethering with maleimide-modified compounds under UV irradiation.[175] The nitrile imine intermediate, which is generated from the tetrazole usually after UV-light

irradiation,[394] can quickly react with a range of functional groups including thiols, amines, acids, and heterocycles.[395-400] For instance, Heiler *et al.* have demonstrated the application of photo-induced click reactions: nitrile imine-mediated tetrazole/ene cycloaddition (NITEC) and nitrile imine-carboxylic acid ligation (NICAL), for the synthesis of single chain polymer nanoparticles in pure water.[401] Aside from the efficient but gentle modification of materials using light, the resulting product is fluorescent[402] and can therefore be easily tracked in biological systems, which makes the tetrazole photo-click reaction attractive for bioconjugation[400] as it can be used in living cells.[400]

The aim of this work is to explore the NICAL reaction as a pathway to directly functionalize cellulose nanomaterials, which can further be employed as a drug delivery system in water without any requirement of additional functionalization prior to surface modification. Taking advantage of the abundance of carboxylic acid groups on the surface after TEMPO-oxidation, cellulose nanofibers were modified *via* tetrazole-acid photo click chemistry under UV irradiation resulting in colloidally stable cellulose nanomaterials that are fluorescent, allowing direct analysis of uptake of these drug carriers by cells. Reversible addition-fragmentation chain transfer (RAFT) polymerization using a tetrazole-based RAFT agent was employed to generate the reactive polymer, which was subsequently clicked onto TEMPO-oxidized cellulose nanofibers (CNFs). Poly(2-hydroxyethyl acrylate) (PHEA) was chosen as the aqueous polymer due to its high solubility in aqueous media (**Scheme 4.2**). Doxorubicin hydrochloride was then loaded onto the polymer-coated cellulose nanofibers (PHEA-*g*-CNFs), retained by the excess of carboxylate groups on CNFs. The polymer-coated CNFs was then loaded with various amount of doxorubicin to explore the relationship between drug loading content and bioactivity.

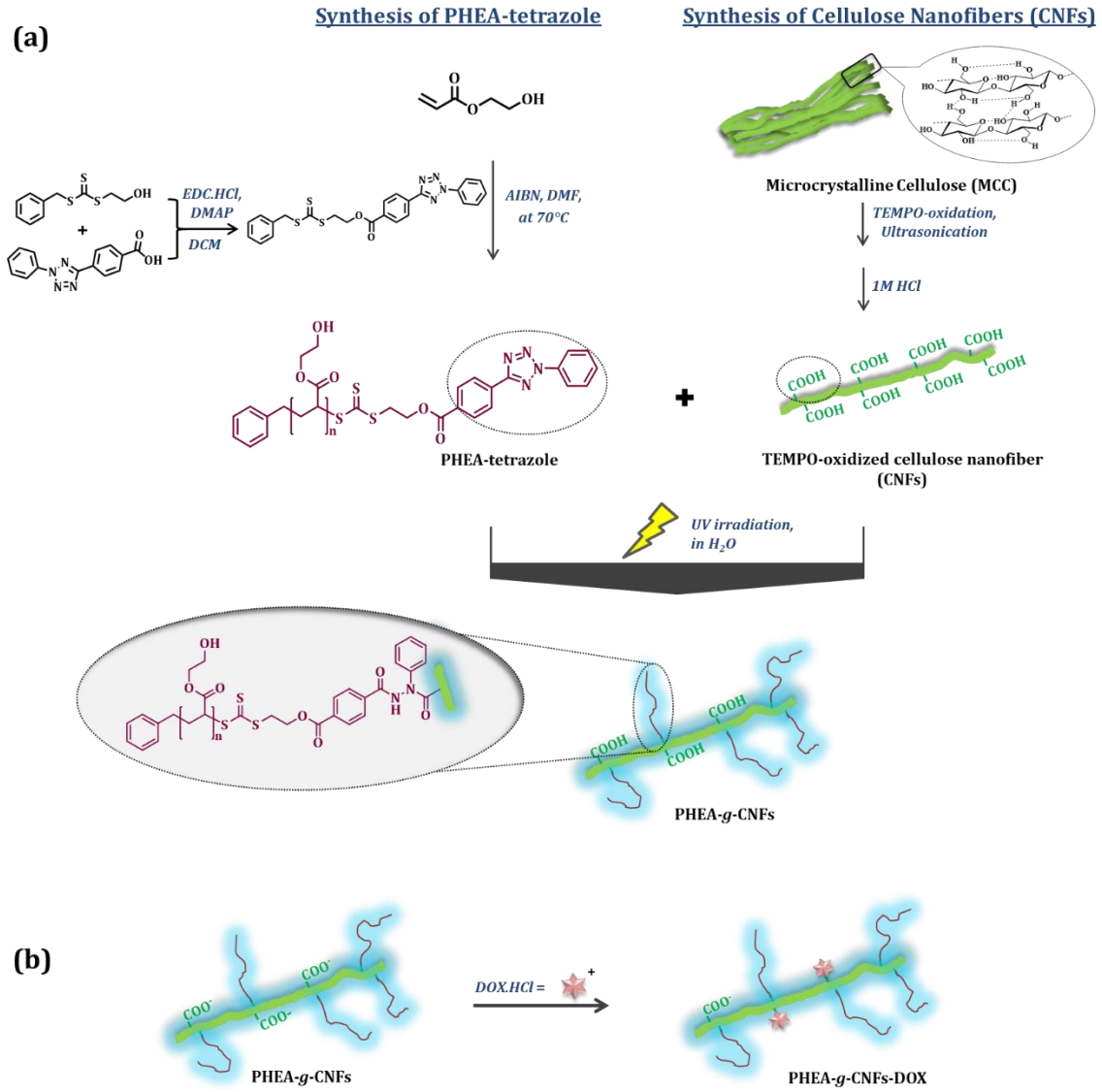

Scheme 4.2. (a) General synthetic routes for the synthesis of self-fluorescent PHEA-*g*-CNFs *via* tetrazole-acid click chemistry under UV irradiation at ambient temperature, as well as **(b)** their electrostatic interaction with doxorubicin hydrochloride (DOX.HCl) for drug delivery application.

4.3. Results and Discussions

4.3.1. Synthesis of RAFT agent bearing a tetrazole functionality

The aim of this project is the generation of functionalized and self-fluorescent cellulose nanofibrils using NICAL as a modification pathway. Here, we employed poly(2-hydroxyethyl acrylate) (PHEA) as a model hydrophilic homopolymer bearing a tetrazole moiety, which can react with abundant carboxylic acid groups on the surface of cellulose nanofibrils (CNFs). First, CNFs bearing carboxylic acid functionalities were prepared *via* mechanically assisted TEMPO-mediated oxidation combined with acid treatment according to the procedure mentioned in **Chapter 3**. In the next step, a RAFT agent carrying a tetrazole moiety was synthesized *via a* three-step procedure.

First, the trithiocarbonate-based RAFT agent bearing hydroxyl group named benzyl (2-hydroxyethyl) carbonotrithioate was prepared by reacting 2-mercaptoethanol and carbon disulphide (CS_2) in the presence of potassium phosphate tribasic (K_3PO_4) and acetone, followed by the addition of benzyl bromide. A slightly viscous yellow oil after purification *via* silica gel column chromatography was obtained. The yellow colour here is the characteristic of trithiocarbonates. The final product obtained, in 81 % of yield, was submitted for ^{1}H-NMR in $CDCl_3$ (**Figure 4.1**), where the signals at δ = 7.40 - 7.20 ppm, 4.64 ppm, 3.92 ppm and 3.63 ppm are respectively assigned to the aromatic protons and methylene (CHphenyl CH_2-, -CH_2CH_2OH, -CH_2CH_2OH) protons.

Second, 4-(2-phenyl-2H-tetrazole-5-yl) benzoic acid was also synthesized *via* multi-step method. 4-((2-(phenylsulfonyl)hydrazineylidene)methyl)benzoic acid was first prepared by reacting 4-formylbenzoic acid and benzenesulfonyl hydrazide in ethanol. The desired red was obtained by reacting the precipitated reagents with benzenediazonium chloride in pyridine at -10 °C, in which benzenediazonium chloride was synthesized by mixing sodium nitrite, aniline and hydrochloric acid in water/ethanol (2: 1.24, v/v). After extraction of the crude product, the final product in the form of pale red solid (50 % yield) was analysed by ^{1}H-NMR in $CDCl_3$ (**Figure 4.2**). The characteristic peaks at δ = 8.30 ppm, 8.18 ppm, 7.72 ppm and 7.65 ppm corresponding to the protons from two phenyl rings confirmed the formation

of the desired product. The existence of the functional carboxylic acid group was confirmed by the signal at δ = 13.26 ppm.

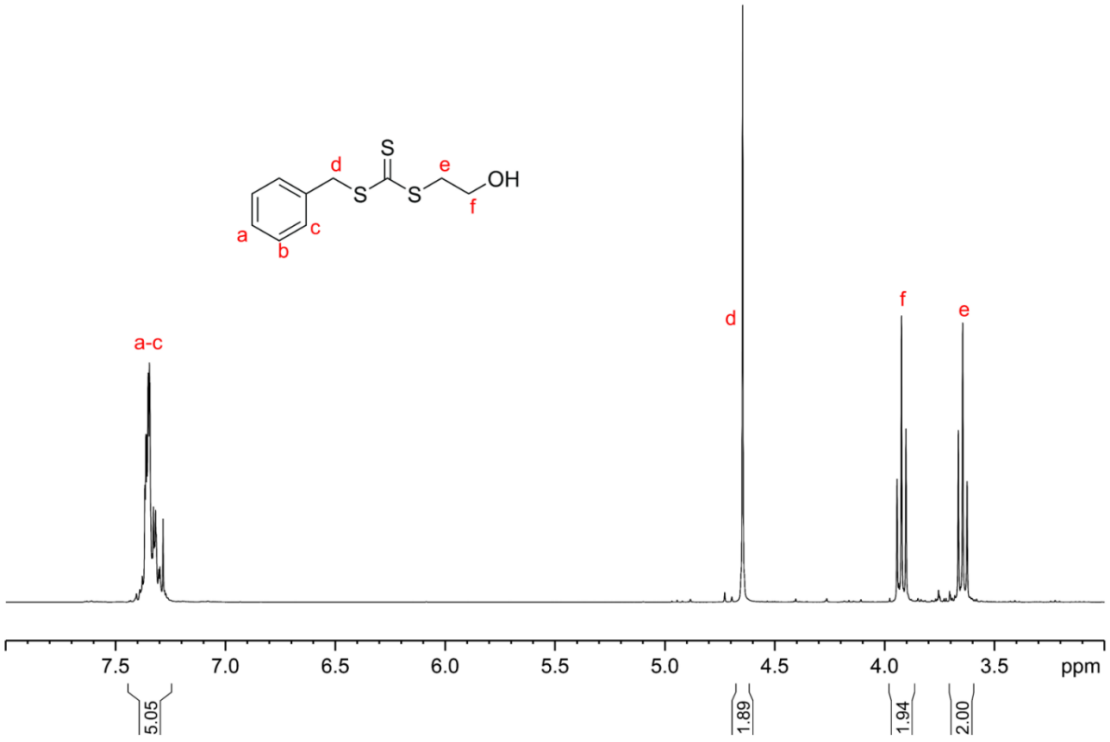

Figure 4.1. ^{1}H-NMR spectrum of benzyl (2-hydroxyethyl) carbonotrithioate [BHCT] in $CDCl_3$.

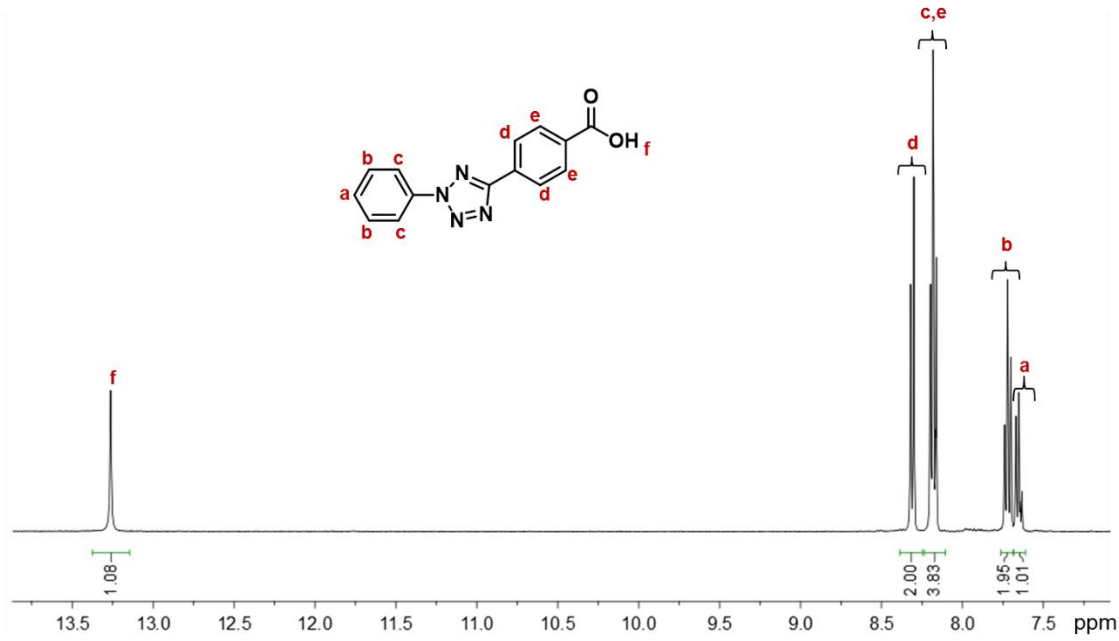

Figure 4.2. ^{1}H-NMR spectrum of 4-(2-phenyl-2H-tetrazole-5-yl) benzoic acid in $CDCl_3$.

The two synthesized molecules were then reacted *via* EDC/NHS coupling in anhydrous DCM, resulting in 2-(((benzylthio)carbonothioyl)thio)ethyl 4-(2-phenyl-2H-tetrazol-5-yl)benzoate. The crude RAFT agent carrying the tetrazole functionality was purified by silica gel column chromatography to yield 65 % of the final product as dark red viscous oil, which was characterised *via* ^{1}H-NMR and ^{13}C-NMR (**Figure 4.3 and 4.4**). According to ^{1}H-NMR, the successful synthesis was confirmed by the corresponding signals at δ = 8.39 ppm, 8.25 ppm, and 7.69 – 7.51 ppm (the protons of phenyl-tetrazole groups), at δ = 7.40 – 7.30 ppm (C*H*phenyl-CH_2-), at δ = 4.70 – 4.60 (CHphenyl-C*H*$_2$-, and -C(S)S-CH_2C*H*$_2$-), and at δ = 3.85 ppm (-C(S)S-C*H*$_2$$CH_2$-). The integrations of the signals were in agreement with the number of protons in the structure of desired molecule, which was furthered confirmed by ^{13}C-NMR (**Figure 4.4**).

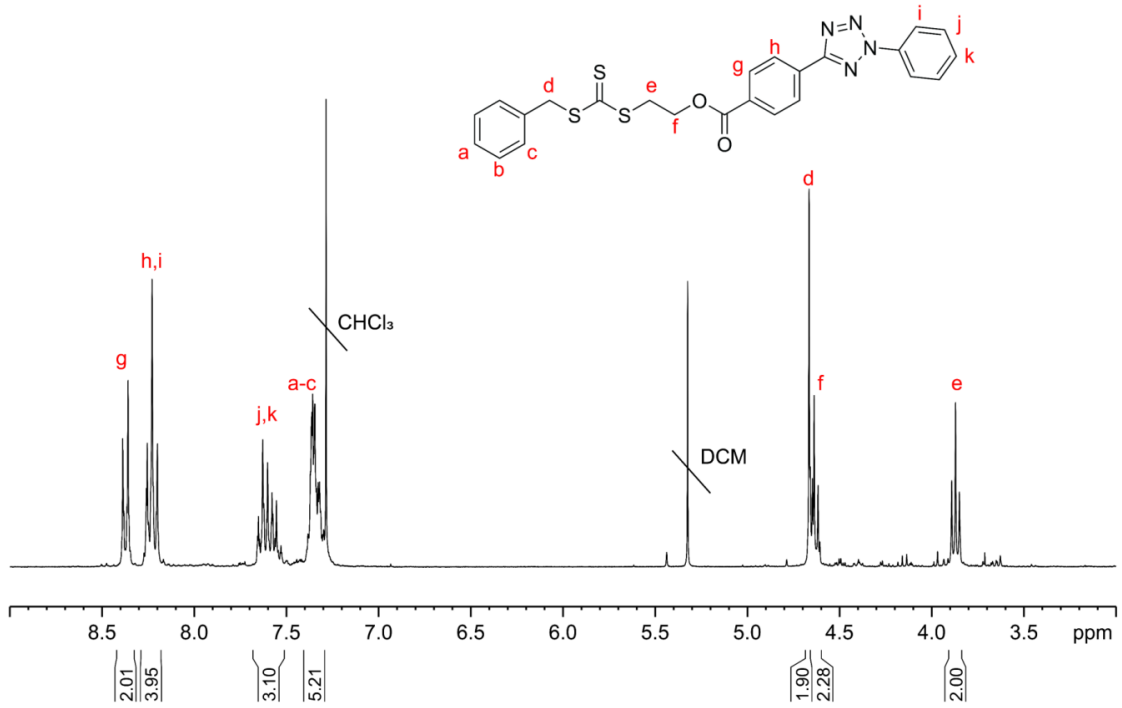

Figure 4.3. ^{1}H-NMR spectrum of 2-(((benzylthio)carbonothioyl)thio)ethyl 4-(2-phenyl-2H-tetrazol-5-yl)benzoate [RAFT agent bearing tetrazole functionality] in $CDCl_3$.

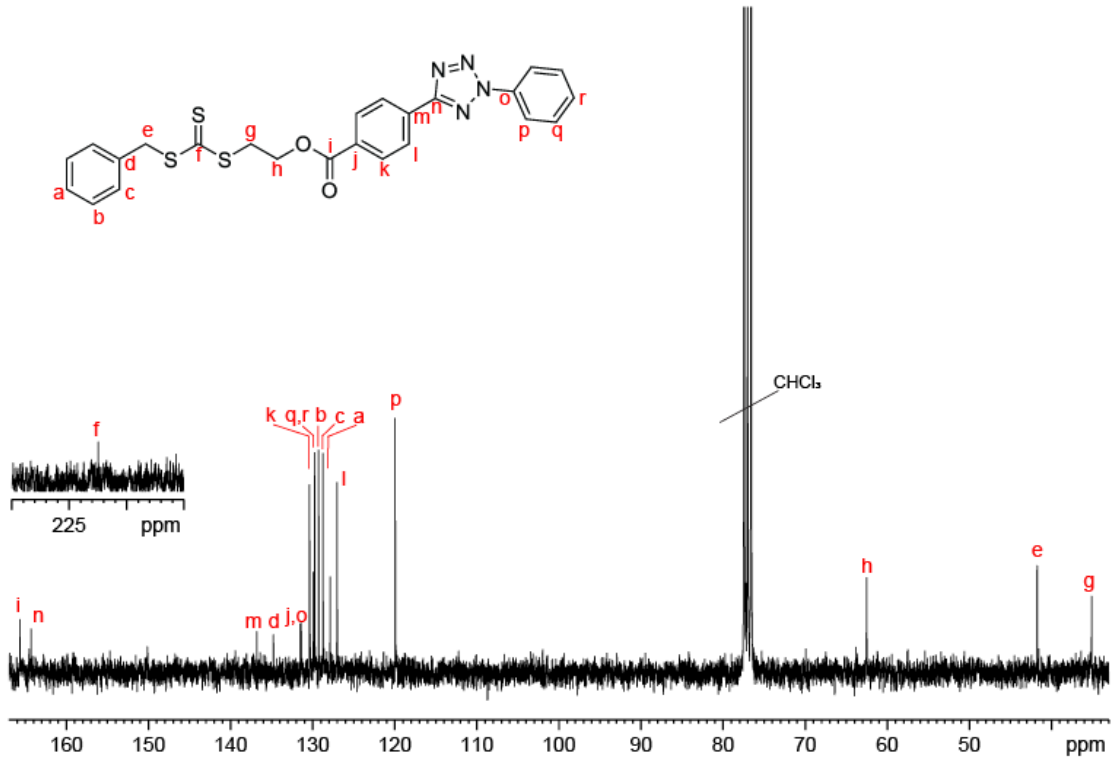

Figure 4.4. ^{13}C-NMR spectrum of 2-(((benzylthio)carbonothioyl)thio)ethyl 4-(2-phenyl-2H-tetrazol-5-yl)benzoate [RAFT agent bearing tetrazole functionality] in $CDCL_3$.

4.3.2. Synthesis of poly(2-hydroxyethyl acrylate) bearing tetrazole moiety [PHEA-tetrazole]

The synthesized RAFT agent was subsequently employed to synthesize PHEA bearing a tetrazole moiety. The polymerization was performed *via* RAFT polymerization in the presence of RAFT-tetrazole and AIBN as an initiator in the ratio of [M]: [RAFT]: [AIBN] = 100: 1: 0.1 in DMF at a concentration of 2.64 M. After heating at 70 °C for 2 hr, the mixture was analysed by ^{1}H-NMR to determine the monomer conversion which was calculated to be 85 % by comparing the intensity of the peak at δ = 4.02 ppm and 4.13 ppm which corresponds to two protons (-CO(O)CH_2-) located in the polymer and residual monomer, respectively. After purifying the crude product by dialysis against methanol for 2 days, the resulting PHEA-tetrazole was measured by SEC to have a molecular weight of M_n = 22600 gmol^{-1} and a dispersity $Đ$ of 1.21. The bimodality here was probably due to the high monomer conversion (**Figure 4.5**). End group analysis was determined by ^{1}H-NMR confirming

the presence of the aromatic groups and the RAFT end group fidelity was observed to be approximately 75 % (**Figure 4.6**).

Conversion (%)	85
Repeating units	85
$M_{n(theo.)}$ (g mol^{-1})	10400
$M_{n(SEC)}$ (g mol^{-1})	22600
$Đ$	1.21

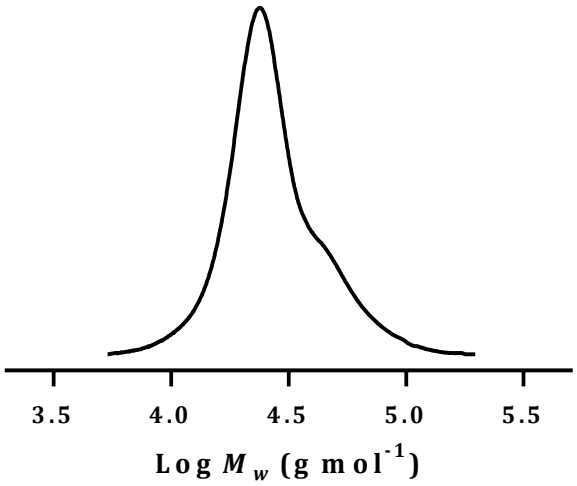

Figure 4.5. SEC curve of synthesized tetrazole-terminated PHEA dissolved in DMF.

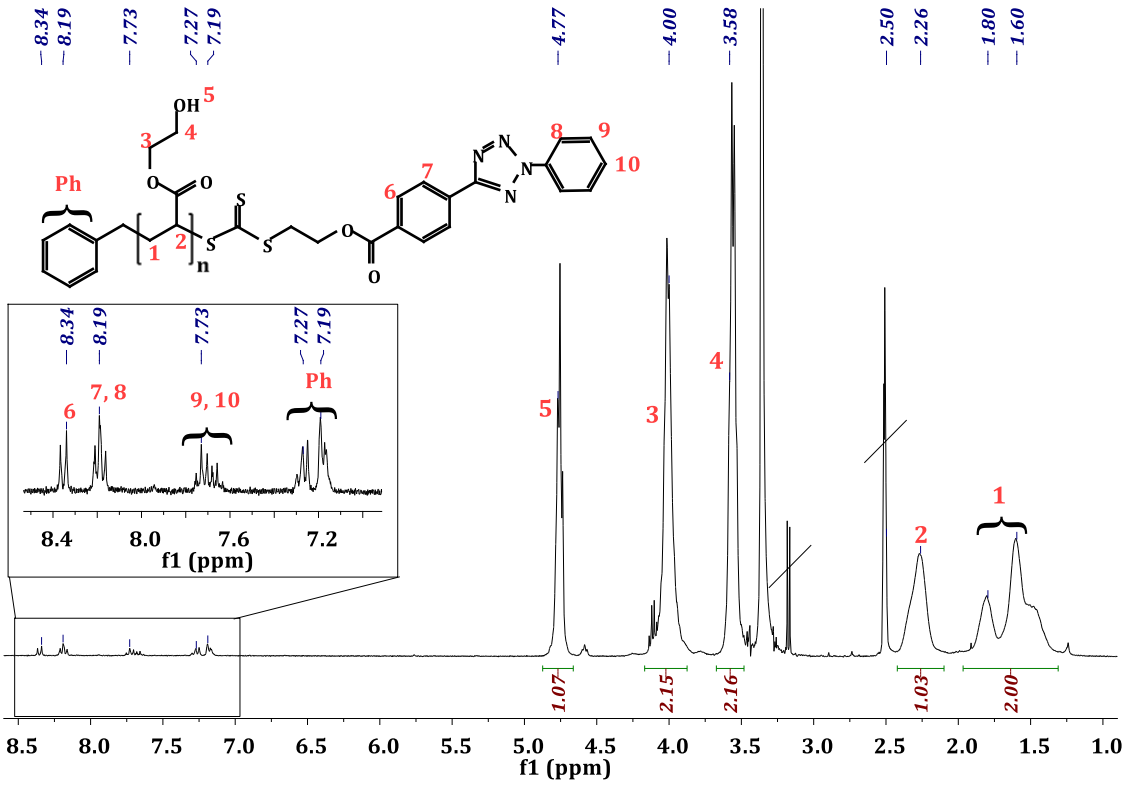

Figure 4.6. ^{1}H-NMR spectrum of synthesized tetrazole-terminated PHEA in DMSO-d_6.

4.3.3. Photo-induced click reaction between PHEA-tetrazole and pentanoic acid under ambient condition

Prior to the photo-induced coupling reactions of tetrazole-terminated PHEA and the carboxylic acids functionalities on CNFs, the reaction was tested using pentanoic acid as a model compound. Moreover, the polymer alone was illuminated to identify potential side reactions. According to the general mechanism illustrated in **Scheme 4.3**, UV-irradiation initially triggers the liberation of nitrogen and the formation of nitrile imines, which can be converted into 1*H*-diazirines and imidoylnitrenes.[177, 403]

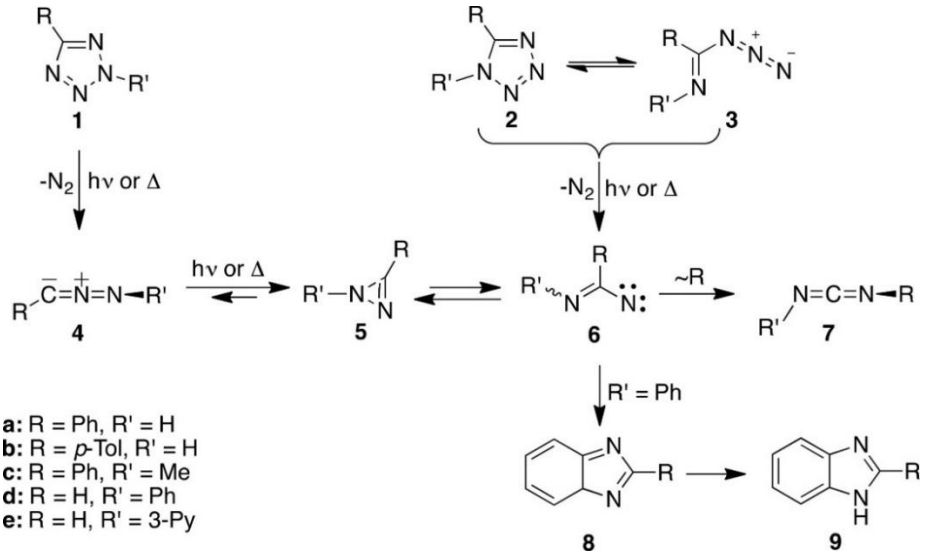

Scheme 4.3. Photolysis of tetrazole reprinted with permission from (ref.[395]). Copyright by 2018 American Chemical Society.

These reactive intermediates are now prone to various reactions. Although the reaction is predominantly used to react the nitrile imine with vinyl functionalities in a 1,3-dipolar cycloaddition,[404] it became apparent that this group can react with other nucleophiles such as thiols,[405] amines,[400, 405] carboxylates[9400] and to a very small extent alcohols.[405] The polymers in aqueous solution with and without pentanoic acid were irradiated with UV-light (Arimed B6 UV lamp, λ = 326 nm, 1.58 mW cm^{-2}) for 8 hr and the reaction was monitored using fluorescence spectroscopy (**Figure 4.7 and 4.9**). In the absence of pentanoic acid, a fluorescent product with an emission maximum λ_{max} of 490 nm was formed within 15 min. After an increase in fluorescence for two hours, the solution started to lose its fluorescence (**Figure**

4.7). This can potentially be assigned to a cascade of reaction proposed by Scheiner and Dinda, who observed that the photolysis of 2,5-diphenyltetrazole results initially in the formation of coloured 1,2-bis-phenylazo-1,2-diphenylethylene, which is then transformed into presumably non-coloured 2,4,5-triphenyl-1,2,3-triazole, a dimerization product.[406] This dimerization is evident in the molecular weight analysis of the polymer by SEC after 8 hr of irradiation (**Figure 4.8**), which reveals the presence of a second polymer with a molecular weight of 45,000 g mol^{-1}.

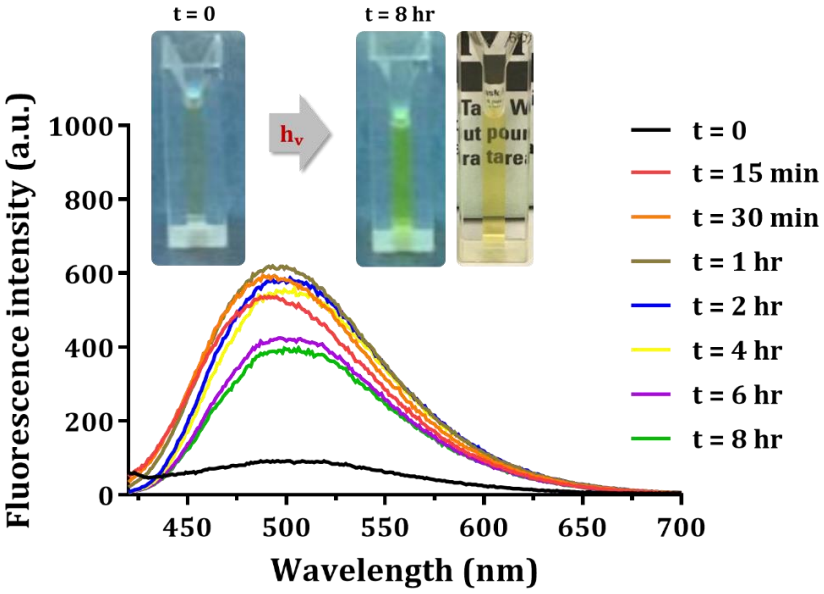

Figure 4.7. Changes of the fluorescence intensity after irradiation of an aqueous solution of PHEA bearing a tetrazole end functionality (excitation wavelength =390 nm), (Arimed B6 UV lamp, λ = 326 nm, 1.58 mW cm^{-2}).

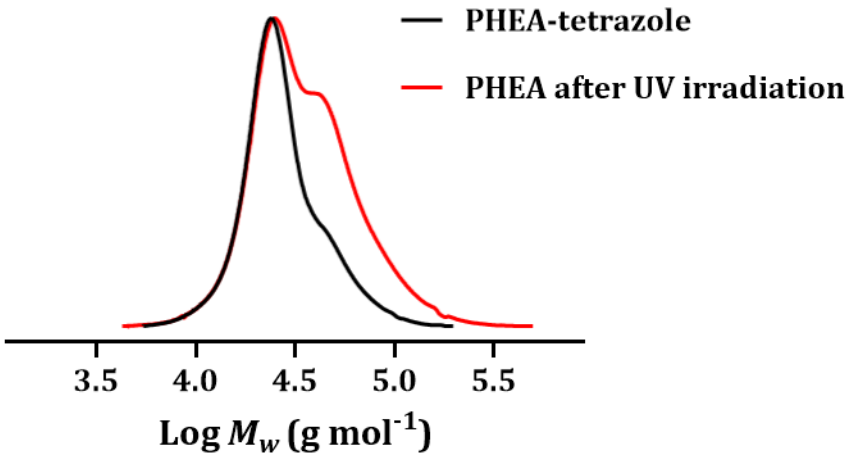

Figure 4.8. SEC analysis (DMF) of PHEA with tetrazole functionality (black) and after illumination of the polymer in water for 8 hr (red) using Arimed B6 UV lamp (λ = 326 nm, 1.58 mW cm^{-2}).

The addition of pentanoic acid in a ratio of tetrazole to carboxylic acid of 1: 4 triggers the competitive 1,3-dipolar cycloaddition reaction, also named the nitrile imine-carboxylic acid ligation (NICAL), which leads to the fluorescent product as shown in **Scheme 4.1** and **4.2**. The fluorescent intensity increases over the course of six hours and remains constant after that, indicative of maximum conversion (**Figure 4.9**). This reaction is rather slow and the introduction of electron-donating groups on the phenyl functionality could increase the rate.[400] The ^{1}H-NMR spectra reveals the appearance of the reacted pentanoic acid. Comparing the methyl group of the acid at δ = 0.86 ppm with the aromatic group belonging to the R-group of the RAFT functionality at δ = 7.35 – 7.11 ppm (**Figure 4.10**) reveals the almost complete reaction. SEC analysis displays a reduced high molecular weight shoulder in the polymer isolated after 8 hr reaction time although the dimer formation is still clearly visible indicative of the presence of two competing reactions (**Figure 4.11**). In the subsequent reaction with CNFs, these polymer dimer side products can easily be removed from the final polymer-coated CNFs *via* precipitation.

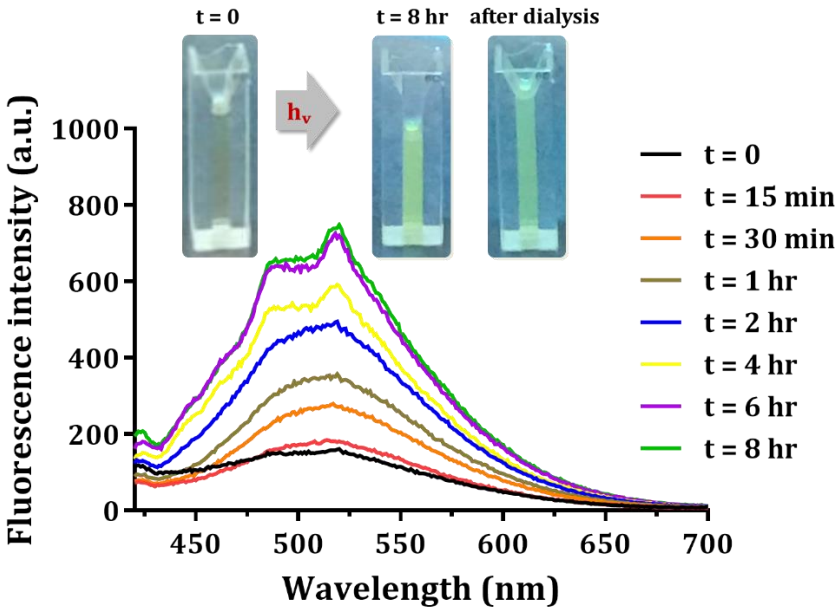

Figure 4.9. Changes of the fluorescence intensity after irradiation of an aqueous solution of PHEA bearing a tetrazole end functionality with pentanoic acid (excitation wavelength = 390 nm) (Arimed B6 UV lamp, λ = 326 nm, 1.58 mW cm^{-2}).

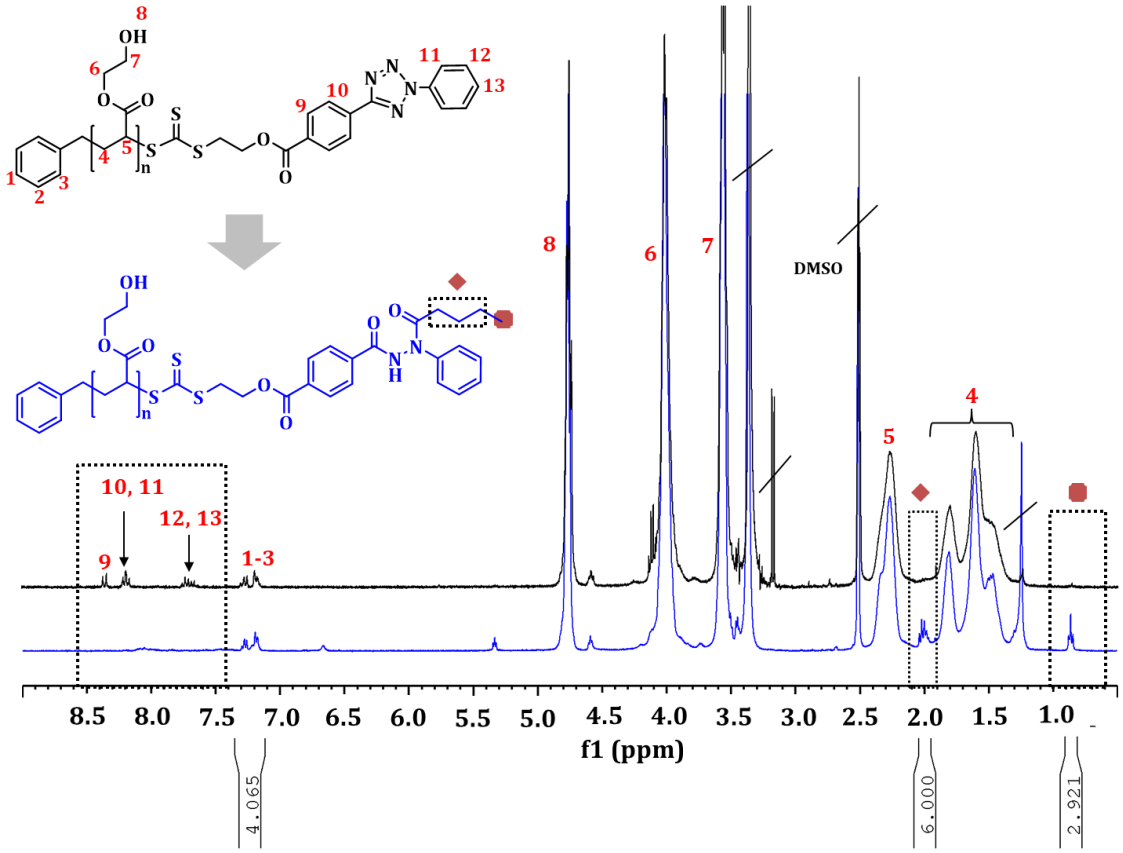

Figure 4.10. ^{1}H-NMR spectra of PHEA-tetrazole before and after reaction with pentanoic acid under UV-irradiation (Arimed B6 UV lamp, λ = 326 nm, 1.58 mW cm^{-2}) for 8 hr. The spectra were recorded in DMSO-d_6.

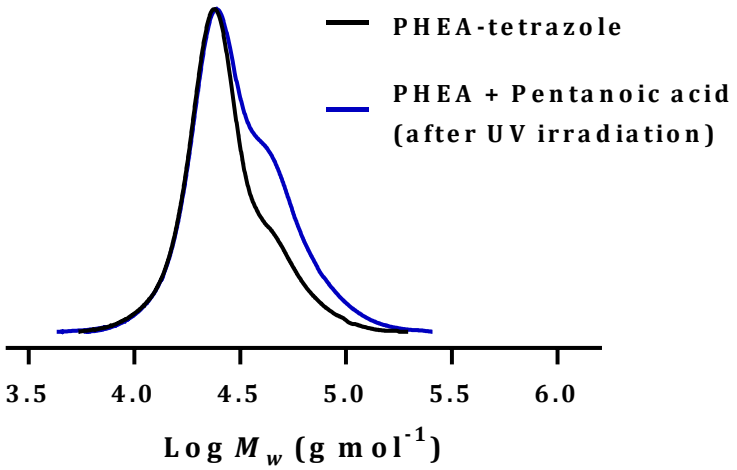

Figure 4.11. SEC analysis (DMF) of PHEA with tetrazole functionality (black) after reaction with pentanoic acid (blue) under UV irradiation for 8 hr in aqueous media (Arimed B6 UV lamp, λ = 326 nm, 1.58 mW cm^{-2}).

4.3.4. Synthesis of self-fluorescent cellulose nanofibers *via* photo-induced click reaction

The polymer was now mixed with CNFs at a ratio of tetrazole to carboxylic groups of 1: 4.2 in aqueous solution. The control of the pH value is crucial as variation in pH can lead to the formation of undesired products .[400] The reaction was again monitored using fluorescence spectroscopy revealing a slightly slower reaction rate to the one with pentanoic acid despite comparable tetrazole concentrations (**Figure 4.12**). The purification of the product was performed by centrifugation and washing with dioxane/methanol mixture (50: 50, v/v) to remove unreacted polymer, followed by dialysis against milli-Q water and freeze-drying. The emission spectrum of the purified sample was again recorded, confirming that the fluorescence is indeed the result of the reaction on CNFs (**Figure 4.13**) as PHEA-tetrazole or CNFs do not show any fluorescence at the emission maximum λ_{max} = 515 nm. A control sample of a mixture of PHEA-tetrazole and CNFs, stirred for 10 hr in the absence of light, did not display any fluorescence, highlighting the necessary use of UV irradiation (**Figure 4.13**).

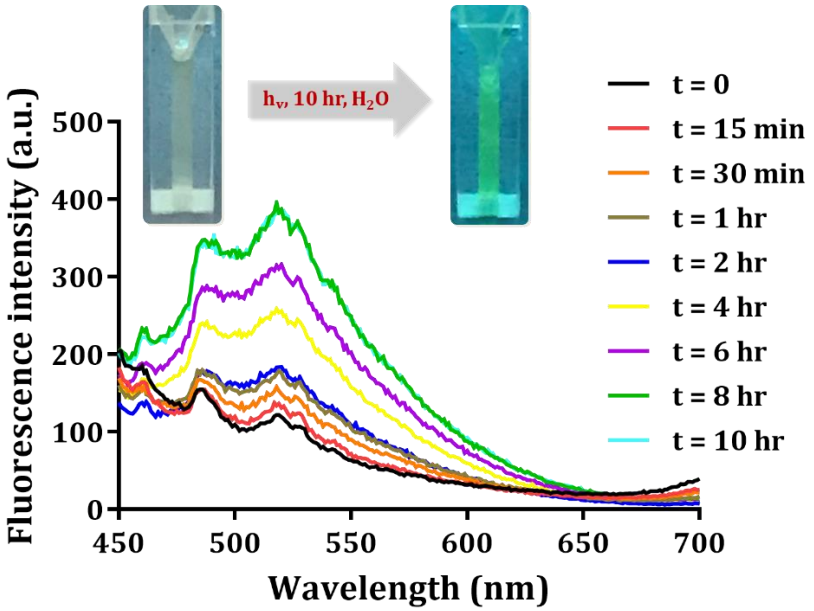

Figure 4.12. Changes of the fluorescence intensity after irradiation of an aqueous solution of PHEA-tetrazole with CNFs at different time intervals (excitation wavelength =380 nm) (Arimed B6 UV lamp, λ = 326 nm, 1.58 mW cm^{-2}).

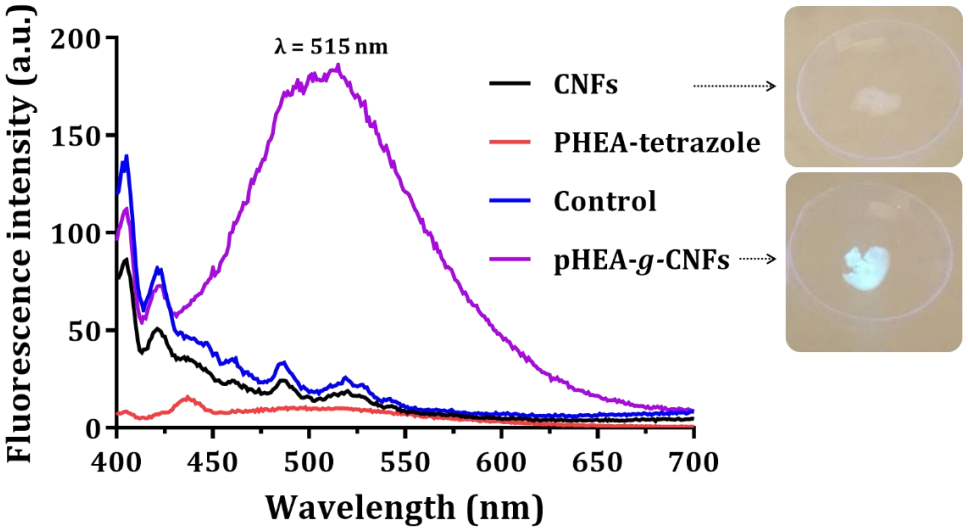

Figure 4.13. Emission spectrum of purified PHEA-*g*-CNFs in aqueous media at excitation wavelength = 380 nm compared to the spectrum of the PHEA-tetrazole and CNFs alone and to a control sample (a mixture of PHEA-tetrazole and CNFs left in darkness for 10 hr). The visual evidence for the fluorescence properties of PHEA-*g*-CNFs compared to CNFs under UV irradiation are shown in the pictures.

Moreover, the thermal degradation was recorded by TGA from room temperature to 700 °C at a heating rate of 10 °C min^{-1} under air. The degradation temperature of PHEA-*g*-CNFs at around 361 °C confirmed the existence of polymer chains on the surface. However, the quantitative analysis to calculate the grafting efficiency was not possible in this case as PHEA-tetrazole and CNFs cannot be clearly distinguished due to overlapping thermal behaviour (**Figure 4.14**). It seems however, that the grafting density may not be high as the PHEA-tetrazole decomposition is not clearly visible.

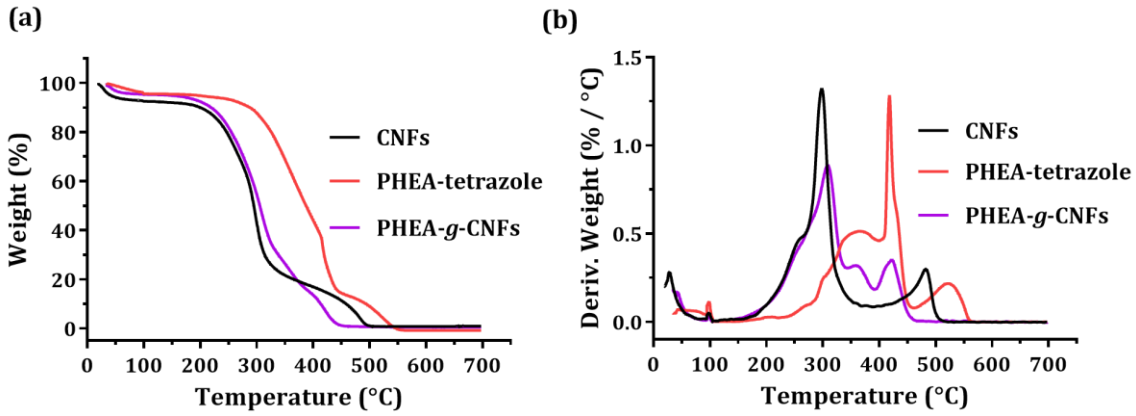

Figure 4.14. Thermogravimetric analysis of CNFs, PHEA-tetrazole and PHEA-*g*-CNFs at a heating rate of 10 °C min^{-1} under air (**a** and **b**).

Moreover, the re-dispersed PHEA-*g*-CNFs after freeze-drying showed higher colloidal stability than CNFs in aqueous solution at 1 mg mL^{-1} concentration and can therefore serve as drug carrier (**Figure 4.15**).

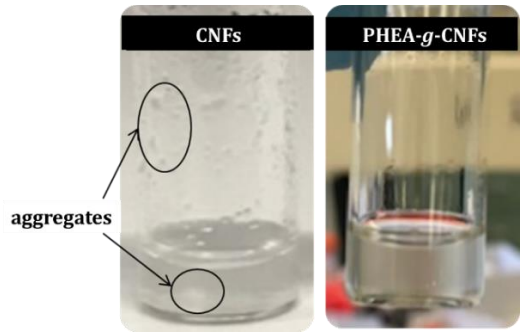

Figure 4.15. Aqueous dispersibility tests for CNFs (left) and PHEA-*g*-CNFs (right) at the same concentration of CNFs.

4.3.5. *In vitro* cytotoxicity and cellular uptake studies of PHEA-*g*-CNFs

The toxicity of PHEA-*g*-CNFs was tested using MCF-7 breast cancer cell lines. The incubation of various concentrations of the nanofibers with the cells for 72 hr did not impart any toxicity (**Figure 4.16**). Here, it seems that cellulose nanomaterials serve as nutrient to cells, resulting in more than 100 % cell growth at higher concentration. The cellular uptake of the nanoparticles was subsequently evaluated using laser scanning confocal microscopy (LSCM) for 2 hr and 24 hr (**Figure 4.17**). The polymer coated CNFs are clearly visible (green) inside the cells due to the self-fluorescence of the material. Please note, no additional fluorophores were used. Staining of the lysosomes (red) reveals the co-localization with PHEA-*g*-CNFs indicative of an uptake by endocytosis.

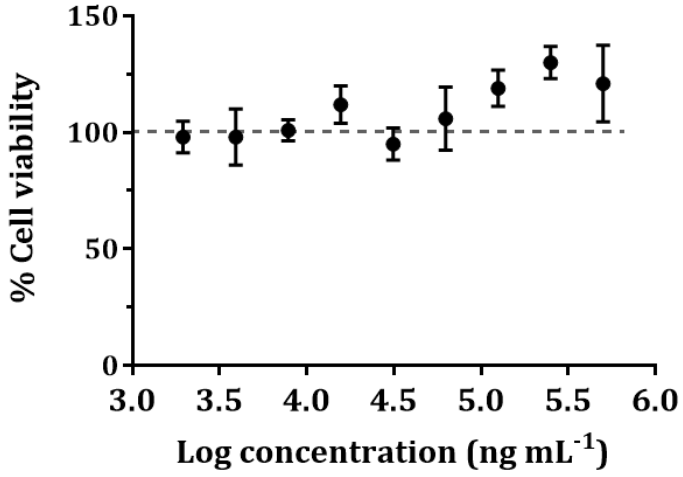

Figure 4.16. Viability (%) of breast cancer cell line (MCF-7) after being exposed to an aqueous dispersion containing PHEA-*g*-CNFs for 3 days (starting concentration = 0.5 mg mL^{-1}).

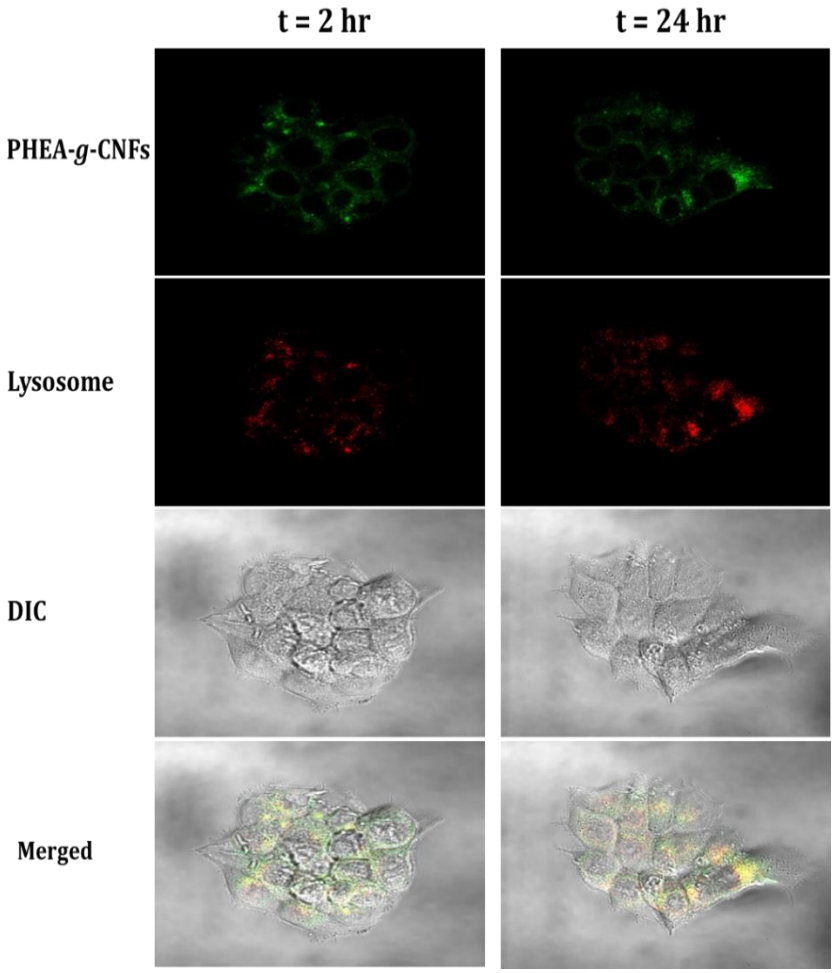

Figure 4.17. Confocal microphotographs of MCF-7 cells after incubation with aqueous dispersion of PHEA-*g*-CNFs at 37 °C for 2 hr and 24 hr. The yellow colour in the merged picture indicates the localization of nanofibers (PHEA-*g*-CNFs) in the lysosomes. The green and red colours represent PHEA-*g*-CNFs and lysosome, respectively.

4.3.6. Binding doxorubicin hydrochloride on the surface of cellulose nanofibers *via* electrostatic interaction (PHEA-*g*-CNFs-DOX)

The nanofibers were subsequently loaded with the hydrochloride salt of doxorubicin (DOX.HCl) by stirring various amounts of the drug with PHEA-*g*-CNFs in PBS buffer (pH 7.4). The positively charged drugs was loaded onto the negatively charged CNFs by electrostatic interactions.[407] After stirring for 27 hr, the drug loaded PHEA-*g*-CNFs were separated from the free drug by centrifugation and the amount of drug loaded was determined by analysing the supernatant *via* UV-Vis spectroscopy. Initial inspection reveals substantial drug loading as the solution of the drug loaded PHEA-*g*-CNFs takes on the red colour of DOX.HCl (**Figure 4.18**). The amount of loaded DOX.HCl was elucidated and drug loading efficiency as well as drug loading capacity was calculated using the molar absorptivity of DOX.HCl. The standard curve of DOX.HCl used for the determination of the amount of drug on the surface is shown in **Figure 4.19**. As expected, the fraction of loaded drug (drug loading capacity) increased with increasing amount of drug (**Figure 4.18**). What is rather unusual though is that the drug loading efficiency increases with increasing amount of drug, suggesting a more concentrated solution of DOX.HCl in PBS buffer pushes relatively more drug into the drug carrier. The origin of this behaviour is unclear and usually not observed in the literature. Large amounts of DOX.HCl in the feed solution will increase the ionic strength but also reduce the hydrophilicity of the solution, due to the large lipophilic character of the drug structure.[408] This may affect the conformation of the PHEA and CNFs themselves allowing better diffusion of the drugs to the negatively charged sites on the CNFs. It could also be possible that the initial presence of DOX.HCl alters the properties of the CNFs towards a more hydrophobic environment, attracting more drugs bound by π-stacking.[409-411]

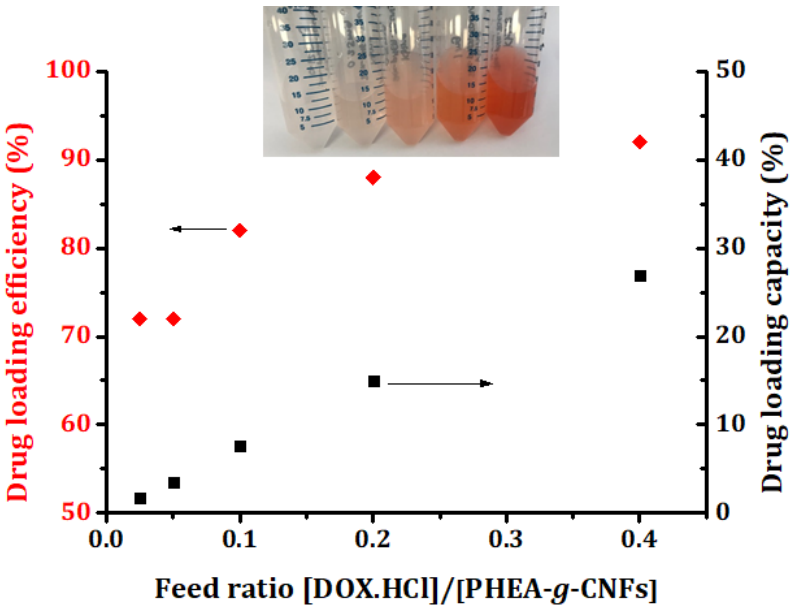

Figure 4.18. Drug loading efficiency (%) and drug loading capacity (%) *vs* weight feed ratio of DOX.HCl to PHEA-*g*-CNFs. The insert shows the appearance of the drug loaded nanoparticles after purification from the lowest (left) to the highest (right) drug loading capacity.

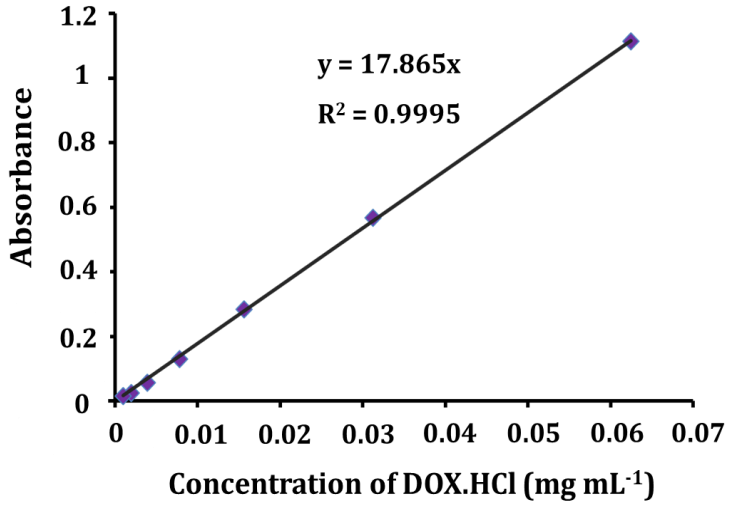

Figure 4.19. Standard curve of DOX.HCl in methanol by using UV-Vis spectroscopy (excitation wavelength = 496 nm).

The purified PHEA-*g*-CNFs-DOX with 1.7 % drug loading capacity was submitted for FT-IR characterization, which shows that the existence of PHEA on CNFs (**Figure 4.20**). The presence of attached PHEA is mainly evident from the increased absorption peak at around 2970 cm^{-1}. The new band at 1602 cm^{-1} could be either the CONH stretching vibration or DOX.HCl.

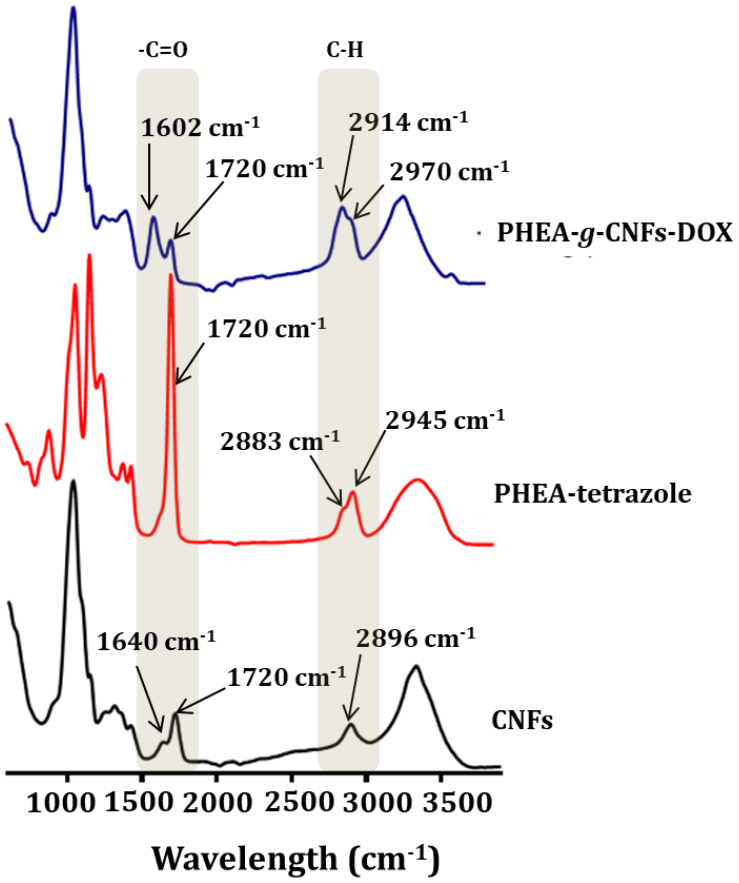

Figure 4.20. FT-IR spectra of CNFs (black), PHEA-tetrazole (red) and PHEA-*g*-CNFs-DOX (1.7 % drug loading capacity) (blue).

The grafted polymer (PHEA) is more visible in the ^{1}H-NMR study, but CNFs and the drug are barely visible (**Figure 4.21**). ^{1}H-NMR signals corresponding to CNFs appear typically between 5 and 3 ppm. A signal at around 3.6 ppm is evidence for the presence of CNFs, but the majority of signals are invisible due to the relaxation time of crystalline CNFs.

According to the characterization *via* DLS, PHEA-*g*-CNFs-DOX (1.7 % drug loading capacity) was found to have a hydrodynamic diameter of around D_h= 503.1 nm (PDI= 0.34) and a zeta-potential of -29.6 mV (**Figure 4.22**). The strong negative zeta-potential suggests that the polymer is only able to partially shield the charged carboxylate on the CNFs. One positive aspect is the negative surface charges can efficiently repel albumin binding (**Figure 4.22 b**).

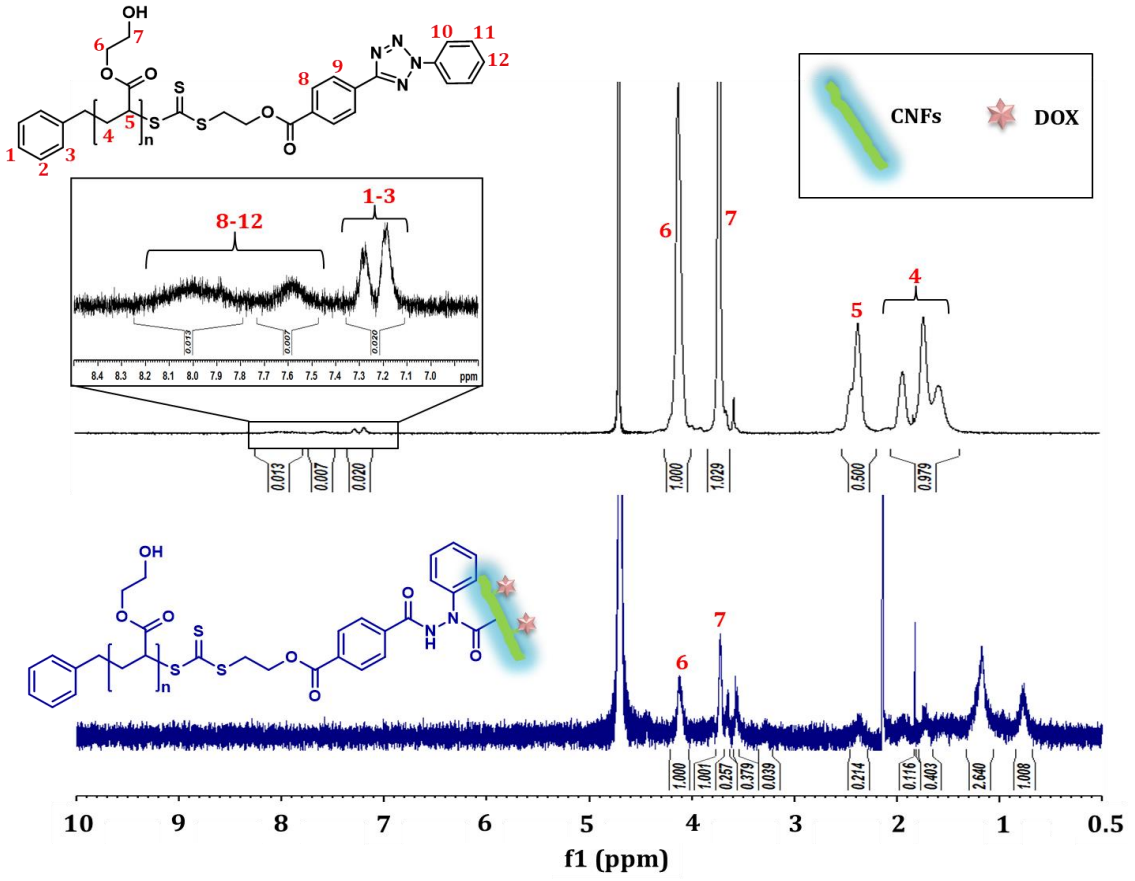

Figure 4.21. ^{1}H-NMR spectra of PHEA-tetrazole (black) and PHEA-*g*-CNFs-DOX (1.7 % drug loading capacity) (blue). The spectra were recorded in D_2O.

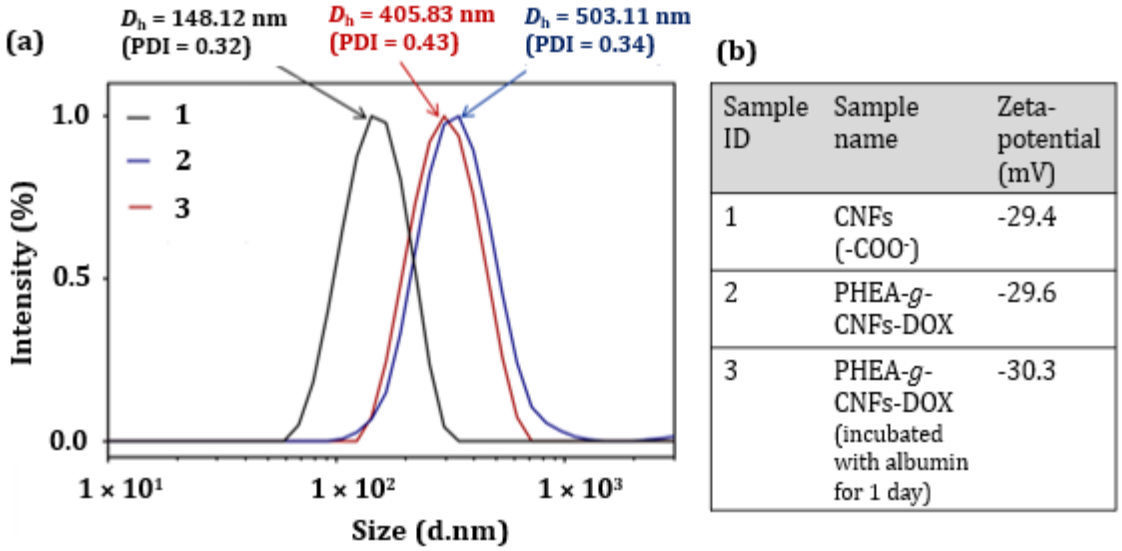

Sample ID	Sample name	Zeta-potential (mV)
1	CNFs (-COO$^-$)	-29.4
2	PHEA-*g*-CNFs-DOX	-29.6
3	PHEA-*g*-CNFs-DOX (incubated with albumin for 1 day)	-30.3

Figure 4.22. Size distribution of CNFs (-COO$^-$) (1, black). **(a)** Size distributions of PHEA-*g*-CNFs-DOX (1.7 % drug loading capacity) before (2, blue) and after incubation with albumin for one day (3, dark red), and **(b)** a table for the zeta-potential of each CNFs sample.

4.3.7. *In vitro* cytotoxicity and cellular uptake study

Cell proliferation studies on MCF-7 cells revealed an increased toxicity with increasing drug loading capacity (**Figure 4.23**). This is expected as each PHEA-*g*-CNFs carries more drug meaning that one nanofiber is significantly more toxic. The cell needs to take up less drug carriers, thus doing less work, to receive a large load of drug. However, this is not always the case as the drug can alter the properties of the drug carrier lowering the bioactivity of nanoparticles with high amount of drugs.[50, 412-414]

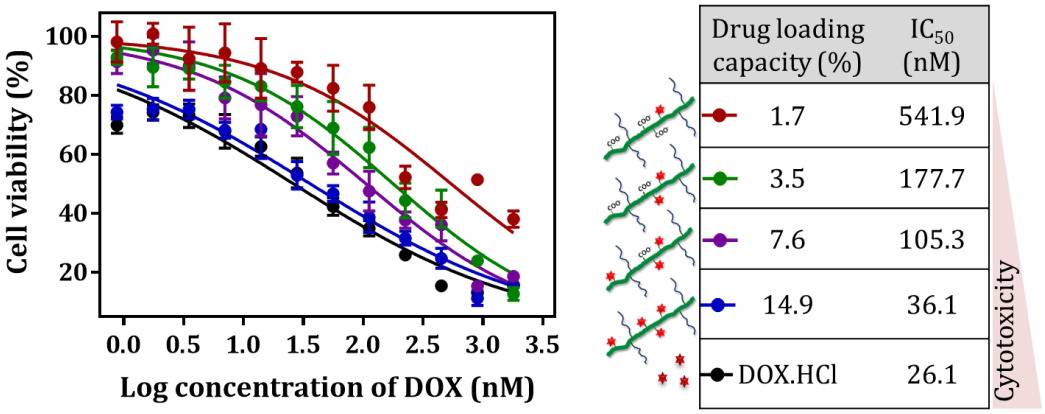

Figure 4.23. The effects of drug loading capacity of PHEA-*g*-CNFs on cell viability against MCF-7 cell line. The cell viability tests were performed after incubating the cells with drug-loaded PHEA-*g*-CNFs at 37°C for 2 days.

To understand the increased activity with higher drug loading, two cell uptake experiments were carried out using flow cytometry. The fluorescence signal of DOX.HCl was followed, not that of the drug carrier. In one scenario, the solutions were adjusted to the same drug concentration, thus only a small amount of drug carrier is present in the sample with the highest drug loading capacity (**Figure 4.24 left**, **Table 4.1** for concentrations). The MCF-7 cells were incubated for 2 hr and the cell association was measured by flow cytometry following the fluorescent DOX.HCl. It is evident that PHEA-*g*-CNFs with large amounts of DOX.HCl are more efficient in delivering the drug as less drug carriers need to be shuttled into the cell. This can now be compared to the cell uptake when using the same PHEA-*g*-CNFs concentration. The raw data naturally reveals a lower fluorescent intensity associated with the MCF-7 cells in the case of low drug loading content, owing to the lower loading of fluorescent drugs (**Figure 4.24 middle**). This data can now be re-analysed by

taking the difference in fluorescent intensity into account to obtain a cell association relative to each other. In this case, the sample with the lowest drug loading was omitted as the overall low fluorescence gave unreliable results. **Figure 4.24** (**right**) reveals that the cellular association is independent from the drug loading capacity. As a result, the higher toxicity can be explained simply by the larger amount of drug per drug carrier.

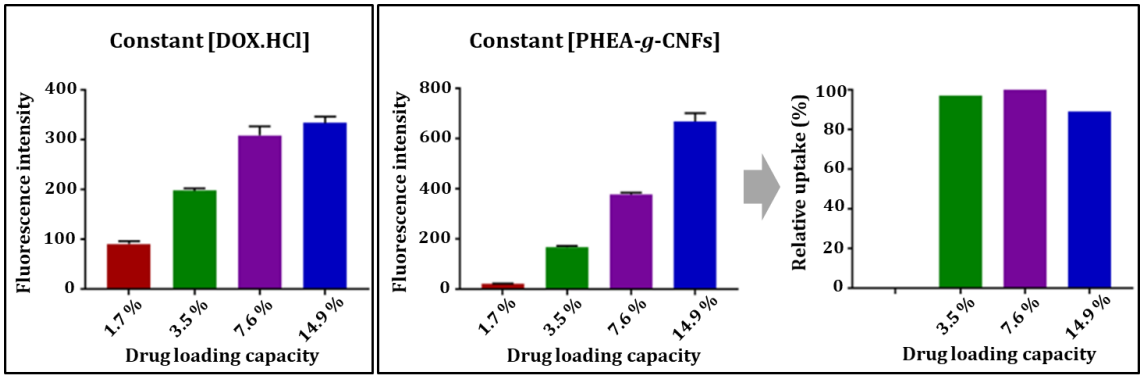

Figure 4.24. Flow cytometry analyses of MCF-7 cells after treatment with PHEA-*g*-CNFs-DOX at constant drug concentration of 8.87 μg mL^{-1} (left) and at constant PHEA-*g*-CNFs of 108.18 μg mL^{-1} (middle, raw data) (right, corrected data).

4.4. Conclusions

In summary, we reported a simple and facile method to prepare functional cellulose nanoparticles with self-fluorescent properties, enhanced aqueous dispersibility and low toxicity *via* NICAL click chemistry under mild reaction conditions. The synthesized PHEA-*g*-CNFs were successfully taken up by MCF-7 cells within 2 hr. Loading of DOX.HCl at different amounts revealed that the *in vitro* cytotoxicity of drug loaded nanofibers against cancer cells was significantly influenced by the drug loading capacity. This study provided valuable insight into the potential applications of click reactions by endowing superior properties like fluorescence and aqueous dispersibility to cellulose nanofibers, thereby making it beneficial for biomedical applications.

4.5. Experimental Procedure

4.5.1. Synthesis of benzyl (2-hydroxyethyl) carbonotrithioate [BHCT]

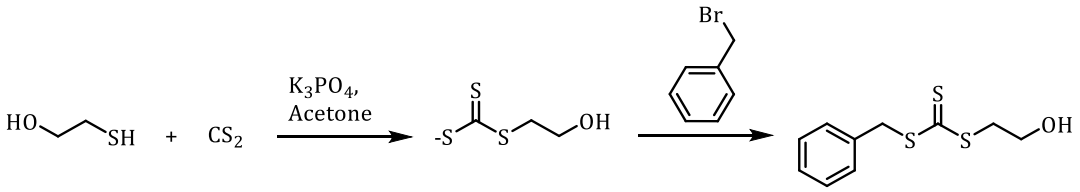

Scheme 4.4. Schematic illustration for the synthesis of benzyl (2-hydroxyethyl) carbonotrithioate [BHCT].

2-Mercaptoethanol (0.9 mL, 12.8 mmol) was added to a stirred suspension of potassium phosphate tribasic (K_3PO_4) (2.7g, 12.8 mmol) in acetone (50 mL) and stirred for 15 min. When carbon disulphide (CS_2) (1.23 mL, 20.5 mmol) was added to the mixture, the solution turned yellow and was kept under stirring for 30 min. After addition of benzyl bromide (1.52 mL, 12.8 mmol), potassium bromide (KBr) precipitation was observed, and the mixture was stirred for 2 more hours. The resulting mixture was then filtered, and solvent was removed under reduced pressure. The obtained concentrated crude product was purified by column chromatography (cyclohexane/ethyl acetate 70: 30 v/v) to yield a slightly viscous yellow oil (2.53 g, 81 %).

^{1}H-NMR (300 MHz, $CDCl_3$): δ/ppm = 7.4 – 7.2 (5H, m, C*H*phenyl), 4.64 (2H, s, -CHphenyl C*H*$_2$-), 3.92 (2H, t, -CH_2CH_2OH), and 3.63 (2H, t, -CH_2CH_2OH).

4.5.2. Synthesis of 4-(2-phenyl-2H-tetrazole-5-yl) benzoic acid

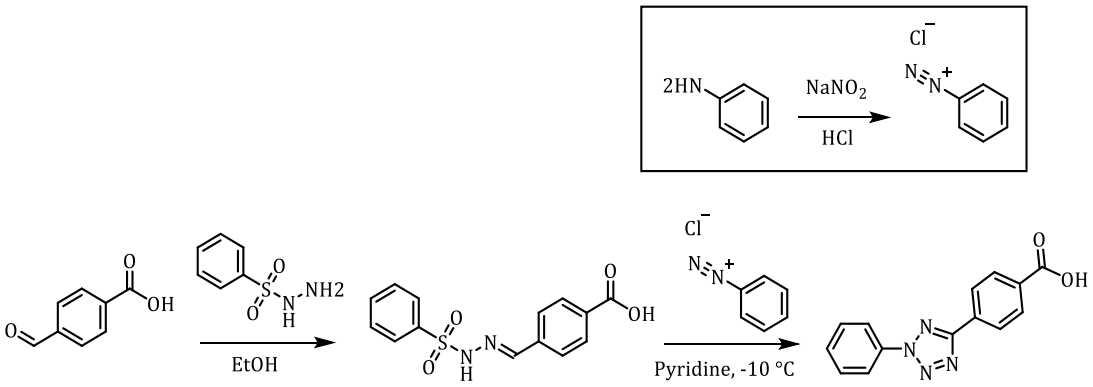

Scheme 4.5. Schematic illustration for the synthesis of 4-(2-phenyl-2H-terazole-5-yl) benzoic acid.

4-Formylbenzoic acid (2.5 g, 1.67 mmol) was dissolved in ethanol (150 mL). Benzenesulfonyl hydrazide (2.87 g, 1.67 mmol) was added to the pale-yellow solution and stirred for 30 min. Milli-Q water (130 mL) was added and a white precipitate formed. The precipitate was then collected by filtration and dried under vacuum. A solution of sodium nitrite (1.15 g, 1.67 mmol) in milli-Q water (8 mL) was added to a cooled solution of aniline (1.55 g, 1.67 mol) in water/ethanol (26 mL, 1: 1, v/v) and concentrated hydrochloric acid (5 mL). The white precipitate was dissolved in pyridine (250 mL) and the aniline solution was slowly added to this solution at -10 °C and stirred for 1 hr. Ethyl acetate (300 mL) was added to the resulting red solution and the top layer was collected. Concentrated hydrochloric acid (3 N, up to 800 mL) was added to the ethyl acetate solution. A red precipitate formed at the phase interface and was collected by filtration and dried under vacuum. The desired product was obtained as a pale red solid (2.2 g, 50 %).

^{1}H-NMR (400 MHz, DMSO-d_6): δ/ppm = 13.26 (1H, s, CHphenyl COO*H*), 8.30 (2H, m, C*H*phenyl), 8.18 (4H, m, C*H*phenyl), 7.72 (2H, m, C*H*phenyl), and 7.65 (1H, m, C*H*phenyl).

4.5.3. Synthesis of 2-(((benzylthio)carbonothioyl)thio)ethyl 4-(2-phenyl-2H-tetrazol-5-yl)benzoate [tetrazole-bearing RAFT agent]

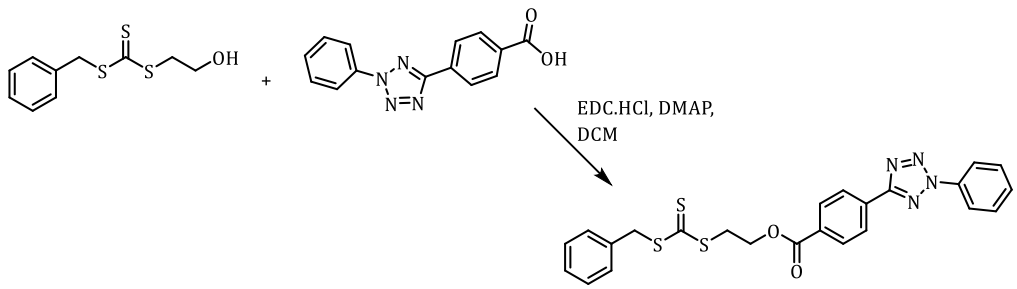

Scheme 4.6. Schematic illustration for the synthesis of 2-(((benzylthio)carbonothioyl)thio) ethyl 4-(2-phenyl-2H-tetrazol-5-yl)benzoate [tetrazole-bearing RAFT agent].

4-(2-phenyl-2H-tetrazol-5-yl)benzoic acid (195 mg, 0.74 mmol) and *N*-(3-dimethylaminopropyl)-*N*′-ethylcarbodiimide hydrochloride (EDC.HCl) (152 mg, 0.80 mmol) were dissolved in dichloromethane (3 mL) and stirred in darkness for 15 min. Benzyl (2-hydroxyethyl) carbonotrithioate (150 mg, 0.61 mmol) and a

catalytic amount of 4-(dimethylamino)pyridine (DMAP) were added and the solution was stirred (in darkness) overnight. The solution was washed with acidic water (pH 4 - 5) to remove unreacted EDC and urea by-product, and then the organic solvent was removed under reduced pressure. The residue was purified by column chromatography (cyclohexane/ethyl acetate 80: 20 v/v) to yield the product as dark red viscous oil (195.3 mg, 65 %).

^{1}H-NMR (300 MHz, $CDCl_3$): δ/ppm = 8.39 (2H, d, C*H*phenyl-tetrazole), 8.25 (4H, m, C*H*phenyl-tetrazole), 7.69 – 7.51 (3H, m, C*H*phenyl-tetrazole), 7.4 – 7.3 (5H, m, C*H*phenyl), 4.7 – 4.6 (4H, m, CH_2), and 3.85 (2H, t, -C(S)SCH_2-).

4.5.4. Synthesis of poly(2-hydroxyethyl acrylate)bearing tetrazole moiety [PHEA-tetrazole]

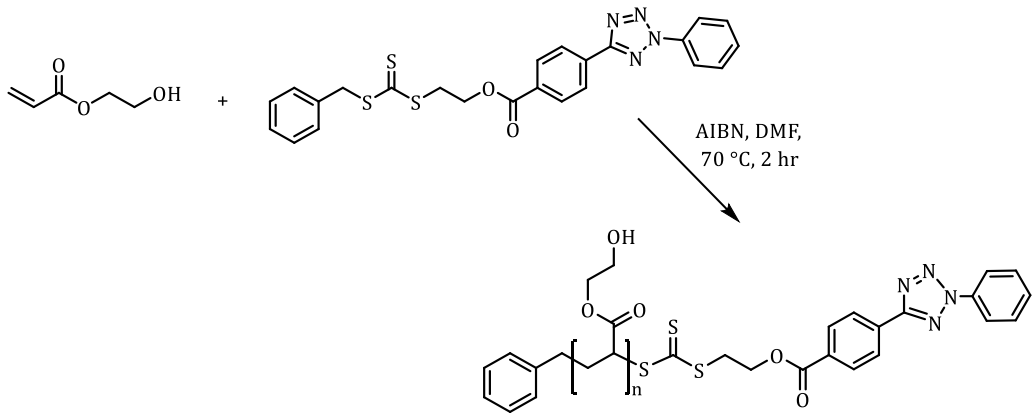

Scheme 4.7. Schematic illustration for the synthesis of PHEA-tetrazole.

In a glass vial, 2-hydroxyethyl acrylate (HEA) (919 mg, 7.91 mmol), RAFT-tetrazole (39 mg, 79.14 µmol), and the initiator AIBN (1.3 mg, 7.91 µmol) were dissolved in *N,N*-dimethylformamide (DMF) (concentration = 2.64 M). The glass vial sealed with rubber septum was then degassed with nitrogen gas for 45 min. The polymerization was performed at 70 °C for 2 hr to achieve 85% of monomer conversion. The reaction was stopped by introducing air to the mixture and placing the vial in an ice bath. The resulting polymer was purified *via* dialysis against methanol (MeOH) for 2 days and then dried under vacuum. The monomer conversion and molecular weight of the pure polymer were analysed *via* ^{1}H-NMR and SEC. The broad

polydispersity index was due to the high monomer conversion, but it did not affect further experiments carried out by using synthesized polymers.

4.5.5. Photo-induced click reaction between PHEA-tetrazole and pentanoic acid under ambient condition

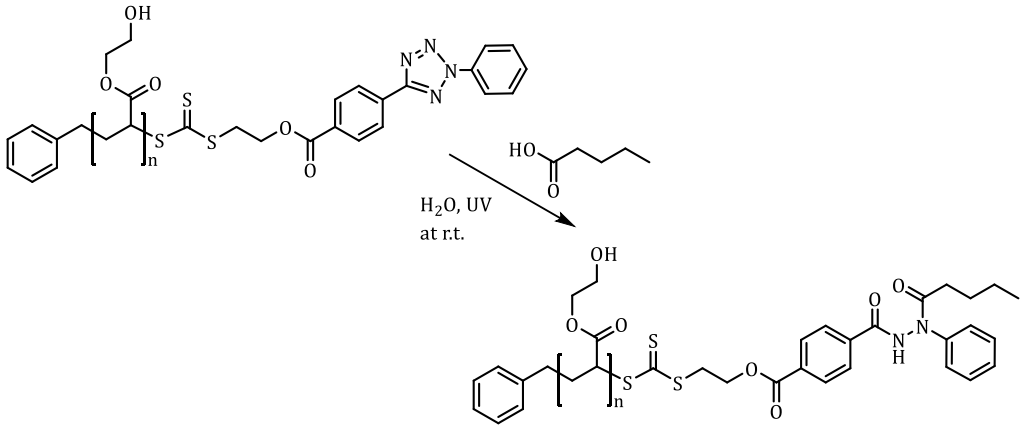

Scheme 4.8. Schematic illustration for the photosynthesis of PHEA-tetrazole and pentanoic acid under ambient condition.

The photo-click reaction between tetrazole and acid moieties were carried out under ambient conditions in aqueous media. Firstly, the mixture of PHEA-tetrazole (40.00 mg, 3.85 μmol) and pentanoic acid (1.64 mg, 16.03 μmol) in 200 μL of milli-Q water was added into 1 mL quartz cuvette and stirred vigorously. Then the solution was irradiated under UV (Arimed B6 UV lamp, λ = 326 nm, 1.58mW cm^{-2}) under constant stirring at room temperature. For the purpose of kinetic study, the changes in fluorescence intensity were monitored by using a fluorescence spectrophotometer after irradiating the solution at different time intervals: t =0, 15 min, 30 min, 1 hr, 2 hr, 4 hr, 6 hr, and 8 hr. For the control experiment, the same reaction condition was employed in the absence of pentanoic acid.

4.5.6. Synthesis of self-fluorescent cellulose nanofibers *via* photo-induced click reaction

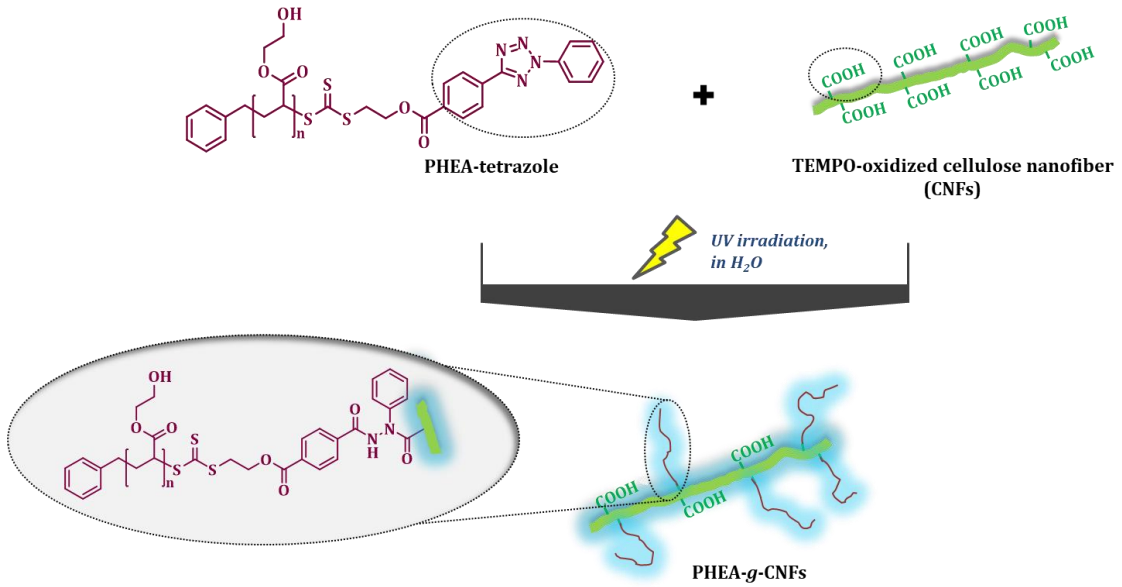

Scheme 4.9. Reaction scheme for the synthesis of self-fluorescent cellulose nanofibers by grafting PHEA onto surface *via* photo-induced tetrazole-COOH click reaction.

Self-fluorescent cellulose nanofibers were obtained by covalently tethering tetrazole end-functionalized PHEA onto the surface of TEMPO-oxidized cellulose nanofibers (CNFs) *via* light-triggered tetrazole-acid click reaction under ambient condition. In a 1 mL quartz cuvette, CNFs gel (9.75 mg of dry solid, 16.09 µmol of carboxylic acid groups) was mixed with PHEA-tetrazole (40 mg, 3.86 µmol) and dispersed in 800 µL of milli-Q water. After homogenising the dispersion by continuous stirring, it was submitted for UV-irradiation using Arimed B6 UV lamp (λ = 326 nm, 1.58 mW cm^{-2}) in aqueous media while stirring at room temperature. For the kinetic study, the reaction conditions were monitored by the changes in fluorescence intensity using a fluorescence spectrophotometer after irradiating the solution at different time intervals: t = 0, 15 min, 30 min, 1 hr, 2 hr, 4 hr, 6 hr, 8 hr, and 10 hr. After, the starting materials (PHEA-tetrazole) and possible by-products (block copolymers due to the reaction between tetrazole moieties themselves) were removed by precipitating and centrifuging (at 7000 rpm for 10 min) the crude sample in dioxane/methanol mixture (50: 50 v/v) for several times. The precipitated PHEA-grafted cellulose nanofibers (PHEA-*g*-CNFs) were then dialysed against milli-Q

water for one day to completely remove the organic solvent and submitted for freeze-drying to achieve the sample in fluffy solid form. The properties of the pure PHEA-*g*-CNFs were then characterized *via* UV-Vis and fluorescence spectroscopy. The size distribution and zetapotential analyses of CNFs before and after surface grafting with PHEA were performed by dynamic light scattering (DLS). For the experiments on albumin binding, 0.7 mg of PHEA-*g*-CNFs and 3.5 mg albumin were vigorously stirred in 1 mL of water. The size change of nanoparticles was recorded by DLS after one day.

4.5.7. *In vitro* cell viability assay

The cytotoxicity tests for the PHEA-*g*-CNFs with and without drugs were carried out by a standard sulforhodamine B colorimetric proliferation assay (SRB assay). The breast cancer cell line MCF-7 was seeded in 96-well cell culture plates at a density of 4000 cells per well and incubated at 37 °C in 5 % CO_2 for 24 hr. The samples were then sterilized by UV irradiation for 15 min in a bio-safety cabinet and then the growth medium (Dulbecco's Modified Eagle's Medium, DMEM) was replaced with 100 µL of fresh double concentrated medium. Subsequently, 100 µL of serially diluted (double dilution) samples were added to the plates. After incubation at 37 °C for 72 hr, the culture medium was removed and the live cells were fixed in 10 % (w/v) trichloroacetic acid (TCA) for 30 min at 4 °C, followed by washing the plates five times with milli-Q water. Then, the TCA-fixed cells were stained by adding 100 µL of 0.4 % (w/v) SRB dissolved in 1 % acetic acid. After leaving the plates for 20 min in dark, SRB was decanted and the plates were washed five times with 1 % acetic acid to remove unbound dye. After removing the excess of moisture by air-drying for a few hours, 200 µL of 10 mM Tris buffer was added to each well and left for 5 min to solubilize the dye (SRB). The absorbance was determined at 490 nm using a Bio-Rad BenchMark Microplate reader. The obtained data was analyzed and plotted using GraphPad Prism 8.0, in which non-treated cells were used as controls. The cell viability was calculated using optical density (OD):

$$\text{Cell viability (\%)} = \frac{\text{OD}_{490,\text{sample}} - \text{OD}_{490,\text{blank}}}{\text{OD}_{490,\text{control}} - \text{OD}_{490,\text{blank}}} \times 100$$

4.5.8. *In vitro* cellular uptake study for PHEA-*g*-CNFs by laser scanning confocal microscopy (LSCM)

Observations on the cellular uptake and fluorescence property of synthesized polymer-grafted cellulose nanofibers (PHEA-*g*-CNFs) were carried out *via* laser scanning confocal microscopy (LSCM). Firstly, cells were seeded in 35 mm fluorodish (World Precision Instruments) at a density of 3×10^4 per dish and cultured in 2 mL of DMEM cell culture medium at 37 °C in 5 % CO_2 for 24 hr. When the cells reached sufficient confluency, the medium was replaced with 1 mL of fresh double concentrated medium and 1 mL of sample dispersion at the concentration of 0.5 mg mL^{-1}. After incubating the cells at 37 °C for 2 hr and 24 hr, the cells were washed three times with PBS. The cells were then stained with LysoTracker Red DND-99 (Invitrogen) for 1 min, followed by washing with PBS. Then the cells were mounted in PBS and observed under a Zeiss LSM 780 laser scanning confocal microscope system equipped with a Diode 405-30 laser and an argon laser and a DPSS 561-10 laser (excitation wavelength: 405 nm and emission wavelengths: 490 – 590 nm, respectively) connected to a Zeiss Axio Observer.Z1 inverted microscope (Air 20×/0.8 NA objective). The Zen2012 imaging software (Zeiss) was used for image acquisition and processing.

4.5.9. Binding doxorubicin hydrochloride on the surface of cellulose nanofibers *via* electrostatic interaction (PHEA-*g*-CNFs-DOX)

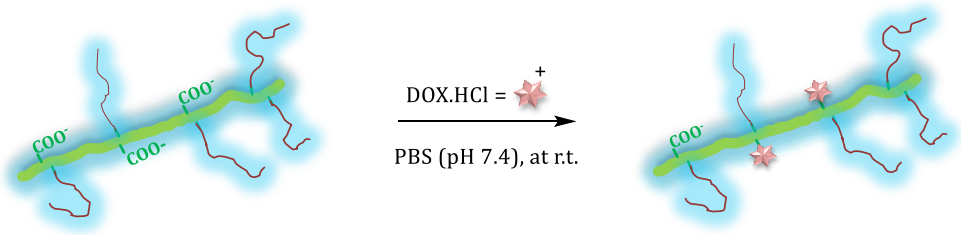

Scheme 4.10. Schematic illustration for binding doxorubicin hydrochloride (DOX.HCl) on the surface of CNFs *via* electrostatic interaction in PBS (at pH = 7.4) at room temperature.

Binding doxorubicin hydrochloride (DOX.HCl) on the surface of PHEA-*g*-CNFs was performed *via* electrostatic interaction in phosphate buffered saline (PBS,

pH 7.4). To prepare a range of drug-loaded samples with different amount of drugs on the surface, the stock solution of DOX.HCl was first prepared by dissolving 4 mg of DOX.HCl in 2 mL of milli-Q water. Then the desired volume of stock solution was diluted into five vials containing 5 mg of PHEA-*g*-CNFs in 1 mL of double concentrated PBS (pH 7.4). More milli-Q water was added to all vials to adjust the volume of the solution to 2 mL and initially added drug concentrations to 0.125 mg, 0.25 mg, 0.5 mg, 1 mg and 2 mg respectively. The reaction was then stirred at 600 rpm for 27 hr at room temperature. The samples were purified by several cycles of precipitation and centrifugation in methanol at 6000 rpm for 15 min. After each cycle, the supernatant containing free DOX.HCl was collected, dried and re-dissolved in certain volume of methanol for UV-Vis analysis to calculate the drug loading efficiency. The maximum excitation wavelength of DOX.HCl was 496 nm. Then, the precipitated drug loaded samples were further dialyzed against milli-Q water for one day, followed by freeze-drying.

4.5.10. *In vitro* cellular uptake study for drug loaded PHEA-*g*-CNFs by flow cytometry

Cellular uptake studies for drug-loaded PHEA-*g*-CNFs samples were performed by flow cytometry. Firstly, MCF-7 cells were seeded in 6-well plates at a density of 3×10^5 cells per well and incubated at 37 °C in 5 % CO_2 for two days. Then the cultured medium (DMEM) was replaced with 1 mL of fresh double concentrated medium and 1 mL of sample solution. The data for the experiments using constant PHEA-*g*-CNFs concentration and constant DOX.HCl concentration are shown in the **Table 4.1**. After incubating the cells with sample solution at 37 °C for 2 hr, the cell monolayer was washed with cold PBS three times and treated with trypsin/EDTA to detach the cells. After that, the cells were collected, centrifuged and resuspended in cold Hank's buffer. The cells suspension was submitted for flow cytometry analysis on BD FACSCanto™II Analyser (BD Biosciences, San Jose, USA, excitation wavelength = 488 nm and emission wavelength = 585 nm), and the results were collected by analysing at least 20,000 cell events. Raw data was analysed using FlowJo

software and the results were reported as the median of the distribution of cell fluorescent intensity.

Table 4.1. The concentration of PHEA-*g*-CNFs or DOX.HCl treated to the cells.

	[DOX.HCl] constant = 8.87 μg mL^{-1}	[PHEA-*g*-CNFs] constant = 108.18 μg mL^{-1}
Sample ID (based on drug loading capacity/ %)	[PHEA-*g*-CNFs] (μg mL^{-1})	[DOX.HCl] (μg mL^{-1})
1.7	491.13	1.95
3.5	108.18	8.87
7.6	50.20	19.11
14.9	22.94	41.83

CHAPTER - 5

Modification *via* Passerini Reaction:

The Design of Thermo-Responsive

&

Colloidally Stable CNFs

https://doi.org/10.1021/acsmacrolett.8b00051

CNFs = Cellulose Nanofibers

Table of Content

5.1. Overview

The three-component Passerini reaction (Passerini 3-CR) is regarded as an effective functionalization approach which can be carried out under mild and fast reaction conditions. In this study, we investigated the application of Passerini 3-CR for the synthesis of thermo-responsive cellulose fibrils by covalently tethering poly(*N*-isopropylacrylamide) in aqueous condition at ambient temperature. The three components, a TEMPO-oxidized cellulose nanofiber bearing carboxylic acid moieties (CNFs-COOH), a functionalized polymer with aldehyde group (PNIPAm-COH) and a cyclohexyl isocyanide, were reacted in one-pot resulting in 36 % of grafting efficiency within 30 min. The chemical coupling was evidenced by improved aqueous dispersibility, which was further confirmed by FT-IR, TGA, UV-Vis, and turbidity study. It was observed that the grafting efficiency is strongly dependent on the chain length of the polymer. Furthermore, AFM and X-ray diffraction measurements affirmed the suitability of the proposed method for chemical modification of cellulose nanofibers without significantly compromising the original morphology and structural integrity.

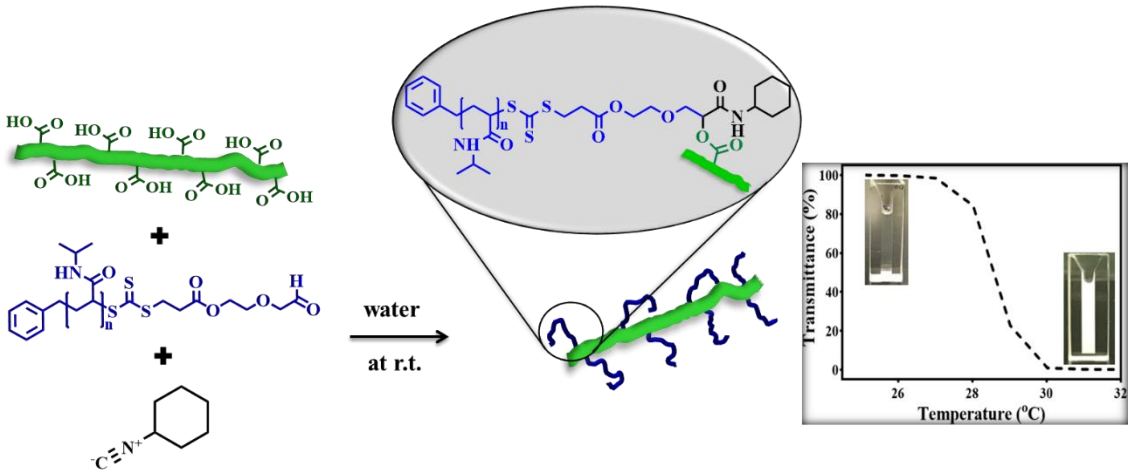

Scheme 5.1. Schmetic illustration for the synthesis of PNIPAm-grafted cellulose nanofibers (PNIPAm-*g*-CNFs) *via* three-component Passerini reaction.

5.2. Introduction

Nanocellulose is one of the most outstanding biomaterials due to unique physical, chemical and biological properties.[415, 416] Numerous nanocellulose-based materials have been investigated for wide applications in various fields including: medical, food, paper, composite, etc.[416, 417] However, aggregation of nanocellulose is often encountered in aqueous media, which poses a major obstacle in developing these materials for various applications.[418] This has led to extensive studies on surface modification techniques to minimize inter-and intra-hydrogen bonding between cellulose chains to improve functionality.[148] Amongst various surface modification techniques, physical or chemical grafting of polymers onto cellulose nanofibers (CNFs) is the most promising approach triggering significant outcomes.[224, 419] Taking advantage of abundant carboxylic acid groups present on the surface of CNFs prepared *via* TEMPO-mediated oxidation pre-treatment[373], synthetic polymers can be covalently attached onto nanofibers *via* various chemical treatments including esterification, etherification and amidation reactions.[224, 420] As a result of the moisture sensitivity of the system, the tedious and lengthy solvent exchange processes of nanofibrils have to be performed prior to the surface functionalization.[421] To overcome this limitation, we investigated nitrile imine-mediated tetrazole/ carboxylic acid ligation (NICAL) reaction as an surface modification technique which can be processed under mild aqueous conditions (**Chapter 4**). However, apart from the fluorescent and biological properties of resulting products (polymer-grafted CNFs), the grafting was not efficient. Hence, we herein explored an alternative method which can efficiently tether polymers on CNFs under mild reaction conditions without disrupting the original morphology and structural integrity of CNFs.

Our approach is based on the Passerini reaction, which is one of the multicomponent reactions (MCRs) containing three reagents - an aldehyde/ - a ketone, carboxylic acid, and an isocyanide - reacting in one-pot to generate an α-acyloxy carboxamide intermediate.[422] The three-component Passerini reaction (Passerini 3-CR) has captured the special attention of both academic and industrial scientists due to the carbenic reactivity of isocyanides lead to the quick and easy synthesis of a larger variety of multifunctional products with excellent yields, at or below room temperature.[423] For instance, Meier and co-workers reported the divergent synthesis of a

variety of functional monomers such as tuneable acrylate monomers[424], AB-type monomers bearing carboxylic acid and aldehyde moieties[425], as well as asymmetric α,ω-dienes containing an acrylate and a terminal olefin[426]. Such monomers were then directly polymerized in a polyaddition approach applying the Passerini 3-CR for the formation of sequence-controlled and high-molecular-weight polymers with different side chains.[425-427] In other studies, it was described that the Passerini 3-CR was successfully used as an efficient approach for the divergent[428] and convergent[429] synthesis of well-designed dendrimers. In addition, Söyler *et. al.* has recently reported the successful surface modification of succinylated cellulose by employing small molecular model of Passerini components under mild conditions.[430]

We are interested in the application of the Passerini 3-CR as a versatile approach to covalently tether a series of synthesized polymers onto cellulose nanofibers (CNFs) in aqueous condition at the ambient temperature. This has been achieved *via* the design of polymers with aldehyde end group functionality, which can be easily obtained using functional RAFT agents. The underpinning idea was demonstrated here using poly(*N*-isopropylacrylamide) PNIPAm as a model polymer. an extensively studied thermo-responsive hydrophilic polymer, which can undergo phase transition from a soluble to an insoluble state (coil-to-globule) in aqueous solution at its lower critical solution temperature (LCST) of approximately 32 °C.[431] The structural changes and their LCST value close to physiological temperature are desired for various fields, especially biomedical applications.[432, 433] A range of thermo-responsive nanoparticles, including polymer-protein conjugates[434] and PNIPAm hydrogel[435], has been described in the literature for drug delivery purposes to release therapeutics upon temperature variations within the body. In the case of cellulose, Porsh *et. al.* reported the designing of thermo-responsive cellulose particles by grafting copolymers of) oligo(ethylene glycol) methyl ether methacrylate ($OEGMA_{300}$) and di(ethylene glycol) methyl ether methacrylate (DEGMA from hydroxylpropyl cellulose *via* surface-initiated ARGET ATRP. [436] Recently, Hufendiek and co-workers elegantly showed that the successful synthesis of temperature-responsive cellulose by photochemically grafting maleimide endcapped poly(*N*-isopropylacrylamide) PNIPAm-maleimide to cellulose-tetrazole.[437]

In this work, we demonstrated the preparation of thermo-responsive CNFs by chemically grafting PNIPAm onto TEMPO-oxidized cellulose nanofibers (CNFs) *via* Passerini reaction. The three components involved in this reaction are CNFs with carboxylic acid moieties (CNFs-COOH), a PNIPAm with aldehyde end functionality (PNIPAm-COH) synthesized *via* Reversible Addition-Fragmentation Chain-Transfer (RAFT) polymerization technique, and a cyclohexyl isocyanide. The efficiency of the surface modification approach, and the properties, especially structural integrity and thermal tunability, of the grafted products (PNIPAm-*g*-CNFs) were confirmed *via* various analytical techniques including XRD, TGA, AFM and turbidimetry. The overall experimental procedure is illustrated in **Scheme 5.2**.

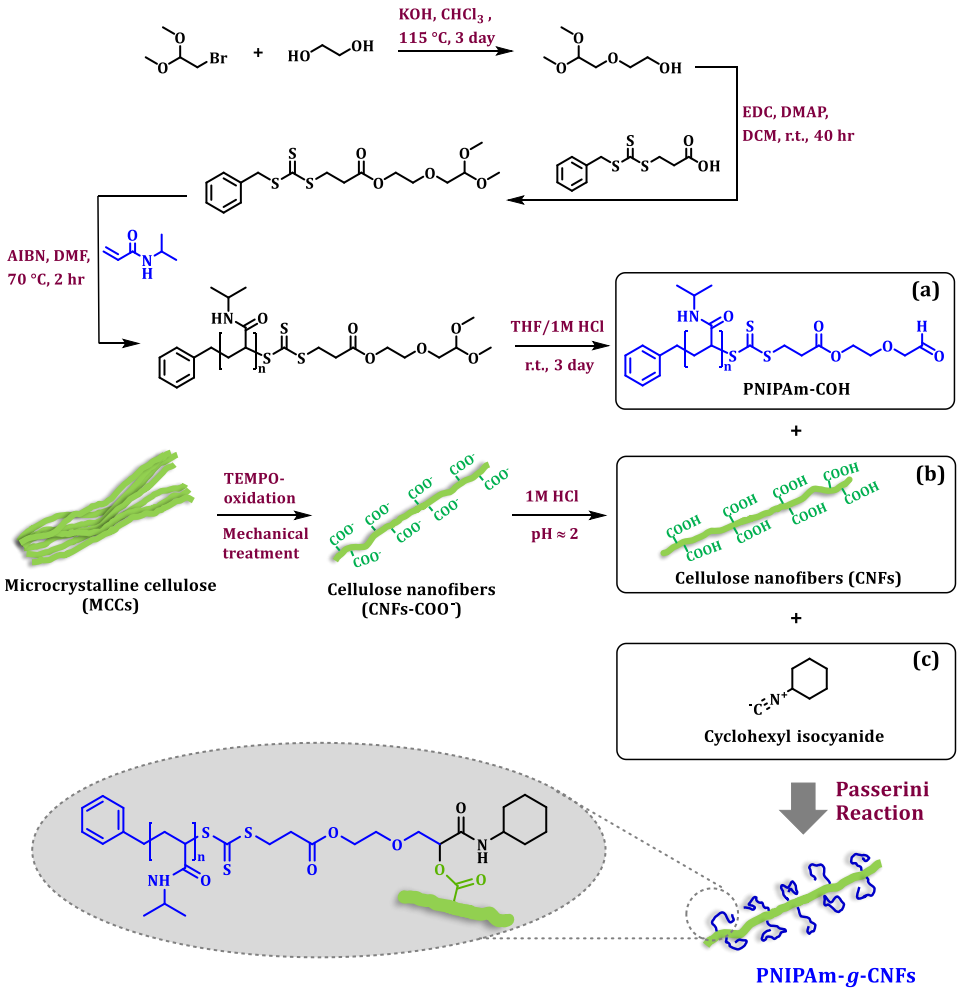

Scheme 5.2. Schematic illustration of the synthesis of polymer-grafted cellulose fibrils (PNIPAm-*g*-CNFs) *via* Passerini 3-CR using PNIPAm-COH (a), TEMPO-oxidized cellulose fibrils carrying acid groups (CNFs-COOH) (b), and cyclohexyl isocyanide (c) reacted in water at ambient temperature.

5.3. Results and Discussions

5.3.1. Synthesis of aldehyde-terminated RAFT agent

Most polymer grafting strategies require organic solvent or pre-treatment of cellulose nanomaterials with functional groups. Here we aim to employ the three-component Passerini reaction as an attractive technique to directly functionalize cellulose nanofibers (CNFs) using the aqueous CNFs gel in a one-pot process without any requirement of solvent switching procedure. In this process, polymers with aldehyde groups are directly reacted with TEMPO-oxidized CNFs bearing acid moieties.[73] The resulting grafted CNFs were expected to be well-dispersed in water and therefore suitable for drug delivery.

In order to fulfil this aim, CNFs bearing carboxylic acid functionalities were firstly prepared *via* mechanically assisted TEMPO-mediated oxidation combined with acid treatment according to the procedure discussed in **Chapter 3**. The next step was the synthesis of the functional RAFT-agent carrying aldehyde moiety. BSPA (3-benzylsulfanylthiocarbonylsulfanylpropionic acid), a common type of RAFT-agent bearing carboxylic acid moiety was synthesized according to the procedure as described previously in the literature.[438] The BSPA RAFT agent was then converted to protected aldehyde group *via* two-step procedure. The synthesis was started with the preparation of 2-(2,2-dimethoxy-ethoxy)-ethanol by a substitution reaction of commercially available reagents: ethylene glycol and bromoacetaldehyde dimethyl acetal. After purifying the crude by extraction with chloroform and water for 5 times, the resulting product was dried and characterized by ^{1}H-NMR, where the signals at 4.50 ppm and 3.37 ppm are corresponding to the protons from acetal group: C*H*(OCH_3)$_2$ and (OCH_3)$_2$. The methylene protons (-CH_2OH, - CH_2OCH_2, -CHCH_2O-) appeared in the range of 3.69 – 3.52 ppm, and the proton from O*H* appeared at 2.86 ppm (**Figure 5.1**). Then the RAFT agent was subsequently synthesized by reacting the 2-(2,2-dimethoxy-ethoxy)-ethanol with BSPA *via* EDC/DMAP coupling technique in anhydrous DCM under ambient temperature. The yellow viscous oil was purified by extraction with water, followed by silica gel chromatography, and characterised by ^{1}H-NMR analysis. According to **Figure 5.2**, the successful synthesis of triothiocarbonate RAFT agent with acetal protecting group can be confirmed by the

acetal peak at 3.27 ppm (6H, $(OCH_3)_2$) and aromatic protons appearing at 7.45 – 7.24 ppm (5H, C*H*phenyl). The intensity of acetal peak had a reasonably good agreement with the signals corresponding to the rest of the molecule.

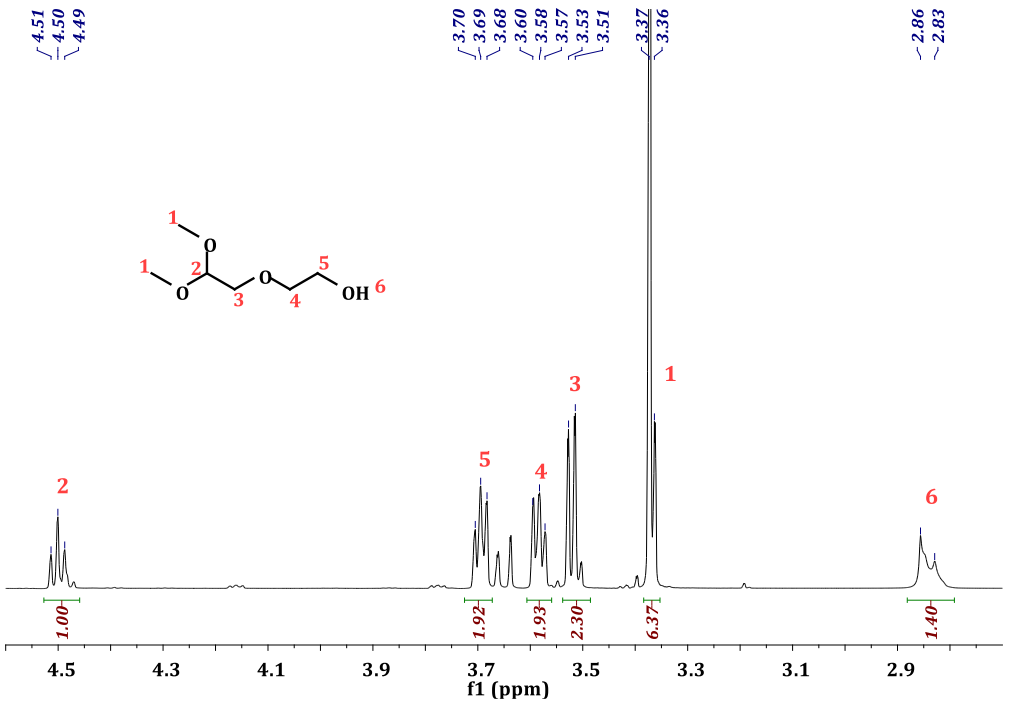

Figure 5.1. ^{1}H-NMR spectrum of 2-(2,2-dimethoxy-ethoxy)-ethanol in $CDCl_3$.

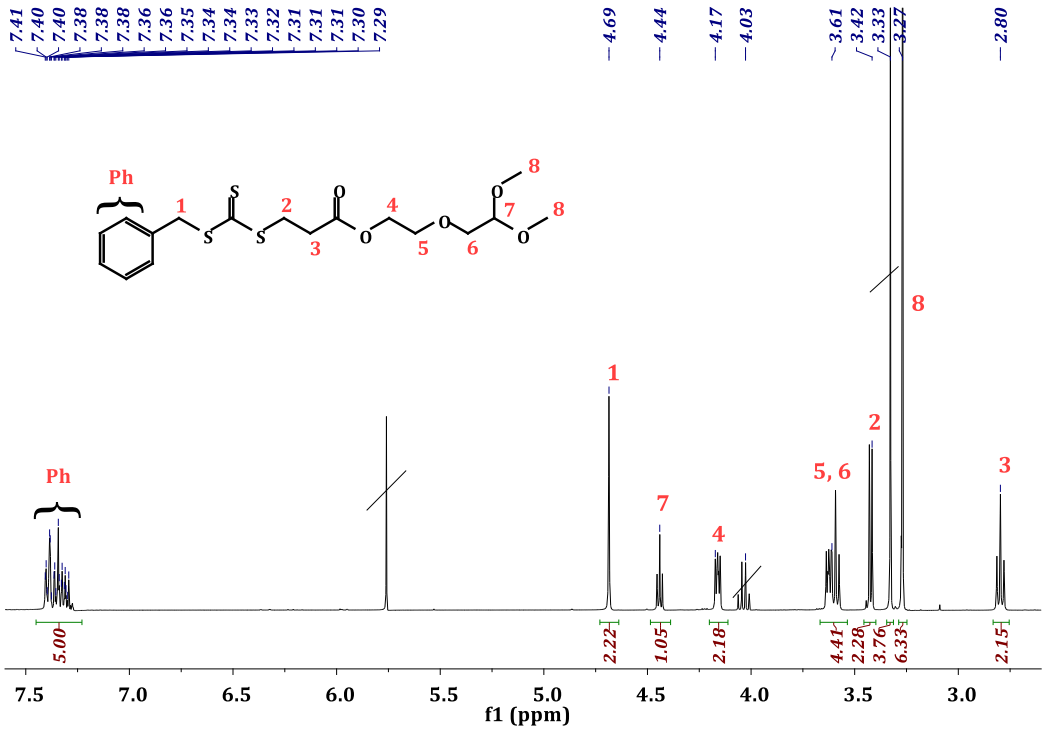

Figure 5.2. ^{1}H-NMR spectrum of 2-(2,2-dimethoxy-ethoxy)ethyl [3(benzylthiocarbonothioylthio)propanoate] (trithio RAFT-acetal) in DMSO-d_6.

5.3.2. Synthesis of PNIPAm homopolymer bearing aldehyde end group

Firstly, poly(*N*-isopropylacrylamide) PNIPAm carrying acetal/protected aldehyde end functionality was synthesized *via* Reversible Addition-Fragmentation Chain-Transfer (RAFT) polymerization. The RAFT agent (RAFT-acetal) was subsequently employed to prepare a set of five PNIPAm polymers with different lengths (DP_n = 12, 66, 89, 108 and 158), which were then employed to investigate the influence of the reaction time and the molecular weight on the success of the Passerini reaction. The readers are referred to **Table 5.3** for the experimental conditions especially the ratio between monomer (NIPAm), RAFT agent and initiator (AIBN) for all polymer syntheses. The number-average degree of polymerization (DP_n) was determined by ^{1}H-NMR by comparing the integration of the signal at 4.08 ppm (NH from residual monomer) to that at 3.93 ppm (NH from polymer). Moreover, according to the ^{1}H-NMR of pure product by dialysis against methanol, the proton peak at 3.42 ppm confirmed the existence of acetal (protected aldehyde) end group on the polymer chain (**Figure 5.4 a**). Furthermore, SEC traces revealed a narrow molecular weight distribution (*Đ*) below 1.2 for all polymers confirming that the polymerization took place in a well-controlled manner (**Figure 5.3 and Table 5.1**).

Table 5.1. Properties of synthesized PNIPAm-acetals obtained from ^{1}H-NMR and SEC analyses.

Sample name	Conversion (%)	Degree of polymerization (DP_n)	$M_{n(theo)}$ (g mol^{-1})	$M_{n\ (SEC)}$ (g mol^{-1})	*Đ*
$PNIPAm_{12}$	61	12	1800	3600	1.16
$PNIPAm_{66}$	66	66	7900	14000	1.14
$PNIPAm_{89}$	89	89	10500	17900	1.15
$PNIPAm_{108}$	54	108	12600	21900	1.13
$PNIPAm_{158}$	79	158	18300	29200	1.18

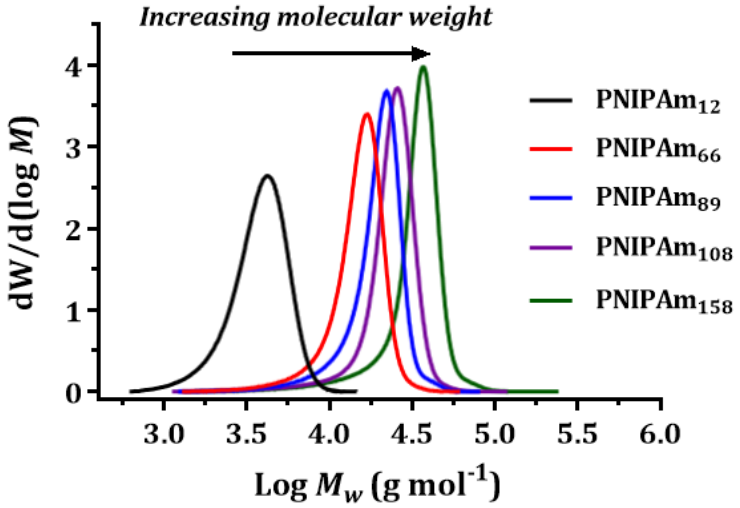

Figure 5.3. SEC traces of a library of synthesized PNIPAm-acetal with different chain lengths.

The aldehyde end-functionality of PNIPAm was subsequently liberated in 1 M HCl in THF. According to ^{1}H-NMR shown in **Figure 5.4**, the decreasing intensity of the peak at 3.42 ppm correspond to the dimethyl acetal group as well as the appearance of a peak at 9.74 ppm confirmed the successful synthesis of PNIPAm carrying an aldehyde end functionality (PNIPAm-COH).

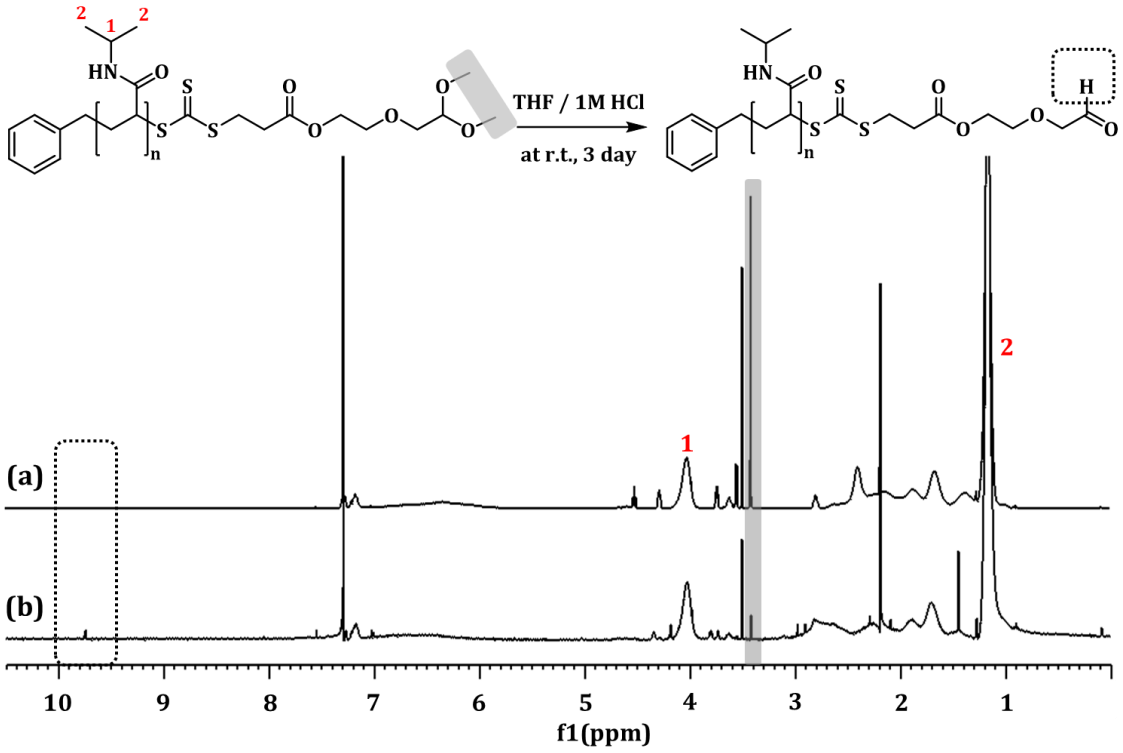

Figure 5.4. Sample ^{1}H-NMR spectra of PNIPAm$_{12}$ (I) **(a)** before deprotection (PNIPAm-acetal) and **(b)** after deprotection (PNIPAm-COH) in $CDCl_3$.

5.3.3. Determination of the feasibility of three-component Passerini reaction (Passerini 3-CR) *via* ^{1}H-NMR and UV-Vis analyses

Surface modification of CNFs with the synthesized PNIPAm was carried out *via* three-component Passerini reaction (Passerini 3-CR) in aqueous media at ambient temperature. In order to determine the efficiency and suitability of the reaction conditions, a test experiment was carried out using a small molecule model based on PNIPAm$_{12}$-COH (**Table 5.1**), methacrylic acid as an acid component and cyclohexyl isocyanide employing similar reaction condition to the following reaction with CNFs. According to the ^{1}H-NMR (**Figure 5.5**), the complete disappearance of aldehyde peak at 9.74 ppm and the appearance of a peak at around 5.4 ppm, as a result of the formation of a new product, was observed after 2 days. As dialysis was employed for purification, the yield of the pure product was calculated to be almost 100 %. This approach is desirable as 56 % of aldehyde was reacted within 30 min, which was calculated by comparing the aldehyde peak at 9.74 ppm before and after reaction.

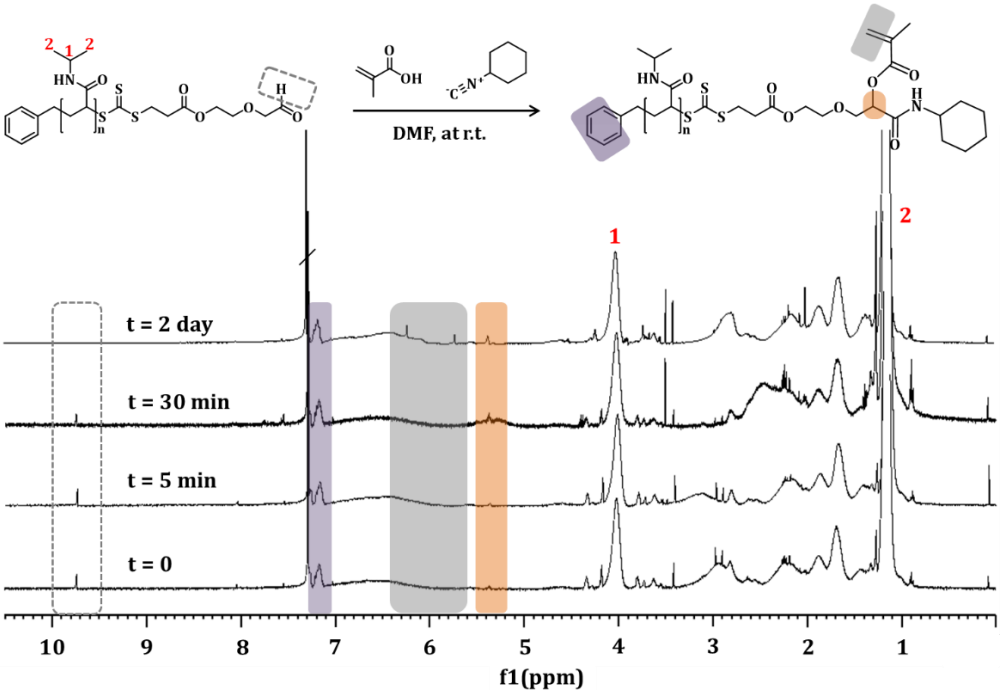

Figure 5.5. ^{1}H-NMR spectra of purified PNIPAm$_{12}$-COH reacted with methacrylic acid and cyclohexyl isocyanide *via* Passerini reaction at different time intervals. The spectra were recorded in $CDCl_3$.

At the same time, the thiocarbonyl group of the RAFT polymer was found to be stable as evidenced by UV-Vis absorption at 310 nm, which was measured in

DMSO and remained unchanged even after 2 days of reaction (**Figure 5.6**). The stability of the RAFT end functionality under these conditions is not only of interest for further surface analysis, but it can also be used as UV-Vis active marker to quantify the amount of polymer grafted onto CNFs.

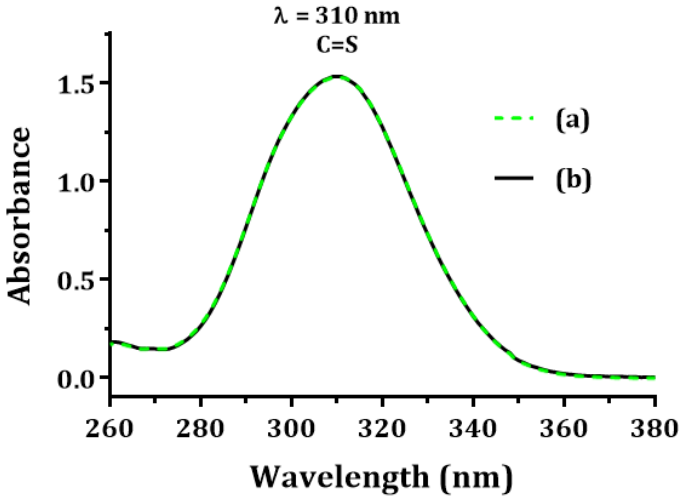

Figure 5.6. RAFT stability *via* UV-Vis analysis of **(a)** PNIPAm$_{12}$-COH and **(b)** PNIPAm after reacted with methacrylic acid and cyclohexyl isocyanide *via* Passerini reaction. The spectra were recorded in DMSO. The same concentration was used for both samples.

5.3.4. Grafting PNIPAm onto CNFs *via* Passerini 3-CR

Grafting efficiency vs time

After confirming the feasibility of this one-pot three-component reaction under mild reaction condition, the surface functionalization of CNFs was carried out at ambient temperature. Initially, PNIPAm$_{89}$-COH (**Table 5.1**) was employed and the grafting efficiency at different time intervals (t = 0.5 hr, 2 hr, 4 hr, 6 hr, and 24 hr) was monitored by UV-Vis analysis using the RAFT end group. As shown in **Figure 5.7 and 5.8**, the successful surface modification was confirmed by the strong absorbance value at 305 nm due to the $\pi \rightarrow \pi^*$ transition of the C=S bonds of the RAFT polymer.[439] As the model reaction showed that the RAFT functionality is intact under Passerini reaction conditions, the UV-Vis active RAFT end group could be employed as a direct indicator of the amount of polymer on the surface. In order to ensure that the detected polymer was attached to the CNFs and not just adsorbed, all samples were extensively purified by precipitation in ethyl acetate 6 times, followed by dialysis

against water for one day. UV-Vis spectroscopy was subsequently used to determine the percent grafting efficiency and calculated by comparing the amount of grafted polymers to the amount of initially added polymers (the standard curve of PNIPAm$_{89}$-COH can be found in **Figure 5.21**). The increasing absorbance of the purified product indicates PNIPAm reacted swiftly in the first 30 min, followed by a constant growth over 24 hr. The slower conversion rate from 6 hr to 24 hr was expected, and less polymer will gain access to the carboxylic acid groups on the surface. The grafting efficiency was calculated to be 36 % at 0.5 hr and 57 % at 24 hr. **Figure 5.9** depicts the increased dispersibility of PNIPAm$_{89}$-*g*-CNFs in water after 30 min of reaction time compared to unmodified CNFs, indicating that the amount of polymer grafted within short period of time was sufficient to help the dispersion of nanoparticles well in water.

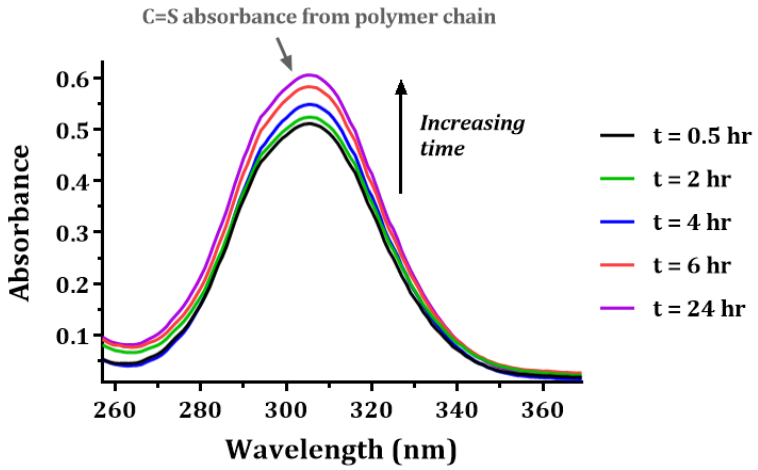

Figure 5.7. UV-Vis analysis of PNIPAm$_{89}$-*g*-CNFs *via* Passerini 3-CR at different time intervals. Spectra were recorded in milli-Q water at the concentration of 1 mg mL^{-1}.

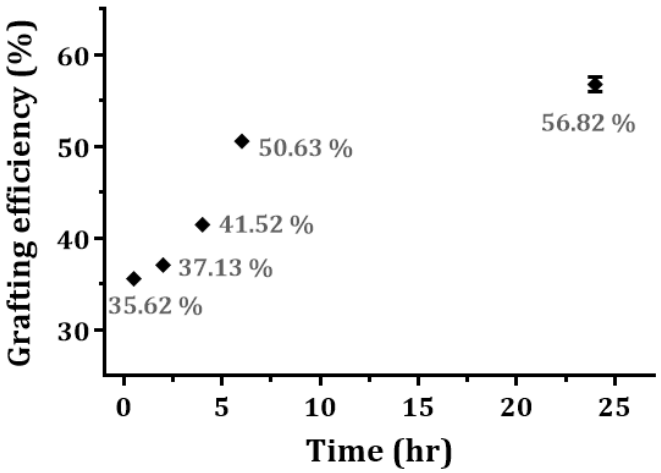

Figure 5.8. Grafting efficiency of PNIPAm$_{89}$-*g*-CNFs *vs* reaction time.

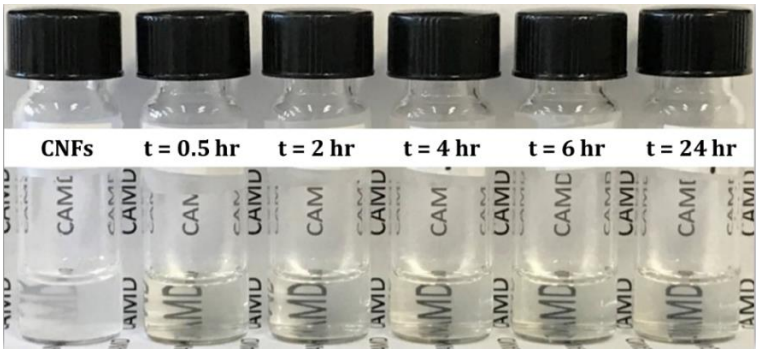

Figure 5.9. Dispersibility tests of PNIPAm$_{89}$-*g*-CNFs reacted at different time intervals. Concentration of CNFs = 1 mg mL^{-1} in milli-Q water.

Although the growth of the amount of polymer on the surface is evident, it is possible that adsorbed polymer remains on the surface despite several washing and dialysis steps. To explore this in more detail, a control experiment was carried out by incubating PNIPAm$_{89}$-COH (**Table 5.1**) and CNFs with or without (control) isocyanide for one day. Following the reaction or incubation, both samples were purified by precipitation, dialysis, and lyophilization as mentioned earlier. ^{1}H-NMR spectroscopy of PNIPAm-*g*-CNFs (prepared *via* Passerini 3-CR) was recorded in D_2O revealing the characteristic peaks at δ = 2.29 - 0.75 ppm and δ = 3.83 ppm corresponding to the protons from PNIPAm (**Figure 5.10**). While the existence of polymers on the surface was clearly visible, the signals corresponding to cellulose at 5 - 3 ppm are suppressed. Here, ^{1}H-NMR of the control sample was not possible to record as the isolated CNFs after incubation with PNIPAm-COH showed only limited solubility in aqueous and organic media, indicative of only a negligible amount of PNIPAm on the surface.

Analysis in the solid state as with FT-IR allowed for a better insight. As depicted in **Figure 5.11**, it was observed that PNIPAm$_{89}$-*g*-CNFs gave new peaks in the IR spectrum that correspond to the amide stretch at 1650 cm^{-1} and amide bend at 1541 cm^{-1} of PNIPAm, indicating the successful surface modification. In contrast, the percentage of adsorbed polymer in the control sample was significantly lower, indicating some polymer chain attachment to the surface of CNFs.

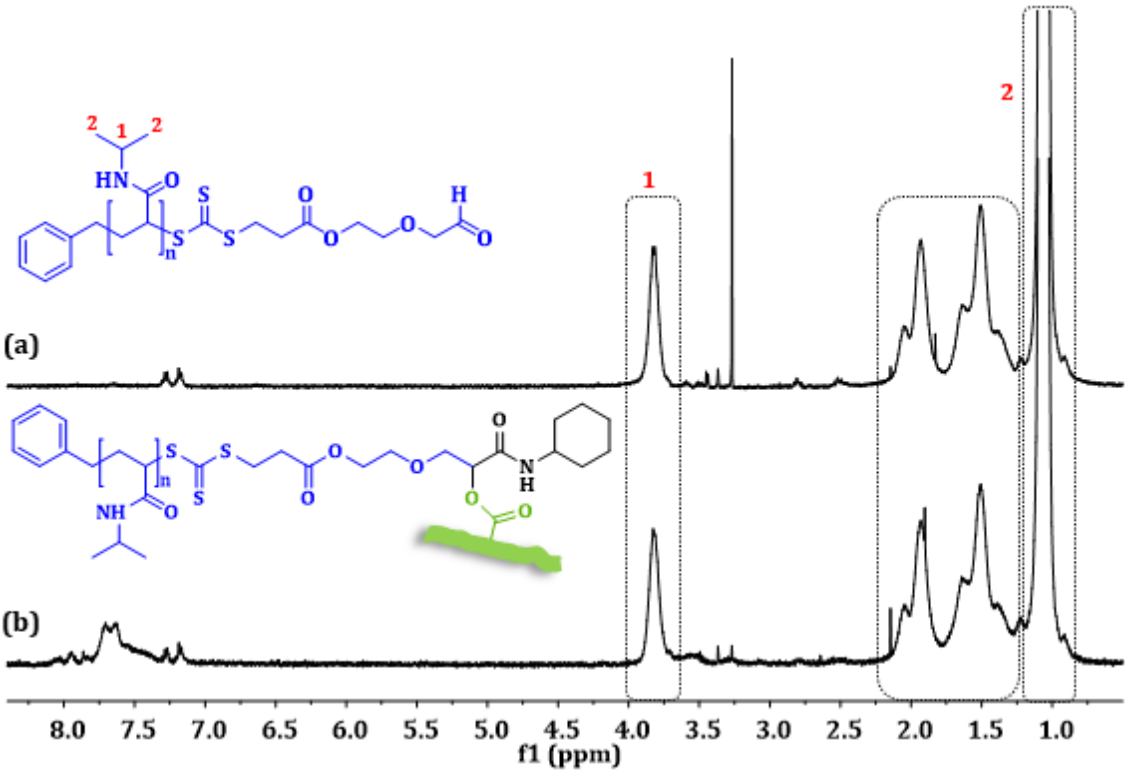

Figure 5.10. (a) ^{1}H-NMR spectra of PNIPAm$_{89}$-COH and **(b)** PNIPAm$_{89}$-*g*-CNFs prepared *via* Passerini 3-CR. The spectra were recorded in D_2O.

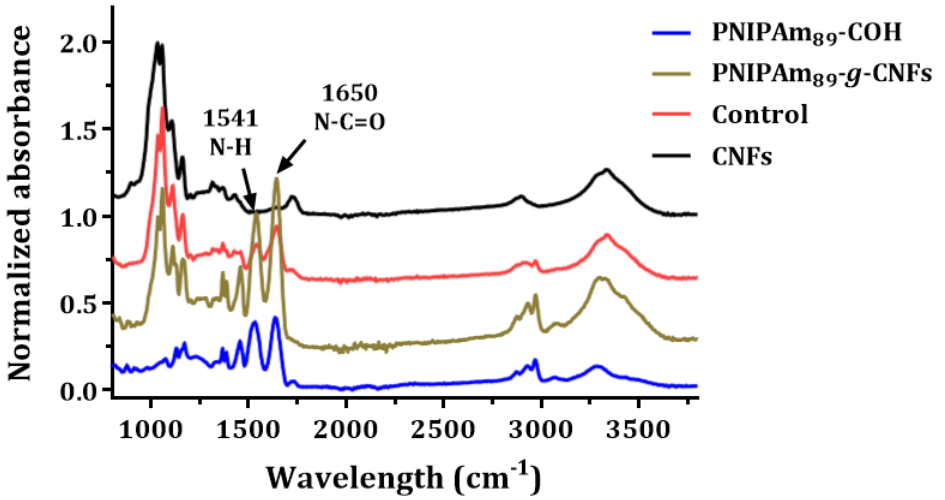

Figure 5.11. FT-IR spectra of CNFs, control sample, PNIPAm$_{89}$-*g*-CNFs, and PNIPAm$_{89}$-COH.

Surface chemistry of modified CNFs

To better understand the surface chemistry of CNFs, UV-Vis analysis was conducted as this allowed analysis at lower concentrations compared to NMR (**Figure 5.12**). Even though both samples showed the appearance of absorption bands at 305 nm indicating the existence of polymers, the absorbance value of control sample was much weaker than that of PNIPAm$_{89}$-*g*-CNFs (**Figure 5.12**), which is in agreement with the FT-IR results. It can be concluded that a small fraction of polymer was adsorbed onto the surface of CNFs *via* physical adsorption. However, in this case, the cellulose nanofibrils were insoluble in water. This was confirmed by performing solubility tests on both substrates, i.e. PNIPAm$_{89}$-*g*-CNFs and a control sample prepared by mixing CNFs and PNIPAm$_{89}$-COH. The former resulted in a clear solution, while the latter resulted in a turbid solution (**Figure 5.13**).

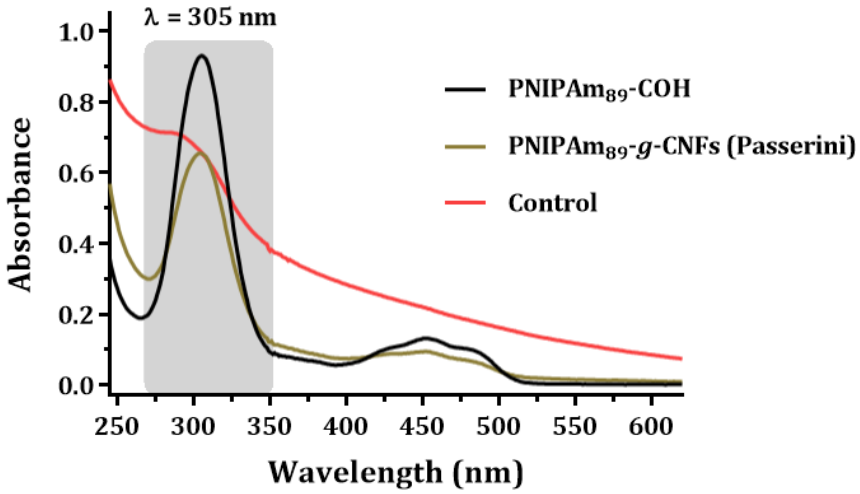

Figure 5.12. UV-Vis analyses of PNIPAm$_{89}$-COH (III), PNIPAm$_{89}$-*g*-CNFs and control sample. The spectra are recorded in milli-Q water.

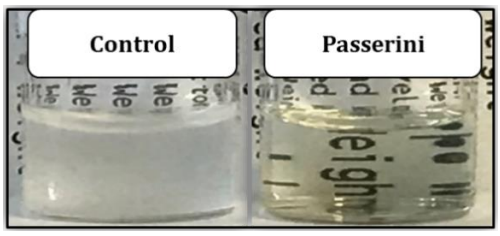

Figure 5.13. Dispersibility tests of control sample and PNIPAm$_{89}$-*g*-CNFs prepared *via* Passerini reaction. The same concentration of CNF in milli-Q water (1 mg mL^{-1}) was used for both samples.

DLS analysis in neutral aqueous condition showed an increase in hydrodynamic diameter from 126 nm for CNFs to 215 nm for PNIPAm$_{89}$-*g*-CNFs with a narrow size distribution (PDI = 0.2) (**Figure 5.14**). In contrast, the control sample contained large particles in dispersion. In light of these, it can be concluded that the polymer chains were indeed successfully attached onto CNFs mainly *via* chemical binding, contributing to an improved aqueous dispersibility *via* steric stabilization.

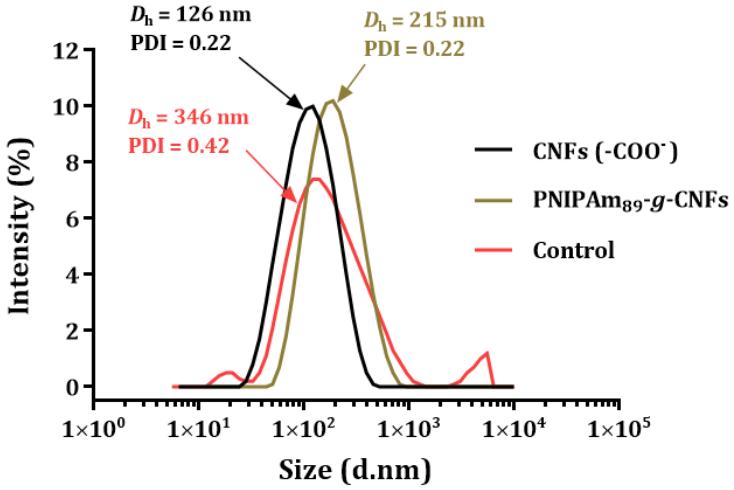

Figure 5.14. DLS measurements of CNFs (-COO$^-$), PNIPAm$_{89}$-*g*-CNFs and the control sample at the concentration of 1 mg mL^{-1} in milli-Q water.

Structural integrity of modified CNFs

Encouraged by the surface modification results, the effect of surface grafting towards the morphology of nanoparticles was studied by AFM. The AFM images displayed in **Figure 5.15** confirm the attachment of polymers on the surface of CNFs. The structural and morphological integrity of cellulose nanofibers did not appear to be affected by the surface modification nor by the grafted polymers.

The structural integrity of unmodified (CNFs) and modified (PNIPAm$_{89}$-*g*-CNFs, t = 24 hr) cellulose nanomaterials were further confirmed by XRD (**Figure 5.16**). The unmodified sample was crystalline in nature as evidenced by the peaks at 2θ = 17.91° (1 1 0), 26.59° (2 0 0), and 40.87°. After grafting, a broad halo between the (1 1 0) and (2 0 0) plane appears suggesting the presence of amorphous polymers. The crystallinity index (CI) of the cellulose was calculated by comparing the intensity of the (2 0 0) peak (I_{200}, 2θ = 26.59°) and the intensity between the (2 0 0)

and (1 1 0) peaks (I_{AM}, 2θ = 21.98°).[350] The result shows that the crystallinity decreased from 56 % to 26 % after surface grafting, which was most likely due to the addition of amorphous polymers. However, the performed surface modification still preserved the crystallinity to a large extent. This result is in contrast to previous finding by Biswal *at el.*, which described a loss in crystallinity of cellulose after grafting polymers onto the surface due to disruption of the original ordered structure.[440] Hence, it could be insisted that functional cellulose nanoparticles with intact morphology and crystal integrity were obtained by surface modification with PNIPAm *via* Passerini 3-CR. In addition, the formed bond between cellulose and polymer was observed to be stable even at low pH as evidenced by the dispersibility study at pH 3.6 (**Figure 5.16**, pictures).

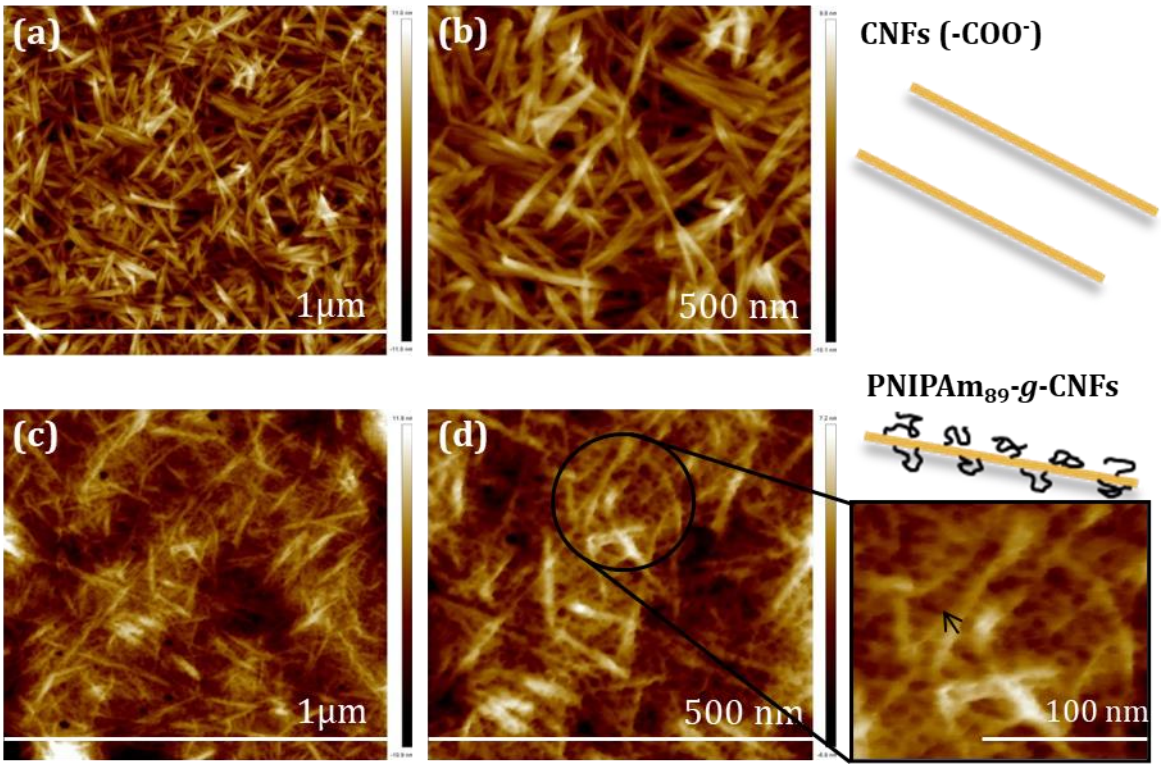

Figure 5.15. AFM images of TEMPO-oxidized CNFs (-COO^-) **(a)** and **(b)**. AFM images of $PNIPAm_{89}$-*g*-CNFs (III, t = 24 hr) **(c)** and **(d)**. The pictures were taken in low and high magnifications and the black arrows indicate the presence of polymer chains in the dried state.

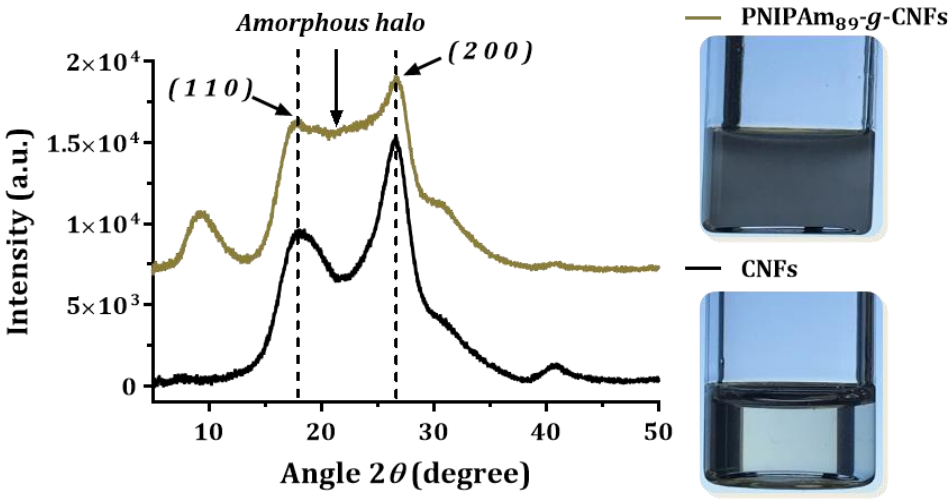

Figure 5.16. X-ray diffractograms of CNFs and PNIPAm$_{89}$-*g*-CNFs (t = 24 hr) (left) and the aqueous dispersibility of CNFs and PNIPAm$_{89}$-*g*-CNFs at pH 3.6 (right).

Influence of PNIPAm chain length on grafting efficiency and thermal behaviour of PNIPAm-g-CNFs

In the next step, the effect of the molecular weight of PNIPAm on the grafting efficiency was studied. CNFs were modified with synthesized PNIPAm with different chain lengths (PNIPAm$_{66}$-COH, PNIPAm$_{108}$-COH and PNIPAm$_{158}$-COH, **Table 5.1**). The UV-Vis analysis depicted in **Figure 5.17** shows the decreased presence of RAFT end groups belonging to grafted chains. This is caused by increasing molecular weight of PNIPAm and a lower amount of polymers tethered to the surface. The amount of grafted polymers (PNIPAm$_{66}$, PNIPAm$_{108}$ or PNIPAm$_{158}$) was differentiated according to the molarity and weight percentage: PNIPAm$_{66}$ (5.2×10^{-5} M, 0.04 wt %), PNIPAm$_{108}$ (4.0×10^{-5} M, 0.05 wt %) and pNIPAm$_{158}$ (3.0×10^{-5} M, 0.06 wt %). Taking into account, the molecular weight and the amount of tethered chains calculated from the UV-Vis absorption (the standard curves of polymers can be found in **Figure 5.22**), the relationship between grafting efficiency and molecular weight can be elucidated (**Figure 5.18**). Again, significantly improved dispersibility at CNFs concentrations of 1 mg mL^{-1} was observed for all grafted cellulose in water, as evidence of the covalent grafting of polymers on CNFs (**Figure 5.19**). The LCST behaviour of all grafted samples in water (concentration = 10 mg mL^{-1}) was investigated by increasing the temperature from 25 to 40 °C. Due to a coil-to-globule transformation of PNIPAm, the solution turned turbid at the cloud point (≈ at 30 °C) as

depicted in **Figure 5.20**. It was found that the cloud point was not strongly influenced by changing the molecular weight of grafted polymers. This finding is in agreement with the previous predictions reported in the literature.[441]

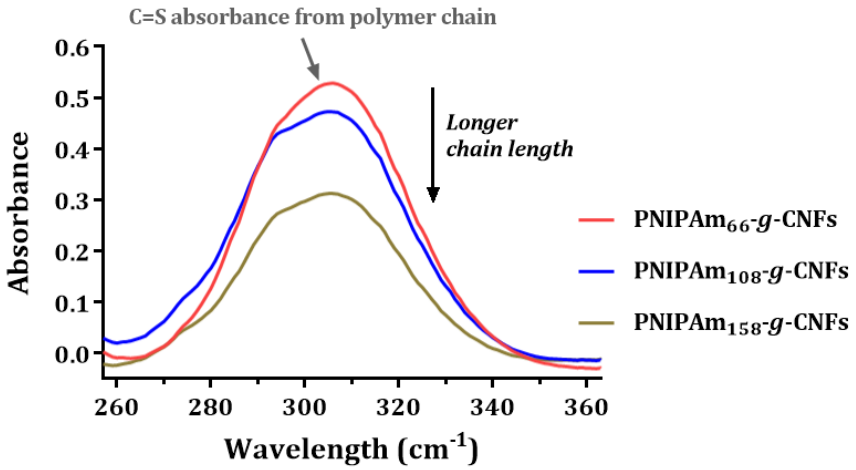

Figure 5.17. UV-Vis spectra of PNIPAm-*g*-CNFs after surface grafting for 30 min. Concentration of nanoparticles in milli-Q water = 1 mg mL^{-1}.

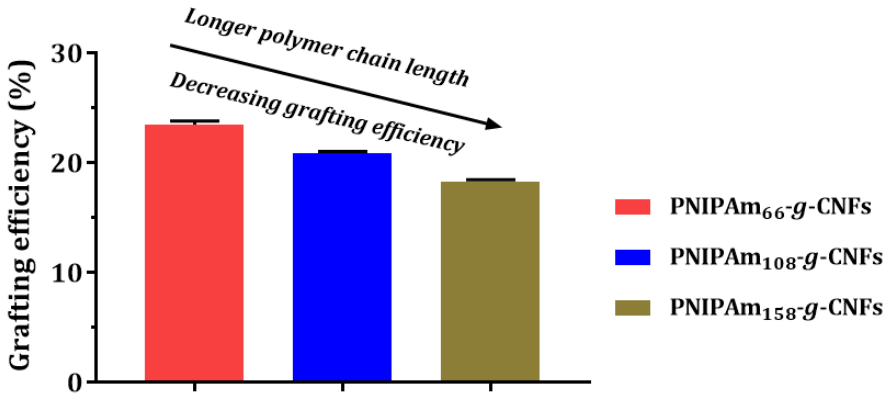

Figure 5.18. Grafting efficiency of PNIPAm-*g*-CNFs depending on the chain length of grafted polymers.

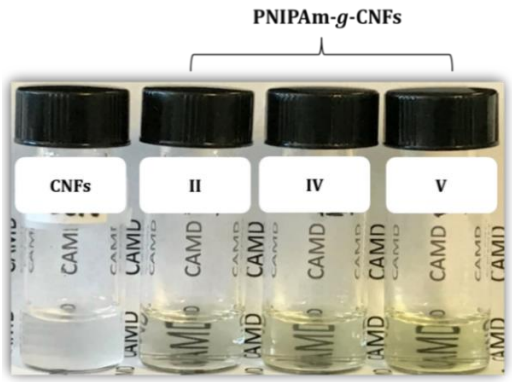

Figure 5.19. Aqueous dispersibility tests of CNFs and PNIPAm-*g*-CNFs (II, IV, V) (1 mg mL^{-1} of CNFs). Samples II, IV and V stand for PNIPAm$_{66}$-*g*-CNFs, PNIPAm$_{108}$-*g*-CNFs and PNIPAm$_{158}$-*g*-CNFs.

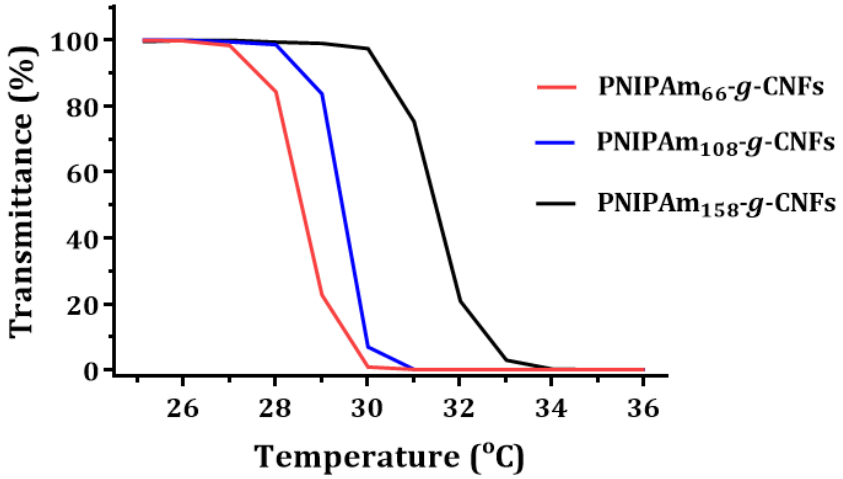

Figure 5.20. LCST behaviour of PNIPAm$_{66}$-*g*-CNFs, PNIPAm$_{108}$-*g*-CNFs and PNIPAm$_{158}$-*g*-CNFs. Heating rate = 1 °C min^{-1}.

Next, TGA measurement was performed to analyse the thermal properties of all prepared PNIPAm-*g*-CNFs samples (**Figure 5.21**). In this experiment, 10 mg of freeze-dried samples were heated from 25 – 700 °C at the heating rate of 10 °C min^{-1} in air. The initial weight loss at 25 – 100 °C is due to the evaporation of absorbed water in the material. In case of PNIPAm$_{66}$-*g*-CNFs, enhanced thermal stability was observed as compared to CNFs. In addition to this, the thermal stability of nanoparticles was obviously influenced by the chain length of grafted polymers as the thermal decomposition temperature at 50 % mass loss of PNIPAm-*g*-CNFs increased with the chain length of PNIPAm. All thermal properties of the samples are summarized in **Table 5.2**.

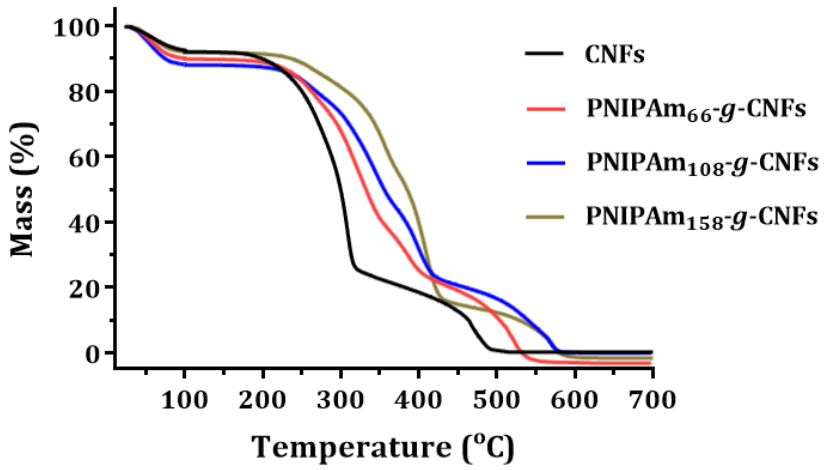

Figure 5.21. TGA curves of CNFs before and after surface grafting with PNIPAm *via* Passerini reaction.

Table 5.2. Thermal properties of CNFs before and after surface grafting with PNIPAm.

Sample name	T_d for 50 % of mass loss (°C)	T_{cp} (°C)
CNFs	295	-
PNIPAm$_{66}$-*g*-CNFs	321	28.6
PNIPAm$_{108}$-*g*-CNFs	344	29.4
PNIPAm$_{158}$-*g*-CNFs	373	31.5

T_d = thermal decomposition temperature, T_{cp} = cloud point temperature

Standard curves

The standard curves of all PNIPAm-COH samples used for the calculation of the grafting efficiency of PNIPAm-*g*-CNFs are presented in **Figure 5.21**. The standard curves were plotted according to the UV-Vis absorbances of all synthesized polymers.

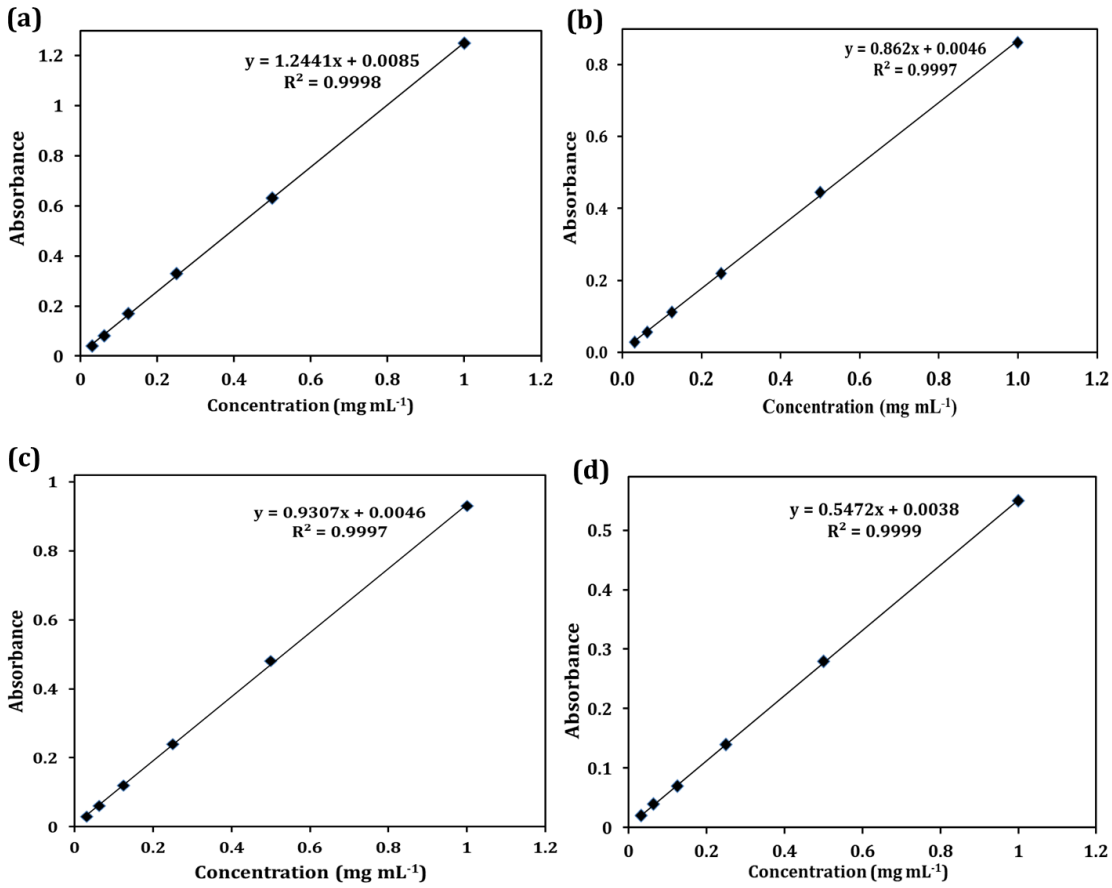

Figure 5.22. Standards curves of polymers obtained from UV-Vis analysis: **(a)** PNIPAm$_{66}$-COH, **(b)** PNIPAm$_{89}$-COH, **(c)** PNIPAm$_{108}$-COH, **(d)** PNIPAm$_{158}$-COH.

5.4. Conclusions

In summary, Paseerini reaction was found as an efficient approach to modify CNFs with functional polymers. Tethering PNIPAm as a model polymer on CNFs generated functional cellulose nanomaterials with thermal sensitivity and colloidal stability. Thermo-responsive nanoparticles are known promising materials for heat-triggered drug release system, while the colloidal stability of nanoparticles is essential in terms of circulation in the blood stream and avoiding the recognition by macrophages before entering the target site. To the best of our knowledge, this is the very first report of the use of three-component Passerini reaction to modify TEMPO-oxidized cellulose nanofibers (CNFs) with thermo-responsive polymers (PNIPAm). The advantage of this reaction is that it is simple and can be performed under mild condition in aqueous media without tedious solvent exchange processes. Moreover, it provided relatively high polymer grafting efficiency on CNFs within short period of time, resulting in improved aqueous dispersibility of CNFs with structural integrity. Furthermore, it is possible to prepare a large library of different polymers using the RAFT process and the shown functional RAFT agent, we applied this versatile approach for further experiments on the generation of surface modified cellulose nanomaterials for cancer immunotherapy, which will be discussed in **Chapter 6**.

5.5. Experimental Procedure

5.5.1. Synthesis of 2-(2,2-dimethoxy-ethoxy)-ethanol

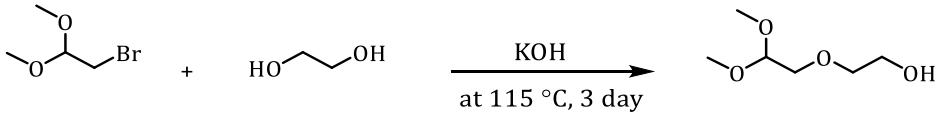

Scheme 5.3. Synthesis of 2-(2,2-dimethoxy-ethoxy)-ethanol.

The mixture of potassium hydroxide (KOH) (15.0 g, 0.27 mol) and ethylene glycol (37.5 mL) was refluxed at 115 °C under stirring. Once the KOH was completely dissolved, bromoacetaldehyde dimethyl acetal (15.6 mL, 0.13 mol) was added drop-wise over 35 min. After stirring at 115 °C for 3 days, the resulting suspension was allowed to cool to ambient temperature and diluted with 150 mL of water to dissolve the precipitated salt. The solution was then extracted with chloroform (5 × 50 mL) and dried over magnesium sulfate, followed by filtration. Finally, the solvent was removed under reduced pressure to give the desired dimethyl acetal product as a yellow viscous liquid (8.16 g).

^{1}H-NMR (400 MHz, $CDCl_3$): δ/ppm = 4.50 (1H, -C*H*$(OCH_3)_2$), 3.69 (2H, -C*H*$_2$OH), 3.58 (2H, -CH_2OCH_2-), 3.52 (2H, -CHC*H*$_2$O-), 3.37 (6H, (OC*H*$_3$)$_2$), and 2.86 ppm (1H, -CH_2OH).

5.5.2. Synthesis of 2-(2,2-dimethoxy-ethoxy) ethyl 3-(benzylthiocarbonothioylthio)propanoate [RAFT-acetal]

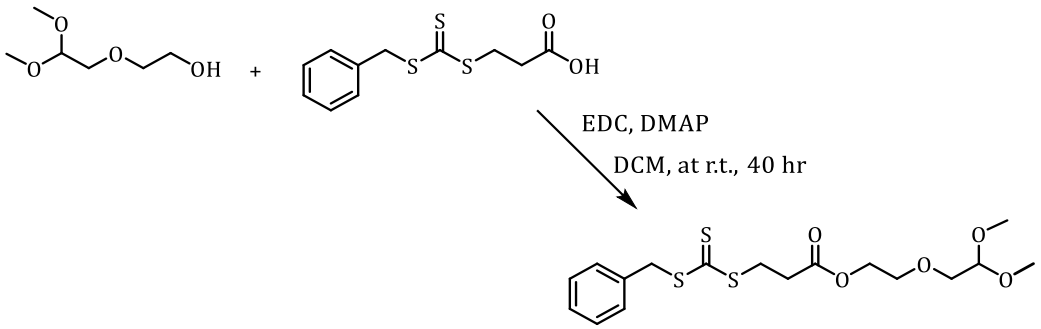

Scheme 5.4. Synthesis of chain transfer agent carrying acetal functionality (RAFT-acetal).

3-benzylsulfanylthiocarbonylsulfanylpropionic acid (BSPA) (1.5 g, 5.5 mmol) and 2-(2,2-dimethoxy-ethoxy)-ethanol (4.0 g, 26.8 mmol) was dissolved in 30 mL of anhydrous DCM and cooled to 0 °C. The mixture of *N*-(3-dimethylaminopropyl)-*N*′-ethylcarbodiimide hydrochloride (EDC.HCl) (2.8 g, 14.6 mmol) and 4-(dimethylamino)pyridine (DMAP) (0.69 g, 5.6 mmol) in 20 mL of anhydrous DCM was added to the RAFT solution dropwise. After finishing the dropwise addition, the solution was stirred at 0 °C for 2 hr and then at room temperature for 40 hr. The resulting mixture was washed several times with 50 mL of water and dried over magnesium sulfate. Solvent was then removed under reduced pressure and further purified by flash chromatography in hexane: ethyl acetate (1: 1). After removing organic solvent, final product was obtained as a yellow viscous liquid (1.16 g).

^{1}H-NMR (400 MHz, $CDCl_3$): δ/ppm = 7.45 – 7.24 (5H, C*H*phenyl), 4.67 (2H, CHphenyl C*H*$_2$-), 4.44 (1H, -C*H*$(OCH_3)_2$), 4.16 (2H, -C*H*$_2$CH$_2$O-), 3.66 – 3.55 (4H, -C*H*$_2$OC*H*$_2$-), 3.43 (2H, -C*H*$_2$CH$_2$CO-), 3.27 (6H, -(OC*H*$_3$)$_2$), and 2.80 (2H, -CH$_2$C*H*$_2$CO-).

5.5.3. Synthesis of homopolymers

Synthesis of PNIPAm carrying acetal (protected aldehyde) end functionality via Reversible Addition-Fragmentation Chain-Transfer (RAFT) polymerization

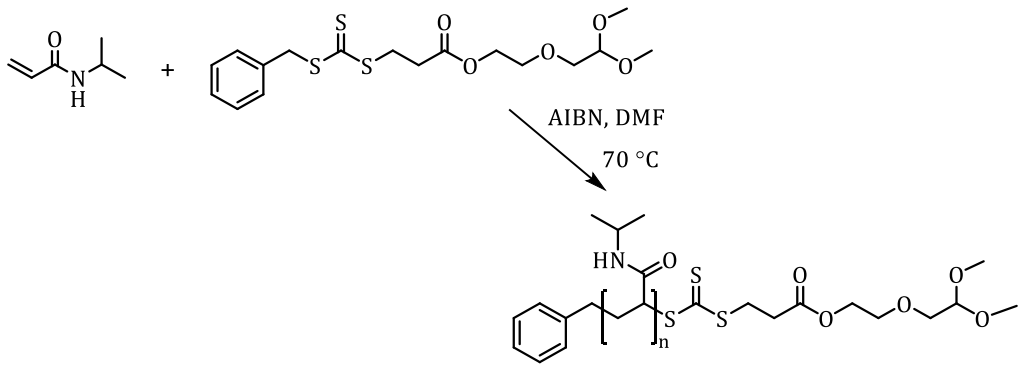

Scheme 5.5. Synthesis of PNIPAm carrying acetal functionality.

A series of PNIPAm homopolymers with five different chain lengths were synthesized *via* RAFT polymerization in *N,N*-dimethylformamide (DMF) as solvent. NIPAm and the other reagents (see **Table 5.3** for mass and concentration) were dissolved in DMF at monomer concentration of 5.89 M. The reaction mixture was added

to the glass vial equipped with a magnetic stirrer bar. The glass vial was then sealed with a rubber septum, placed in an ice bath, and deoxygenated by purging with nitrogen for 45 min. The air-tight glass vial was then immersed in an oil bath at 70 °C to start polymerization. After a desired time, the polymerization was stopped by placing the reaction mixture in an ice bath for 15 min. The monomer conversion was determined by ^{1}H-NMR in $CDCl_3$. The polymer was purified by dialysis against milli-Q water for a day, followed by dialysis against methanol for one more day using 3.5 kDa MWCO membrane (1 kDa MWCO membrane was used for the shortest polymer chain). After removal of solvent under vacuum, the molecular weight and molecular weight distribution of PNIPAm were analysed by using size exclusion chromatography (SEC).

Table 5.3. Experimental conditions for the preparation of PNIPAm-acetal with different chain lengths.

Sample name	NIPAm	RAFT-acetal	AIBN	[NIPAm]: [RAFT]: [AIBN]	Reaction time (min)
$PNIPAm_{12}$	1 g 8.84 mmol	178 mg 442 µmol	7.20 mg 44.2 µmol	20: 1: 0.1	60
$PNIPAm_{66}$	1 g 8.84 mmol	35.80 mg 88.3 µmol	1.45 mg 8.83 µmol	100: 1: 0.1	45
$PNIPAm_{89}$	1 g 8.84 mmol	35.80 mg 88.3 µmol	1.45 mg 8.83 µmol	100: 1: 0.1	120
$PNIPAm_{108}$	1 g 8.84 mmol	18 mg 44.2 µmol	0.67 mg 4.44 µmol	200: 1: 0.1	45
$PNIPAm_{158}$	1 g 8.84 mmol	18 mg 44.2 µmol	0.67 mg 4.44 µmol	200: 1: 0.1	90

Deprotection of acetal end group of PNIPAm to aldehyde (Formation of PNIPAm-COH)

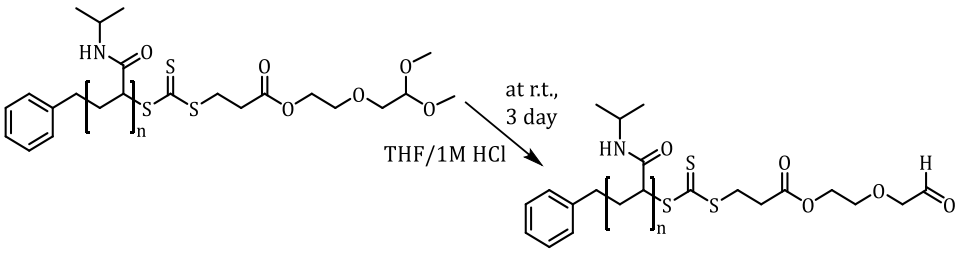

Scheme 5.6. Synthesis of PNIPAm bearing aldehyde functionality.

Deprotection for all PNIPAm-acetal samples was carried out in the mixture of tetrahydrofuran (THF) and 1 M hydrochloric acid (HCl). To describe in detail, PNIPAm-acetal (≈ 200 mg) was dissolved in the mixture of THF (3 mL) and 1 M HCl (2.5 mL), followed by being stirred for approximately 3 days at room temperature to achieve the efficient deprotection. The obtained PNIPAm-COH samples were then purified by dialysis against milli-Q water for a day and methanol for one more day, and then the solvent was removed under reduced pressure. According to ^{1}H-NMR spectra before and after deprotection, significant decrease in a peak at 3.42 ppm representing 6 H from dimethyl acetal group and appearance of a peak at 9.74 ppm representing the formation of aldehyde end group after deprotection confirm the successful synthesis of PNIPAm-COH.

5.5.4. Determination of the feasibility of three-component Passerini reaction (Passerini 3-CR) *via* ^{1}H-NMR and UV-Vis analyses

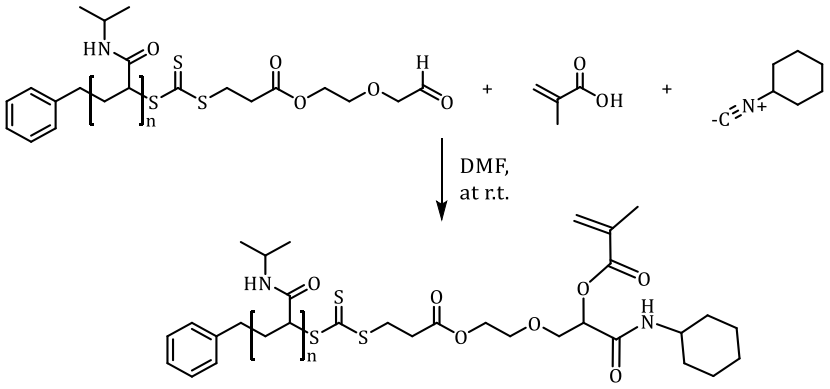

Scheme 5.7. Three component Passerini reaction between PNIPAm-COH, methacrylic acid and cyclohexyl isocyanide.

This experiment was performed using PNIPAm$_{12}$-COH and methacrylic acid as an acid component. Firstly, PNIPAm$_{12}$-COH (20 mg, 11.6 µmol) and methacrylic acid (1 mg, 11.6 µmol) were dissolved in 0.75 mL of DMF, and then cyclohexyl isocyanide (1.26 mg, 11.6 µmol) was added to the mixture. The reaction was left stirring at ambient temperature and each sample was taken out at 5 min, 30 min and 2 days. The final product was purified by dialysis against methanol for a day, and the solvent was removed under vacuum. Then the samples (PNIPAm before and after the reaction) were analysed by ^{1}H-NMR in $CDCl_3$.

5.5.5. Surface grafting *via* multicomponent Passerini reaction

Grafting PNIPAm onto CNFs via Passerini 3-CR

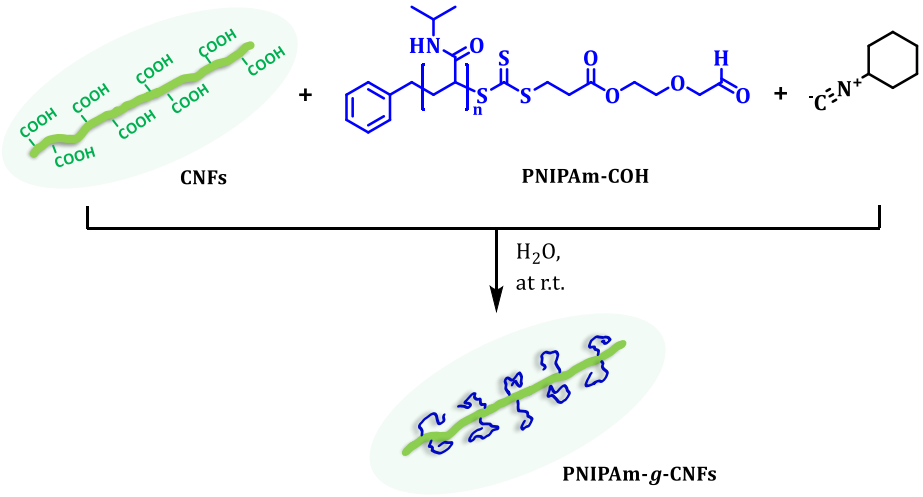

Scheme 5.8. Synthesis of PNIPAm-*g*-CNFs *via* Passerini reaction.

Grafting PNIPAm onto CNFs was carried out *via* Passerini 3-CR in milli-Q water at ambient temperature. The reaction involves CNFs, PNIPAm-COH and cyclohexyl isocyanide as shown in **Scheme 5.8**.

Grafting efficiency vs time

PNIPAm$_{89}$-COH (**Table 5.1**) was used for the analysis of grafting efficiency over time. First, a solution of PNIPAm$_{89}$-COH (367.5 mg, 35.19 µmol) in 2.2 mL of milli-Q water was added to the round-bottom flask containing 9.2 mL of CNFs gel (92 mg of dry CNFs, 151.8 µmol of -COOH). After that, cyclohexyl isocyanide (80.78 mg, 739.86 µmol) was slowly added to the CNFs dispersion while stirring. Then the mixture was continuously stirred at room temperature, followed by taking 1 mL of dispersion from the flask at each time point (t = 0.5 hr, 2 hr, 4 hr, 6 hr and 24 hr) for further analysis. The samples were then purified by six cycles of precipitation-centrifugation (at 5000 rpm for 5 min)-sonication (by using bench sonicator for 3 min). The purification process of PNIPAm$_{89}$-*g*-CNFs was continued by dialysis against methanol for a day and milli-Q water for one more day using 12 k – 14 kDa MWCO membrane. Finally, the samples were freeze-dried for 2 days in order to remove

water. UV-Vis analysis was then performed to determine the grafting efficiency by using the following equation.

$$\text{Grafting Efficiency (\%)} = \frac{\text{Mass of polymer grafted onto CNFs}}{\text{Mass of polymer added initially}} \times 100$$

Investigation on surface chemistry of modified CNFs

In order to study the surface adsorption behaviour, control reactions with and without (control) isocyanide were performed for a day in aqueous condition. PNIPAm$_{89}$-COH (40 mg, 3.83 μmol) in 2.2 mL of milli-Q water and cyclohexyl isocyanide (8.78 mg, 80.42 μmol) were added to the 1 mL of CNFs gel (10 mg of dry CNFs, 16.5 μmol of -COOH groups) in the round-bottom flask under stirring for a day. A control sample was performed by simply mixing PNIPAm$_{89}$-COH and CNFs without adding cyclohexyl isocyanide. Then the dispersion was purified using the same procedure mentioned above, followed by lyophilization. Subsequently, both samples were submitted for ^{1}H-NMR and FT-IR analyses. According to the comparison of the ^{1}H-NMR spectrum of PNIPAm$_{89}$-*g*-CNFs prepared *via* Passerini 3-CR with that of PNIPAm$_{89}$-COH (III) in D_2O, the characteristic peaks at δ = 2.29 - 0.75 ppm and δ = 3.83 ppm corresponding to the protons from PNIPAm confirm the existence of polymers on CNFs. Here, ^{1}H-NMR of control sample was not recorded due to the limited solubility in aqueous and organic media. In case of FT-IR spectra, the peaks corresponding to the amide bend and amide stretch of PNIPAm at 1541 and 1650 cm^{-1} were observed, indicating the existence of polymer chains on the surface. The particle size distribution was performed by DLS, in which less than 1 mg mL^{-1} of sample solution was employed. Each measurement was repeated three times.

Analysis of the structural integrity of modified CNFs

The PNIPAm$_{89}$-*g*-CNFs (t = 24 hr) was used to characterize the morphology and the crystallinity *via* AFM and XRD analyses. AFM images were recorded to confirm that the surface modification of CNFs with synthesized PNIPAm$_{89}$ was successfully performed without disrupting the original morphology of CNFs. Moreover, the samples were exposed to X-ray diffraction (XRD) analysis to determine the effect of

surface grafting approach and the existence of $PNIPAm_{89}$ on the crystallinity of CNFs. The crystallinity index of CNFs was calculated with the following equation:

$$\text{CI}\ (\%) = \frac{I_{200} - I_{\text{AM}}}{I_{200}} \times 100$$

Where CI is crystallinity index, I_{200} is the intensity of diffraction of the (2 0 0) peak, I_{AM} is the intensity of the amorphous material.

Influence of PNIPAm chain length *on grafting efficiency and thermal behaviour of PNIPAm-g-CNFs*

The analysis of the influence of chain length of PNIPAm on the grafting efficiency was performed using polymer chains (PNIPAm-COH) with different number of monomer units: 66 DP_n, 108 DP_n and 158 DP_n, in aqueous media. The detail experimental conditions were described in **Table 5.4**. The PNIPAm-COH dissolved in 0.2 mL of milli-Q water and 1 mL of CNFs gel (10 mg of dry CNFs, 16.5 µmol of -COOH groups) were added to a glass vial, followed by the addition of cyclohexyl isocyanide while stirring. The mixtures were then continuously stirred for 30 min at room temperature. The same purification process as the analysis of grafting efficiency over time was applied. Thermal analyses were performed by TGA, in which approximately 10 mg of freeze-dried samples were heated from 25 to 700 °C at the rate of 20 °C min^{-1}.

Table 5.4. Experimental conditions for grafting PNIPAm-COH onto cellulose nanofibers (CNFs). The molar ratios between three components were kept the same.

Sample name	CNFs	PNIPAm-COH	Cyclohexyl isocyanide
$PNIPAm_{66}$-*g*-CNFs	10 mg 16.50 µmol of -COOH	30 mg 3.83 µmol	8.78 mg 80.42 µmol
$PNIPAm_{108}$-*g*-CNFs	10 mg 16.50 µmol of -COOH	48 mg 3.83 µmol	8.78 mg 80.42 µmol
$PNIPAm_{158}$-*g*-CNFs	10 mg 16.50 µmol of -COOH	70 mg 3.83 µmol	8.78 mg 80.42 µmol

CHAPTER - 6

Designing Cellulose-based Nanomaterials

for

Cancer Immunotherapy

Table of Content

6.1. Overview

In this study, we explored the design of cellulose-based nanomaterials for cancer immunotherapy. Firstly two types of polymers: (2-hydroxyethyl acrylate) ($PHEA_{37\text{-}Cy5}$) and poly(2-(dimethylamino)ethyl acrylate) $PDMAEA_{12}$, were synthesized *via* reversible-addition fragmentation chain transfer (RAFT) polymerization. Surface co-grafting was subsequently performed *via* three component Passerini reaction by simply mixing the polymers with aldehyde groups, cellulose nanofibers bearing acid moieties and cyclohexyl isocyanides in DMF overnight at ambient temperature. Then, the drug loading onto synthesized nanoparticles ($PHEA_{37\text{-}Cy5}$-$PDMAEA_{12}$)-*g*-CNFs was conducted by electrostatic interaction between cationic PDMAEA and anionic immune chemokines/recombinant murine MIP-1α (CCL3). The possible rate of release was determined by hydrolysis kinetics of $PDMAEA_{12}$ in water *via* ^{1}H-NMR. The resulting drug-loaded nanoparticles were observed to have *in vitro* stability, low cytotoxicity, and relatively high penetration into 2D and 3D cell models.

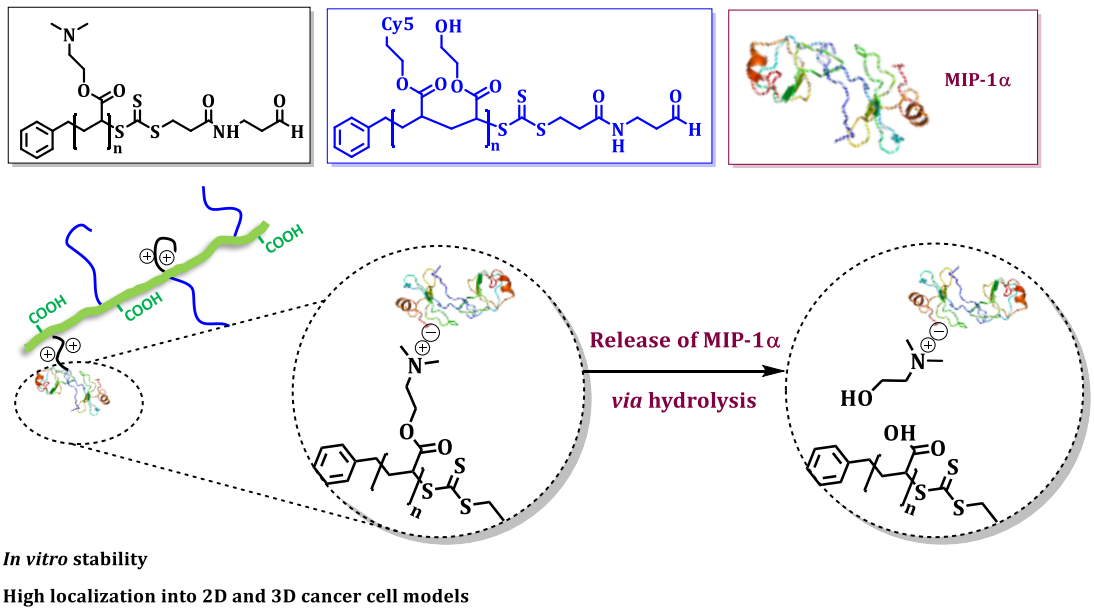

Scheme 6.1. Overall scheme for the design of cellulose-based nanomaterials prepared *via* three-component Passerini reaction for efficient binding and release of immune chemokines (MIP-1α).

6.2. Introduction

Immunotherapy is a promising treatment for dysfunctions including cancer, chronic inflammation, and allergy by stimulating the host immunological system to recognize and combat invading pathogenic microorganisms.[442, 443] This approach has especially been investigated to either passively or actively detect and kill cancer cells, which undergoes three sequential phases: elimination, equilibrium, and escape.[442, 444-446] Most of the tumour cells are eradicated in the elimination phase by both innate (in which T cells are a critical mediator) and adaptive immune cells, which are mainly regulated by the inflammatory cytokine, on the surface of tumour cells.[444, 447, 448] The cancer cells escaping from this phase enter the equilibrium phase, which is the longest in cancer immunoediting, and emerge with various mutations to increase their immune tolerance. In the escape phase, tumour cells evade immune recognition and continue to grow in an uncontrolled manner, leading to malignancies.[445, 448, 449]

Active cancer immunotherapy by delivering an antibody-cytokine as an immune stimulator to the tumour microenvironment has been attracting a great interest to limit the tumour cell populations.[450-455] Cytokines are small proteins with molecular weight of less than 30 kDa and can be found in the tumour microenvironment to effectively modulate immune cells to respond against cancer tumour.[450-456] Delivering cytokines for active immunotherapy increases the cytokine concentration in the tumour microenvironment for efficient signalling and activating a variety of immune effectors, including T-cells, natural killer (NK) cells, macrophages, and monocytes, followed by eradicating tumour cells and inhibiting the growth of human malignancy.[450-455] Cytokines include interleukins (IL), interferons (IFN), chemokines, and tumour necrosis factors.[452, 454, 455] Among them, chemokines hold particular promise for vaccination strategies in immunological research as they are expressed on a wide variety of tumour cells and enable binding to nearly 20 unique receptors.[457] Immune chemokines are capable of recruiting various types of leukocytes such as lymphocytes, macrophage/monocytes and dendritic cells for regulating host immune responses to tumours.[458-460] Chemokines are a large family containing more than 50 members,[457] but they are divided into four major groups: the C, CC, CXC and CX_3C chemokines based on the shared cysteine sequence elements (Cys – Cys).[459]

CXC chemokines target neutrophils or fibroblasts, while some others such as CXCL8/IL-8 and CXCL10/IP-10 target T cells. In contrast, the CC chemokines such as microphage inflammatory protein-1α/CCL3/Recombinant Murine MIP-1α target several effector cells including monocytes, dendritic cells, NK cells, $CD41^+$ and $CD81^+$ T cells *via* the CCR1 and CCR5 receptors.[458-460] MIP-1α, a small (<14 kDa) protein containing 69 amino acid residues, exhibits a highly anionic convex surface and mostly neutral concave surface, as well as binding to CCR1 receptors.[461, 462] Zeng *et. al.* investigated both time- and dose-dependent expressions of MIP-1α in the accumulation and activation of the innate immune system in murine bacterial pneumonia.[463] In addition, Zibert and co-workers explored the combined injection of MIP-1α with interleukin-2 (IL-20 or granulocyte-macrophage colony-stimulating factor (GM-CSF) into mice bearing pre-existing leukemia/lymphoblastic malignancy. The results demonstrated the significant survival rates and observed the recruitment of major effector cells: $CD41^+$ and $CD81^+$ T cells at the vaccination sites.[464]

The vaccination strategy for cancer immunotherapy has been developed by utilizing nanoparticles to preferentially deliver the immunoregulating agent into the tumour microenvironment. Nanovaccines have been identified to improve vaccine efficiency and regulate the immune response *in vivo*.[465, 466] Nanovaccines that can be employed for immunoregulation can be incorporated into polymeric nanoparticles, nanoemulsions and virus-like particles. The advantage of nanotechnologies is that the properties of nanoparticles such as size, shape, surface charge and hydrophilicity/hydrophobicity can be precisely controlled based on the characteristics of immunochemokines.[465] In general, the delivery of proteins or peptide molecules by polymeric nanoparticles have been reviewed by Du *et. al..*[467] The researchers may design the carrier through different approaches such as protein/peptide-containing liposome or the protein/peptide-polymer conjugates based on the nature of selected protein/peptide.[468] In particular, charged proteins can electrostatically interact with block copolymers containing a neutral and oppositely charged blocks, resulting in the formation of polyion complex (PIC) micelles.[469]

In case of delivering anionic MIP-1α, cationic polymers such as polyethylenimine (PEI), poly(L-lysine), poly(2-dimethylaminoethyl acrylate) (PDMAEA) are necessary to form the polyion complex. Amongst them, PDMAEA seems to be an

attractive candidate due to their non-toxicity and capability to release therapeutics by their self-catalysed degradation properties in aqueous media. According to the study undertaken by Truong *et. al.,* the ester group located on the side chain of polymer degrades to poly(acrylic acid) (PAA) and 2-dimethylaminoethanol (DMAE) in water. The degradation rate can be varied depending on the molecular weight of the polymer and the pH of the solution. The polymers and released side products after degradation were confirmed to be non-toxic.[470]

The focus of this chapter was to design nanoparticles that can efficiently bind and release immunostimulators/chemokines (MIP-1α) in the cancer microenvironment. To achieve this, our interest was directed at the application of cellulose nanomaterials for cancer immunotherapy. We firstly prepared the cellulose nanofibers (CNFs) according to the procedure presented in **Chapter 3** *via* combined chemical (TEMPO-mediated oxidation) and mechanical (high intensity ultrasonication) treatments. Subsequently, CNFs were modified with the copolymers poly(2-hydroxyethyl acrylate) (PHEA) labelled with cyanine 5 and poly(2-(dimethylamino)ethyl acrylate) (PDMAEA), *via* a three-component Passerini reaction. This approach involves reacting the acid groups from CNFs with the aldehyde end group functionalities from copolymers, and cyclohexyl isocyanides under ambient conditions. The idea behind grafting two copolymers on CNFs is that PHEA is responsible for the colloidal stability of CNFs in aqueous media and the cationic PDMAEA serves as a reaction site for negatively charged MIP-1α binding. Importantly, the polyelectrolytes are either weak or strong so that the release therapeutics bound *via* electrostatic interaction depends strongly on the degree of ionisation of charges at physiological pH.[471] This problem was alleviated by the hydrolytic nature of the PDMAEA, which converts the cationic polymers into negatively charged carboxylic acid, leading to the release of anionic immunostimulator in time-, temperature- and pH-dependent manner. The overall synthesis scheme for this project is shown in **Scheme 6.2**. The chemical and biological activity of designed nanoparticles ((PHEA-PDMAEA)-*g*-CNFs) were determined by a variety of instrumental analyses including ^{1}H-NMR, DLS, UV-Vis, LSCM, and flow cytometry.

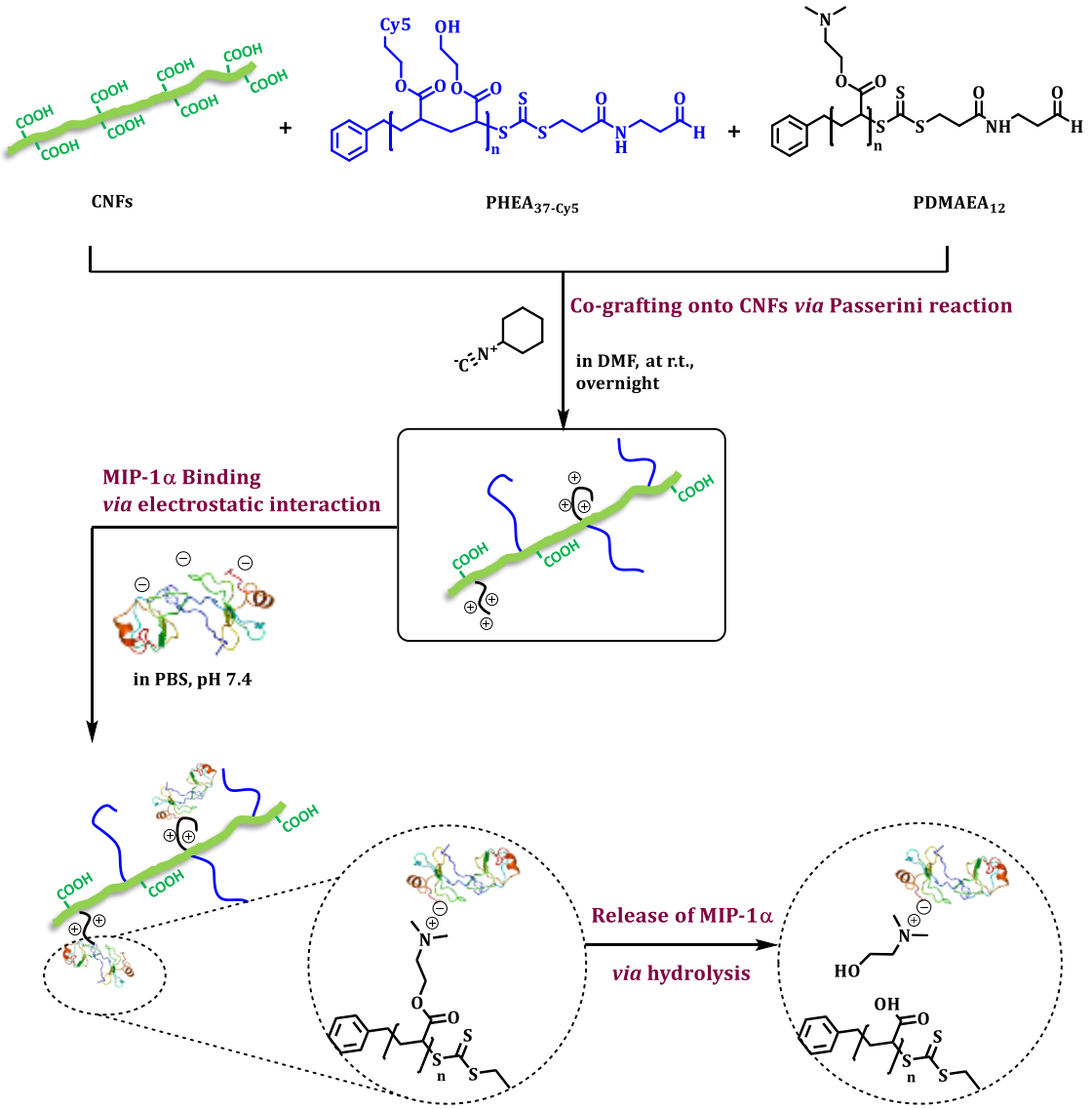

Scheme 6.2. Overall Scheme for the design of cellulose nanoparticles for efficient delivery and release of immune chemokines (MIP-1α). Cy5 stands for cyanine 5 dye.

6.3. Results and Discussions

6.3.1. Synthesis of aldehyde-terminated RAFT agent

The work in this chapter was to modify the surface of cellulose nanomaterials to generate a biocompatible polymer coating for the delivery of chemokines (MIP-1α) for cancer immunotherapy. This was achieved by covalently tethering functional polymer chains on the surface of CNFs *via* Passerini reaction which involves three components: a carboxylic acid, an aldehyde and an isocyanide. The process of preparation is similar to the method reported in **Chapter 5** and also illustrated in **Scheme 6.2**. In brief, cellulose nanofibers bearing carboxylic acid functionalities were prepared *via* mechanically assisted TEMPO-mediated oxidation combined with acid treatment as mentioned in **Chapter 3**. Secondly, a range of aldehyde-terminated polymers were prepared *via* RAFT polymerization in the presence of an aldehyde functionalized chain transfer (RAFT) agent. However, we replaced the RAFT agent used earlier with one containing an amide bond instead of an ester due to the higher hydrolytic stability under a variety of reaction conditions.[472]

The synthesis of the RAFT agent bearing aldehyde group was carried out *via* a two-step procedure. Briefly, the RAFT agent with the protected aldehyde group was initially synthesized by reacting 3-(benzylthiocarbonothioylthio) propanoic acid and 1-amino-3,3-diethoxypropane by EDC/DMAP coupling reaction. The obtained acetal group was then converted to aldehyde groups under acidic conditions. After purification *via* flash column chromatography and drying *in vacuo*, the yellow viscous oil was obtained at 34 % yield. Evidence of the successful synthesis of chain transfer agent was gathered from ^{1}H- and ^{13}C-NMR (**Figure 6.1** and **6.2**). The signals at δ =7.34 to 7.26 ppm, 4.60 ppm, 3.66 – 3.61 ppm, 2.76 – 2.74 ppm are respectively assigned to the aromatic protons and methylene (CHphenyl C*H*$_2$-, -C(S)SC*H*$_2$-, -C*H*$_2$C(O)NH-) protons. The signal at δ = 6.01 ppm is ascribed to the resonance of the proton of amide bond and the methylene bond next to it shifted to δ = 3.57 – 3.51 ppm. The absence of the signals in the region of δ = 4 – 3.7 ppm representing the methylene groups from diethyl acetal is consistent with the successful deprotection process. The sharp singlet at δ = 9.79 ppm was assigned to the aldehyde moiety and its intensity had a reasonably good agreement with the signals corresponding to the

rest of the molecule. The aldehyde carbon was also visible at δ=201 ppm in ^{13}C-NMR (**Figure 6.2**).

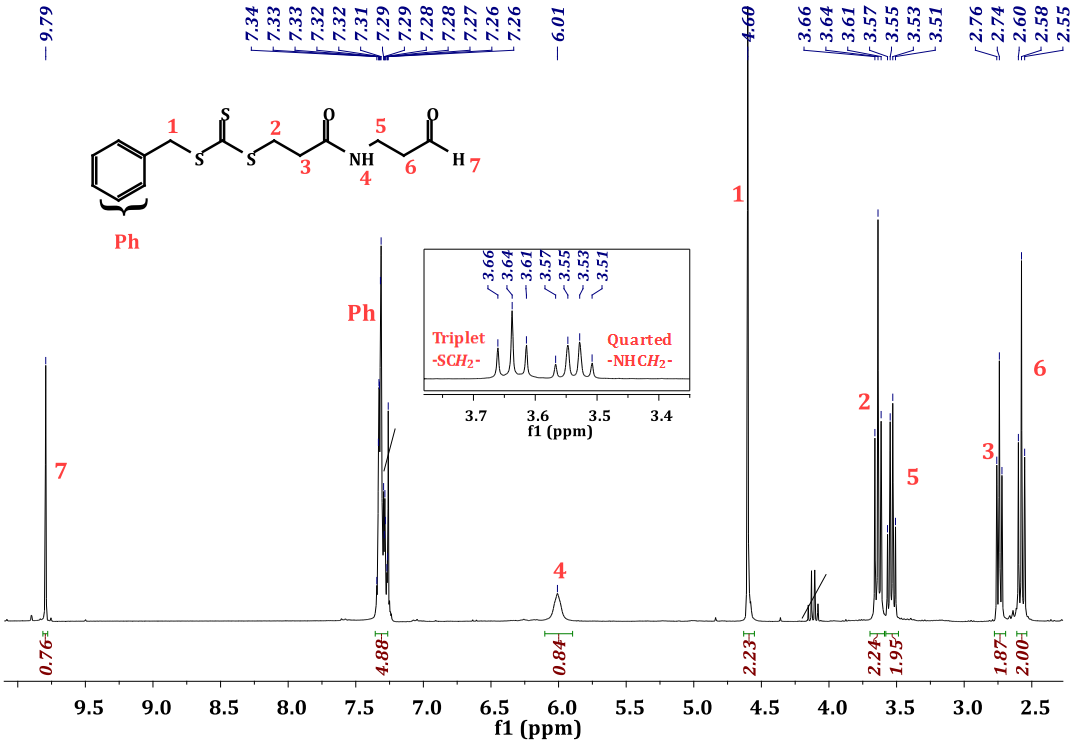

Figure 6.1. ^{1}H-NMR spectra of *N*-(2-formylethyl)-3-(benzylthiocarbonothioylthio) propionamide (RAFT-aldehyde) in $CDCl_3$.

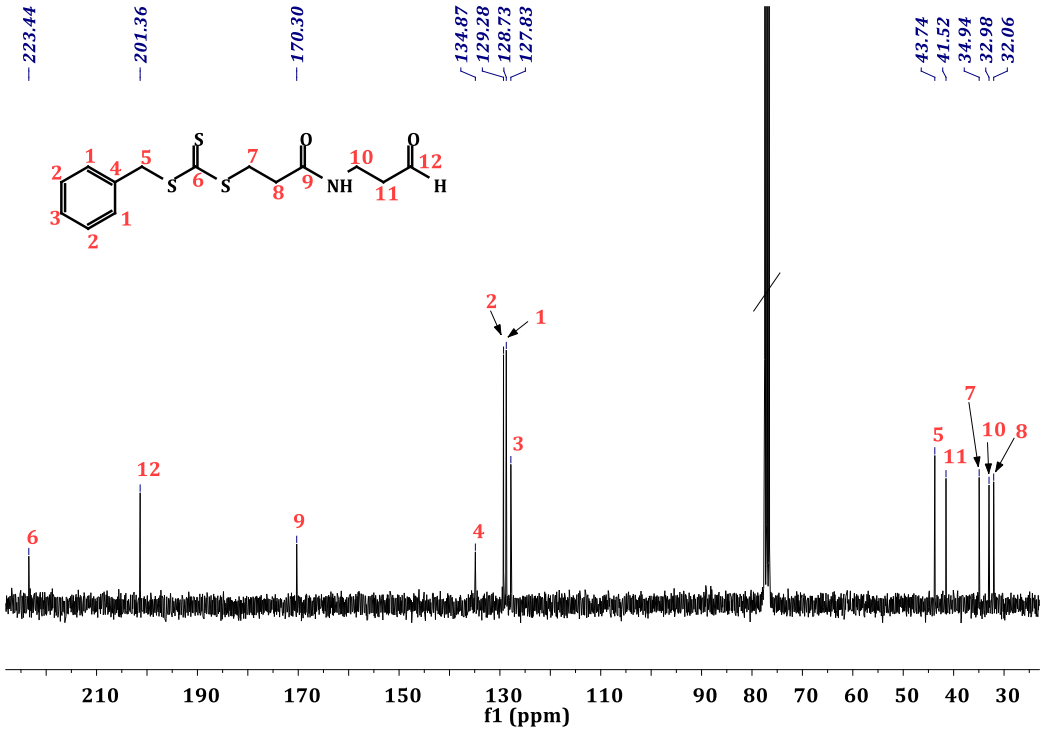

Figure 6.2. ^{13}C-NMR spectra of *N*-(2-formylethyl)-3-(benzylthiocarbonothioylthio) propionamide (RAFT-aldehyde) in $CDCl_3$.

6.3.2. Synthesis of homopolymers: $PHEA_{37}$ and $PDMAEA_{12}$ with aldehyde end functionality

The aldehyde-functionalized chain transfer agent was subsequently employed in the synthesis of homopolymers. The cationic polymer PDMAEA can interact with the negatively charged chemokines MIP-1α *via* electrostatic interactions, whereas PHEA ensures colloidal stability of the nanoparticles in aqueous media. Both homo-polymerizations were performed *via* RAFT polymerization in the presence of aldehyde-functionalized RAFT agent and AIBN as an initiator at the ratio of [M]: [RAFT]: [AIBN] = 82 : 1 : 0.08 in DMF at a monomer concentration of 2 M. After polymerizing HEA and DMAEA monomers for 2 hr and 4 hr, respectively at 65 °C, the ^{1}H-NMR spectra of crude polymer mixture in deuterated solvent: DMSO-d_6 for PHEA, and $CDCl_3$ for PDMAEA, were recorded. The monomer conversion was determined by comparing the integrations of resonance signals corresponding to the methylene protons from polymer chain and residual monomer. More specifically, 46 % of HEA conversion (37 repeating units in each polymer chain) was calculated by comparing the signals at δ = 4.13 ppm and 4.02 ppm which correspond to two protons (-C*H*$_2$CO(O)), while 14.6 % of DMAEA conversion (12 repeating units in each polymer chain) was determined by comparing the signals at δ = 3.66 ppm and 3.82 ppm of corresponding protons from -C*H*$_2$N(CH_3)$_2$. Then the crude products were purified by different techniques: PHEA was purified *via* dialysis against methanol for 2 days while PDMAEA was purified by repeated precipitation in hexane. The purity of homopolymers and the existence of aldehyde moiety, which was crucial for future surface grafting reaction, were also confirmed by ^{1}H-NMR. **Figure 6.3** and **6.4** represent the ^{1}H-NMR spectra of pure and $PDMAEA_{12}$ and $PHEA_{37}$. The clear evidence of the aldehyde end group functionality was confirmed by the corresponding peaks at δ = 9.81 ppm and 9.63 ppm for $PDMAEA_{12}$ and $PHEA_{37}$ respectively.

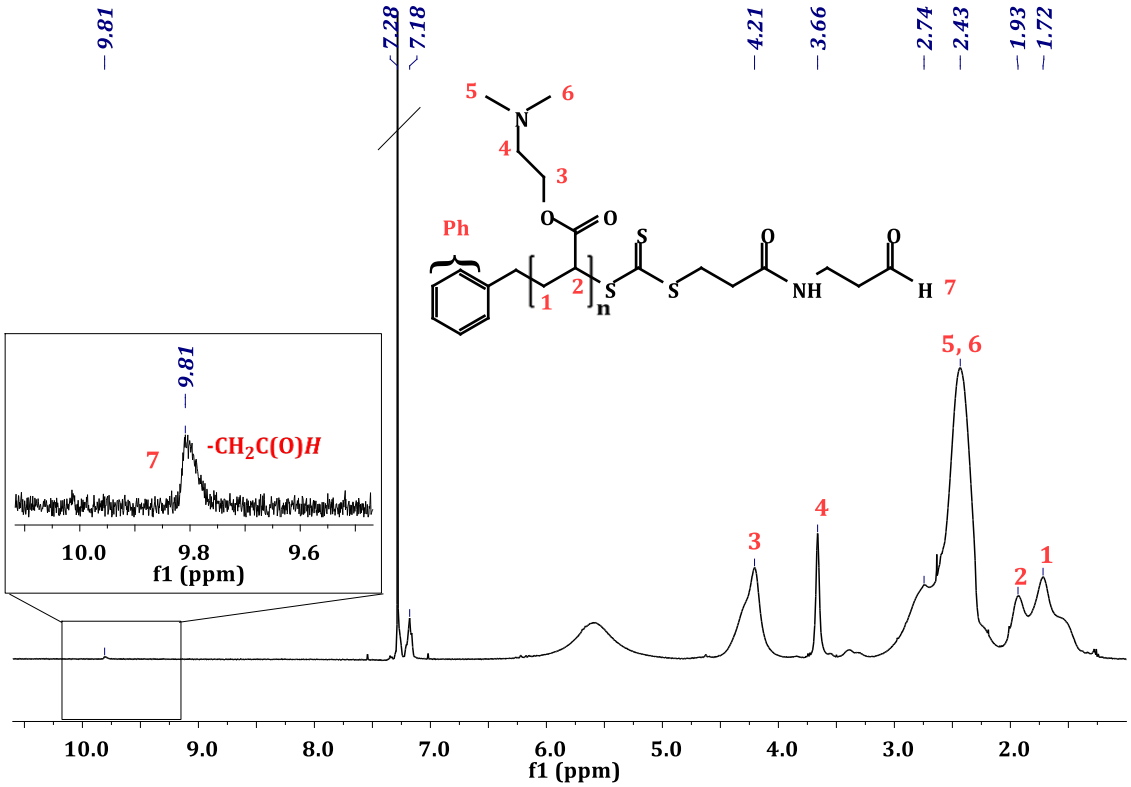

Figure 6.3. ^{1}H-NMR spectrum of aldehyde-functionalized $PDMAEA_{12}$ in $CDCl_3$.

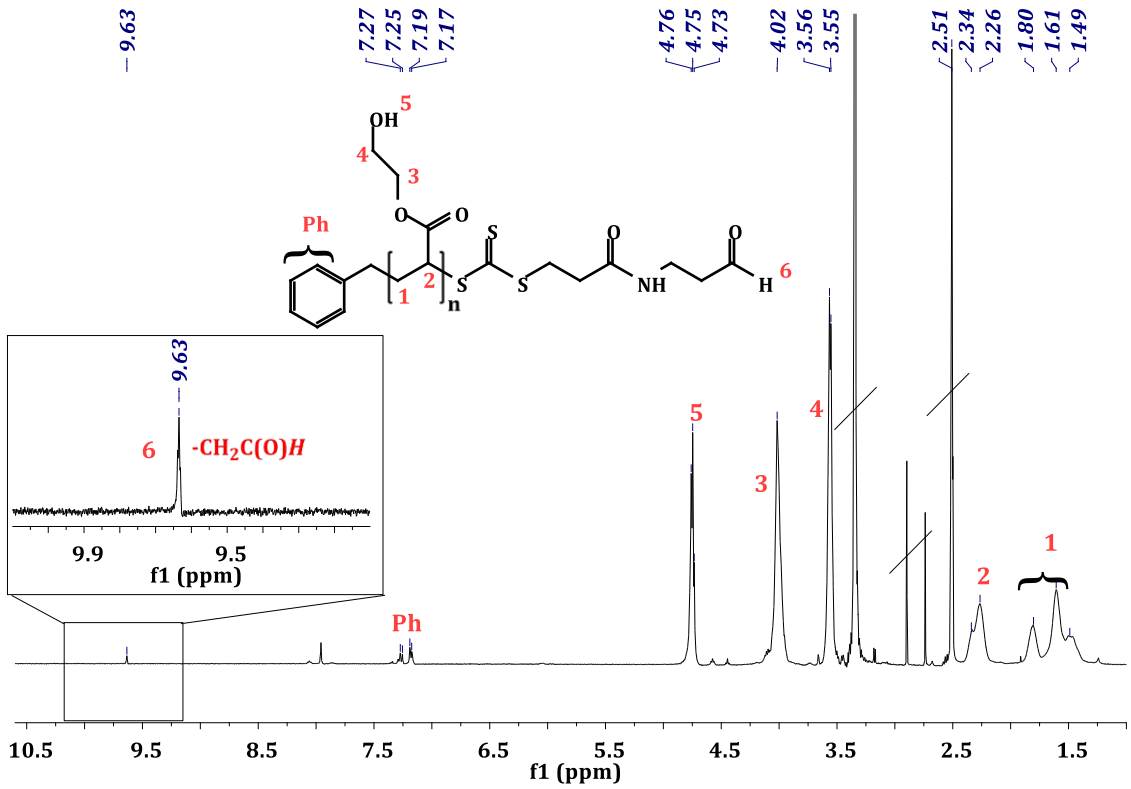

Figure 6.4. ^{1}H-NMR spectrum of aldehyde-functionalized $PHEA_{37}$ in DMSO-d6.

The molecular weight and molecular weight distribution of the homo-polymers were determined by SEC in DMF as eluent. The molecular weight of $PHEA_{37}$ was measured to be M_n =15000 g mol^{-1} with a dispersity $Đ$ = 1.21 and that for $PDMAEA_{12}$ was measured to be M_n =2740 g mol^{-1} with a dispersity of $Đ$ = 1.27. The resulting polymers show symmetrical unimodal distribution without a shoulder and tailing peak, representing of the absence of significant side reactions (**Figure 6.5**).

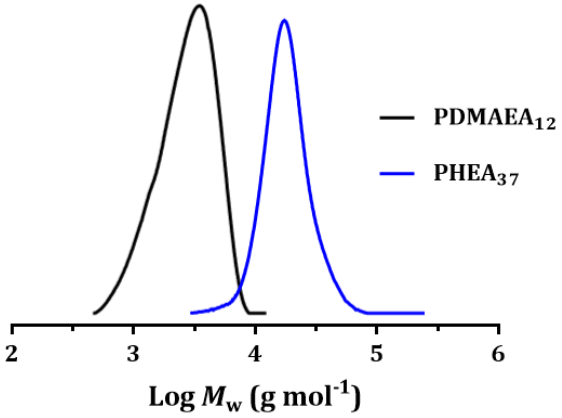

Figure 6.5. SEC traces of synthesized homopolymers: $PDMAEA_{12}$ (in black) and $PHEA_{37}$ (in blue). Samples were dissolved in DMF.

6.3.3. Synthesis of Cyanine 5 (Cy5) acid and fluorescently labelled $PHEA_{37}$

In this project, cyanine 5 fluorescent dye was chosen for the purpose of bio-imaging due to its bright fluorescence in the visible region ($\lambda_{max(excitation)}$ is between 615 and 710 nm),[473] high extinction coefficients, high sensitivities, and suitability for the imaging of molecules in living cell. Cyanine 5 was synthesized *via* a two-step process according to the literature.[473, 474] Firstly, the starting indolium intermediate was prepared by the alkylation reaction between indoles (2,3,3-trimethyl-3*H*-indole) with alkyl halides. The intermediate was obtained after refluxing the mixture of indoles, 6-bromohexanoic acid, potassium iodide in acetonitrile at 85 °C for a day. After purification, the brown salts in a reasonably good yield of 27 % was obtained. The typical ^{1}H-NMR spectrum of the prepared indolium intermediate is shown in **Figure 6.6**. The signal at δ = 7.98 – 7.60 ppm is assigned to the resonance of the protons of the aromatic ring. All signals representing methylene protons appeared at δ = 4.47 – 4.42 ppm (7), 1.85 ppm (8), 1.42 ppm (9), 1.56 – 1.54 ppm (10), and

2.25 – 2.21 ppm (11) respectively, while three methyl protons were corresponded by the peaks at δ = 1.56 – 1.54 ppm (5) and 2.84 ppm (6). In addition, the agreement in the integration value of hydrogens in the molecule confirmed that the indolium intermediate with high purity has been successfully prepared.

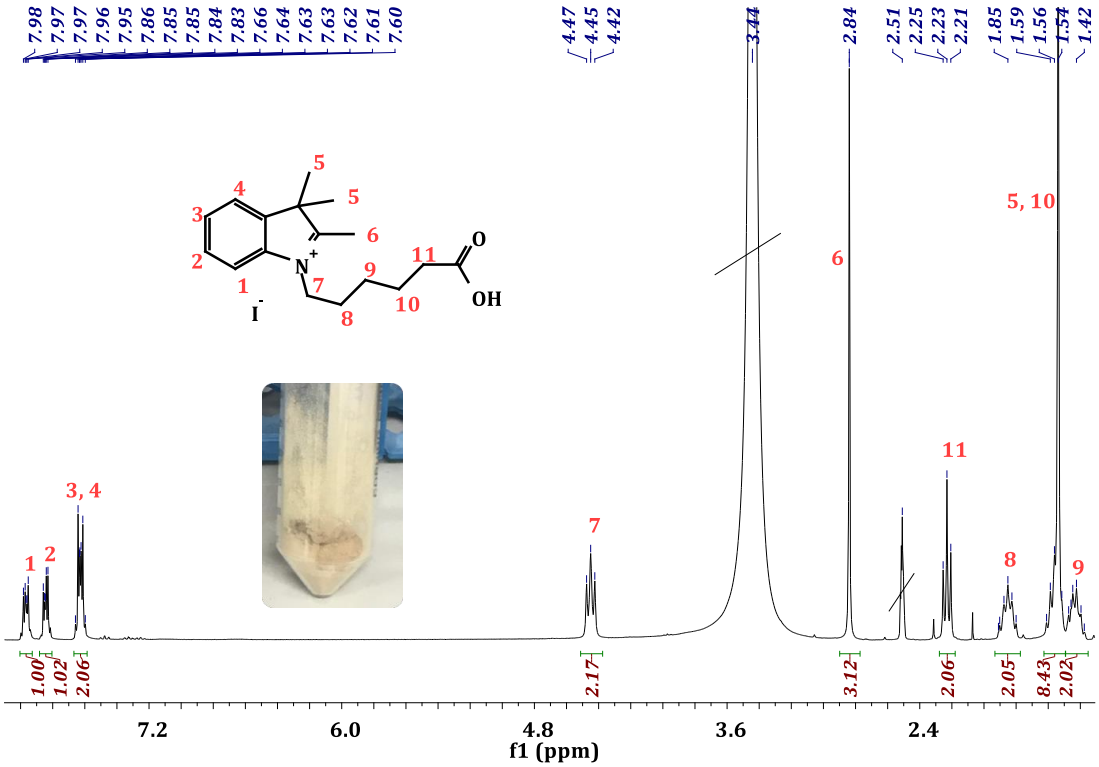

Figure 6.6. ^{1}H-NMR spectrum of synthesized indolium intermediate in DMSO-d_6.

To synthesize the cyanine dye (Cy5), the obtained indolium salt was heated together with malonaldehyde bis(phenylimine) monohydrochloride dissolved in acetic anhydride to 120 °C in order to form hemicyanines. After treating the mixture with 1,2,3,3-tetramethyl-3*H*-indolium iodide in pyridine, the formation of cyanine 5 fluorescent dye was observed by the colour change to dark blue within 18 hr of stirring at room temperature. The obtained crude product was purified by precipitation and column chromatography. It is here important to flash the column with pure methanol at the end to obtain purple fraction which was confirmed to be the pure product according to ^{1}H-NMR in DMSO-d_6 (**Figure 6.7**). The final product was obtained in the form of blue foam or brown crystals. Unfortunately, due to the difficult separation, the final cyanine 5 product was obtained with low yield of 18.45 %. According to the recorded ^{1}H-NMR, the corresponding protons from the aromatic rings

and along the conjugated bridge appeared around the region between δ = 8.5 ppm and 6 ppm, confirming the successful synthesis of cyanine 5 fluorescent dye. Also, evidence for the purity of final product was obtained by the equal integration ratios between corresponding signals. Moreover, the excitation wavelength was recorded by UV-Vis analysis (**Figure 6.8**) revealing a maximum absorption wavelength of synthesized fluorescent dye at 648 nm in DMSO.

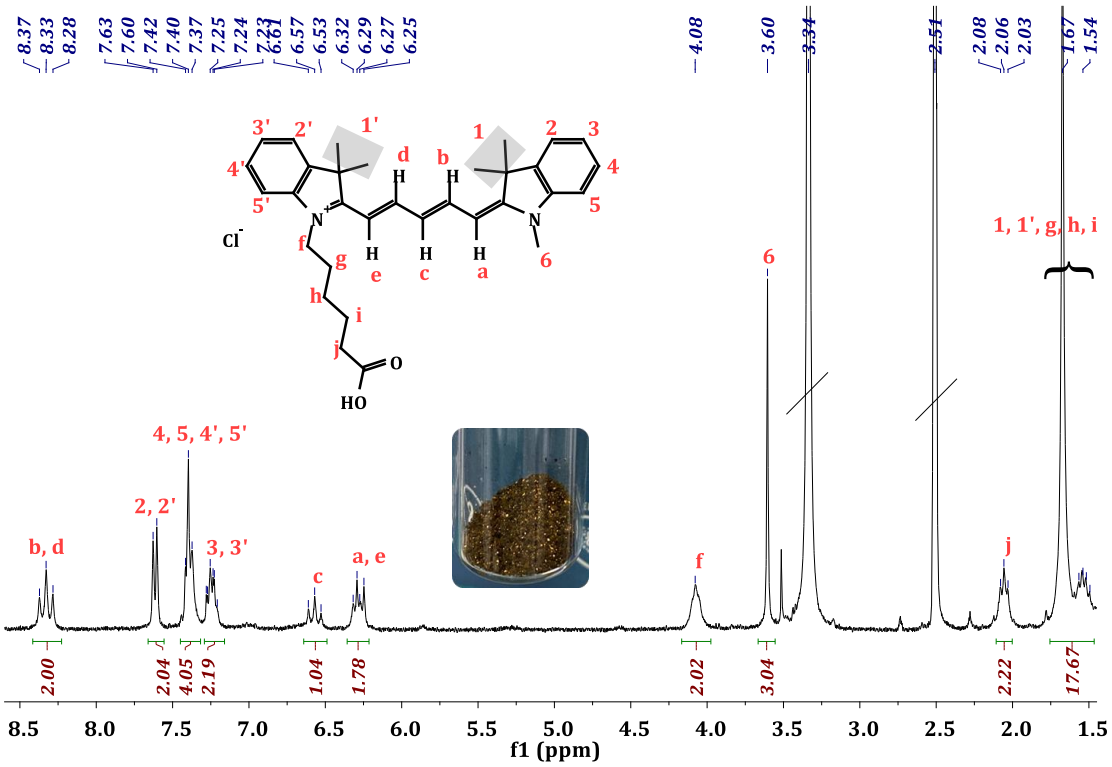

Figure 6.7. ^{1}H-NMR spectrum of synthesized cyanine 5 acid in DMSO-d_6.

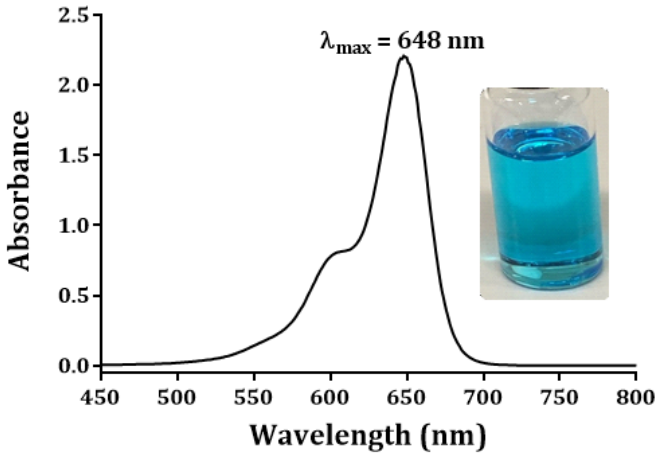

Figure 6.8. UV-Vis spectrum showing the excitation wavelength of cyanine 5 acid at a concentration less than 1 mg mL^{-1} in DMSO.

Taking the advantage of acid groups on cyanine 5, post-polymerization modifications was performed for the introduction of the fluorophore on the side chains of $PHEA_{37}$ *via* coupling reaction. The hydroxyl groups on polymer chains can readily react with carboxylic acid groups in the presence of DCC/DMAP coupling agents under mild reaction condition. The reaction was conducted in anhydrous DMF using 1: 0.03 equivalent of $PHEA_{37}$ polymer chain and cyanine 5. After removing the excess dye by dialysis against methanol, the fluorescent polymer sample was ready for the surface grafting reaction.

6.3.4. Hydrolysis kinetics of $PDMAEA_{12}$ in PBS at pH 7.4

The surface grafting reaction was previously performed in aqueous media; however, PDMAEA can be degraded slowly to poly(acrylic acid) (PAA) and DMAE *via* a self-catalysed hydrolysis process in water as illustrated in **Scheme 6.3**.[470, 475] Thus, we studied the degradation rate of PDMAEA in aqueous media (the mixture of D_2O and 2 × concentrated PBS (1: 1 v/v)) at pH 7.4. The samples were incubated at room temperature and 37 °C at various time intervals: 15 min, 20 hr, and 40 hr. According to ^{1}H-NMR, shown in **Figure 6.9**, the appearance of a new peak at 3.62 ppm corresponding to 2 protons of DMAE is evident. This new peak emerged already after 15 min, and its integration area increased with over time. Moreover, it was observed that the degradation rate was 1.5 times higher at 37 °C according to the comparison shown in **Figure 6.10**. This finding also helped to predict the possible rate of therapeutic release in biological media.

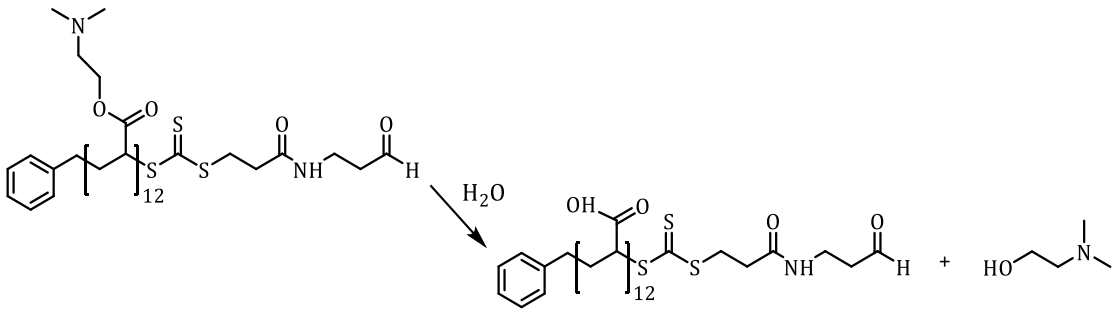

Scheme 6.3. Schematic illustration for the hydrolysis of PDMAEA in PBS at pH 7.4.

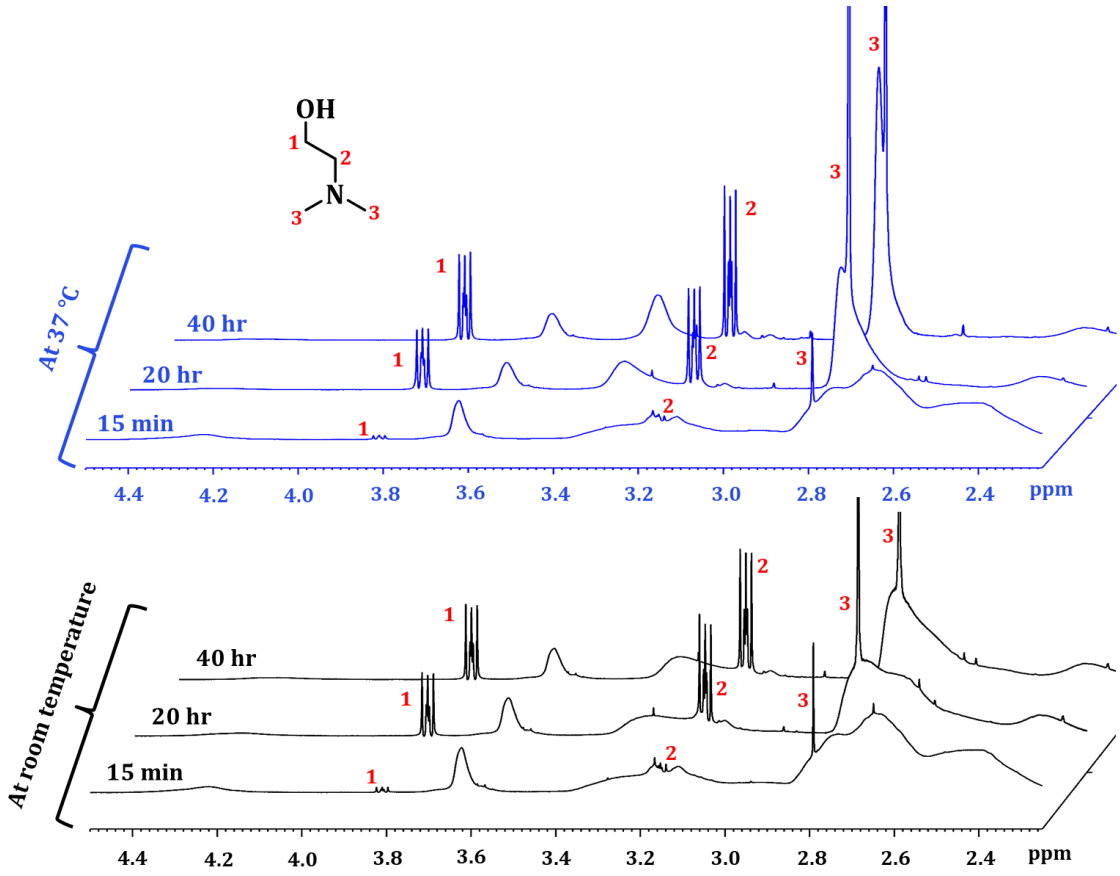

Figure 6.9. ^{1}H-NMR spectra of PDMAEA$_{12}$ in D_2O and PBS (2 × concentrated, pH 7.4) incubated at room temperature and 37 °C. The spectra were recorded at different time intervals.

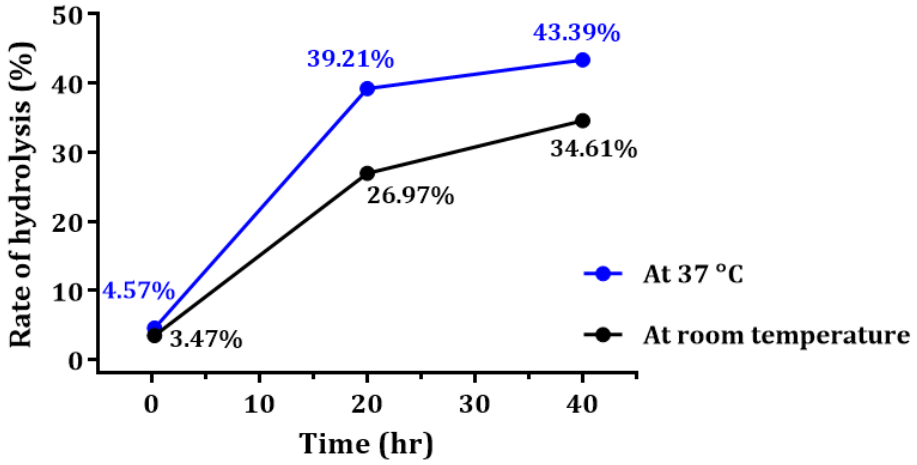

Figure 6.10. Rate of hydrolysis of PDMAEA$_{12}$ in D_2O and PBS (2 × concentrated, pH 7.4) incubated at room temperature and 37 °C *vs* different time intervals.

6.3.5. Investigation on the factors affecting surface grafting efficiency

Before undertaking the co-grating reaction, the factors influencing the surface grafting efficiency was firstly investigated. In this study, $PHEA_{37}$ was employed as a model polymer, in which aldehyde end groups on polymer chains will chemically react with acid groups on the surface of CNFs in the presence of cyclohexyl isocyanide *via* Passerini reaction. The reactions were undertaken at different conditions based on the type of solvent and concentration. More specifically, the first sample was performed in CNFs gel itself (the amount of water contained in the gel is approximately 1 mL), and other three samples were diluted in solvent: water, water and methanol, and water and DMF. Except for CNFs gel sample, all other samples were reacted under the same concentration at ambient temperature. Here the final concentration was calculated by taking approximately 1 mL of water in CNFs gel. The well dispersibility straight of the reaction mixture after the reaction was recorded in **Figure 6.11**, confirming that the attachment of polymers on the surface occurred. Here, the exception is that $PHEA_{37\text{-}Cy5}$ was used for the last sample resulting in the light blue colour.

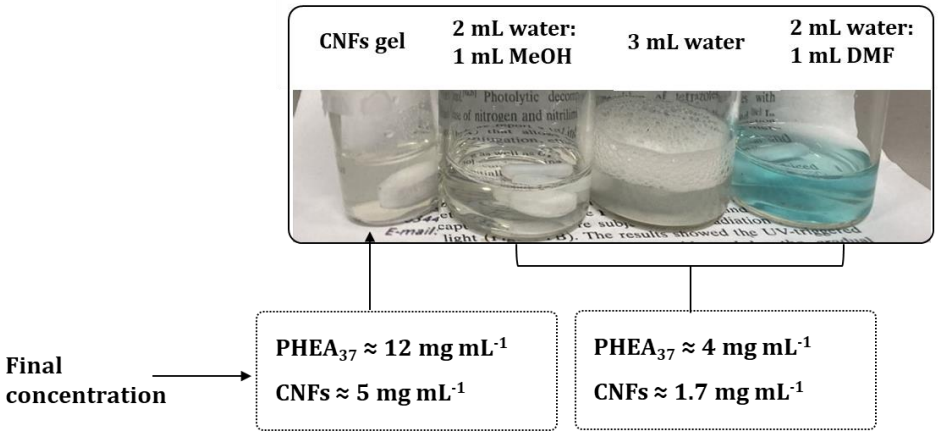

Figure 6.11. The dispersibility of reaction mixture straight after the surface modification with $PHEA_{37}$ under different condition. The solvent volume and final concentration were calculated by taking approximately 1 mL of water content in CNFs gel into account.

Due to the well dispersion after the reaction, it was not possible to collect the polymer-grafted CNFs by precipitation and centrifugation method. Considering this, the dialysis was initially carried out to mainly remove organic solvent and freeze drying. The obtained freeze-dried samples were easier to be collected by

precipitation. Here, it is crucial to be noted that the precipitation must be undertaken to efficiently remove the unreacted polymer chains. According to the experience throughout the project, the dialysis itself was not capable of complete purification no matter how large the MWCO of the dialysis membrane. After washing the samples with methanol for a few times until the clear supernatant was achieved, the product was dialysed against water for a day to remove methanol, followed by freeze-drying. The grafting efficiency of dried polymer-grafted CNFs were determined by UV-Vis analysis at the concentration of 2 mg mL^{-1} in milli-Q water (**Figure 6.12**). For comparison, the absorption spectra of $PHEA_{37}$ at the concentration of 1 mg mL^{-1} in milli-Q water was included. The strong absorbance value at 305 nm was due to the $\pi \rightarrow \pi^*$ transition of the thiocarbonyl (C=S) bonds of the RAFT polymer. [476]

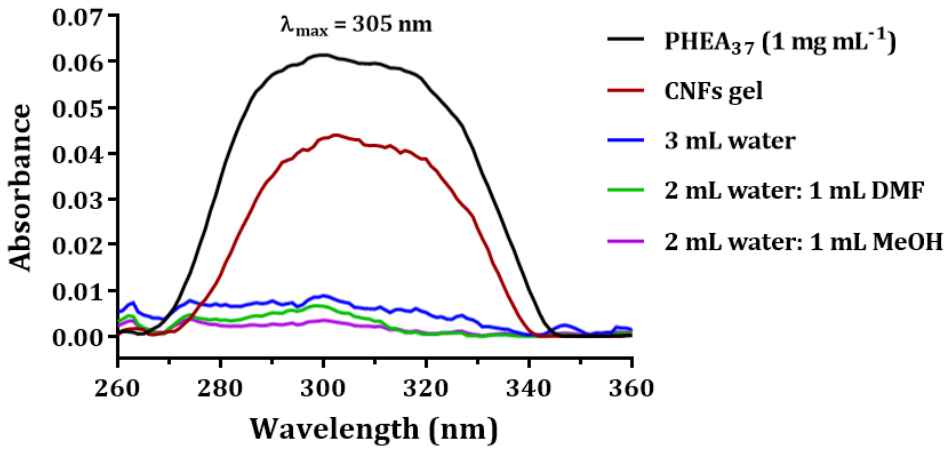

Figure 6.12. UV-Vis spectra of CNFs after surface modification with $PHEA_{37}$ under various solvent systems. The analysis was performed in milli-Q water at the concentration of 2 mg mL^{-1} for $PHEA_{37}$-*g*-CNFs samples and 1 mg mL^{-1} $PHEA_{37}$ sample. The solvent volume was calculated by taking approximately 1 mL of water content in CNFs gel into account.

The spectra illustrated that the sample prepared using the CNF gel only revealed a more efficient grafting process. By using the absorbance maximum of $PHEA_{37}$ solution as a standard, the percent grafting efficiency was calculated by using following equation and the results are shown in **Figure 6.13.**

$$\text{Grafting efficiency (\%)} = \frac{\text{Mass of polymer grafted}}{\text{Mass of polymer in feed}} \times 100$$

The grafting efficiency is defined as the percentage of polymer grafted on total CNFs. The calculation was performed by comparing the mass of grafted

polymers on the surface to the amount of initially added polymer. The results described that up to 23 % of grafting efficiency was achieved when the reaction was performed in the CNFs gel only. However, a significant decrease in grafting efficiency was observed when the system proceeded in diluted condition. Moreover, the surface modification of CNFs with polymers was less successful when a mixture of water and organic solvent was used at the same concentration, although these differences may be within error. It can be concluded that polymers could be grafted onto CNFs using various solvent mixtures but more important is the use of the highest possible concentration, which is the CNFs gel as obtained. If the reaction needs to proceed in organic solvent, DMF is preferable to methanol for higher grafting efficiency, but it is recommended to reduce the volume of the solvent.

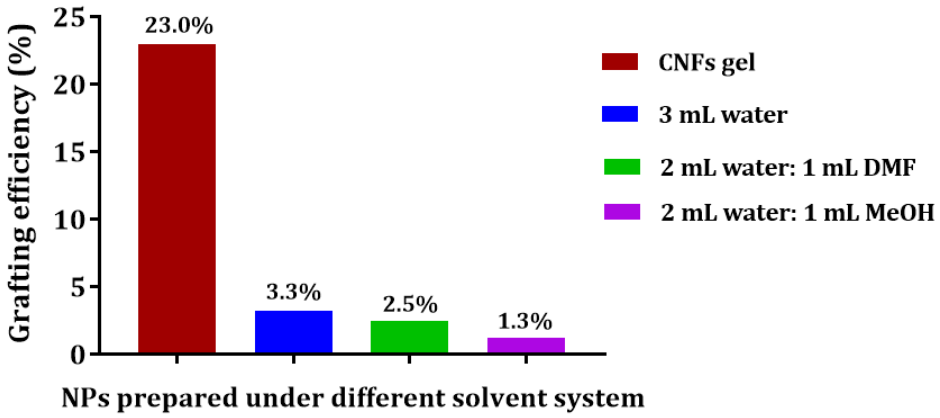

Figure 6.13. The trend of grafting efficiency (the ratio between the number of polymers in grafted and that in feed) depending on applied solvent system during grafting reaction. The analysis was performed in milli-Q water at the concentration of 2 mg mL^{-1}. NPs = nanoparticles ($PHEA_{37}$-*g*-CNFs).

6.3.6. Co-grafting of $PHEA_{37\text{-}Cy5}$ and $PDMAEA_{12}$ onto CNFs *via* Passerini Reaction in organic solvent

After investigating the appropriate condition for surface grafting reaction, it was planned to perform the co-grafting reaction at concentrated condition in DMF considering the possible degradation of PDMAEA in water through hydrolysis of the ester groups on the polymer side chains. As the reaction was supposed to be in the water free system, freeze-dried CNFs was used and redispersed in a small volume of DMF. In this experiment, three grafted samples were prepared by keeping the molar

ratio of carboxyl groups on CNFs and $PHEA_{37\text{-}Cy5}$ constant at 1: 0.25, but varying the molar ratio of $PDMAEA_{12}$ (1.04, 0.74 and 0.31 respectively). The obtained grafted nanoparticles were purified by precipitating four times in water. A clear supernatant was taken as a sign for the complete removal of unreacted polymer chains (**Figure 6.14**, picture insert). The percentage of grafting efficiency, calculated by using the calibration curves shown in **Figure 6.15**, and the molar ratio of homopolymers on the grafted CNFs were listed in **Table 6.1**. Here, low grafting efficiency was expected not only due to the low yield in organic solvent according to the studies mentioned above, but also the general poor re-dispersibility of CNFs in organic solvents. Therefore, it is crucial to always sonicate the CNFs dispersion by using a bench sonicator before starting the reaction. **Figure 6.14** depicts the relationship between the molar ratio of $PDMAEA_{12}$ to $PHEA_{37\text{-}Cy5}$ in the feed prior to the reaction and in grafted sample. Interestingly, it seems that the ratio of grafted polymers was similar (2: 1) independent of the initial feed ratio. The origin of this unexpected behaviour was not clear, but it was probably due to the higher grafting efficiency of short chain polymers. For instance, when only one $PHEA_{37\text{-}Cy5}$ chain, which was twice longer than $PDMAEA_{12}$, was tethered at each time, it was possible two $PDMAEA_{12}$ chains could attach on the surface. Overall zeta potential results obtained from DLS analysis showed that the amount of negative charges on CNFs decreased after modification reaction, confirming the successful surface grafting reaction. After the kinetic study was performed, the sample 2 was chosen for further experiments and analyses.

Table 6.1. The information on initial and final molar ratios of CNFs: $PHEA_{37\text{-}Cy5}$: $PDMAEA_{12}$, the grafting efficiency (a percentage of polymers on total CNFs based on the comparison between the mass of grafted and initially added polymers) (%) and zeta potential of nanoparticles measured by DLS.

Sample no.	Components	Initial molar ratio of CNFs: $PHEA_{37\text{-}cy5}$: $PDMAEA_{12}$	Grafting efficiency (%)		Final molar ratio of CNFs: $PHEA_{37\text{-}Cy5}$: $PDMAEA_{12}$	Zeta potential (DLS)
			$PHEA_{37\text{-}cy5}$	$PDMAEA_{12}$		
1	CNFs: $PHEA_{37\text{-}Cy5}$: $PDMAEA_{12}$	1: 0.25: 1.04	7.3	3.9	1: 0.019: 0.04	-5.94
2		1: 0.25: 0.74	6.2	5.2	1: 0.016: 0.038	-8.67
3		1: 0.25: 0.31	8.3	12.4	1: 0.021: 0.039	-11.3
CNFs						-15.77

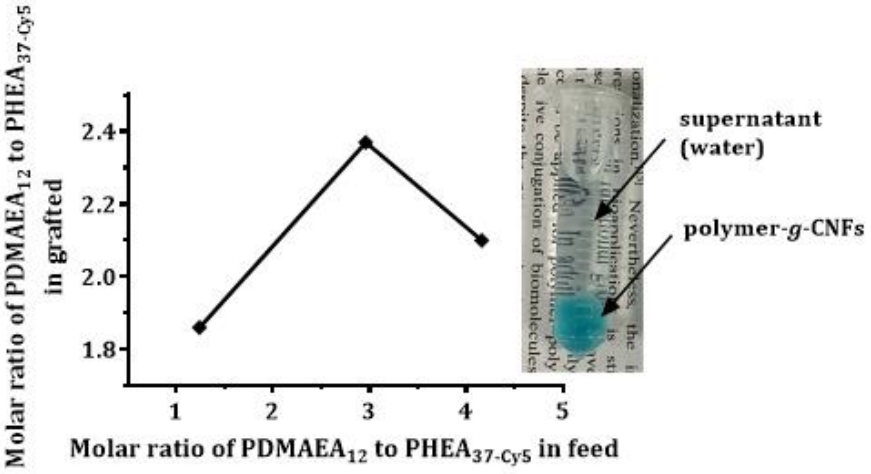

Figure 6.14. The graph presenting the molar ratio of $PDMAEA_{12}$ to $PHEA_{37\text{-}cy5}$ in grafted *vs* that in feed. The picture insert shows the example of polymer grafted nanoparticles precipitated in water.

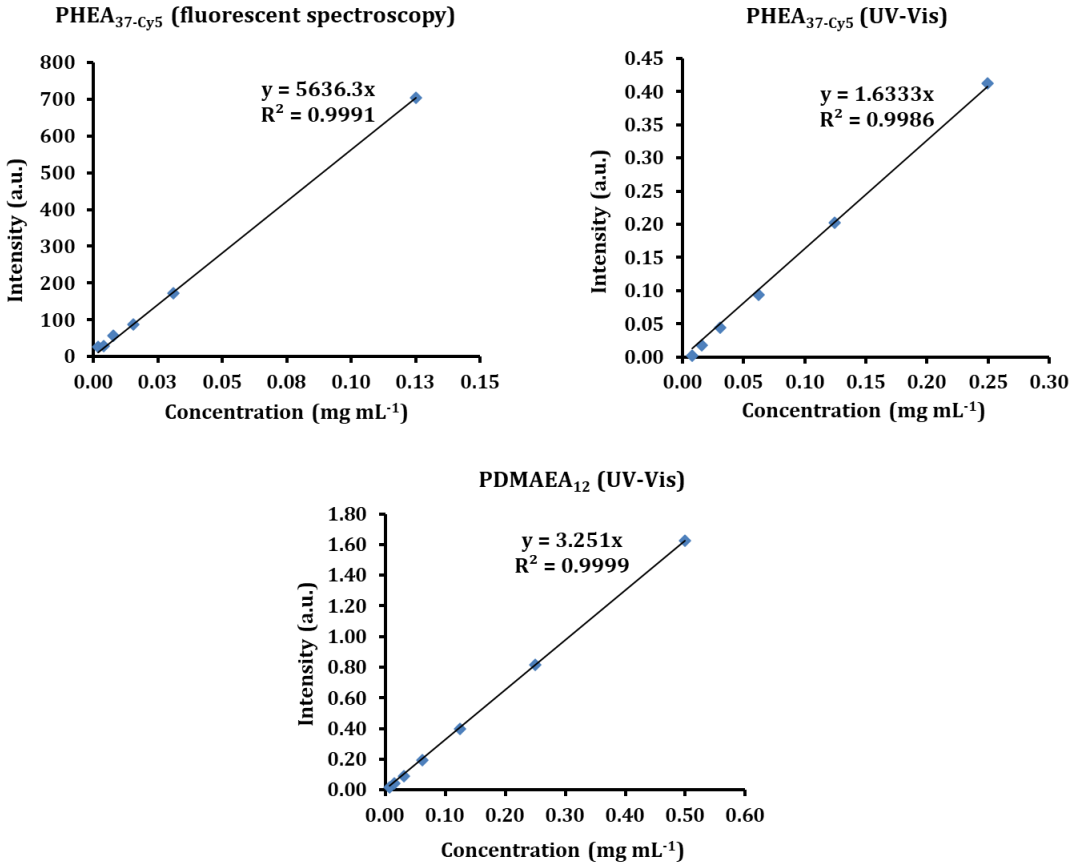

Figure 6.15. Standard curves of $PHEA_{37\text{-}cy5}$ obtained from fluorescent spectroscopy (upper left) and from UV-Vis analysis (upper right). The standard curve of $PDMAEA_{12}$ obtained from UV-Vis analysis (right).

The successful surface grafting was further confirmed by FT-IR spectra. According to **Figure 6.16**, it was observed that (PHEA$_{37\text{-}Cy5}$-PDMAEA$_{12}$)-*g*-CNFs gave a new peak in the spectrum corresponding to the amide II band at 1573 cm^{-1} of PDMAEA, and the higher intensity of a peak at 1725 cm^{-1} that corresponds to the C=O indicate the successful occurrence of surface modification. Moreover, the fluorescent property of grafted nanoparticles was confirmed by fluorescent spectrophotometry at the working concentration of 1 mg mL^{-1} in milli-Q water. The result shows that the nanoparticles emit the light at the wavelength of 670 nm, confirming that the obtained (PHEA$_{37\text{-}Cy5}$-PDMAEA$_{12}$)-*g*-CNFs are suitable for further biological experiments in order to track the uptake of nanoparticles inside the cells (**Figure 6.17**).

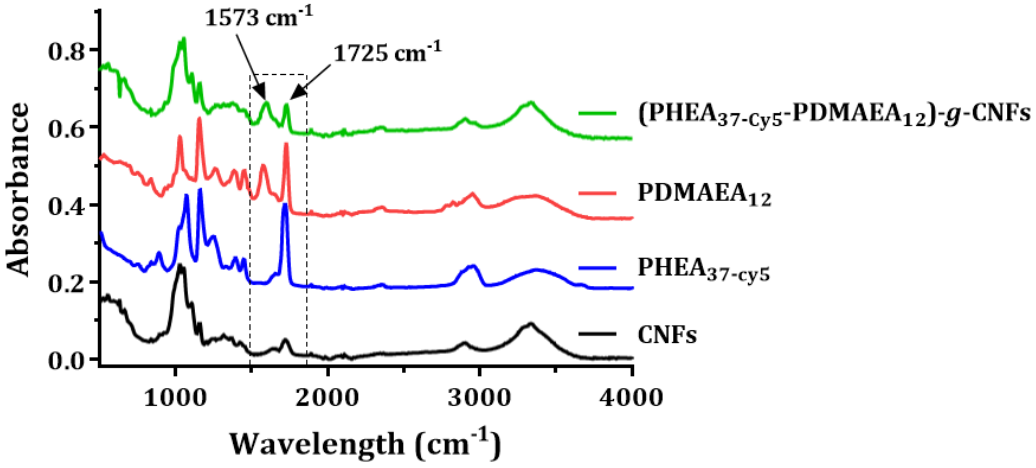

Figure 6.16. FT-IR spectra of CNFs, PHEA$_{37\text{-}Cy5}$, PDMAEA$_{12}$, and (PHEA$_{37\text{-}Cy5}$-PDMAEA$_{12}$)-*g*-CNFs.

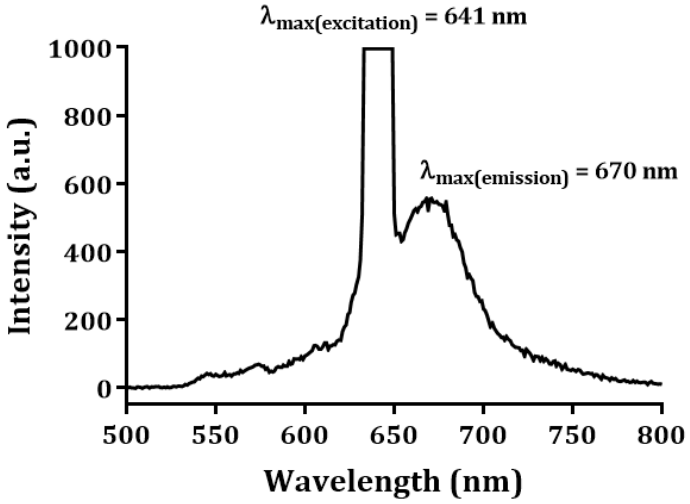

Figure 6.17. The fluorescent spectrum of (PHEA$_{37\text{-}Cy5}$-PDMAEA$_{12}$)-*g*-CNFs in water. $\lambda_{max(excitation)}$ = 641 nm, Voltage = 800 volts, concentration = 1 mg mL^{-1}.

The next step is to investigate the self-catalysed hydrolysis rate of $PDMAEA_{12}$ grafted on CNFs. This study was performed by using the same procedure employed in the degradation experiments of $PDMAEA_{12}$ homopolymers. Briefly, two samples were prepared in a mixture of D_2O and 2 × concentrated PBS (1: 1 v/v)) at pH 7.4. The degradation rate was monitored by ^{1}H-NMR after incubating the samples at room temperature and 37 °C for 15 min, 20 hr and 40 hr respectively. Like previous finding on free $PDMAEA_{12}$ chains, a new peak at 3.83 ppm is evidence of the hydrolysis of grafted PDMAEA to DMAE (**Figure 6.18**). The degradation was calculated by comparing the integration of signals at 3.83 ppm and 3.62 ppm but the accurate results might not be obtained due to the noises on the spectra. The integration of these new peak increased over time. Even though the rate of hydrolysis after 15 min could not be determined, that after 20 hr and 40 hr were calculated as follow: 26.6 % and 31 % at room temperature, and 38.1 % and 45.8 % at 37 °C. Similar to the previous observations, the rate of degradation was higher at 37 °C than at ambient temperature.

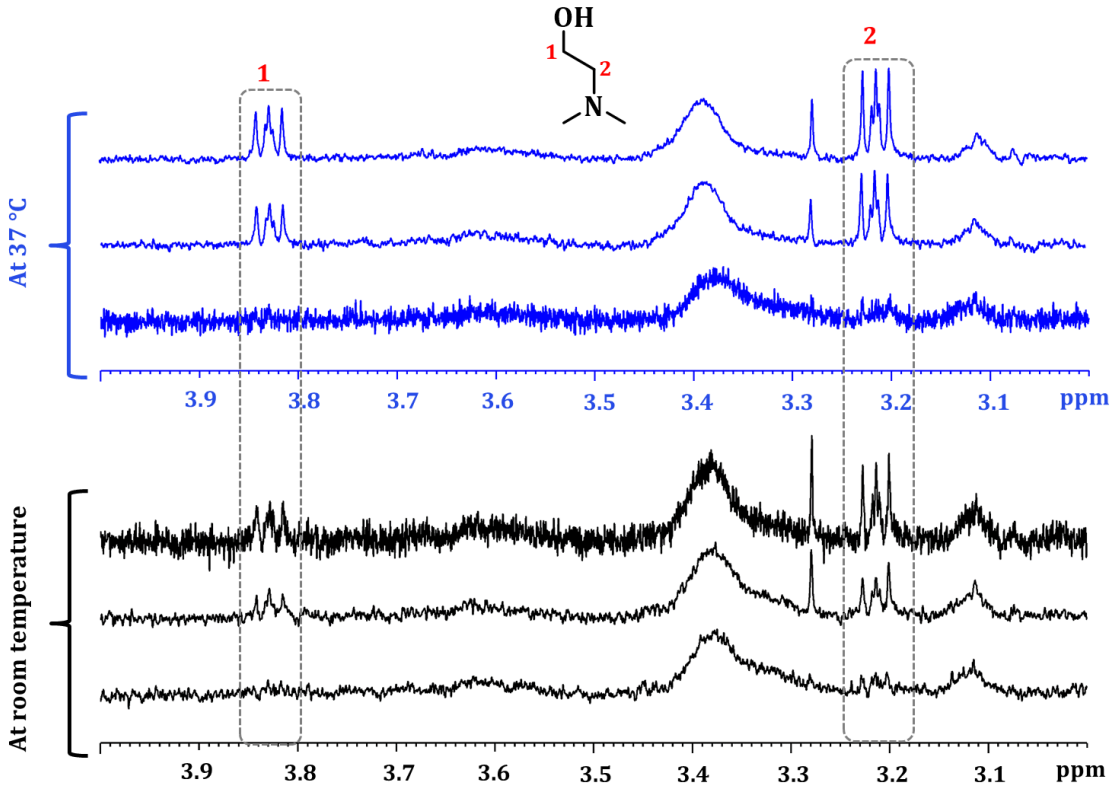

Figure 6.18. ^{1}H-NMR spectra of ($PHEA_{37\text{-}Cy5}$-$PDMAEA_{12}$)-*g*-CNFs in D_2O and PBS (2 × concentrated, pH 7) incubated at room temperature and 37 °C at different time intervals.

The dipsersiblity of (PHEA$_{37\text{-}Cy5}$-PDMAEA$_{12}$)-*g*-CNFs in aqueous media was recoreded at different pH levels as shown **Figure 6.19**. The modified nanoparticles were dispersed in aqueous media at the concentration of 250 µg mL^{-1} and sonicated using a bench sonicator for 10 min. It was observed that a clear dispersion was achieved at high pH around 9, which is probably due to the deprotonation of all amino groups of PDMAEA$_{12}$. At very high pH values, only the negative charged carboxylate groups on the CNFs are presented. At lower pH values the positive charged PDMAEA$_{12}$ may electrostatically interact with negative charges on CNFs. In order to achieve a clear dispersion at pH values of biological relevance, an extended sonication time between 20 – 25 min, depending on the concentration of nanoparticles, needs to be performed. It is also crucial to note that the sonication needs to be performed under cold condition to prevent the degradation of PDMAEA$_{12}$ grafted on the surface of CNFs.

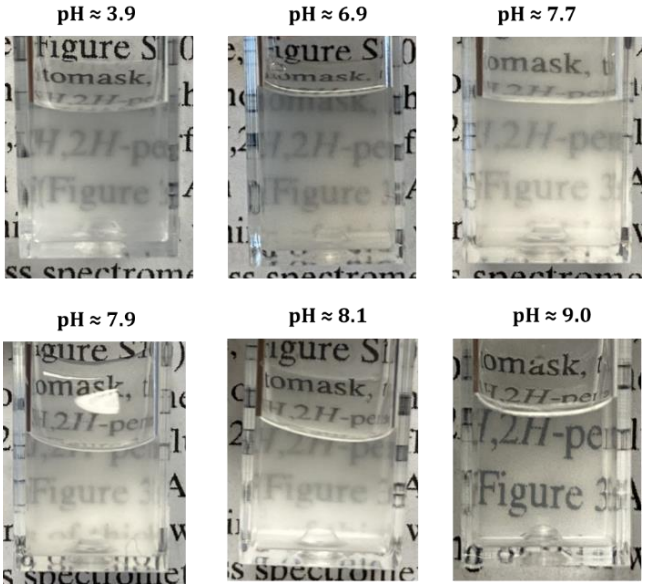

Figure 6.19. Dipersibility test of (PHEA$_{37\text{-}Cy5}$-PDMAEA$_{12}$)-*g*-CNFs in aqueous condition at different pH levels. The concentration of nanoparticles was 250 µg mL^{-1}.

6.3.7. *In vitro* stability of (PHEA$_{37\text{-}Cy5}$-PDMAEA$_{12}$)-*g*-CNFs

After determining the chemical composition of (PHEA$_{37\text{-}Cy5}$-PDMAEA$_{12}$)-*g*-CNFs and the stability in water, the behaviour in biological media was studied. In biological fluids (cell cultures or body fluid), the extracellular proteins can immediately associate with nanoparticles, creating the so-called protein corona, which can

be sufficiently long lived to alter the aggregation state and surface properties of nanoparicles.[477, 478] This in turn critically affects the interactions of the nanoparticles with the cells, altering biological responses.[479] Several studies have been conducted to investigate the influence of nanoparticle properties such as size, shape, and surface structure on protein adsorption, which affects cellular uptake and cytotoxicity.[143, 358, 480-488] Barbalinardo and co-workers showed that citrate-capped silver nanoparticles were stabilized by serum protein in the cell culture medium, and consequently internalized by mouse embryonic fibroblasts (NIH-3T3). These nanoparticles displayed time- and dose-dependent toxicity, whereas uncoated nanoparticles did not result in any internalization or cytotoxicity.[489] Moreover, Anderson *et. al.* observed that an enhanced cytotoxicity and uptake by L929 fibroblasts when the gold nanoparticles were functionalized with poly(di(ethylene glycol) methyl ether methacrylate-*co*-oligo(ethylene glycol) methyl methacrylate) (poly(MeO_2MA_x -*co*-$OEGMA_y$)) brushes.[490] Similar findings have been reported in many studies.[491-494] On the other hand, the protein adsorbed on the surface mitigates the cellular uptake in some cases.[495, 496] In the process of cellular uptake, nanoparticles firstly adhere to the cell membrane, followed by subsequent internalization *via* energy-dependent pathways. However, it was reported that the presence of a protein corona reduced nanoparticle adhesion with cell membranes, causing a decrease in uptake efficiency.[497-499] Moreover, the formation of protein coronas in the bloodstream can stimulate and/or suppress immune cell responses.[500]

As variations in surface properties of nanoparticles (e.g. size, and surface charge) may have a significant impact on protein adsorption, we herein investigated the behaviour of synthesized ($PHEA_{37\text{-}Cy5}$-$PDMAEA_{12}$)-*g*-CNFs in terms of their hydrodynamic size in serum containing cell culture medium. The nanoparticles were therefore incubated in fetal bovine serum (FBS) supplemented cell culture medium (Dulbecco's Modified Eagle's Medium, DMEM) at the concentration of 50 μg mL^{-1}. The changes in the hydrodynamic size was then recorded by DLS after exposed to cell culture medium for various time points: 0 hr, 1 hr, 2 hr, 4 hr, 6 hr and 8 hr. **Figure 6.20** showed the comparison between hydrodynamic diameters of synthesized ($PHEA_{37\text{-}Cy5}$-$PDMAEA_{12}$)-*g*-CNFs with and without exposure to cell culture medium (DMEM). By comparing with the control nanoparticles suspended in pure water, it

was observed that there was an increase in hydrodynamic diameter of nanoparticles in biological fluid, which was more obvious after 4 hr of incubation as indicative of the formation of protein corona. The peaks between 1 and 100 nm are due to the small biomolecules in the culture medium. Although there was a gradual increment in mean diameter, the significant agglomerates based on the interaction with serum components were not observed. The *in vitro* stability of designed nanoparticles can lead to the prolong circulation in the blood stream after administration into the body.

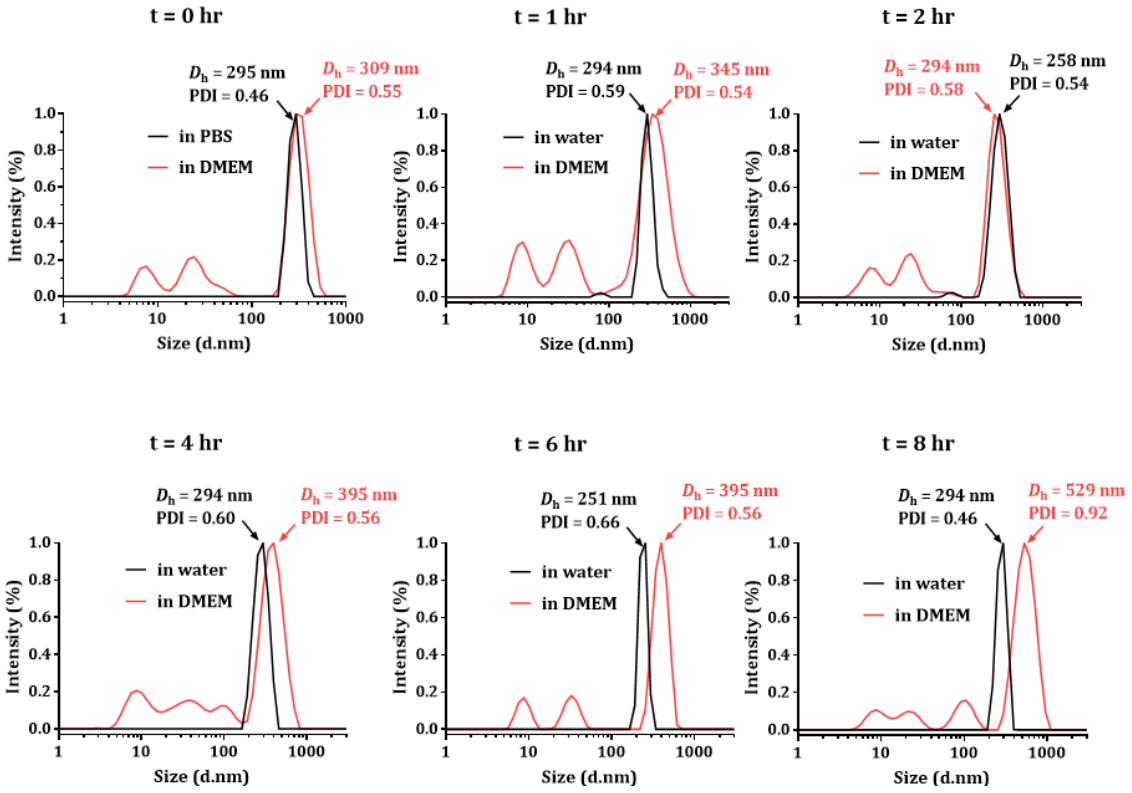

Figure 6.20. The comparison between hydrodynamic diameters of synthesized ($PHEA_{37\text{-}Cy5}$-$PDMAEA_{12}$)-*g*-CNFs with and without exposure to cell culture medium (DMEM) at the concentration of 50 µg mL^{-1}.

6.3.8. Binding MIP-1α chemokines on ($PHEA_{37\text{-}Cy5}$-$PDMAEA_{12}$)-*g*-CNFs *via* electrostatic interaction

Investigation on the particle size distribution by DLS

The MIP-1α chemokines were loaded onto the synthesized ($PHEA_{37\text{-}Cy5}$-$PDMAEA_{12}$)-*g*-CNFs *via* electrostatic interaction by taking an advantage of cationic

$PDMAEA_{12}$ on the surface of nanoparticles and the predominantly anionic charge of MIP-1α (isoelectric point at pH 4.7). The experiment was performed in pH 7.4 PBS while keeping the solution cold to slow down the degree of $PDMAEA_{12}$ hydrolysis. The size distribution of polymer-*g*-CNFs in PBS at the concentration of 100 μg mL^{-1} was initially recorded, followed by the addition of MIP-1α (62.5 ng) every 2 hr until it reached 0.25 % of chemokines loading content at 8 hr. The loading content was calculated by comparing the mass of MIP-1α with the mass of nanoparticles. The hydrodynamic diameters of MIP-1α-loaded samples at each time point was recorded by DLS, which was then compared with the control samples prepared in an absence of MIP-1α. Here, the significant changes in the particle size was not observed due to the binding low molecular weight chemokines onto grafted CNFs (**Figure 6.21**).

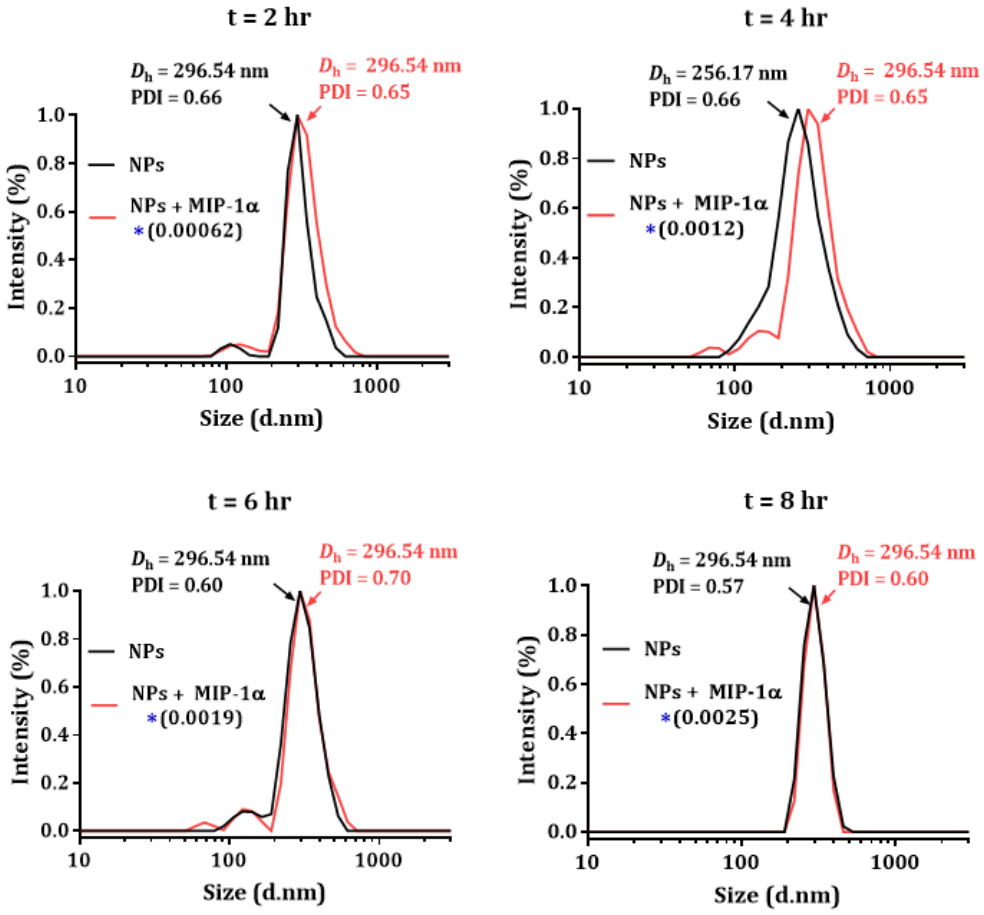

Figure 6.21. The comparison between hydrodynamic diameters of synthesized ($PHEA_{37\text{-}Cy5}$-$PDMAEA_{12}$)-*g*-CNFs with and without exposure to serial concentration of MIP-1α chemokines. Polymer concentration = 100 μg mL^{-1} in pH 7.4 PBS. NPs means ($PHEA_{37\text{-}Cy5}$-$PDMAEA_{12}$)-*g*-CNFs. * MIP-1α loading content.

Investigation on MIP-1α binding at different nanoparticle concentrations via BD™ cytometric bead array (CBA) assay

The investigation on the binding of selected chemokines at various concentrations of (PHEA$_{37\text{-}Cy5}$-PDMAEA$_{12}$)-*g*-CNFs was carried out by BD™ cytometric bead array (CBA) assay. The process of CBA assay generally involves four steps as illustrated in **Figure 6.22**: (1) Capturing target chemokines by specific antibodies on the surface of capture beads upon mixing and incubation, (2) Binding biotinylated detection antibodies to the chemokine bound on the capture bead, forming capture bead-chemokine-detection antibody sandwiches, (3) Addition of streptavidin-phycoerythrin (SA-PE) to bind to the biotinylated detection antibodies, which provides fluorescent intensities in proportion to the amount of bound analyte, (4) Determination and quantification of fluorescent signal using a flow cytometer. The collected data were then used to determine the concentration of analytes based on the known standard curve using the LEGENDplex™ data analysis software.[501, 502]

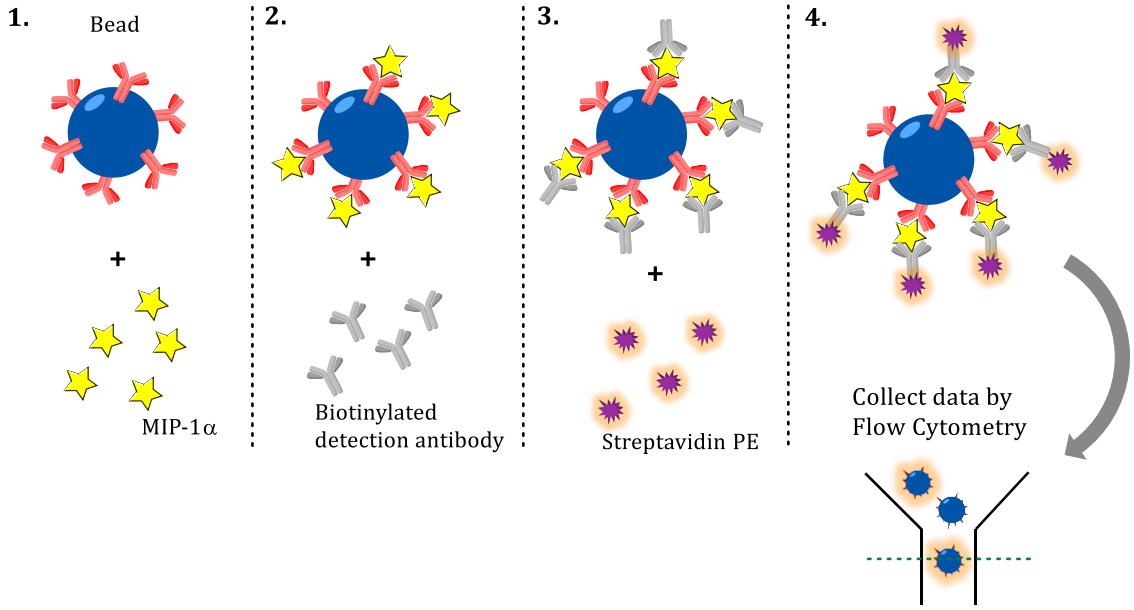

Figure 6.22. The step-by-step process BD™ cytometric bead array (CBA) assay for the quantification of MIP-1α.

The concept behind the sample analysis is as followed: The unbound MIP-1α on nanoparticles were firstly collected by centrifugal filtration and submitted for quantification *via* CBA assay. The obtained data was subsequently used to calculate the amount of chemokines attached on the surface of designed nanoparticles.

According to **Figure 6.23**, the unbound chemokines were virtually undetectable when higher mass ratio of MIP-1α and NPs (1: 4.6×10^3 and 1: 9.2×10^3) was used, while 15.6 ng mL^{-1} was detected for the sample with less amount of NPs with the mass ratio of 1: 2.3×10^3 MIP-1α: NPs. Based on these results, it was interpreted that 38.8 ng of MIP-1α was bound when 1: 2.3×10^3 MIP-1α: NPs (mass ratio) was used.

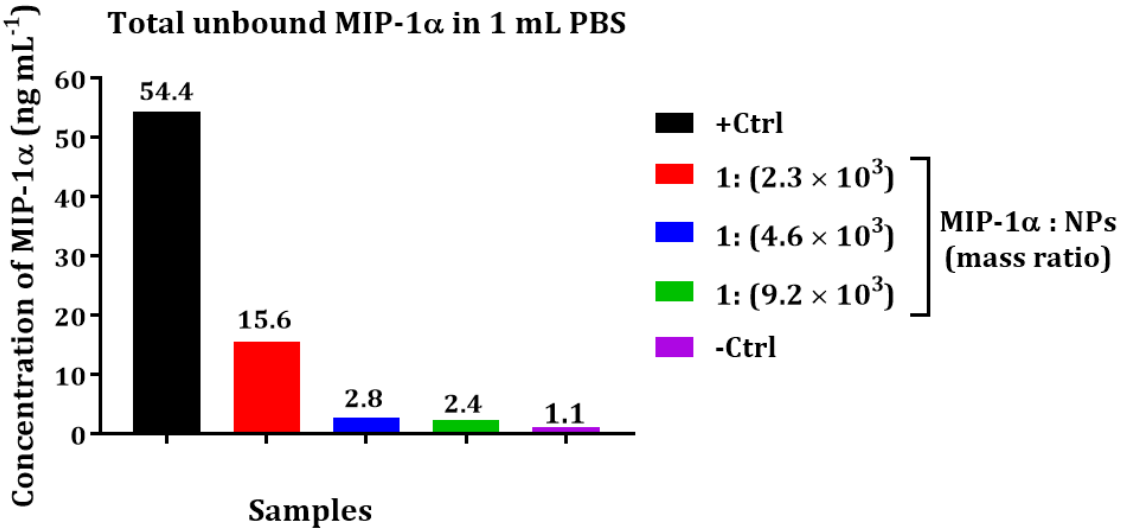

Figure 6.23. The concentration of unbound MIP-1α to nanoparticles determined by BD™ cytometric bead array (CBA) assay. All chemokines binding to ($PHEA_{37\text{-}Cy5}$-$PDMAEA_{12}$)-*g*-CNFs were performed in 1 mL PBS (pH 7.4). +Ctrl and -Ctrl stand for positive control (54.4 ng of MIP-1α in 1 mL PBS), and negative control (only PBS), respectively. NPs = nanoparticles (($PHEA_{37\text{-}Cy5}$-$PDMAEA_{12}$)-*g*-CNFs).

6.3.9. Biological experiments of ($PHEA_{37\text{-}Cy5}$-$PDMAEA_{12}$)-*g*-CNFs

In vitro cell viability assay

The breast cancer cell line MCF-7 was chosen to test the cytotoxicity of the synthesized ($PHEA_{37\text{-}Cy5}$-$PDMAEA_{12}$)-*g*-CNFs at the maximum concentration of 0.5 mg mL^{-1}. After incubation at various concentrations of the grafted CNFs with the cells for 48 hr, it was observed that the nanoparticles were relatively non-toxic below the chosen concentration (**Figure 6.24**) and can therefore be used for further biological experiments.

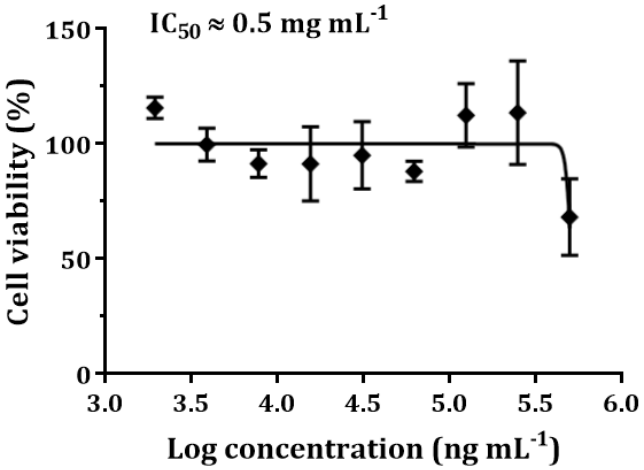

Figure 6.24. *In vitro* cell viability (%) assay of ($PHEA_{37\text{-}Cy5}$-$PDMAEA_{12}$)-*g*-CNFs against MCF-7 cancer cells at the maximum concentration of 0.5 mg mL^{-1}.

In vitro cellular uptake study by Laser Scanning Confocal Microscopy (LSCM)

The cellular uptake of fluorescently labelled nanoparticles ($PHEA_{37\text{-}Cy5}$-$PDMAEA_{12}$)-*g*-CNFs by MCF-7 breast cancer cells was subsequently monitored by using laser scanning confocal microscopy (LSCM). The imaging was performed by taking the advantage of cyanine 5 on nanoparticles. In this study, the cells were incubated with 0.25 mg mL^{-1} of nanoparticles for 2 hr and 8 hr. The results presented in **Figure 6.25** showed a high uptake of nanoparticles even after 2 hr of incubation by MCF-7 cells. The nuclei in blue colour and surrounding nanoparticles in red colour confirm the successful accumulation of synthesized polymers-grafted cellulose nanofibers inside the cells.

To further quantify the cellular uptake, the fluorescent intensity was measured by flow cytometric analysis. The results were subsequently normalized by taking the fluorescence of nanoparticles into account. As shown in **Figure 6.26**, the significant difference from the control (non-treated cells) was already observed after 2 hr of cell exposure to nanoparticles at the concentration of 250 µg mL^{-1}. Furthermore, the progressive accumulation was still found after 8 hr of incubation at 37 °C. The relatively high cellular uptake might be caused by the rod-like morphology or the surface charge of cellulose nanomaterials.[358, 503]

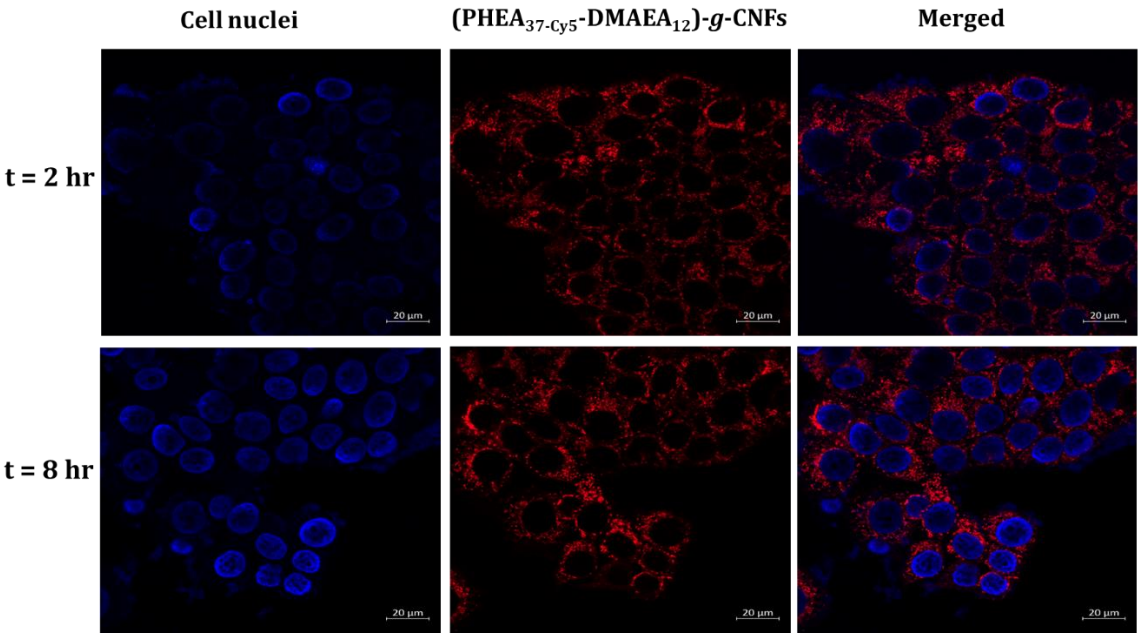

Figure 6.25. Confocal microphotographs of MCF-7 cells after incubation with aqueous dispersion of ($PHEA_{37\text{-}Cy5}$-$PDMAEA_{12}$)-*g*-CNFs at 37 °C for 2 hr and 8 hr. The blue colour represents the cell nuclei stained with Hoechst 33342 and the red colour represents the ($PHEA_{37\text{-}Cy5}$-$PDMAEA_{12}$)-*g*-CNFs.

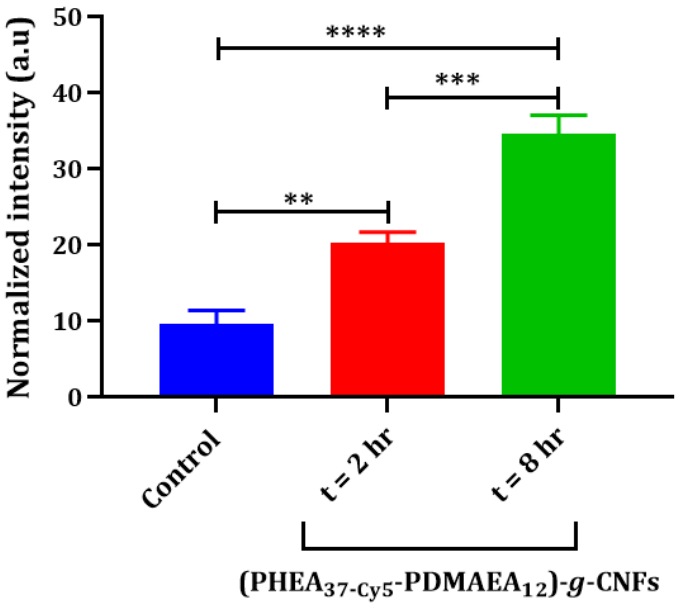

Figure 6.26. Normalized fluorescence intensity of nanoparticles inside MCF-7 cancer cells determined by flow cytometry.

Penetration and uptake of nanoparticles in 3D tumour spheroids

Moreover, the tumour penetration ability of nanoparticles ((PHEA$_{37\text{-}Cy5}$-PDMAEA$_{12}$)-*g*-CNFs) was assessed using a WM-983c melanoma spheroid model, which was designed by the group of Maté Biro in School of Medicine, UNSW, Australia. The tumour spheroid was surrounded by a collagen/mt-CAFs (metastatic cancer-associated fibroblasts) matrix. After incubating the tumour spheroid with drug carriers ((PHEA$_{37\text{-}Cy5}$-PDMAEA$_{12}$)-*g*-CNFs) at the concentration of 1 mg mL^{-1}, the penetration and localization of nanoparticles within 18 min and 18 hr were monitored by laser scanning confocal microscopy (LSCM). **Figure 6.27** displays the quantification of uptake by measuring the mean intensity of nanoparticles inside and outside the spheroid within 18 hr of incubation. In accordance with the measured cellular uptake, the nanoparticles were readily taken up by the spheroid. It is however unclear if the elongated nanoparticles, which have a high aspect ratio, take the transcellular or paracellular route. Moreover, it was observed that the penetration seems to be ongoing even after the set time frame. The successful cellular uptake was also visualized by confocal images shown **in Figure 6.28**, in which dark blue represents the melanoma spheroid, cyan represents cancer-associated fibroblasts (mt-CAFs), and magenta represents nanoparticles. The magenta fluorescence signal in tumour indicates the localization of nanoparticles in the core of tumour spheroid. As expected, penetration into 3D spheroid took longer time comparing with that into 2D cell culture model.

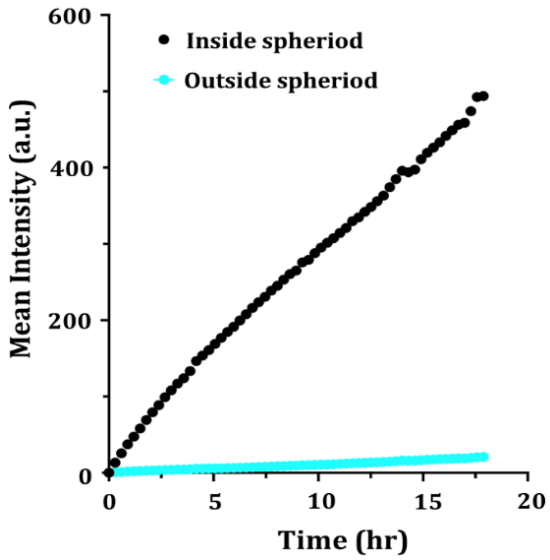

Figure 6.27. Monitored mean fluorescence intensity of designed (PHEA$_{37\text{-}Cy5}$-PDMAEA$_{12}$)-*g*-CNFs inside and outside the 3D spheroid over an 18-hr period.

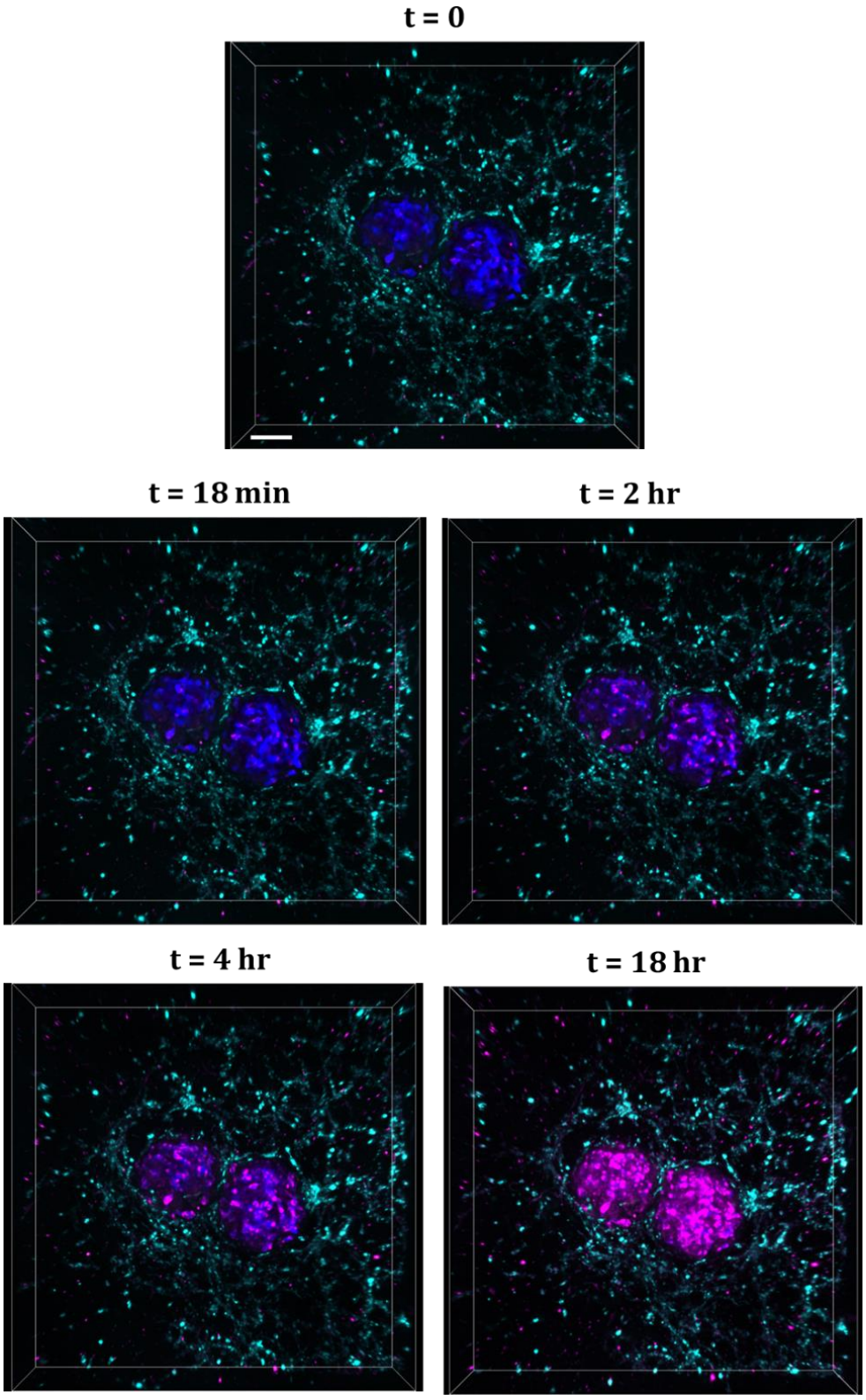

Figure 6.28. Penetration of designed ($PHEA_{37\text{-}Cy5}$-$PDMAEA_{12}$)-*g*-CNFs into WM-983c melanoma spheroid monitored *via* Laser Scanning Confocal Microscopy. Dark blue: Melanoma spheroid, cyan: cancer-associated fibroblasts, and magenta: ($PHEA_{37\text{-}Cy5}$-$PDMAEA_{12}$)-*g*-CNFs. NPs means nanoparticles (($PHEA_{37\text{-}Cy5}$-$PDMAEA_{12}$)-*g*-CNFs). The scale bar = 100 µm.

6.4. Conclusion

In summary, we reported a design of fluorescent cellulose-based nanomaterials ((PHEA$_{37\text{-}Cy5}$-PDMAEA$_{12}$)-*g*-CNFs) *via* three-component Passerini reaction to efficiently bind immunochemokines (MIP-1α). Our studies showed that the synthesized nanoparticles exhibited high *in vitro* stability in biological media as well as non-toxic behaviour against MCF-7 cancer cell lines. But the application of nanoparticles needs to be carefully undertaken due to the hydrolysis behaviour of PDMAEA chains especially at high temperature. According to the cellular penetration and localization assay in 2D and 3D cell models, it was observed that nanoparticles were successfully internalized into both cell models even after 2 hr of incubation time. Our results highlight the application of Passerini reaction to prepare cellulose-based functional materials that have the biological properties to achieve efficient delivery of therapeutic agents into tumours.

6.5. Experimental Procedure

6.5.1. Synthesis of *N*-(2-formylethyl)-3-(benzylthiocarbonothioylthio)propionamide (RAFT agent)

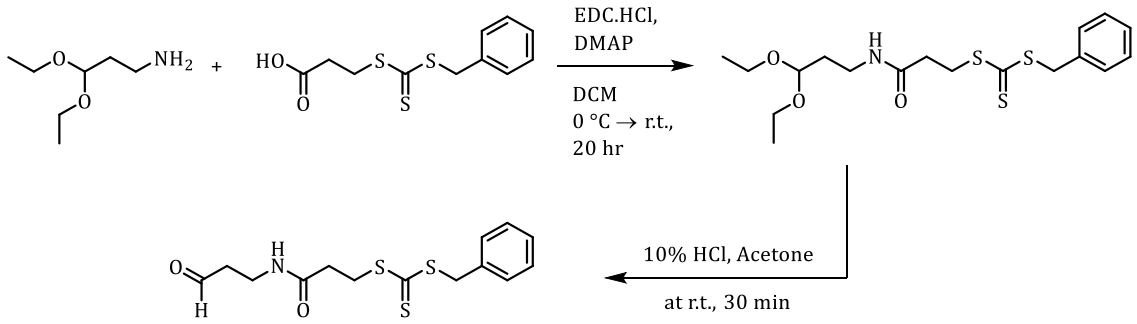

Scheme 6.4. Schematic illustration for the synthesis of aldehyde-functionalized chain transfer agent.

3-(benzylthiocarbonothioylthio)propanoic acid (5.18 mmol, 1.41 g) and *N*-(3-dimethylaminopropyl)-*N'*-ethylcarbodiimide hydrochloride (EDC.HCl) (7.82 mmol, 1.50 g) were dissolved in anhydrous DCM (15 mL) and the solution was cooled on an ice water bath. After 30 min, a solution of 1-amino-3,3-diethoxypropane (3.40 mmol, 0.50 g) and 4-(dimethylamino)pyridine (DMAP) (1.39 mmol, 0.17 g) in anhydrous DCM (5 mL) was added dropwise while stirring. After 1 hr, the reaction was allowed to warm up to room temperature and left for 22 hr. Then, the solution was diluted with DCM (40 mL) and extracted with water (3 × 50 mL) and then brine (2 × 50 mL). The organic phase was dried over magnesium sulfate ($MgSO_4$) and concentrated under vacuum. To remove unreacted acetal, the residue was dissolved in 1 mL of acetone, followed by the dropwise addition of 10 % aqueous solution of hydrochloric acid (1 mL) into the reaction mixture. After 30 min of stirring at room temperature, the solution was diluted with DCM (50 mL) and extracted with water (3 × 50 mL), then brine (1 × 50 mL). The organic phase was dried over $MgSO_4$ and concentrated under vacuum. Crude product was purified by silica gel flash chromatography (hexane: ethyl acetate 5: 1 → 1: 1) to afford *N*-(2-formylethyl)-3-(benzylthiocarbonothioylthio) propionamide as yellow oil (0.586 g, 34 %).

^{1}H-NMR (400 MHz, $CDCl_3$): δ/ppm = 9.79 (1H, -$CH_2C(O)H$), δ = 7.34 - 7.26 (5H, C*H*phenyl), δ = 6.01 (1H, -C(O)N*H*-), δ = 4.60 (2H, CHphenyl CH_2-), δ = 3.66 – 3.61 (2H, 2H, -C(S)SCH_2-), δ = 3.57 – 3.51 (-NHCH_2-), δ = 2.76 – 2.74 (2H, -CH_2C(O)NH-), and δ = 2.60 – 2.55 (2H, -CH_2C(O)H).

^{13}C-NMR (400 MHz, $CDCl_3$): δ/ppm = 223.44 (-S*C*(S)S-), 201.36 (-CH_2*C*(O)H-), 170.30 (-CH_2*C*(O)NH-), 134.87 (phenyl, *ipso*), 129.28 (phenyl, *ortho*), 128.73 (phenyl, *meta*), 127.83 (phenyl, *para*), 43.74 (phenyl CH*C*H_2-), 41.52 (-*C*H_2C(O)H-), 34.94 (-C(S)S*C*H_2-), 32.98 (-C(O)NH*C*H_2-), and 32.06 (-*C*H_2C(O)NH-).

6.5.2. Synthesis of aldehyde-terminated polymers

Synthesis of poly(2-hydroxyethyl acrylate) PHEA$_{37}$

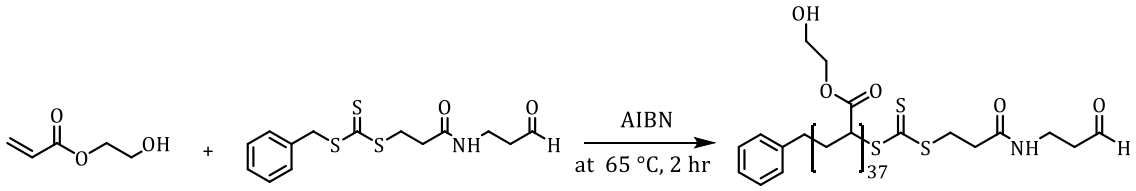

Scheme 6.5. Schematic illustration for the synthesis of PHEA$_{37}$.

The hydrophilic monomer, 2-hydroxyethyl acrylate was polymerized *via* RAFT polymerization using synthesized aldehyde-terminated RAFT agent. In a glass vial, 2-hydroxyethyl acrylate (HEA) (2.00 g, 17.22 mmol), RAFT-aldehyde (68.78 mg, 210.04 µmol), and the initiator AIBN (2.75 mg, 16.80 µmol) were dissolved in *N,N*-dimethylformamide (DMF). The molar ratio of [HEA]: [RAFT]: [AIBN] was 82: 1: 0.08 and a monomer concentration was 2 M. The flask containing the mixture was sealed with rubber septum and the solution was degassed with nitrogen purging for 45 min. The polymerization was performed at 65 °C for 2 hr to achieve 46 % monomer conversion. Then the polymerization was ceased by introducing air to the mixture and placing the vial in an ice bath for 15 min. The resulting polymer was purified *via* dialysis against methanol (MeOH) for 2 days and then dried under vacuum. The pure polymer was characterized *via* ^{1}H-NMR and SEC. M_n (SEC) =15000 g mol^{-1} and $Đ$ = 1.21.

Synthesis of poly(2-(dimethylamino)ethyl acrylate) PDMAEA$_{12}$

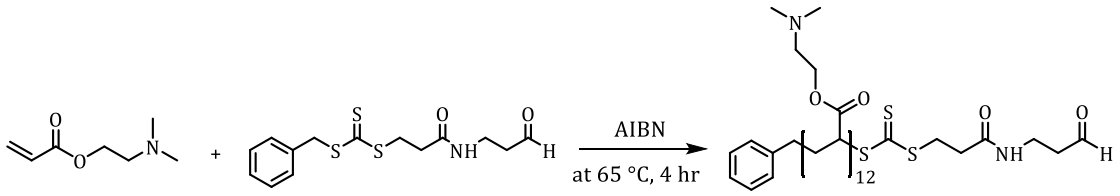

Scheme 6.6. Schematic illustration for the synthesis of PDMAEA$_{12}$.

The polymerization procedure of PDMAEA$_{12}$ was similar to the synthesis of PHEA$_{37}$. Firstly, 2-(dimethylamino) ethyl acrylate monomer/DMAEA (3.00 g, 20.95 mmol), RAFT-aldehyde (83.93 mg, 0.21 mmol) and AIBN initiator (3.43 mg, 20.91 µmol) were dissolved in DMF (7.27 mL) in a round bottom flask. The concentration of monomer was 2 M and the molar ratio of [DMAEA]: [RAFT]: [AIBN] was 100: 1: 0.1. The solution was degassed with nitrogen purging for 45 min, and then placed into a preheated oil bath at 65 °C. The polymerization was stopped after 4 hr by introducing air to the solution and placing the vial in an ice bath for 15 min. The resulting polymer was purified by precipitation four times into hexane and the obtained pure polymer was dried under vacuum. The monomer conversion and molecular weight of the pure polymer were analysed *via* ^{1}H-NMR and SEC. M_n (SEC) =2740 g mol^{-1} and $Đ$ = 1.27.

6.5.3. Synthesis of cyanine-5 (Cy5) fluorescent dye

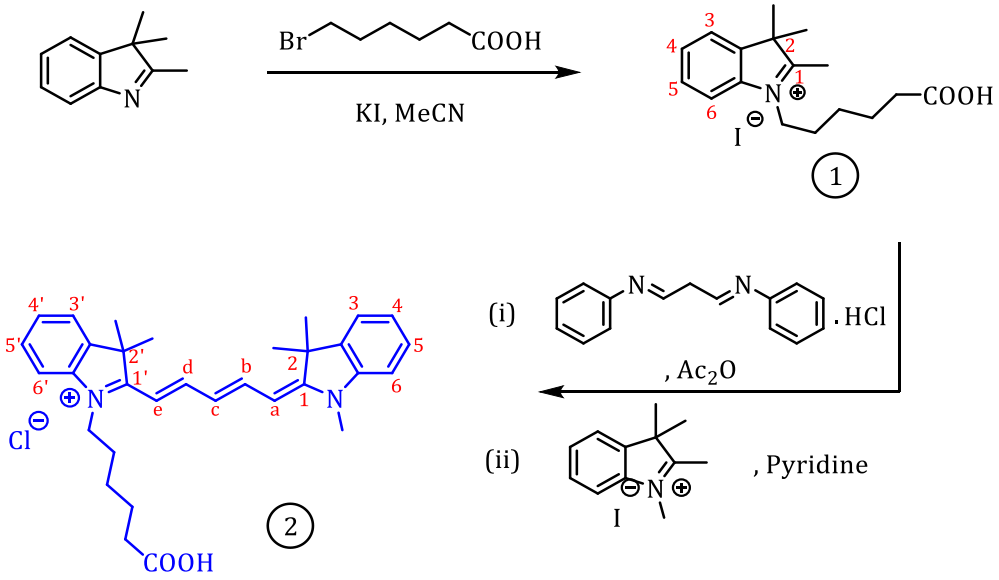

Scheme 6.7. Schematic illustration for the synthesis of cyanine 5 (compound 2).

The synthesis of cyanine 5 was performed according to the procedure from the literature[473, 474] using a two-step method. The intermediate 1 (1-(5-Carboxypentyl)-2,3,3-trimethyl-3*H*-indolium iodide) was synthesized by dissolving 2,3,3-trimethyl-3*H*-indole (2.5 g, 15.5 mmol), 6-bromohexanoic acid (3.9 g, 20.2 mmol) and potassium iodide (3.4 g, 20.2 mmol) in acetonitrile in a round bottom flask. The reaction mixture was then heated to 85 °C and refluxed for a day. The reaction mixture was then allowed to cool down to room temperature and filtered. After removing the solvent under vacuum, the concentrated crude was precipitated five times into cold diethyl ether until brown precipitated salts were obtained. After drying the solid under reduced pressure, intermediate 1 with a yield of 1.725 g, 4.299 mmol (27 %) was obtained.

^{1}H-NMR (400 MHz, DMSO-d$_6$): δ/pp m = 7.98 – 7.95 (m, 1H, 6-*H*), δ = 7.86 – 7.83 (m, 1H, 3-*H*), δ = 7.66 – 7.60 (m, 2 H, 4-*H*, 5-*H*), δ = 4.47 – 4.42 (t, 2H, -NC*H*$_2$-), δ = 2.84 (s, 3H, 1-C*H*$_3$), δ = 2.25 – 2.21 (t, 2 H, C*H*$_2$C(O)OH), δ = 1.85 (m, 2H, -NCH$_2$C*H*$_2$-), δ = 1.61 – 1.52 (m, 8H, C*H*$_2$CH$_2$C(O)OH, 2-C*H*$_3$), and 1.47 – 1.38 (m, 2H, -NCH$_2$CH$_2$C*H*$_2$-).

Secondly, the synthesized indolium intermediate was employed to synthesize cyanine 5 acid fluorescent dye. The indolium intermediate 1 (1 g, 2.52 mmol) and malonaldehyde bis(phenylimine) monohydrochloride (0.75 g, 3 mmol) were dissolved in acetic anhydride (6 mL) and the solution was heated to 120 °C under reflux condition. After 30 min, the reaction was allowed to cool down to room temperature, followed by the addition of 1,2,3,3-tetramethyl-3*H*-indolium iodide (1.04 g, 3.5 mmol) and pyridine (5.72 mL). The reaction was left stirring for 18 hr, the formation of cyanine 5 was observed by the change in the colour of the solution to dark blue. After concentrating the mixture under vacuum at 50 °C, the residue was precipitated in hexane (100 mL) twice. After that, the obtained blue oil was diluted in chloroform (100 mL), extracted with water (2 × 100 mL) and then brine (100 mL). The organic phase was then dried over MgSO$_4$, filtered, and concentrated under vacuum. Finally, the crude product was purified by flash column chromatography (chloroform: acetone: methanol 7: 2: 0.2 → 7: 2: 0.6). After removing the impurities, the last purple fraction was flushed out using pure methanol. Pure fractions were then

concentrated under vacuum to collect the product in the form of crystals with a yield of 238 mg, 0.46 mmol (18.45 %).

^{1}H-NMR (400 MHz, DMSO-d_6): δ/ppm = 8.37 – 8.28 (t, 2H, b-*H*, d-*H*), δ = 7.63 – 7.60 (d, 2H, 3-*H*, 3'-*H*), δ = 7.42 – 7.37 (m, 4H, 5-*H*, 6-*H,* 5'-*H*, 6'-*H*), δ = 7.28 – 7.21 (m, 2H, 4-*H*, 4'-*H*), δ = 6.61 – 6.53 (t, 1H, c-*H*), δ = 6.32 – 6.25 (m, 2H, e-*H*, a-*H*), δ = 4.08 (m, 2H, -NC*H*$_2$-), δ = 3.60 (s, 3H, -NC*H*$_3$-), 2.08 – 2.03 (t, 2H, -C*H*$_2$C(O)OH-), and 1.67 – 1.54 (m, 18H, 2-C*H*$_3$, 2'-C*H*$_3$, -NCH$_2$C*H*$_2$C*H*$_2$C*H*$_2$-).

6.5.4. Fluorescent labelling of $PHEA_{37}$

The preparation of fluorescently labelled $PHEA_{37}$ was carried out by using synthesized cyanine 5 acid under mild reaction condition. Cyanine dye (3 mg, 4.59 μmol) and *N*,*N*′-Dicyclohexylcarbodiimide (DCC) (11 mg, 53.40 μmol) were dissolved in anhydrous DMF (1.5 mL) and stirred at room temperature for 30 min. After that, $PHEA_{37}$ (700 mg, 0.15 mmol) and 4-(dimethylamino)pyridine (DMAP) (7 mg, 57.30 μmol) dissolved in anhydrous DMF (1 mL) were added to the solution and stirred overnight. The obtained mixture was then dialysed against methanol (1 kDa MWCO) to remove unreacted fluorescent dye, followed by removing the solvent and drying under vacuum.

6.5.5. Hydrolysis kinetics of $PDMAEA_{12}$ in PBS at pH 7.4

The hydrolysis of $PDMAEA_{12}$ in phosphate buffer saline (PBS) at pH 7.4 was performed at room temperature and at 37 °C. Firstly, 7 mg of $PDMAEA_{12}$ was dissolved in the mixture of D_2O and 2 × concentrated PBS (1: 1 v/v) at the concentration of 2.35 mg mL^{-1}. After that, two NMR tubes were filled with 650 μL of solution and incubated at room temperature and 37 °C. The ^{1}H-NMR measurements (400 MHz) were performed at different time intervals: 15 min, 20 hr and 40 hr. The percentage of hydrolysis was calculated according to following equation based on the integrated intensity of signals at δ = 3.62 ppm and 3.81 ppm. (I = intensity of the peak)

$$\text{Hydrolysis (\%)} = \frac{I_{3.62}}{I_{3.62} + I_{3.81}} \times 100$$

6.5.6. Investigation on the factors affecting surface grafting efficiency

In this approach, $PHEA_{37}$ was employed as a model polymer to be grafted on CNFs under various solvent systems. The CNFs gel (876 mg containing 5 mg of dry solid, 4.62 µmol of -COOH groups) and $PHEA_{37}$ (11.9 mg, 2.57 µmol) were added to each glass vial. In this experiment, less viscous CNFs gel was used to obtain an efficient surface modification reaction (**Chapter 3**). The mixture was then dissolved in different solvent system, followed by slow addition of cyclohexyl isocyanide (8.78 mg, 0.08 mmol, 10 µL). **Figure 6.29** illustrates the different solvent systems applied in this experiment. To be noted here is that CNFs gel itself contain approximately 1 mL of water content. Therefore, the final solvent volume and concentration was calculated by taking the water content of CNFs gel into account. After stirring overnight, the obtained dispersion was dialysed against milli-Q water (12 – 15 kDa MWCO) for two days to remove organic solvent, small molecules, and free polymers, followed by freeze drying. The dried samples were redispersed in methanol and centrifuged at 14000 rpm for 10 min. The washing by centrifuge was repeated several times to completely remove unattached polymer chains. Then dialysed against water for one day to remove methanol, followed by freeze drying. The dried polymer-grafted CNFs samples were analysed *via* UV-Vis.

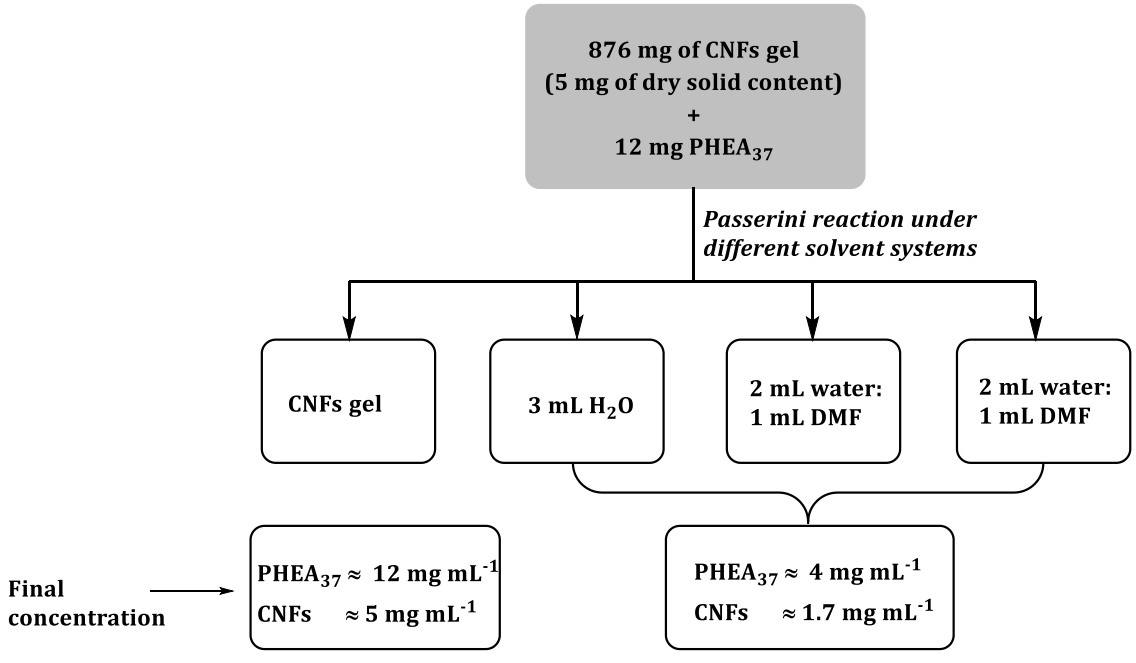

Figure 6.29. Synthesis of $PHEA_{37}$-grafted CNFs under various solvent systems.

6.5.7. Co-grafting of $PHEA_{37\text{-}Cy5}$ and $PDMAEA_{12}$ onto CNFs *via* Passerini Reaction in organic solvent

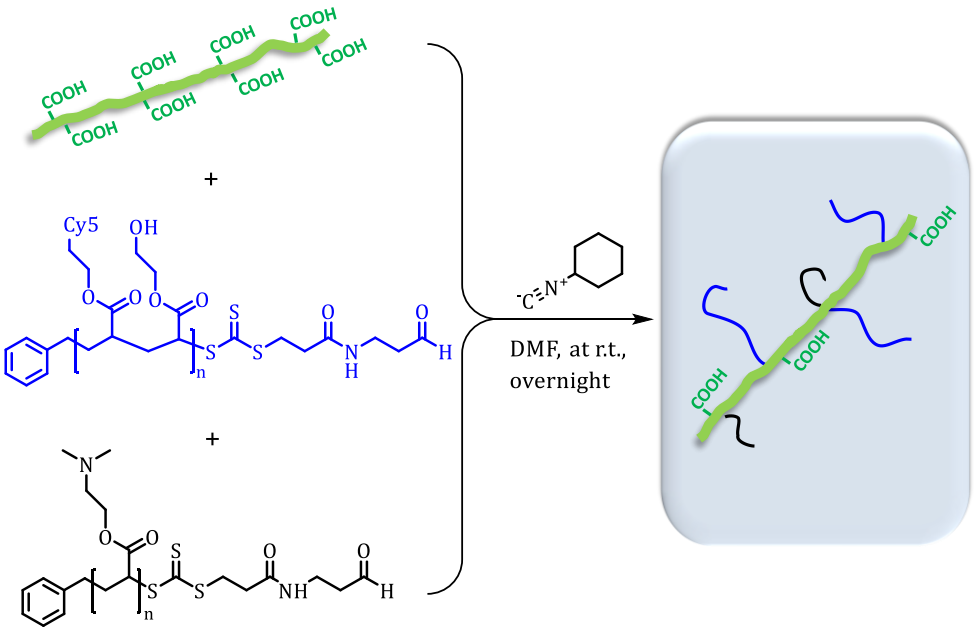

Scheme 6.8. Schematic illustration for the preparation of polymer-grafted CNFs *via* Passerini reaction under mild conditions.

The covalent tethering of homopolymers onto CNFs was performed *via* a three-component Passerini reaction under mild conditions. The dried CNFs (10 mg, 16.5 µmol of -COOH groups) was dispersed in DMF (0.3 mL) in a glass vial and sonicated using the bench sonicator for 15 – 30 min. On the other hand, $PHEA_{37}$ (20 mg, 4.32 µmol) dissolved in DMF (0.2 mL) was added to three vials containing 35 mg, 25 mg, and 10.7 mg of $PDMAEA_{12}$, followed by the addition of mixture to the CNFs dispersion. Finally, the cyclohexyl isocyanide (17.56 mg, 0.16 mmol, 20 µL) was slowly added to the mixture. After overnight stirring at room temperature, the polymer modified CNFs were collected by precipitating in water (1.5 mL) and centrifugation at 15000 rpm for 10 mins. The purification was repeated six times until almost clear supernatant was achieved. After freeze drying the collected modified cellulose nanomaterials, the samples were submitted for characterizations using UV-Vis, FT-IR, DLS and ^{1}H-NMR. **Table 6.2** listed the initial ratios of CNFs and homopolymers added to perform the surface modification reaction.

Table 6.2. The initial ratio of CNFs, $PHEA_{37}$ and $PDMAEA_{12}$ for surface modification reaction.

Sample number	Components	Initial mass ratio of CNFs: $PHEA_{37}$: $PDMAEA_{12}$ (mg)	Initial molar ratio of -COOH groups from CNFs: $PHEA_{37}$: $PDMAEA_{12}$ (mol)
1	CNFs: $PHEA_{37}$: $PDMAEA_{12}$	10: 20: 35	1: 0.25: 1.04
2		10: 20: 25	1: 0.25: 0.74
3		10: 20: 10.7	1: 0.25: 0.31

Calculation of grafting efficiency

The determination of grafting efficiency was performed using two characterizations: fluorescent spectrophotometer and UV-Vis. Firstly, the calibration curves for both polymer chains: $PHEA_{37\text{-}Cy5}$ and $PDMAEA_{12}$, were prepared by dissolving in milli-Q water.

Calibration curves of $PHEA_{37\text{-}Cy5}$

via fluorescent spectrophotometer: The standard solutions were obtained by serial dilution of 0.125 mg mL^{-1} to 0.0312, 0.0156, 0.0078, 0.0039, and 0.0020 mg mL^{-1}. The excitation and emission wavelengths were 648 nm and 657 nm.

via UV-Vis: The standard solutions were obtained by serial dilution of 249.60 µg mL^{-1} to 124.80, 62.40, 31.20, 15.60, 7.80 µg mL^{-1}.

Calibration curves of $PDMAEA_{12}$

via UV-Vis: The standard solutions were obtained by serial dilution of 499.2 µg mL^{-1} to 249.6, 124.8, 62.4, 31.2, 15.6, and 7.8 µg mL^{-1}.

Calculation of grafting efficiency

The polymer-grafted CNFs were dissolved in milli-Q water at the concentration of 1 mg mL^{-1}. The sample was firstly submitted to fluorescent spectrophotometer for the determination of the amount of grafted $PHEA_{37\text{-}Cy5}$ by taking the advantage of conjugated cyanine 5 fluorescent dye which has the emission at λ_{max} =

657 nm ($PDMAEA_{12}$ was not fluorescent). Second, the obtained mass of $PHEA_{37\text{-}Cy5}$ from fluorescent spectrophotometer was used to calculate the possible UV-Vis absorption intensity by using a standard curve. Third, the total amount of grafted polymers on the surface of cellulose nanomaterials was determined by UV-Vis absorption intensity, from which the calculated intensity of $PHEA_{37\text{-}Cy5}$ was subtracted. The remaining intensity was equal to the intensity of $PDMAEA_{12}$, which was converted to mass by using its calibration curve.

Hydrolysis kinetics of ($PHEA_{37\text{-}Cy5}$-$PDMAEA_{12}$)-g-CNFs in PBS at pH 7.4

The hydrolysis of synthesized polymer-grafted CNFs in phosphate buffer saline (PBS) at pH 7.4 was performed at room temperature and at 37 °C. Firstly, 1 mg of nanoparticles was dissolved in the mixture of D_2O and 2 × concentrated PBS (1: 1 v/v) at the concentration of 0.5 mg mL^{-1}. After that, two NMR tubes were filled with 650 µL of solution, sonicated for 15 min to obtain fully dispersed nanoparticles, and incubated at room temperature and 37 °C. The ^{1}H-NMR measurements (400 MHz) were performed at different time intervals: 15 min, 20 hr and 40 hr. The percentage of hydrolysis was determined by comparing the integrated intensity of signals at δ = 3.62 ppm and 3.83 ppm. The calculation was carried out by using following equation. (I = intensity of the peak)

$$\text{Hydrolysis (\%)} = \frac{I_{3.62}}{I_{3.62} + I_{3.83}} \times 100$$

6.5.8. *In vitro* stability of ($PHEA_{37\text{-}Cy5}$-$PDMAEA_{12}$)-*g*-CNFs

In this experiment, Dulbecco's Modified Eagle's Medium (DMEM) was used as cell culture medium. In a glass vial, freeze-dried polymer-*g*-CNFs (100 µg containing 5.2 nmol of $PDMAEA_{12}$) was suspended in 1 mL of milli-Q water and sonicated using a bench sonicator for 15 min, followed by the addition of 1 mL of DMEM (2 × concentrated). Blank sample was prepared by dispersing polymer-*g*-CNFs (100 µg containing 5.2 nmol of $PDMAEA_{12}$) in 2 mL of milli-Q water. Then the stability of the

particle size in cell culture medium was measured by DLS after stirring at various time points: 0 hr, 1 hr, 2 hr, 4 hr, 6 hr and 8 hr at room temperature.

6.5.9. Binding MIP-1α chemokines on ($PHEA_{37\text{-}Cy5}$-$PDMAEA_{12}$)-*g*-CNFs *via* electrostatic interaction

Investigation on the particle size distribution by DLS

The experiment was performed in pH 7.4 phosphate buffer saline (PBS) and the general plan is as follow. Firstly, freeze-dried polymer-*g*-CNFs (100 μg, 7.8 nmol of $PDMAEA_{12}$) was suspended in 1.5 mL of PBS (pH 7.4) and sonicated for 15 min to obtain clear suspension. Then MIP-1α (62.5 ng, 8.01 μmol) was added to the suspension every 2 hr and the size analysis was carried out by using DLS. The blank sample was prepared using the same procedure but not adding chemokines. Here, the reactions were performed under cold condition to slow down the hydrolysis rate of $PDMAEA_{12}$.

Investigation on MIP-1α binding at different nanoparticle concentrations via BD™ cytometric bead array (CBA) assay

The amount of MIP-1α bound onto ($PHEA_{37\text{-}Cy5}$-$PDMAEA_{12}$)-*g*-CNFs was quantified *via* CBA assay by using BioLegend's LEGENDplex™ multi-analyte flow assay kit. The analysis was kindly performed by a member of Biro group in School of Medicine at UNSW, Australia. The detailed procedure is as follows:

Step 1: Three nanoparticle samples were prepared by suspending ($PHEA_{37\text{-}Cy5}$-$PDMAEA_{12}$)-*g*-CNFs in 1 mL of PBS (pH 7.4) at the concentration of 500 μg mL^{-1}, 250 μg mL^{-1} and 125 μg mL^{-1}. The dispersions were then sonicated using a bench sonicator under cold condition to achieve clear dispersion. Subsequently, 54.4 ng of MIP-1α was added to each nanoparticle dispersion and stirred for 4 hr under cold condition to achieve MIP-1α-($PHEA_{37\text{-}Cy5}$-$PDMAEA_{12}$)-*g*-CNFs. Then the unbound MIP-1α was collected by using

Amicon® ultra-0.5 centrifugal filter 30K devices (volume up to 500 µL) and centrifuging at 14000 × *g* for 20 min.

Step 2: The unbound MIP-1α solutions, control samples: 54.4 ng of MIP-1α in 1 mL of PBS as positive control, and PBS as negative control, and standard samples were incubated with capture beads for 2 hr in a V-bottom 96 well plate. The plate was then centrifuged at 250 × *g* for 5 min. After discarding the supernatant, the plate was washed with 200 µL of wash buffer per well, followed by centrifugation and discarding the supernatant.

Step 3: 25 µL of detection antibodies was added to each well. After incubation for 1 hr, the plate was centrifuged, followed by discarding the supernatant. Afterwards, 25 µL of streptavidin-phycoerythrin (SA-PE) was added to each well and then the plate was incubated for 30 min. After that, the plate was washed by following the previous process: centrifuging, discarding the supernatant, and washing with 200 µL of wash buffer.

Step 4: Finally, the analyte bound beads were resuspended in 150 µL of wash buffer and transferred to FACS tubes for the determination by a flow cytometer. The fluorescent intensity of SA-PE was read for MIP-1α captured beads and the concentration of unbound MIP-1α onto nanoparticles was calculated based on the known standard curve.

6.5.10. Biological experiments of ($PHEA_{37\text{-}Cy5}$-$PDMAEA_{12}$)-*g*-CNFs

In vitro cell viability assay

The cytotoxicity tests for the polymer-grafted CNFs were carried out by a standard sulforhodamine B colorimetric proliferation assay (SRB assay). The breast cancer cell line MCF-7 was seeded in 96-well cell culture plates at a density of 4000 cells per well and incubated at 37 °C in 5 % CO_2 for 24 hr. The samples were then sterilized by UV irradiation for 15 min in a bio-safety cabinet and then the growth medium (Dulbecco's Modified Eagle's Medium, DMEM) was replaced with 100 µL of fresh 2 × concentrated medium. Subsequently, 100 µL of serially diluted samples (2 × dilution) starting from 1 mg mL^{-1} to 0.0039 mg mL^{-1} were added to the plates. After

incubation at 37 °C for 48 hr, the culture medium was removed and the live cells were fixed in 10 % (w/v) trichloroacetic acid (TCA) for 30 min at 4 °C, followed by washing the plates five times with milli-Q water. Then, the TCA-fixed cells were stained by adding 100 µL of 0.4 % (w/v) SRB dissolved in 1 % acetic acid. After leaving the plates for 20 min in dark, SRB was decanted and the plates were washed five times with 1 % acetic acid to remove unbound dye. After removing the excess of moisture by air-drying for a few hours, 200 µL of 10 mM Tris buffer was added to each well and left for 5 min to solubilize the dye (SRB). The absorbance was determined at 490 nm using a Bio-Rad BenchMark Microplate reader. The obtained data were analyzed and plotted using GraphPad Prism 8.0, in which non-treated cells were used as controls. The cell viability was calculated using optical density (OD):

$$\text{Cell viability (\%)} = \frac{\text{OD}_{490,\text{sample}} - \text{OD}_{490,\text{blank}}}{\text{OD}_{490,\text{control}} - \text{OD}_{490,\text{blank}}} \times 100$$

In vitro cellular uptake study by Laser Scanning Confocal Microscopy (LSCM)

MCF-7 cell lines were used to observe the cellular uptake of polymers-grafted CNFs at different time intervals. Firstly, cells were seeded in 35 mm fluoro dish (World Precision Instruments) at the density of 1×10^5 per dish and cultured in 2 mL of DMEM cell culture medium at 37 °C in 5 % CO_2 for 24 hr. When the cells reached sufficient confluency, the medium was replaced with 1 mL of fresh 2 × concentrated medium and 1 mL of sample dispersion (500 µg mL^{-1} in pH 7.4 PBS). After incubating the cells at 37 °C for 2 hr and 8 hr, the cells were washed three times with PBS. The cells were then stained with Hoechst 33342 for 10 mins, followed by gentle washing three times with PBS. Then the cells were mounted in PBS and observed under a Zeiss LSCM 800 laser scanning confocal microscope system equipped with a Diode laser: 405, 488, 561 and 640 nm and an argon laser and a DPSS 561-10 laser (excitation wavelength: 405 nm and emission wavelengths: 490 – 590 nm, respectively) connected to a Zeiss Axio Observer.Z1 inverted microscope (Air 20×/0.8 NA objective). The Zen Blue 2.5 Imaging software was used for image acquisition and processing.

In vitro cellular uptake study by flow cytometry

Cellular uptake studies of nanoparticles ($PHEA_{37\text{-}Cy5}$-$PDMAEA_{12}$)-*g*-CNFs were performed by flow cytometry. Firstly, MCF-7 cells were seeded in 6-well plates at a density of 3×10^5 cells per well and incubated at 37 °C in 5 % CO_2 for two days. Then the cultured medium (DMEM) was replaced with 0.5 mL of fresh 2 × concentrated medium and 0.5 mL of sample solution. The final concentration of nanoparticles was 250 μg mL^{-1}. After incubating the cells with sample solution at 37 °C for 2 hr and 8 hr, the cell monolayer was washed with cold PBS three times and treated with trypsin/EDTA to detach the cells. After that, the cells were collected, centrifuged and resuspended in cold Hank's buffer. The cells suspension was submitted for flow cytometry analysis on BD FACSCanto™II Analyser (BD Biosciences, San Jose, USA, excitation wavelength = 645 nm and emission wavelength = 660 nm), and the results were collected by analysing at least 20,000 cell events. Raw data was analysed using FlowJo software and the results were reported as the median of the distribution of cell fluorescent intensity.

Penetration and uptake of nanoparticles in 3D tumour spheroids

The analysis was kindly performed by a member of Biro group in School of Medicine at UNSW, Australia. The detail protocol for the preparation of tumour spheroid in collagen/mt-CNFs (cancer-associated fibroblasts) matrix is as follows.

Spheroid preparation

To generate spheroids, WM-983c melanoma cells at the density of 1000 cells in 50 μL of complete media were seeded in ultra-low-attachment 96-well plate and incubated at 37 °C over the weekend.

Background on mt-CAFs (KPC SKPCE40)

Cancer-associated fibroblasts (mt-CAF) cells were derived from a highly metastatic pancreatic cancer mouse model: Pdx1-Cre; LSL-K-rasG12D/+; LSL-p53R172H/+ (KPC).

Matrix preparation (≈ 2.5 mg mL^{-1})

The matrix preparation was performed under cold condition. 9.4 µL of 1 N NaOH was added to 414 µL of collagen (pipette tips stored at -30 °C), followed by the addition of 97.44 µL of 10 × MEM. Here, the collagen was thoroughly mixed to achieve the homogeneous suspension. Next, 109.16 µL of the mt-CAF/FBS suspension was added. Then, approximately 200 µL of collagen/mt-CAF mixture was transferred to each well of a 24-well plate and incubated for approximately 4 – 5 min. After that, the prepared spheroids were transferred carefully into an Eppendorf tube, followed by the subsequent addition of 300 µL of collagen/mt-CAF suspension. The mixture (spheroids in collagen/mt-CAF matrix) was carefully transferred into well on top of the collagen/mt-CAF layer, followed by incubation for 45 min to solidify. Afterwards, 500 µL of culture medium: DMEM containing 10 % FBS and 1 % penicillin-streptomycin, was added to the matrix. The obtained matrices were incubated for a day, followed by the addition of 500 µL of culture medium.

CHAPTER - 7

Conclusion

&

Recommendations for Future Works

7.1. Conclusion

The tunable surface properties of cellulose nanomaterials provide versatile scaffolds for their use as drug carriers for intravenous injection. To achieve this goal, it is necessary to modify the cellulose nanomaterials with specific functional molecules. However, the success of surface modification depends on several factors including the nature of cellulose nanomaterials and the reaction conditions.[374, 386, 504] In this thesis, the efficient modification strategies were explored to generate functional cellulose-based nanomaterials with enhanced or new characteristics which are compatible for delivering anti-cancer therapeutics. More specifically, synthetic polymers were covalently tethered onto TEMPO-oxidized cellulose nanofibers (CNFs) by two different approaches: NICAL and Passerini reactions. Successfully, NICAL reaction provided the self-fluorescent polymer-grafted CNFs carriers which could be monitored once inside the cells. On the other hand, Passerini reaction was found an efficient method to design polymer functionalized CNFs and incorporate cytokines (MIP-1α) for the purpose of cancer immunotherapy. The designed nanoparticles ($(PHEA_{37\text{-}Cy5}\text{-}PDMAEA_{12})$-*g*-CNFs) were found having the capability of electrostatically binding MIP-1α, high cellular uptake, non-toxicity, as well as *in vitro* stability in biological fluid. Hence, our studies not only highlight the surface modification techniques to efficiently modify plant-derived cellulose nanofibrils (CNFs) but also the design of CNFs for their use in cancer immunotherapy. The contributions of the thesis on the design and synthesis of functional CNFs aim to extend the benefits of bio-based nanoparticles as drug delivery system.

In **Chapter 3**, native celluloses derived from cotton linters were converted to individual nanofibers less than 10 nm wide by mechanically assisted TEMPO (2,2,6,6-tetramethyl-1-piperidinyloxy)-mediated oxidation. Microfibrils formed by electrostatic repulsion of anionic charges after TEMPO-oxidation were individualized into nanofibrils (CNFs) dispersed in water upon ultrasonic treatment at the concentration of 0.1 – 0.2 % (w/v). Upon HCl treatment at pH ≈ 2, CNFs were obtained with high acid concentration on the surface (1.65 mmol g^{-1} of dry CNFs), pKa of 5.22, 56 % crystallinity and degradation temperature at 252 °C.

Then, we started exploring the surface functionalization pathways to graft polymers onto cellulose nanofibrils (CNFs). In **Chapter 4**, the nitrile imine-

carboxylic acid ligation (NICAL) reaction was employed to chemically click between tetrazole-terminated hydrophilic polymer chains, synthesized *via* reversible addition-fragmentation chain transfer (RAFT) polymerization, and acid (-COOH) groups on CNFs under UV irradiation in aqueous media at room temperature. The resulting polymer-grafted CNFs were obtained with self-fluorescent properties, which can be used to track the nanoparticles when internalized by the cells. Moreover, the time- and dose-dependent bioactivity of doxorubicin (DOX) loaded PHEA-*g*-CNFs (poly(2-hydroxyethyl acrylate)-grafted CNFs) against MCF-7 cancer cells was observed. Nevertheless, the grafting efficiency of polymers attached on CNFs was insufficient; therefore, we further attempted another alternative approach so-called three-component Passerini reaction as discussed in **Chapter 5**. Passerini is the versatile approach between three components (an acid group on CNFs, an aldehyde end functionality of polymer chain, and a cyclohexyl isocyanide) in one pot under ambient conditions. The underpinning idea was to use thermo-responsive polymer (PNIPAm/poly(*N*-isopropylacrylamide)) as a model polymer. The polymer-grafted cellulose nanofibrils (PNIPAm-*g*-CNFs) were obtained with high polymer grafting efficiency (36 % within 0.5 hr of reaction time) and thermo-responsive properties. To be noted here is that the high grafting efficiency was obtained when the reaction was performed under concentrated conditions in water, more specifically in CNFs gel itself without additional solvent. This simple and versatile approach opens up the opportunity to modify cellulose nanomaterials with a large variety of polymer chains maintaining high structural integrity and aqueous dispersibility.

In **Chapter 6**, by using Passerini reaction, we designed cellulose-based nanomaterials ($(PHEA_{37\text{-}Cy5}\text{-}PDMAEA_{12})$-*g*-CNFs) containing two types of polymer chains on the surface to efficiently bind chemokines (MIP-1α) for their use in cancer immunotherapy. The underpinning idea was to bind the anionic chemokines onto cationic PDMAEA and release *via* hydrolysis in aqueous media. It was investigated that the synthesized nanoparticles exhibited high *in vitro* stability in biological fluid and non-toxicity against MCF-7 cancer cells. Moreover, the successful penetration of nanoparticles into *in vitro* 2D (MCF-7 cancer cells) and 3D models designed by using WM-983c melanoma cells embedded in collagen/mt-CAFs matrix were observed.

7.2. Recommendations for Future Works

This thesis discussed the application of NICAL and Passerini techniques to produce functional cellulose nanomaterials with unique properties suitable for drug delivery application. In **Chapter 6**, the design of cellulose-drug delivery system for the purpose of cancer immunotherapy was discussed. It was found that the prepared nanoparticles ((PHEA$_{37\text{-}Cy5}$-PDMAEA$_{12}$)-*g*-CNFs) successfully penetrated 3D tumour spheroid and enabled binding immunostimulators (MIP-1α) *via* electrostatically interaction. The project aims to suppress cancer cells by simply activating natural killing T-cells.

However, the drug release behaviour of synthesized nanoparticles needs to be improved. The fast degradation of PDMAEA due to the hydrolysis behaviour of ester linkages on polymer chains might be a problem in drug delivery application. The designed nanoparticles MIP-1α-(PHEA$_{37\text{-}Cy5}$-PDMAEA$_{12}$)-*g*-CNFs seem to have tendency to cause early release of MIP-1α prior to entering the targeted site. Once anionic chemokines released, the cationic PDMAEA on cellulose nanoparticles might interacts with natural killing T cells and other healthy cells leading to undesired side effects. In this regard, an alternative strategy is required to deliver therapeutics to specific site and provide controlled release therapy.

Considering this, it is recommended to alleviate this problem by replacing PDMAEA with polycations carrying amide linkages as amides resist hydrolysis than ester bonds (**Scheme 7.1**). This approach is expected to optimize the design of cellulose-based drug delivery system for specific cancer treatment with improved efficacy and reduced side effects of premature release. The future will be monitoring the release of MIP-1α from cellulose-based nanoparticles in 3D tumour spheroid with embedded natural killing T-cells. This experiment will help to understand the stimulation behaviour of chemokines to T-cells for cancer elimination.

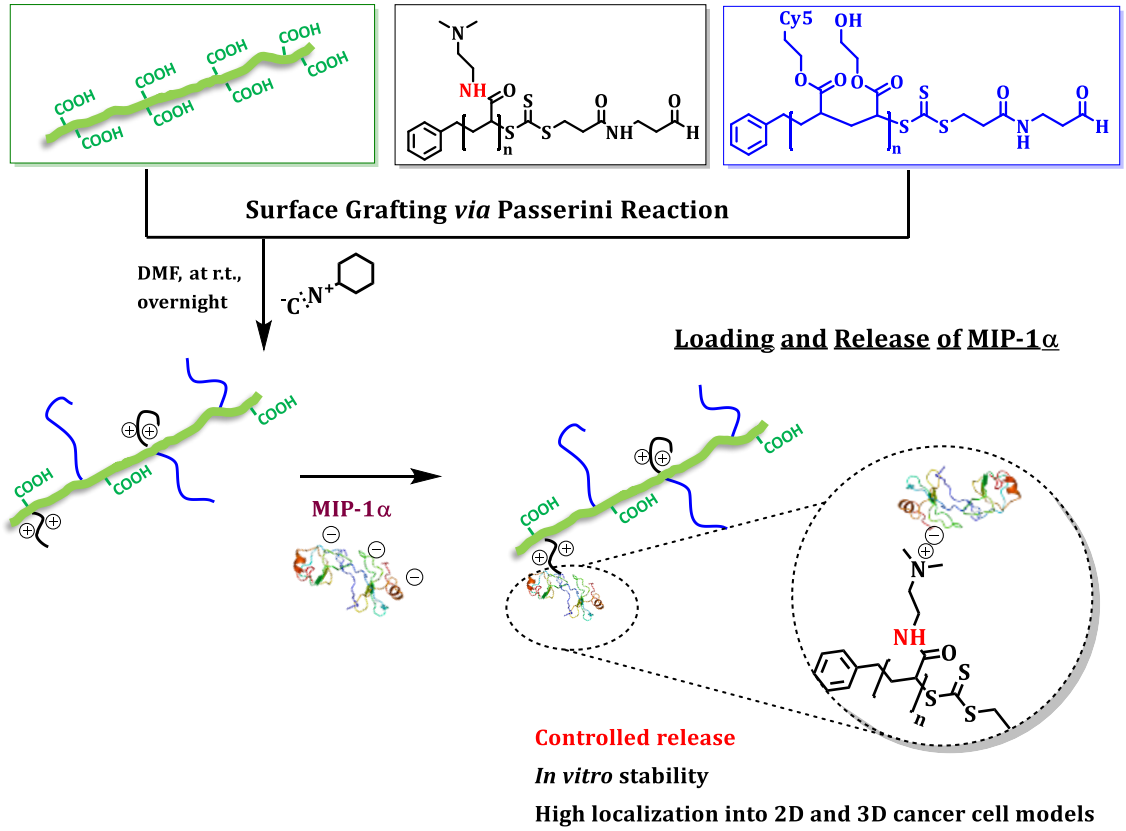

Scheme 7.1. Overall scheme for an alternative design of cellulose-based nanomaterials for binding and controlled release of immune chemokines (MIP-1α).

References

1. Ji, H. F.; Li, X. J.; Zhang, H. Y., Natural products and drug discovery. *EMBO reports* **2009,** *10* (3), 194-200.
2. Martinho, N.; Damgé, C.; Reis, C. P., Recent advances in drug delivery systems. *JBNB* **2011,** *2* (05), 510.
3. Jahangirian, H.; Lemraski, E. G.; Webster, T. J.; Rafiee-Moghaddam, R.; Abdollahi, Y., A review of drug delivery systems based on nanotechnology and green chemistry: green nanomedicine. *Int. J. Nanomed.* **2017,** *12*, 2957.
4. Babu, A.; Templeton, A. K.; Munshi, A.; Ramesh, R., Nanodrug delivery systems: a promising technology for detection, diagnosis, and treatment of cancer. *Aaps Pharmscitech* **2014,** *15* (3), 709-721.
5. Soares, S.; Sousa, J.; Pais, A.; Vitorino, C., Nanomedicine: Principles, Properties, and Regulatory Issues. *Front Chem* **2018,** *6*, 360-360.
6. Shi, J.; Kantoff, P. W.; Wooster, R.; Farokhzad, O. C., Cancer nanomedicine: progress, challenges and opportunities. *Nat Rev Cancer* **2017,** *17* (1), 20-37.
7. Zhu, X.; Vo, C.; Taylor, M.; Smith, B. R., Non-spherical micro- and nanoparticles in nanomedicine. *Mater. Horiz.* **2019,** *6* (6), 1094-1121.
8. Ernsting, M. J.; Murakami, M.; Roy, A.; Li, S. D., Factors controlling the pharmacokinetics, biodistribution and intratumoral penetration of nanoparticles. *J. Control. Release : official journal of the Controlled Release Society* **2013,** *172* (3), 782-94.
9. Cai, R.; Chen, C., The Crown and the Scepter: Roles of the Protein Corona in Nanomedicine. *Adv. Mater. 0* (0), 1805740.
10. Geng, Y.; Dalhaimer, P.; Cai, S.; Tsai, R.; Tewari, M.; Minko, T.; Discher, D. E., Shape effects of filaments versus spherical particles in flow and drug delivery. *Nature nanotechnology* **2007,** *2* (4), 249-55.
11. Maeda, H.; Wu, J.; Sawa, T.; Matsumura, Y.; Hori, K., Tumor vascular permeability and the EPR effect in macromolecular therapeutics: a review. *J. Control Release : official journal of the Controlled Release Society* **2000,** *65* (1-2), 271-84.
12. Cabral, H.; Matsumoto, Y.; Mizuno, K.; Chen, Q.; Murakami, M.; Kimura, M.; Terada, Y.; Kano, M. R.; Miyazono, K.; Uesaka, M.; Nishiyama, N.; Kataoka, K., Accumulation of sub-100 nm polymeric micelles in poorly permeable tumours depends on size. *Nature nanotechnology* **2011,** *6* (12), 815-23.
13. Shah, P. N.; Lin, T. Y.; Aanei, I. L.; Klass, S. H.; Smith, B. R.; Shaqfeh, E. S. G., Extravasation of Brownian Spheroidal Nanoparticles through Vascular Pores. *Biophys. J.* **2018,** *115* (6), 1103-1115.
14. Liu, Z.; Cai, W.; He, L.; Nakayama, N.; Chen, K.; Sun, X.; Chen, X.; Dai, H., In *vivo* biodistribution and highly efficient tumour targeting of carbon nanotubes in mice. *Nat. Nanotechnol.* **2007,** *2* (1), 47-52.
15. Park, J.-H.; von Maltzahn, G.; Zhang, L.; Schwartz, M. P.; Ruoslahti, E.; Bhatia, S. N.; Sailor, M. J., Magnetic Iron Oxide Nanoworms for Tumor Targeting and Imaging. *Adv. Mater.* **2008,** *20* (9), 1630-1635.
16. Park, J.-H.; von Maltzahn, G.; Zhang, L.; Derfus, A. M.; Simberg, D.; Harris, T. J.; Ruoslahti, E.; Bhatia, S. N.; Sailor, M. J., Systematic Surface Engineering of Magnetic Nanoworms for In vivo Tumor Targeting. *Small* **2009,** *5* (6), 694-700.

17. Geng, Y.; Dalhaimer, P.; Cai, S.; Tsai, R.; Tewari, M.; Minko, T.; Discher, D. E., Shape Effects of Filaments Versus Spherical Particles in Flow and Drug Delivery. *Nat. Nanotechnol.* **2007,** *2* (4), 249-255.
18. Salatin, S.; Maleki Dizaj, S.; Yari Khosroushahi, A., Effect of the surface modification, size, and shape on cellular uptake of nanoparticles. *Cell Biol. Inter.* **2015,** *39* (8), 881-890.
19. Chithrani, B. D.; Ghazani, A. A.; Chan, W. C. W., Determining the Size and Shape Dependence of Gold Nanoparticle Uptake into Mammalian Cells. *Nano Lett.* **2006,** *6* (4), 662-668.
20. Chithrani, B. D.; Chan, W. C. W., Elucidating the Mechanism of Cellular Uptake and Removal of Protein-Coated Gold Nanoparticles of Different Sizes and Shapes. *Nano Lett.* **2007,** *7* (6), 1542-1550.
21. Zhang, K.; Fang, H.; Chen, Z.; Taylor, J.-S. A.; Wooley, K. L., Shape Effects of Nanoparticles Conjugated with Cell-penetrating Peptides (HIV Tat PTD) on CHO Cell Uptake. *Bioconjugate Chem.* **2008,** *19* (9), 1880-1887.
22. Florez, L.; Herrmann, C.; Cramer, J. M.; Hauser, C. P.; Koynov, K.; Landfester, K.; Crespy, D.; Mailänder, V., How Shape Influences Uptake: Interactions of Anisotropic Polymer Nanoparticles and Human Mesenchymal Stem Cells. *Small* **2012,** *8* (14), 2222-2230.
23. Shimoni, O.; Yan, Y.; Wang, Y.; Caruso, F., Shape-Dependent Cellular Processing of Polyelectrolyte Capsules. *ACS Nano* **2013,** *7* (1), 522-530.
24. Zhao, J.; Lu, H.; Wong, S.; Lu, M.; Xiao, P.; Stenzel, M. H., Influence of nanoparticle shapes on cellular uptake of paclitaxel loaded nanoparticles in 2D and 3D cancer models. *Polym. Chem.* **2017,** *8* (21), 3317-3326.
25. Zhao, J.; Stenzel, M. H., Entry of nanoparticles into cells: the importance of nanoparticle properties. *Polym. Chem.* **2018,** *9* (3), 259-272.
26. Justice, S. S.; Hunstad, D. A.; Cegelski, L.; Hultgren, S. J., Morphological plasticity as a bacterial survival strategy. *Nat. Rev. Micro.* **2008,** *6* (2), 162-168.
27. Brakhage, A. A.; Bruns, S.; Thywissen, A.; Zipfel, P. F.; Behnsen, J., Interaction of phagocytes with filamentous fungi. *Curr. Opin. Microbiol.* **2010,** *13* (4), 409-415.
28. Möller, J.; Luehmann, T.; Hall, H.; Vogel, V., The Race to the Pole: How High-Aspect Ratio Shape and Heterogeneous Environments Limit Phagocytosis of Filamentous Escherichia coli Bacteria by Macrophages. *Nano Lett.* **2012,** *12* (6), 2901-2905.
29. Barua, S.; Yoo, J.-W.; Kolhar, P.; Wakankar, A.; Gokarn, Y. R.; Mitragotri, S., Particle shape enhances specificity of antibody-displaying nanoparticles. *Proc. Natl. Acad. Sci. USA* **2013,** *110* (9), 3270-3275.
30. Karagoz, B.; Esser, L.; Duong, H. T.; Basuki, J. S.; Boyer, C.; Davis, T. P., Polymerization-Induced Self-Assembly (PISA) - control over the morphology of nanoparticles for drug delivery applications. *Polym. Chem.* **2014,** *5* (2), 350-355.
31. Qiu, L.; Xu, C.-R.; Zhong, F.; Hong, C.-Y.; Pan, C.-Y., Fabrication of Functional Nano-objects through RAFT Dispersion Polymerization and Influences of Morphology on Drug Delivery. *ACS Appl. Mater. Interfaces* **2016,** *8* (28), 18347-18359.
32. Zhao, J.; Lu, H.; Xiao, P.; Stenzel, M. H., Cellular Uptake and Movement in 2D and 3D Multicellular Breast Cancer Models of Fructose-Based Cylindrical

Micelles That Is Dependent on the Rod Length. *ACS Appl. Mater. Interfaces* **2016,** *8* (26), 16622-16630.
33. Zhao, J.; Lu, H.; Yao, Y.; Ganda, S.; Stenzel, M. H., Length vs. stiffness: which plays a dominant role in the cellular uptake of fructose-based rod-like micelles by breast cancer cells in 2D and 3D cell culture models? *J. Mater. Chem. B* **2018,** *6* (25), 4223-4231.
34. Kou, L.; Sun, J.; Zhai, Y.; He, Z., The endocytosis and intracellular fate of nanomedicines: Implication for rational design. *Asian J. Pharm. Sci.* **2013,** *8* (1), 1-10.
35. Chu, Z.; Zhang, S.; Zhang, B.; Zhang, C.; Fang, C.-Y.; Rehor, I.; Cigler, P.; Chang, H.-C.; Lin, G.; Liu, R., Unambiguous observation of shape effects on cellular fate of nanoparticles. *Sci. Rep.* **2014,** *4*, 4495.
36. Foster, J. C.; Varlas, S.; Couturaud, B.; Coe, Z.; O'Reilly, R. K., Getting into Shape: Reflections on a New Generation of Cylindrical Nanostructures' Self-Assembly Using Polymer Building Blocks. *J. Am. Chem. Soc.* **2019,** *141* (7), 2742-2753.
37. Pushpamalar, J.; Veeramachineni, A. K.; Owh, C.; Loh, X. J., Biodegradable polysaccharides for controlled drug delivery. *ChemPlusChem* **2016,** *81* (6), 504-514.
38. Deepa, B.; Abraham, E.; Cordeiro, N.; Mozetic, M.; Mathew, A. P.; Oksman, K.; Faria, M.; Thomas, S.; Pothan, L. A., Utilization of various lignocellulosic biomass for the production of nanocellulose: a comparative study. *Cellulose* **2015,** *22* (2), 1075-1090.
39. Sczostak, A. In *Cotton linters: an alternative cellulosic raw material*, Macromol. Symposia, Wiley Online Library: 2009; pp 45-53.
40. Sundarraj, A. A.; Ranganathan, T. V., A review on cellulose and its utilization from agro-industrial waste. *Drug Inven. Today* **2018,** *10*, 89-94.
41. Khalil, H. A.; Bhat, A.; Yusra, A. I., Green composites from sustainable cellulose nanofibrils: A review. *Carbohydr. Polym.* **2012,** *87* (2), 963-979.
42. Cosgrove, D. J., Growth of the plant cell wall. *Nat. Rev. Mol. Cell Biol.* **2005,** *6* (11), 850-861.
43. Thomas, L. H.; Forsyth, V. T.; Šturcová, A.; Kennedy, C. J.; May, R. P.; Altaner, C. M.; Apperley, D. C.; Wess, T. J.; Jarvis, M. C., Structure of Cellulose Microfibrils in Primary Cell Walls from Collenchyma. *Plant Physiol.* **2013,** *161* (1), 465-476.
44. KONDO, T., The assignment of IR absorption bands due to free hydroxyl groups in cellulose. *Cellulose* **1997,** *4* (4), 281.
45. Lin, N.; Dufresne, A., Nanocellulose in biomedicine: Current status and future prospect. *Eur. Polym. J.* **2014,** *59* (Supplement C), 302-325.
46. Park, S.; Baker, J. O.; Himmel, M. E.; Parilla, P. A.; Johnson, D. K., Cellulose crystallinity index: measurement techniques and their impact on interpreting cellulase performance. *Biotechnol. Biofuels* **2010,** *3* (1), 10.
47. Nishiyama, Y.; Sugiyama, J.; Chanzy, H.; Langan, P., Crystal structure and hydrogen bonding system in cellulose Iα from synchrotron X-ray and neutron fiber diffraction. *J. Am. Chem. Soc.* **2003,** *125* (47), 14300-14306.
48. Nishiyama, Y.; Langan, P.; Chanzy, H., Crystal structure and hydrogen-bonding system in cellulose Iβ from synchrotron X-ray and neutron fiber diffraction. *J. Am. Chem. Soc.* **2002,** *124* (31), 9074-9082.
49. Lin, N.; Dufresne, A., Nanocellulose in biomedicine: Current status and future prospect. *Eur.n Polym. J.* **2014,** *59*, 302-325.

50. Zhou, X.; Chang, C.; Zhou, Y.; Sun, L.; Xiang, H.; Zhao, S.; Ma, L.; Zheng, G.; Liu, M.; Wei, H., A comparison study to investigate the effect of the drug-loading site on its delivery efficacy using double hydrophilic block copolymer-based prodrugs. *J. Mater. Chem. B* **2017,** *5* (23), 4443-4454.
51. Wang, Q.; Zhao, X.; Zhu, J. Y., Kinetics of Strong Acid Hydrolysis of a Bleached Kraft Pulp for Producing Cellulose Nanocrystals (CNCs). *Ind. Eng. Chem. Res.* **2014,** *53* (27), 11007-11014.
52. Arai, K.; Horikawa, Y.; Shikata, T., Transport Properties of Commercial Cellulose Nanocrystals in Aqueous Suspension Prepared from Chemical Pulp via Sulfuric Acid Hydrolysis. *ACS Omega* **2018,** *3* (10), 13944-13951.
53. Cheng, M.; Qin, Z.; Chen, Y.; Hu, S.; Ren, Z.; Zhu, M., Efficient Extraction of Cellulose Nanocrystals through Hydrochloric Acid Hydrolysis Catalyzed by Inorganic Chlorides under Hydrothermal Conditions. *ACS Sustain. Chem. Eng.* **2017,** *5* (6), 4656-4664.
54. Hu, Z.; Marway, H. S.; Kasem, H.; Pelton, R.; Cranston, E. D., Dried and Redispersible Cellulose Nanocrystal Pickering Emulsions. *ACS Macro Lett.* **2016,** *5* (2), 185-189.
55. Hu, Z.; Cranston, E. D.; Ng, R.; Pelton, R., Tuning Cellulose Nanocrystal Gelation with Polysaccharides and Surfactants. *Langmuir* **2014,** *30* (10), 2684-2692.
56. Aïssa, K.; Karaaslan, M. A.; Renneckar, S.; Saddler, J. N., Functionalizing Cellulose Nanocrystals with Click Modifiable Carbohydrate-Binding Modules. *Biomacromolecules* **2019**.
57. De France, K. J.; Badv, M.; Dorogin, J.; Siebers, E.; Panchal, V.; Babi, M.; Moran-Mirabal, J.; Lawlor, M.; Cranston, E. D.; Hoare, T., Tissue Response and Biodistribution of Injectable Cellulose Nanocrystal Composite Hydrogels. *ACS Biomater. Sci. Eng.* **2019,** *5* (5), 2235-2246.
58. Spinella, S.; Samuel, C.; Raquez, J.-M.; McCallum, S. A.; Gross, R.; Dubois, P., Green and Efficient Synthesis of Dispersible Cellulose Nanocrystals in Biobased Polyesters for Engineering Applications. *ACS Sustain. Chem. Eng.* **2016,** *4* (5), 2517-2527.
59. Hu, Z.; Berry, R. M.; Pelton, R.; Cranston, E. D., One-Pot Water-Based Hydrophobic Surface Modification of Cellulose Nanocrystals Using Plant Polyphenols. *ACS Sustain. Chem. Eng.* **2017,** *5* (6), 5018-5026.
60. Khalil, H. A.; Davoudpour, Y.; Islam, M. N.; Mustapha, A.; Sudesh, K.; Dungani, R.; Jawaid, M., Production and modification of nanofibrillated cellulose using various mechanical processes: a review. *Carbohydr. Polym.* **2014,** *99*, 649-665.
61. Lv, D.; Du, H.; Che, X.; Wu, M.; Zhang, Y.; Liu, C.; Nie, S.; Zhang, X.; Li, B., Tailored and Integrated Production of Functional Cellulose Nanocrystals and Cellulose Nanofibrils via Sustainable Formic Acid Hydrolysis: Kinetic Study and Characterization. *ACS Sustain. Chem. Eng.* **2019,** *7* (10), 9449-9463.
62. Lu, Q.; Cai, Z.; Lin, F.; Tang, L.; Wang, S.; Huang, B., Extraction of Cellulose Nanocrystals with a High Yield of 88% by Simultaneous Mechanochemical Activation and Phosphotungstic Acid Hydrolysis. *ACS Sustain. Chem. Eng.* **2016,** *4* (4), 2165-2172.
63. Novo, L. P.; Bras, J.; García, A.; Belgacem, N.; Curvelo, A. A. S., Subcritical Water: A Method for Green Production of Cellulose Nanocrystals. *ACS Sustain. Chem. Eng.* **2015,** *3* (11), 2839-2846.

64. Montanari, S.; Roumani, M.; Heux, L.; Vignon, M. R., Topochemistry of Carboxylated Cellulose Nanocrystals Resulting from TEMPO-Mediated Oxidation. *Macromolecules* **2005,** *38* (5), 1665-1671.
65. Benkaddour, A.; Journoux-Lapp, C.; Jradi, K.; Robert, S.; Daneault, C., Study of the hydrophobization of TEMPO-oxidized cellulose gel through two routes: amidation and esterification process. *J. Mater. Sci.* **2014,** *49* (7), 2832-2843.
66. Elazzouzi-Hafraoui, S.; Nishiyama, Y.; Putaux, J.-L.; Heux, L.; Dubreuil, F.; Rochas, C., The shape and size distribution of crystalline nanoparticles prepared by acid hydrolysis of native cellulose. *Biomacromolecules* **2007,** *9* (1), 57-65.
67. Kamelnia, E.; Divsalar, A.; Darroudi, M.; Yaghmaei, P.; Sadri, K., Production of new cellulose nanocrystals from Ferula gummosa and their use in medical applications via investigation of their biodistribution. *Ind. Crops Products* **2019,** *139*, 111538.
68. Hai, L. V.; Son, H. N.; Seo, Y. B., Physical and bio-composite properties of nanocrystalline cellulose from wood, cotton linters, cattail, and red algae. *Cellulose* **2015,** *22* (3), 1789-1798.
69. Leite, A. L. M. P.; Zanon, C. D.; Menegalli, F. C., Isolation and characterization of cellulose nanofibers from cassava root bagasse and peelings. *Carbohydr. Polym.* **2017,** *157*, 962-970.
70. Oun, A. A.; Rhim, J.-W., Isolation of cellulose nanocrystals from grain straws and their use for the preparation of carboxymethyl cellulose-based nanocomposite films. *Carbohydr. Polym.* **2016,** *150*, 187-200.
71. Chang, P. S.; Robyt, J. F., Oxidation of Primary Alcohol Groups of Naturally Occurring Polysaccharides with 2,2,6,6-Tetramethyl-1-Piperidine Oxoammonium Ion. *J. Carbohydr. Chem.* **1996,** *15* (7), 819-830.
72. Fujisawa, S.; Okita, Y.; Fukuzumi, H.; Saito, T.; Isogai, A., Preparation and characterization of TEMPO-oxidized cellulose nanofibril films with free carboxyl groups. *Carbohydr. Polym.* **2011,** *84* (1), 579-583.
73. Khine, Y. Y.; Ganda, S.; Stenzel, M. H., Covalent Tethering of Temperature Responsive pNIPAm onto TEMPO-Oxidized Cellulose Nanofibrils via Three-Component Passerini Reaction. *ACS Macro Lett.* **2018,** *7* (4), 412-418.
74. Faradilla, R. F.; Lee, G.; Rawal, A.; Hutomo, T.; Stenzel, M. H.; Arcot, J., Nanocellulose characteristics from the inner and outer layer of banana pseudo-stem prepared by TEMPO-mediated oxidation. *Cellulose* **2016,** *23* (5), 3023-3037.
75. Saito, T.; Kimura, S.; Nishiyama, Y.; Isogai, A., Cellulose Nanofibers Prepared by TEMPO-Mediated Oxidation of Native Cellulose. *Biomacromolecules* **2007,** *8* (8), 2485-2491.
76. Rattaz, A.; Mishra, S. P.; Chabot, B.; Daneault, C., Cellulose nanofibres by sonocatalysed-TEMPO-oxidation. *Cellulose* **2011,** *18* (3), 585.
77. Visanko, M.; Liimatainen, H.; Sirviö, J. A.; Heiskanen, J. P.; Niinimäki, J.; Hormi, O., Amphiphilic Cellulose Nanocrystals from Acid-Free Oxidative Treatment: Physicochemical Characteristics and Use as an Oil–Water Stabilizer. *Biomacromolecules* **2014,** *15* (7), 2769-2775.
78. Sirviö, J. A.; Kolehmainen, A.; Visanko, M.; Liimatainen, H.; Niinimäki, J.; Hormi, O. E. O., Strong, Self-Standing Oxygen Barrier Films from Nanocelluloses Modified with Regioselective Oxidative Treatments. *ACS Appl. Mater. Interfaces* **2014,** *6* (16), 14384-14390.

79. Ul-Islam, M.; Khan, S.; Ullah, M. W.; Park, J. K., Bacterial cellulose composites: Synthetic strategies and multiple applications in bio-medical and electro-conductive fields. *Biotechnol. J.* **2015,** *10* (12), 1847-1861.
80. Gullo, M.; La China, S.; Petroni, G.; Di Gregorio, S.; Giudici, P., Exploring K2G30 Genome: A High Bacterial Cellulose Producing Strain in Glucose and Mannitol Based Media. *Front. Microbiol.* **2019,** *10* (58).
81. Thorat, Meghana N.; Dastager, S. G., High yield production of cellulose by a Komagataeibacter rhaeticus PG2 strain isolated from pomegranate as a new host. *RSC Advances* **2018,** *8* (52), 29797-29805.
82. Volova, T. G.; Prudnikova, S. V.; Sukovatyi, A. G.; Shishatskaya, E. I., Production and properties of bacterial cellulose by the strain Komagataeibacter xylinus B-12068. *Appl. Microbiol. Biot.* **2018,** *102* (17), 7417-7428.
83. Molina-Ramírez, C.; Castro, M.; Osorio, M.; Torres-Taborda, M.; Gómez, B.; Zuluaga, R.; Gómez, C.; Gañán, P.; Rojas, O. J.; Castro, C., Effect of Different Carbon Sources on Bacterial Nanocellulose Production and Structure Using the Low pH Resistant Strain Komagataeibacter Medellinensis. *Materials* **2017,** *10* (6), 639.
84. Tabaii, M. J.; Emtiazi, G., Comparison of bacterial cellulose production among different strains and fermented media. *Applied food biotechnology* **2016,** *3* (1), 35-41.
85. Mohammadkazemi, F.; Azin, M.; Ashori, A., Production of bacterial cellulose using different carbon sources and culture media. *Carbohyd. Polym.* **2015,** *117*, 518-523.
86. Halib, N.; Perrone, F.; Cemazar, M.; Dapas, B.; Farra, R.; Abrami, M.; Chiarappa, G.; Forte, G.; Zanconati, F.; Pozzato, G.; Murena, L.; Fiotti, N.; Lapasin, R.; Cansolino, L.; Grassi, G.; Grassi, M., Potential Applications of Nanocellulose-Containing Materials in the Biomedical Field. *Materials (Basel, Switzerland)* **2017,** *10* (8).
87. Abeer, M. M.; Mohd Amin, M. C.; Martin, C., A review of bacterial cellulose-based drug delivery systems: their biochemistry, current approaches and future prospects. *J. Pharm. Pharmacol.* **2014,** *66* (8), 1047-61.
88. Sheikhi, A.; Hayashi, J.; Eichenbaum, J.; Gutin, M.; Kuntjoro, N.; Khorsandi, D.; Khademhosseini, A., Recent advances in nanoengineering cellulose for cargo delivery. *J. Controlled Release* **2019,** *294*, 53-76.
89. Martínez Ávila, H.; Schwarz, S.; Feldmann, E.-M.; Mantas, A.; von Bomhard, A.; Gatenholm, P.; Rotter, N., Biocompatibility evaluation of densified bacterial nanocellulose hydrogel as an implant material for auricular cartilage regeneration. *Appl. Microbiol. Biotechnol.* **2014,** *98* (17), 7423-7435.
90. Nguyen, D.; Hägg, D. A.; Forsman, A.; Ekholm, J.; Nimkingratana, P.; Brantsing, C.; Kalogeropoulos, T.; Zaunz, S.; Concaro, S.; Brittberg, M., Cartilage tissue engineering by the 3D bioprinting of iPS cells in a nanocellulose/alginate bioink. *Sci. Rep.* **2017,** *7* (1), 658.
91. Markstedt, K.; Mantas, A.; Tournier, I.; Martínez Ávila, H. c.; Hägg, D.; Gatenholm, P., 3D bioprinting human chondrocytes with nanocellulose–alginate bioink for cartilage tissue engineering applications. *Biomacromolecules* **2015,** *16* (5), 1489-1496.
92. Moritz, S.; Wiegand, C.; Wesarg, F.; Hessler, N.; Müller, F. A.; Kralisch, D.; Hipler, U.-C.; Fischer, D., Active wound dressings based on bacterial

nanocellulose as drug delivery system for octenidine. *Int. J. Pharm.* **2014,** *471* (1-2), 45-55.
93. Liu, J.; Chinga-Carrasco, G.; Cheng, F.; Xu, W.; Willför, S.; Syverud, K.; Xu, C., Hemicellulose-reinforced nanocellulose hydrogels for wound healing application. *Cellulose* **2016,** *23* (5), 3129-3143.
94. De France, K. J.; Hoare, T.; Cranston, E. D., Review of Hydrogels and Aerogels Containing Nanocellulose. *Chem. Mater.* **2017,** *29* (11), 4609-4631.
95. Mo, Y.; Guo, R.; Zhang, Y.; Xue, W.; Cheng, B.; Zhang, Y., Controlled Dual Delivery of Angiogenin and Curcumin by Electrospun Nanofibers for Skin Regeneration. *Tissue engineering. Part A* **2017,** *23* (13-14), 597-608.
96. Guo, R.; Lan, Y.; Xue, W.; Cheng, B.; Zhang, Y.; Wang, C.; Ramakrishna, S., Collagen-cellulose nanocrystal scaffolds containing curcumin-loaded microspheres on infected full-thickness burns repair. *J. Tissue Eng.* **2017,** *11* (12), 3544-3555.
97. Alkhatib, Y.; Dewaldt, M.; Moritz, S.; Nitzsche, R.; Kralisch, D.; Fischer, D., Controlled extended octenidine release from a bacterial nanocellulose/Poloxamer hybrid system. *Eur. J. Pharm. Biopharm. : official journal of Arbeitsgemeinschaft fur Pharmazeutische Verfahrenstechnik e.V* **2017,** *112*, 164-176.
98. Khalid, A.; Khan, R.; Ul-Islam, M.; Khan, T.; Wahid, F., Bacterial cellulose-zinc oxide nanocomposites as a novel dressing system for burn wounds. *Carbohydr. Polym.* **2017,** *164*, 214-221.
99. Mertaniemi, H.; Escobedo-Lucea, C.; Sanz-Garcia, A.; Gandía, C.; Mäkitie, A.; Partanen, J.; Ikkala, O.; Yliperttula, M., Human stem cell decorated nanocellulose threads for biomedical applications. *Biomaterials* **2016,** *82*, 208-220.
100. Madhusudana Rao, K.; Kumar, A.; Han, S. S., Polysaccharide based bionanocomposite hydrogels reinforced with cellulose nanocrystals: Drug release and biocompatibility analyses. *Int. J. Biol. Macromol.* **2017,** *101*, 165-171.
101. Yu, H.-Y.; Wang, C.; Abdalkarim, S. Y. H., Cellulose nanocrystals/polyethylene glycol as bifunctional reinforcing/compatibilizing agents in poly(lactic acid) nanofibers for controlling long-term in vitro drug release. *Cellulose* **2017,** *24* (10), 4461-4477.
102. Huang, L.; Chen, X.; Nguyen, T. X.; Tang, H.; Zhang, L.; Yang, G., Nano-cellulose 3D-networks as controlled-release drug carriers. *J. Mater. Chem. B* **2013,** *1* (23), 2976-2984.
103. Shi, Z.; Li, Y.; Chen, X.; Han, H.; Yang, G., Double network bacterial cellulose hydrogel to build a biology-device interface. *Nanoscale* **2014,** *6* (2), 970-7.
104. Li, S.; Jasim, A.; Zhao, W.; Fu, L.; Ullah, M.; Shi, Z.; Yang, G., Fabrication of pH-electroactive Bacterial Cellulose/Polyaniline Hydrogel for the Development of a Controlled Drug Release System. *ES Mater. Manufacturing* **2018**.
105. Salimi, S.; Sotudeh-Gharebagh, R.; Zarghami, R.; Chan, S. Y.; Yuen, K. H., Production of Nanocellulose and Its Applications in Drug Delivery: A Critical Review. *ACS Sustain. Chem. Eng.* **2019,** *7* (19), 15800-15827.
106. Potzinger, Y.; Kralisch, D.; Fischer, D., Bacterial nanocellulose: the future of controlled drug delivery? *Ther. Deliv.* **2017,** *8* (9), 753-761.

107. Thoorens, G.; Krier, F.; Leclercq, B.; Carlin, B.; Evrard, B., Microcrystalline cellulose, a direct compression binder in a quality by design environment—A review. *Int. J. Pharm.* **2014,** *473* (1), 64-72.
108. Bhandari, J.; Mishra, H.; Mishra, P. K.; Wimmer, R.; Ahmad, F. J.; Talegaonkar, S., Cellulose nanofiber aerogel as a promising biomaterial for customized oral drug delivery. *Int. J. Nanomed.* **2017,** *12*, 2021-2031.
109. Poland, C. A.; Duffin, R.; Kinloch, I.; Maynard, A.; Wallace, W. A.; Seaton, A.; Stone, V.; Brown, S.; Macnee, W.; Donaldson, K., Carbon nanotubes introduced into the abdominal cavity of mice show asbestos-like pathogenicity in a pilot study. *Nature nanotechnology* **2008,** *3* (7), 423-8.
110. Jeevanandam, J.; Barhoum, A.; Chan, Y. S.; Dufresne, A.; Danquah, M. K., Review on nanoparticles and nanostructured materials: history, sources, toxicity and regulations. *Beilstein J. Nanotechnol.* **2018,** *9*, 1050-1074.
111. Davis, J. M. G., The need for standardised testing procedures for all products capable of liberating respirable fibres: the example of materials based on cellulose. *Br. J. Ind. Med.* **1993,** *50* (2), 187-190.
112. Bouwmeester, H.; Lynch, I.; Marvin, H. J.; Dawson, K. A.; Berges, M.; Braguer, D.; Byrne, H. J.; Casey, A.; Chambers, G.; Clift, M. J.; Elia, G.; Fernandes, T. F.; Fjellsbo, L. B.; Hatto, P.; Juillerat, L.; Klein, C.; Kreyling, W. G.; Nickel, C.; Riediker, M.; Stone, V., Minimal analytical characterization of engineered nanomaterials needed for hazard assessment in biological matrices. *Nanotoxicology* **2011,** *5* (1), 1-11.
113. Tatrai, E.; Adamis, Z.; Bohm, U.; Meretey, K.; Ungvary, G., Role of cellulose in wood dust-induced fibrosing alveo-bronchiolitis in rat. *Journal of applied toxicology : JAT* **1995,** *15* (1), 45-8.
114. Muhle, H.; Ernst, H.; Bellmann, B., Investigation of the Durability of Cellulose Fibres in Rat Lungs. *Annals of Work Exposures and Health* **1997,** *41* (inhaled_particles_VIII), 184-188.
115. Camarero-Espinosa, S.; Endes, C.; Mueller, S.; Petri-Fink, A.; Rothen-Rutishauser, B.; Weder, C.; Clift, M. J. D.; Foster, E. J., Elucidating the Potential Biological Impact of Cellulose Nanocrystals. . *Fibers* **2016,** *4*, 21.
116. Camarero-Espinosa, S.; Endes, C.; Mueller, S.; Petri-Fink, A.; Rothen-Rutishauser, B.; Weder, C.; Clift, M. J. D.; Foster, E. J., Elucidating the Potential Biological Impact of Cellulose Nanocrystals. *Fibers* **2016,** *4*, 21.
117. Samulin Erdem, J.; Alswady-Hoff, M.; Ervik, T. K.; Skare, Ø.; Ellingsen, D. G.; Zienolddiny, S., Cellulose nanocrystals modulate alveolar macrophage phenotype and phagocytic function. *Biomaterials* **2019,** *203*, 31-42.
118. Alexandrescu, L.; Syverud, K.; Gatti, A.; Chinga-Carrasco, G., Cytotoxicity tests of cellulose nanofibril-based structures. *Cellulose* **2013,** *20* (4), 1765-1775.
119. Hua, K.; Carlsson, D. O.; Ålander, E.; Lindström, T.; Strømme, M.; Mihranyan, A.; Ferraz, N., Translational study between structure and biological response of nanocellulose from wood and green algae. *Rsc Advances* **2014,** *4* (6), 2892-2903.
120. Ferraz, N.; Strømme, M.; Fellström, B.; Pradhan, S.; Nyholm, L.; Mihranyan, A., In vitro and in vivo toxicity of rinsed and aged nanocellulose–polypyrrole composites. *J. Biomed. Mater. Res. Part A* **2012,** *100* (8), 2128-2138.
121. Harper, B. J.; Clendaniel, A.; Sinche, F.; Way, D.; Hughes, M.; Schardt, J.; Simonsen, J.; Stefaniak, A. B.; Harper, S. L., Impacts of chemical modification on

the toxicity of diverse nanocellulose materials to developing zebrafish. *Cellulose* **2016,** *23* (3), 1763-1775.
122. Wang, H.; He, J.; Zhang, M.; Tam, K. C.; Ni, P., A new pathway towards polymer modified cellulose nanocrystals via a "grafting onto" process for drug delivery. *Polym. Chem.* **2015,** *6* (23), 4206-4209.
123. Yanamala, N.; Kisin, E. R.; Menas, A. L.; Farcas, M. T.; Khaliullin, T. O.; Vogel, U. B.; Shurin, G. V.; Schwegler-Berry, D.; Fournier, P. M.; Star, A., In vitro toxicity evaluation of lignin-(un) coated cellulose based nanomaterials on human A549 and THP-1 cells. *Biomacromolecules* **2016,** *17* (11), 3464-3473.
124. Khalid, A.; Zhang, L.; Tetienne, J.-P.; Abraham, A. N.; Poddar, A.; Shukla, R.; Shen, W.; Tomljenovic-Hanic, S., Intrinsic fluorescence from cellulose nanofibers and nanoparticles at cell friendly wavelengths. *APL Photonics* **2019,** *4* (2), 020803.
125. Tibolla, H.; Pelissari, F. M.; Martins, J. T.; Vicente, A.; Menegalli, F. C., Cellulose nanofibers produced from banana peel by chemical and mechanical treatments: characterization and cytotoxicity assessment. *J. Food hydrocolloids* **2018,** *75*, 192-201.
126. Hosseinidoust, Z.; Alam, M. N.; Sim, G.; Tufenkji, N.; van de Ven, T. G. M., Cellulose nanocrystals with tunable surface charge for nanomedicine. *Nanoscale* **2015,** *7* (40), 16647-16657.
127. ISO10993-5.
128. Moritz, S.; Wiegand, C.; Wesarg, F.; Hessler, N.; Müller, F. A.; Kralisch, D.; Hipler, U.-C.; Fischer, D., Active wound dressings based on bacterial nanocellulose as drug delivery system for octenidine. *Int. J. Pharm.* **2014,** *471* (1-2), 45-55.
129. Chiulan, I.; Mihaela Panaitescu, D.; Nicoleta Frone, A.; Teodorescu, M.; Andi Nicolae, C.; Căşărică, A.; Tofan, V.; Sălăgeanu, A., Biocompatible polyhydroxyalkanoates/bacterial cellulose composites: Preparation, characterization, and in vitro evaluation. *J. Biomed. Mater. Res. A* **2016,** *104* (10), 2576-2584.
130. Cacicedo, M. L.; León, I. E.; Gonzalez, J. S.; Porto, L. M.; Alvarez, V. A.; Castro, G. R., Modified bacterial cellulose scaffolds for localized doxorubicin release in human colorectal HT-29 cells. *Colloids and Surfaces B: Biointerfaces* **2016,** *140*, 421-429.
131. Osorio, M.; Cañas, A.; Puerta, J.; Díaz, L.; Naranjo, T.; Ortiz, I.; Castro, C., Ex Vivo and In Vivo Biocompatibility Assessment (Blood and Tissue) of Three-Dimensional Bacterial Nanocellulose Biomaterials for Soft Tissue Implants. *Sci. Rep.* **2019,** *9* (1), 10553.
132. Dong, S.; Hirani, A. A.; Colacina, K. R.; LEE Lee, Y. W.; Roman, M., Cytotoxicity and cellular uptake of cellulose nanocrystals. *Nano LIFE* **2012,** *02* (03), 1241006.
133. Mahmoud, K. A.; Mena, J. A.; Male, K. B.; Hrapovic, S.; Kamen, A.; Luong, J. H. T., Effect of Surface Charge on the Cellular Uptake and Cytotoxicity of Fluorescent Labeled Cellulose Nanocrystals. *ACS Appl. Mater. Interfaces* **2010,** *2* (10), 2924-2932.
134. Hua, K.; Ålander, E.; Lindström, T.; Mihranyan, A.; Strømme, M.; Ferraz, N., Surface Chemistry of Nanocellulose Fibers Directs Monocyte/Macrophage Response. *Biomacromolecules* **2015,** *16* (9), 2787-2795.

135. Yanamala, N.; Kisin, E. R.; Menas, A. L.; Farcas, M. T.; Khaliullin, T. O.; Vogel, U. B.; Shurin, G. V.; Schwegler-Berry, D.; Fournier, P. M.; Star, A.; Shvedova, A. A., In Vitro Toxicity Evaluation of Lignin-(Un)coated Cellulose Based Nanomaterials on Human A549 and THP-1 Cells. *Biomacromolecules* **2016,** *17* (11), 3464-3473.
136. Du, L.; Arnholt, K.; Ripp, S.; Sayler, G.; Wang, S.; Liang, C.; Wang, J.; Zhuang, J., Biological toxicity of cellulose nanocrystals (CNCs) against the luxCDABE-based bioluminescent bioreporter Escherichia coli 652T7. *Ecotoxicology* **2015,** *24* (10), 2049-2053.
137. DeLoid, G. M.; Cao, X.; Molina, R. M.; Silva, D. I.; Bhattacharya, K.; Ng, K. W.; Loo, S. C. J.; Brain, J. D.; Demokritou, P. J. E. S. N., Toxicological effects of ingested nanocellulose in in vitro intestinal epithelium and in vivo rat models. **2019,** *6* (7), 2105-2115.
138. Colombo, L.; Zoia, L.; Violatto, M. B.; Previdi, S.; Talamini, L.; Sitia, L.; Nicotra, F.; Orlandi, M.; Salmona, M.; Recordati, C.; Bigini, P.; La Ferla, B., Organ Distribution and Bone Tropism of Cellulose Nanocrystals in Living Mice. *Biomacromolecules* **2015,** *16* (9), 2862-2871.
139. DeLoid, G.; Cao, X.; Molina, R. M.; Silva, D. I.; Bhattacharya, K.; Ng, K. W.; Loo, J.; Brain, J.; Demokritou, P., Toxicological effects of ingested nanocellulose in in vitro intestinal epithelium and in vivo rat models. *Environmental Science: Nano* **2019**.
140. Yanamala, N.; Farcas, M. T.; Hatfield, M. K.; Kisin, E. R.; Kagan, V. E.; Geraci, C. L.; Shvedova, A. A., In Vivo Evaluation of the Pulmonary Toxicity of Cellulose Nanocrystals: A Renewable and Sustainable Nanomaterial of the Future. *ACS Sustain. Chem. Eng.* **2014,** *2* (7), 1691-1698.
141. Kovacs, T.; Naish, V.; O'Connor, B.; Blaise, C.; Gagne, F.; Hall, L.; Trudeau, V.; Martel, P., An ecotoxicological characterization of nanocrystalline cellulose (NCC). *Nanotoxicology* **2010,** *4* (3), 255-70.
142. Endes, C.; Camarero-Espinosa, S.; Mueller, S.; Foster, E. J.; Petri-Fink, A.; Rothen-Rutishauser, B.; Weder, C.; Clift, M. J. D., A critical review of the current knowledge regarding the biological impact of nanocellulose. *J. Nanobiotech.* **2016,** *14* (1), 78.
143. Wang, Z.; Tiruppathi, C.; Minshall, R. D.; Malik, A. B., Size and dynamics of caveolae studied using nanoparticles in living endothelial cells. *ACS nano* **2009,** *3* (12), 4110-4116.
144. Elsabahy, M.; Wooley, K. L., Design of polymeric nanoparticles for biomedical delivery applications. *Chem. Soc. Rev.* **2012,** *41* (7), 2545-2561.
145. Tsoi, K. M.; MacParland, S. A.; Ma, X.-Z.; Spetzler, V. N.; Echeverri, J.; Ouyang, B.; Fadel, S. M.; Sykes, E. A.; Goldaracena, N.; Kaths, J. M., Mechanism of hard-nanomaterial clearance by the liver. *Nat. Mater.* **2016,** *15* (11), 1212.
146. Choi, J.; Zhang, Q.; Reipa, V.; Wang, N. S.; Stratmeyer, M. E.; Hitchins, V. M.; Goering, P. L., Comparison of cytotoxic and inflammatory responses of photoluminescent silicon nanoparticles with silicon micron-sized particles in RAW 264.7 macrophages. *J. Appl. Toxicol.* **2009,** *29* (1), 52-60.
147. Čolić, M.; Mihajlović, D.; Mathew, A.; Naseri, N.; Kokol, V., Cytocompatibility and immunomodulatory properties of wood based nanofibrillated cellulose. *Cellulose* **2015,** *22* (1), 763-778.
148. Missoum, K.; Belgacem, M. N.; Bras, J., Nanofibrillated cellulose surface modification: a review. *Materials* **2013,** *6* (5), 1745-1766.

149. Roy, D.; Semsarilar, M.; Guthrie, J. T.; Perrier, S., Cellulose modification by polymer grafting: a review. *Chem. Soc. Rev.* **2009,** *38* (7), 2046-2064.
150. Ding, Q.; Zeng, J.; Wang, B.; Gao, W.; Chen, K.; Yuan, Z.; Xu, J., Influence of binding mechanism on labeling efficiency and luminous properties of fluorescent cellulose nanocrystals. *Carbohydr. Polym.* **2017,** *175*, 105-112.
151. Leng, T.; Jakubek, Z. J.; Mazloumi, M.; Leung, A. C. W.; Johnston, L. J., Ensemble and Single Particle Fluorescence Characterization of Dye-Labeled Cellulose Nanocrystals. *Langmuir* **2017,** *33* (32), 8002-8011.
152. Agustin, M. B.; Nakatsubo, F.; Yano, H., Products of low-temperature pyrolysis of nanocellulose esters and implications for the mechanism of thermal stabilization. *Cellulose* **2016,** *23* (5), 2887-2903.
153. Navarro, J. R. G.; Conzatti, G.; Yu, Y.; Fall, A. B.; Mathew, R.; Edén, M.; Bergström, L., Multicolor Fluorescent Labeling of Cellulose Nanofibrils by Click Chemistry. *Biomacromolecules* **2015,** *16* (4), 1293-1300.
154. Salam, A.; Lucia, L. A.; Jameel, H., Fluorine-based surface decorated cellulose nanocrystals as potential hydrophobic and oleophobic materials. *Cellulose* **2015,** *22* (1), 397-406.
155. Parambath Kanoth, B.; Claudino, M.; Johansson, M.; Berglund, L. A.; Zhou, Q., Biocomposites from Natural Rubber: Synergistic Effects of Functionalized Cellulose Nanocrystals as Both Reinforcing and Cross-Linking Agents via Free-Radical Thiol–ene Chemistry. *ACS Appl. Mater. Interfaces* **2015,** *7* (30), 16303-16310.
156. Espino-Pérez, E.; Domenek, S.; Belgacem, N.; Sillard, C.; Bras, J., Green Process for Chemical Functionalization of Nanocellulose with Carboxylic Acids. *Biomacromolecules* **2014,** *15* (12), 4551-4560.
157. Fumagalli, M.; Sanchez, F.; Molina-Boisseau, S.; Heux, L., Surface-restricted modification of nanocellulose aerogels in gas-phase esterification by di-functional fatty acid reagents. *Cellulose* **2015,** *22* (3), 1451-1457.
158. Hasani, M.; Cranston, E. D.; Westman, G.; Gray, D. G., Cationic surface functionalization of cellulose nanocrystals. *Soft Matter* **2008,** *4* (11), 2238-2244.
159. Dufresne, A., *Nanocellulose, From Nature to High Performance Tailored Materials*. de Gryter: 2012.
160. Raquez, J. M.; Murena, Y.; Goffin, A. L.; Habibi, Y.; Ruelle, B.; DeBuyl, F.; Dubois, P., Surface-modification of cellulose nanowhiskers and their use as nanoreinforcers into polylactide: A sustainably-integrated approach. *Composites Sci. Technol.* **2012,** *72* (5), 544-549.
161. Mabrouk, A. B.; Salon, M. C. B.; Magnin, A.; Belgacem, M. N.; Boufi, S., Cellulose-based nanocomposites prepared via mini-emulsion polymerization: Understanding the chemistry of the nanocellulose/matrix interface. *Coll. Surf. A: Physicochem. Eng. Aspects* **2014,** *448*, 1-8.
162. Yang, J.; Han, C.-R.; Duan, J.-F.; Ma, M.-G.; Zhang, X.-M.; Xu, F.; Sun, R.-C.; Xie, X.-M., Studies on the properties and formation mechanism of flexible nanocomposite hydrogels from cellulose nanocrystals and poly(acrylic acid). *J. Mater. Chem.* **2012,** *22* (42), 22467-22480.
163. Yang, J.; Han, C.-R.; Duan, J.-F.; Ma, M.-G.; Zhang, X.-M.; Xu, F.; Sun, R.-C., Synthesis and characterization of mechanically flexible and tough cellulose nanocrystals–polyacrylamide nanocomposite hydrogels. *Cellulose* **2013,** *20* (1), 227-237.

164. Rahmat, M.; Karrabi, M.; Ghasemi, I.; Zandi, M.; Azizi, H., Silane crosslinking of electrospun poly (lactic acid)/nanocrystalline cellulose bionanocomposite. *Materials science & engineering. C, Materials for biological applications* **2016,** *68*, 397-405.
165. Guo, J.; Fang, W.; Welle, A.; Feng, W.; Filpponen, I.; Rojas, O. J.; Levkin, P. A., Superhydrophobic and Slippery Lubricant-Infused Flexible Transparent Nanocellulose Films by Photoinduced Thiol–Ene Functionalization. *ACS Appl. Mater. Interfaces* **2016,** *8* (49), 34115-34122.
166. Siqueira, G.; Bras, J.; Dufresne, A., New Process of Chemical Grafting of Cellulose Nanoparticles with a Long Chain Isocyanate. *Langmuir* **2010,** *26* (1), 402-411.
167. Girouard, N. M.; Xu, S.; Schueneman, G. T.; Shofner, M. L.; Meredith, J. C., Site-Selective Modification of Cellulose Nanocrystals with Isophorone Diisocyanate and Formation of Polyurethane-CNC Composites. *ACS Appl. Mater. Interfaces* **2016,** *8* (2), 1458-1467.
168. Gwon, J.-G.; Cho, H.-J.; Chun, S.-J.; Lee, S.; Wu, Q.; Lee, S.-Y., Physiochemical, optical and mechanical properties of poly(lactic acid) nanocomposites filled with toluene diisocyanate grafted cellulose nanocrystals. *RSC Adv.* **2016,** *6* (12), 9438-9445.
169. Gwon, J.-G.; Cho, H.-J.; Chun, S.-J.; Lee, S.; Wu, Q.; Li, M.-C.; Lee, S.-Y., Mechanical and thermal properties of toluene diisocyanate-modified cellulose nanocrystal nanocomposites using semi-crystalline poly(lactic acid) as a base matrix. *RSC Adv.* **2016,** *6* (77), 73879-73886.
170. Habibi, Y.; Dufresne, A., Highly Filled Bionanocomposites from Functionalized Polysaccharide Nanocrystals. *Biomacromolecules* **2008,** *9* (7), 1974-1980.
171. Zoppe, J. O.; Peresin, M. S.; Habibi, Y.; Venditti, R. A.; Rojas, O. J., Reinforcing poly(epsilon-caprolactone) nanofibers with cellulose nanocrystals. *ACS Appl. Mater. Interfaces* **2009,** *1* (9), 1996-2004.
172. Abitbol, T.; Palermo, A.; Moran-Mirabal, J. M.; Cranston, E. D., Fluorescent labeling and characterization of cellulose nanocrystals with varying charge contents. *Biomacromolecules* **2013,** *14* (9), 3278-84.
173. Cunha, A. G.; Mougel, J.-B.; Cathala, B.; Berglund, L. A.; Capron, I., Preparation of Double Pickering Emulsions Stabilized by Chemically Tailored Nanocelluloses. *Langmuir* **2014,** *30* (31), 9327-9335.
174. Orelma, H.; Vuoriluoto, M.; Johansson, L.-S.; Campbell, J. M.; Filpponen, I.; Biesalski, M.; Rojas, O. J., Preparation of photoreactive nanocellulosic materials via benzophenone grafting. *RSC Adv.* **2016,** *6* (88), 85100-85106.
175. Hoenders, D.; Guo, J.; Goldmann, A. S.; Barner-Kowollik, C.; Walther, A., Photochemical ligation meets nanocellulose: a versatile platform for self-reporting functional materials. *Mater. Horiz.* **2018,** *5* (3), 560-568.
176. Gómez, F.; Combariza, M.; Blanco-Tirado, C., Facile cellulose nanofibrils amidation using a 'one-pot'approach. *Cellulose* **2017,** *24* (2), 717-730.
177. Abe, M.; Bégué, D.; Silva, H. S.; Dargelos, A.; Wentrup, C., Triplet States of Tetrazoles, Nitrenes, and Carbenes from Matrix Photolysis of Tetrazoles, and Phenylcyanamide as a Source of Phenylnitrene. *J. Phys. Chem. A* **2018,** *122* (37), 7276-7283.
178. Börjesson, M.; Sahlin, K.; Bernin, D.; Westman, G., Increased thermal stability of nanocellulose composites by functionalization of the sulfate groups on

cellulose nanocrystals with azetidinium ions. *J. Appl. Polym. Sci.* **2018,** *135* (10), 45963.
179. Yan, Q.; Zheng, H.-N.; Jiang, C.; Li, K.; Xiao, S.-J., EDC/NHS activation mechanism of polymethacrylic acid: anhydride versus NHS-ester. *RSC Adv.* **2015,** *5* (86), 69939-69947.
180. Benkaddour, A.; Journoux-Lapp, C.; Jradi, K.; Robert, S.; Daneault, C., Study of the hydrophobization of TEMPO-oxidized cellulose gel through two routes: amidation and esterification process. *J. Mater. Sci.* **2014,** *49* (7), 2832-2843.
181. Khine, Y. Y.; Batchelor, R. R.; Lu, H.; Raveendran, R.; Stenzel, M. H., *Marcromol. Rapid Commun.* **2019,** *submitted*.
182. Söyler, Z.; Onwukamike, K. N.; Grelier, S.; Grau, E.; Cramail, H.; Meier, M. A. R., Sustainable succinylation of cellulose in a CO2-based switchable solvent and subsequent Passerini 3-CR and Ugi 4-CR modification. *Green Chem.* **2018,** *20* (1), 214-224.
183. Navarro, J. R.; Bergström, L., Labelling of N-hydroxysuccinimide-modified rhodamine B on cellulose nanofibrils by the amidation reaction. *RSC Adv.* **2014,** *4* (105), 60757-60761.
184. Dong, S.; Roman, M., Fluorescently Labeled Cellulose Nanocrystals for Bioimaging Applications. *J. Am. Chem. Soc.* **2007,** *129* (45), 13810-13811.
185. Pahimanolis, N.; Hippi, U.; Johansson, L.-S.; Saarinen, T.; Houbenov, N.; Ruokolainen, J.; Seppälä, J., Surface functionalization of nanofibrillated cellulose using click-chemistry approach in aqueous media. *Cellulose* **2011,** *18* (5), 1201.
186. Herreros-López, A.; Hadad, C.; Yate, L.; Alshatwi, A. A.; Vicentini, N.; Carofiglio, T.; Prato, M., Synthesis and catalytic activity of gold nanoparticles supported on dendrimeric nanocellulose hybrids. *Eur. J. Organic Chem.* **2016,** *2016* (19), 3186-3192.
187. Filpponen, I.; Argyropoulos, D. S., Regular Linking of Cellulose Nanocrystals via Click Chemistry: Synthesis and Formation of Cellulose Nanoplatelet Gels. *Biomacromolecules* **2010,** *11* (4), 1060-1066.
188. Fatona, A.; Berry, R. M.; Brook, M. A.; Moran-Mirabal, J. M., Versatile Surface Modification of Cellulose Fibers and Cellulose Nanocrystals through Modular Triazinyl Chemistry. *Chem. Mater.* **2018,** *30* (7), 2424-2435.
189. Celebioglu, A.; Demirci, S.; Uyar, T., Cyclodextrin-grafted electrospun cellulose acetate nanofibers via "Click" reaction for removal of phenanthrene. *Appl. Surf. Sci.* **2014,** *305*, 581-588.
190. Zhou, L.; He, H.; Li, M.-C.; Huang, S.; Mei, C.; Wu, Q., Grafting polycaprolactone diol onto cellulose nanocrystals via click chemistry: Enhancing thermal stability and hydrophobic property. *Carbohydr. Polym.* **2018,** *189*, 331-341.
191. Tasdelen, M. A., Diels–Alder "click" reactions: recent applications in polymer and material science. *Polym. Chem.* **2011,** *2* (10), 2133-2145.
192. Shao, C.; Wang, M.; Chang, H.; Xu, F.; Yang, J., A Self-Healing Cellulose Nanocrystal-Poly(ethylene glycol) Nanocomposite Hydrogel via Diels–Alder Click Reaction. *ACS Sustain. Chem. Eng.* **2017,** *5* (7), 6167-6174.
193. Park, K.; Shin, C.; Song, Y.-S.; Lee, H.-J.; Shin, C.; Kim, Y., Recyclable and Mendable Cellulose-Reinforced Composites Crosslinked with Diels–Alder Adducts. *Polymers* **2019,** *11* (1), 117.
194. Guo, J.; Filpponen, I.; Johansson, L.-S.; Heiβler, S.; Li, L.; Levkin, P.; Rojas, O. J., Micro-patterns on nanocellulose films and paper by photo-induced thiol–

yne click coupling: a facile method toward wetting with spatial resolution. *Cellulose* **2018,** *25* (1), 367-375.
195. Sugawara, Y.; Jasinski, N.; Kaupp, M.; Welle, A.; Zydziak, N.; Blasco, E.; Barner-Kowollik, C., Light-driven nitrile imine-mediated tetrazole–ene cycloaddition as a versatile platform for fullerene conjugation. *Chem. Commun.* **2015,** *51* (65), 13000-13003.
196. Song, W.; Wang, Y.; Qu, J.; Madden, M. M.; Lin, Q., A photoinducible 1, 3-dipolar cycloaddition reaction for rapid, selective modification of tetrazole-containing proteins. *Angew. Chem. Inter. Ed.* **2008,** *47* (15), 2832-2835.
197. Hufendiek, A.; Carlmark, A.; Meier, M. A. R.; Barner-Kowollik, C., Fluorescent Covalently Cross-Linked Cellulose Networks via Light-Induced Ligation. *ACS Macro Lett.* **2016,** *5* (1), 139-143.
198. Nair, D. P.; Podgórski, M.; Chatani, S.; Gong, T.; Xi, W.; Fenoli, C. R.; Bowman, C. N., The Thiol-Michael Addition Click Reaction: A Powerful and Widely Used Tool in Materials Chemistry. *Chem. Mater.* **2014,** *26* (1), 724-744.
199. Celebioglu, A.; Demirci, S.; Uyar, T., Cyclodextrin-grafted electrospun cellulose acetate nanofibers via "Click" reaction for removal of phenanthrene. *Appl. Surf. Sci.* **2014,** *305*, 581-588.
200. Navarro, J. R.; Conzatti, G.; Yu, Y.; Fall, A. B.; Mathew, R.; Edén, M.; Bergström, L., Multicolor fluorescent labeling of cellulose nanofibrils by click chemistry. *Biomacromolecules* **2015,** *16* (4), 1293-1300.
201. Arcot, L. R.; Lundahl, M.; Rojas, O. J.; Laine, J., Asymmetric cellulose nanocrystals: thiolation of reducing end groups via NHS–EDC coupling. *Cellulose* **2014,** *21* (6), 4209-4218.
202. Villares, A.; Moreau, C.; Cathala, B., Star-like Supramolecular Complexes of Reducing-End-Functionalized Cellulose Nanocrystals. *ACS Omega* **2018,** *3* (11), 16203-16211.
203. Yanamala, N.; Farcas, M. T.; Hatfield, M. K.; Kisin, E. R.; Kagan, V. E.; Geraci, C. L.; Shvedova, A. A., In vivo evaluation of the pulmonary toxicity of cellulose nanocrystals: a renewable and sustainable nanomaterial of the future. *ACS sustainable chemistry & engineering* **2014,** *2* (7), 1691-1698.
204. Roman, M., Toxicity of cellulose nanocrystals: a review. *Industrial Biotechnology* **2015,** *11* (1), 25-33.
205. Jimenez, A. S.; Jaramillo, F.; Hemraz, U. D.; Boluk, Y.; Ckless, K.; Sunasee, R., Effect of surface organic coatings of cellulose nanocrystals on the viability of mammalian cell lines. *Nanotechnology, science and applications* **2017,** *10*, 123-136.
206. Sunasee, R.; Carson, M.; Despres, H. W.; Pacherille, A.; Nunez, K. D.; Ckless, K., Analysis of the Immune and Antioxidant Response of Cellulose Nanocrystals Grafted with β-Cyclodextrin in Myeloid Cell Lines. *J. Nanomater.* **2019,** *2019*, 9.
207. Guo, J.; Liu, D.; Filpponen, I.; Johansson, L.-S.; Malho, J.-M.; Quraishi, S.; Liebner, F.; Santos, H. A.; Rojas, O. J., Photoluminescent Hybrids of Cellulose Nanocrystals and Carbon Quantum Dots as Cytocompatible Probes for in Vitro Bioimaging. *Biomacromolecules* **2017,** *18* (7), 2045-2055.
208. Rahimi, M.; Shojaei, S.; Safa, K. D.; Ghasemi, Z.; Salehi, R.; Yousefi, B.; Shafiei-Irannejad, V., Biocompatible magnetic tris(2-aminoethyl)amine functionalized nanocrystalline cellulose as a novel nanocarrier for anticancer drug delivery of methotrexate. *New J. Chem.* **2017,** *41* (5), 2160-2168.

209. Gorgieva, S.; Vivod, V.; Maver, U.; Gradišnik, L.; Dolenšek, J.; Kokol, V., Internalization of (bis)phosphonate-modified cellulose nanocrystals by human osteoblast cells. *Cellulose* **2017,** *24* (10), 4235-4252.
210. Liu, Y.; Li, Y.; Yang, G.; Zheng, X.; Zhou, S., Multi-Stimulus-Responsive Shape-Memory Polymer Nanocomposite Network Cross-Linked by Cellulose Nanocrystals. *ACS Appl. Mater. Interfaces* **2015,** *7* (7), 4118-4126.
211. García-Astrain, C.; González, K.; Gurrea, T.; Guaresti, O.; Algar, I.; Eceiza, A.; Gabilondo, N., Maleimide-grafted cellulose nanocrystals as cross-linkers for bionanocomposite hydrogels. *Carbohydr. Polym.* **2016,** *149*, 94-101.
212. Zhao, J.; Li, Q.; Zhang, X.; Xiao, M.; Zhang, W.; Lu, C., Grafting of polyethylenimine onto cellulose nanofibers for interfacial enhancement in their epoxy nanocomposites. *Carbohydr. Polym.* **2017,** *157*, 1419-1425.
213. Lossada, F.; Guo, J.; Jiao, D.; Groeer, S.; Bourgeat-Lami, E.; Montarnal, D.; Walther, A., Vitrimer Chemistry Meets Cellulose Nanofibrils: Bioinspired Nanopapers with High Water Resistance and Strong Adhesion. *Biomacromolecules* **2019,** *20* (2), 1045-1055.
214. Chakrabarty, A.; Teramoto, Y., Recent Advances in Nanocellulose Composites with Polymers: A Guide for Choosing Partners and How to Incorporate Them. *Polymers* **2018,** *10* (5), 517.
215. Patel, D. K.; Dutta, S. D.; Lim, K.-T., Nanocellulose-based polymer hybrids and their emerging applications in biomedical engineering and water purification. *RSC Adv.* **2019,** *9* (33), 19143-19162.
216. Kargarzadeh, H.; Mariano, M.; Huang, J.; Lin, N.; Ahmad, I.; Dufresne, A.; Thomas, S., Recent developments on nanocellulose reinforced polymer nanocomposites: A review. *Polymer* **2017,** *132*, 368-393.
217. Kontturi, E.; Laaksonen, P.; Linder, M. B.; Nonappa; Gröschel, A. H.; Rojas, O. J.; Ikkala, O., Advanced Materials through Assembly of Nanocelluloses. *Adv. Mater.* **2018,** *30* (24), 1703779.
218. Li, N.; Lu, W.; Yu, J.; Xiao, Y.; Liu, S.; Gan, L.; Huang, J., Rod-like cellulose nanocrystal/cis-aconityl-doxorubicin prodrug: A fluorescence-visible drug delivery system with enhanced cellular uptake and intracellular drug controlled release. *Materials Science and Engineering: C* **2018,** *91*, 179-189.
219. Gholami Derami, H.; Jiang, Q.; Ghim, D.; Cao, S.; Chandar, Y. J.; Morrissey, J. J.; Jun, Y.-S.; Singamaneni, S., A Robust and Scalable Polydopamine/Bacterial Nanocellulose Hybrid Membrane for Efficient Wastewater Treatment. *ACS Appl. Nano Mater.* **2019,** *2* (2), 1092-1101.
220. Han, Y.; Wu, X.; Zhang, X.; Zhou, Z.; Lu, C., Dual Functional Biocomposites Based on Polydopamine Modified Cellulose Nanocrystal for Fe3+-Pollutant Detecting and Autoblocking. *ACS Sustain. Chem. Eng.* **2016,** *4* (10), 5667-5673.
221. Wu, X.; Tang, J.; Duan, Y.; Yu, A.; Berry, R. M.; Tam, K. C., Conductive cellulose nanocrystals with high cycling stability for supercapacitor applications. *J. Mater. Chem. A* **2014,** *2* (45), 19268-19274.
222. Tang, J.; Song, Y.; Tanvir, S.; Anderson, W. A.; Berry, R. M.; Tam, K. C., Polyrhodanine Coated Cellulose Nanocrystals: A Sustainable Antimicrobial Agent. *ACS Sustain. Chem. Eng.* **2015,** *3* (8), 1801-1809.
223. Liu, D.; Wu, Q.; Andersson, R. L.; Hedenqvist, M. S.; Farris, S.; Olsson, R. T., Cellulose nanofibril core–shell silica coatings and their conversion into thermally stable nanotube aerogels. *J. Mater. Chem. A* **2015,** *3* (30), 15745-15754.

224. Araki, J.; Wada, M.; Kuga, S., Steric Stabilization of a Cellulose Microcrystal Suspension by Poly(ethylene glycol) Grafting. *Langmuir* **2001,** *17* (1), 21-27.
225. Azzam, F.; Heux, L.; Putaux, J.-L.; Jean, B., Preparation By Grafting Onto, Characterization, and Properties of Thermally Responsive Polymer-Decorated Cellulose Nanocrystals. *Biomacromolecules* **2010,** *11* (12), 3652-3659.
226. Kloser, E.; Gray, D. G., Surface Grafting of Cellulose Nanocrystals with Poly(ethylene oxide) in Aqueous Media. *Langmuir* **2010,** *26* (16), 13450-13456.
227. Guo, M.; Her, S.; Keunen, R.; Zhang, S.; Allen, C.; Winnik, M. A., Functionalization of Cellulose Nanocrystals with PEG-Metal-Chelating Block Copolymers via Controlled Conjugation in Aqueous Media. *ACS Omega* **2016,** *1* (1), 93-107.
228. Solleder, S. C.; Meier, M. A., Sequence control in polymer chemistry through the Passerini three-component reaction. *Angew. Chem. Inter. Ed.* **2014,** *53* (3), 711-714.
229. Schmidt, S.; Koldevitz, M.; Noy, J.-M.; Roth, P. J., Multicomponent isocyanide-based synthesis of reactive styrenic and (meth) acrylic monomers and their RAFT (co) polymerization. *Polym. Chem.* **2015,** *6* (1), 44-54.
230. Wang, Y.-Z.; Deng, X.-X.; Li, L.; Li, Z.-L.; Du, F.-S.; Li, Z.-C., One-pot synthesis of polyamides with various functional side groups via Passerini reaction. *Polym. Chem.* **2013,** *4* (3), 444-448.
231. Kim, Y.; Pourgholami, M. H.; Morris, D. L.; Stenzel, M. H., An Optimized RGD-Decorated Micellar Drug Delivery System for Albendazole for the Treatment of Ovarian Cancer: From RAFT Polymer Synthesis to Cellular Uptake. *Macromol. Biosci.* **2011,** *11* (2), 219-233.
232. Duong, H. T. T.; Nguyen, T. L. U.; Stenzel, M. H., Micelles with surface conjugated RGD peptide and crosslinked polyurea core via RAFT polymerization. *Polym. Chem.* **2010,** *1* (2), 171-182.
233. Lemieux, M.; Minko, S.; Usov, D.; Stamm, M.; Tsukruk, V. V., Direct Measurement of Thermoelastic Properties of Glassy and Rubbery Polymer Brush Nanolayers Grown by "Grafting-from" Approach. *Langmuir* **2003,** *19* (15), 6126-6134.
234. Glasing, J.; Champagne, P.; Cunningham, M. F., Graft modification of chitosan, cellulose and alginate using reversible deactivation radical polymerization (RDRP). *Curr. Opin. Green Sustainable Chem.* **2016,** *2*, 15-21.
235. Assem, Y.; Abou-Zeid, R. E.; Ali, K. A.; Kamel, S., Synthesis of Acrylate-Modified Cellulose via Raft Polymerization and Its Application as Efficient Metal Ions Adsorbent. *Egypt. J. Chem.* **2017**.
236. Cheng, Z.; Liu, Y.; Zhang, D.; Lu, C.; Wang, C.; Xu, F.; Wang, J.; Chu, F., Sustainable elastomers derived from cellulose, rosin and fatty acid by a combination of "graft from" RAFT and isocyanate chemistry. *Int. J. Biol. Macromol.* **2019**.
237. Wang, H. D.; Roeder, R. D.; Whitney, R. A.; Champagne, P.; Cunningham, M. F., Graft modification of crystalline nanocellulose by Cu (0)-mediated SET living radical polymerization. *J. Polym. Sci. Part A: Polym. Chem.* **2015,** *53* (24), 2800-2808.
238. Navarro, J. R. G.; Wennmalm, S.; Godfrey, J.; Breitholtz, M.; Edlund, U., Luminescent Nanocellulose Platform: From Controlled Graft Block

Copolymerization to Biomarker Sensing. *Biomacromolecules* **2016,** *17* (3), 1101-1109.
239. Roy, D.; Guthrie, J. T.; Perrier, S., Graft polymerization: Grafting poly (styrene) from cellulose via reversible addition− fragmentation chain transfer (RAFT) polymerization. *Macromolecules* **2005,** *38* (25), 10363-10372.
240. Carlmark, A.; Larsson, E.; Malmström, E., Grafting of cellulose by ring-opening polymerisation – A review. *Eur. Polym. J.* **2012,** *48* (10), 1646-1659.
241. Bellani, C. F.; Pollet, E.; Hebraud, A.; Pereira, F. V.; Schlatter, G.; Avérous, L.; Bretas, R. E. S.; Branciforti, M. C., Morphological, thermal, and mechanical properties of poly(ε-caprolactone)/poly(ε-caprolactone)-grafted-cellulose nanocrystals mats produced by electrospinning. *J. Appl. Polym. Sci.* **2016,** *133* (21).
242. Lin, N.; Chen, G.; Huang, J.; Dufresne, A.; Chang, P. R., Effects of polymer-grafted natural nanocrystals on the structure and mechanical properties of poly(lactic acid): A case of cellulose whisker-graft-polycaprolactone. *J. Appl. Polym. Sci.* **2009,** *113* (5), 3417-3425.
243. Simão, J. A.; Bellani, C. F.; Branciforti, M. C., Thermal properties and crystallinity of PCL/PBSA/cellulose nanocrystals grafted with PCL chains. *J. Appl. Polym. Sci.* **2017,** *134* (8).
244. Peltzer, M.; Pei, A.; Zhou, Q.; Berglund, L.; Jiménez, A., Surface modification of cellulose nanocrystals by grafting with poly(lactic acid). *Polym. Inter.* **2014,** *63* (6), 1056-1062.
245. Goffin, A.-L.; Raquez, J.-M.; Duquesne, E.; Siqueira, G.; Habibi, Y.; Dufresne, A.; Dubois, P., From Interfacial Ring-Opening Polymerization to Melt Processing of Cellulose Nanowhisker-Filled Polylactide-Based Nanocomposites. *Biomacromolecules* **2011,** *12* (7), 2456-2465.
246. Braun, B.; Dorgan, J. R.; Hollingsworth, L. O., Supra-Molecular EcoBioNanocomposites Based on Polylactide and Cellulosic Nanowhiskers: Synthesis and Properties. *Biomacromolecules* **2012,** *13* (7), 2013-2019.
247. Bitinis, N.; Verdejo, R.; Bras, J.; Fortunati, E.; Kenny, J. M.; Torre, L.; López-Manchado, M. A., Poly(lactic acid)/natural rubber/cellulose nanocrystal bionanocomposites Part I. Processing and morphology. *Carbohydr. Polym.* **2013,** *96* (2), 611-620.
248. Lizundia, E.; Vilas, J. L.; León, L. M., Crystallization, structural relaxation and thermal degradation in Poly(l-lactide)/cellulose nanocrystal renewable nanocomposites. *Carbohydr. Polym.* **2015,** *123*, 256-265.
249. Muiruri, J. K.; Liu, S.; Teo, W. S.; Kong, J.; He, C., Highly Biodegradable and Tough Polylactic Acid–Cellulose Nanocrystal Composite. *ACS Sustain. Chem. Eng.* **2017,** *5* (5), 3929-3937.
250. de Paula, E. L.; Roig, F.; Mas, A.; Habas, J.-P.; Mano, V.; Pereira, F. V.; Robin, J.-J., Effect of surface-grafted cellulose nanocrystals on the thermal and mechanical properties of PLLA based nanocomposites. *Eur. Polym. J.* **2016,** *84*, 173-187.
251. Miao, C.; Hamad, W. Y., In-situ polymerized cellulose nanocrystals (CNC)-poly(l-lactide) (PLLA) nanomaterials and applications in nanocomposite processing. *Carbohydr. Polym.* **2016,** *153*, 549-558.
252. Habibi, Y.; Aouadi, S.; Raquez, J.-M.; Dubois, P., Effects of interfacial stereocomplexation in cellulose nanocrystal-filled polylactide nanocomposites. *Cellulose* **2013,** *20* (6), 2877-2885.

253. Ma, P.; Shen, T.; Lin, L.; Dong, W.; Chen, M., Cellulose-g-poly(d-lactide) nanohybrids induced significant low melt viscosity and fast crystallization of fully bio-based nanocomposites. *Carbohydr. Polym.* **2017,** *155*, 498-506.
254. Habibi, Y.; Goffin, A.-L.; Schiltz, N.; Duquesne, E.; Dubois, P.; Dufresne, A., Bionanocomposites based on poly(ε-caprolactone)-grafted cellulose nanocrystals by ring-opening polymerization. *J. Mater. Chem.* **2008,** *18* (41), 5002-5010.
255. Goffin, A. L.; Raquez, J. M.; Duquesne, E.; Siqueira, G.; Habibi, Y.; Dufresne, A.; Dubois, P., Poly(ε-caprolactone) based nanocomposites reinforced by surface-grafted cellulose nanowhiskers via extrusion processing: Morphology, rheology, and thermo-mechanical properties. *Polymer* **2011,** *52* (7), 1532-1538.
256. Tian, C.; Fu, S.; Habibi, Y.; Lucia, L. A., Polymerization Topochemistry of Cellulose Nanocrystals: A Function of Surface Dehydration Control. *Langmuir* **2014,** *30* (48), 14670-14679.
257. Dadkhah Tehrani, A.; Neysi, E., Surface modification of cellulose nanowhisker throughout graft polymerization of 2-ethyl-2-oxazoline. *Carbohydr. Polym.* **2013,** *97* (1), 98-104.
258. Wohlhauser, S.; Delepierre, G.; Labet, M.; Morandi, G.; Thielemans, W.; Weder, C.; Zoppe, J. O., Grafting Polymers from Cellulose Nanocrystals: Synthesis, Properties, and Applications. *Macromolecules* **2018,** *51* (16), 6157-6189.
259. Liu, S.; Jin, M.; Chen, Y.; Gao, H.; Shi, X.; Cheng, W.; Ren, L.; Wang, Y., High internal phase emulsions stabilised by supramolecular cellulose nanocrystals and their application as cell-adhesive macroporous hydrogel monoliths. *J. Mater. Chem. B* **2017,** *5* (14), 2671-2678.
260. Tang, J.; Lee, M. F. X.; Zhang, W.; Zhao, B.; Berry, R. M.; Tam, K. C., Dual Responsive Pickering Emulsion Stabilized by Poly[2-(dimethylamino)ethyl methacrylate] Grafted Cellulose Nanocrystals. *Biomacromolecules* **2014,** *15* (8), 3052-3060.
261. Wu, Y.; Wang, L.; Qing, Y.; Yan, N.; Tian, C.; Huang, Y., A green route to prepare fluorescent and absorbent nano-hybrid hydrogel for water detection. *Sci. Rep.* **2017,** *7* (1), 4380.
262. Zhou, C.; Wu, Q.; Yue, Y.; Zhang, Q., Application of rod-shaped cellulose nanocrystals in polyacrylamide hydrogels. *J. Coll. Interface Sci.* **2011,** *353* (1), 116-123.
263. Anirudhan, T. S.; Rejeena, S. R.; Binusree, J., Adsorptive Separation of Myoglobin from Aqueous Solutions Using Iron Oxide Magnetic Nanoparticles Modified with Functionalized Nanocrystalline Cellulose. *J. Chem. Eng. Data* **2013,** *58* (5), 1329-1339.
264. Zubik, K.; Singhsa, P.; Wang, Y.; Manuspiya, H.; Narain, R., Thermo-Responsive Poly(N-Isopropylacrylamide)-Cellulose Nanocrystals Hybrid Hydrogels for Wound Dressing. *Polymers* **2017,** *9* (4), 119.
265. Bamford, C. H.; Denyer, R.; Eastmond, G. C., Mechanism of free-radical formation in metal carbonyl + halide systems. Solvent effects. Part 1. *Trans. Faraday Soc.* **1965,** *61* (0), 1459-1469.
266. Lee, Y. R.; Park, D.; Choi, S. K.; Kim, M.; Baek, H. S.; Nam, J.; Chung, C. B.; Osuji, C. O.; Kim, J. W., Smart Cellulose Nanofluids Produced by Tunable Hydrophobic

Association of Polymer-Grafted Cellulose Nanocrystals. *ACS Appl. Mater. Interfaces* **2017,** *9* (36), 31095-31101.
267. Sarac, A. S., Redox polymerization. *Progr. Polym. Sci.* **1999,** *24* (8), 1149-1204.
268. Kedzior, S. A.; Graham, L.; Moorlag, C.; Dooley, B. M.; Cranston, E. D., Poly(methyl methacrylate)-grafted cellulose nanocrystals: One-step synthesis, nanocomposite preparation, and characterization. *Can. J. Chem. Eng.* **2016,** *94* (5), 811-822.
269. Stenstad, P.; Andresen, M.; Tanem, B. S.; Stenius, P., Chemical surface modifications of microfibrillated cellulose. *Cellulose* **2008,** *15* (1), 35-45.
270. Pracella, M.; Haque, M. M.-U.; Puglia, D., Morphology and properties tuning of PLA/cellulose nanocrystals bio-nanocomposites by means of reactive functionalization and blending with PVAc. *Polymer* **2014,** *55* (16), 3720-3728.
271. Kan, K. H. M.; Li, J.; Wijesekera, K.; Cranston, E. D., Polymer-Grafted Cellulose Nanocrystals as pH-Responsive Reversible Flocculants. *Biomacromolecules* **2013,** *14* (9), 3130-3139.
272. Tang, J.; Berry, R. M.; Tam, K. C., Stimuli-Responsive Cellulose Nanocrystals for Surfactant-Free Oil Harvesting. *Biomacromolecules* **2016,** *17* (5), 1748-1756.
273. Yuan, J.; Huang, X.; Li, P.; Li, L.; Shen, J., Surface-initiated RAFT polymerization of sulfobetaine from cellulose membranes to improve hemocompatibility and antibiofouling property. *Polym. Chem.* **2013,** *4* (19), 5074-5085.
274. Stenzel, M. H., Hairy Core-Shell Nanoparticles via RAFT: Where are the Opportunities and Where are the Problems and Challenges? *Macromol. Rapid Commun.* **2009,** *30* (19), 1603-1624.
275. Gregory, A.; Stenzel, M. H., Complex polymer architectures via RAFT polymerization: From fundamental process to extending the scope using click chemistry and nature's building blocks. *Prog. Polym. Sci.* **2012,** *37* (1), 38-105.
276. Perrier, S.; Takolpuckdee, P., Macromolecular design via reversible addition–fragmentation chain transfer (RAFT)/xanthates (MADIX) polymerization. *J. Polym. Sci. Part A: Polym. Chem.* **2005,** *43* (22), 5347-5393.
277. Boujemaoui, A.; Mazières, S.; Malmström, E.; Destarac, M.; Carlmark, A., SI-RAFT/MADIX polymerization of vinyl acetate on cellulose nanocrystals for nanocomposite applications. *Polymer* **2016,** *99*, 240-249.
278. Anžlovar, A.; Huskić, M.; Žagar, E., Modification of nanocrystalline cellulose for application as a reinforcing nanofiller in PMMA composites. *Cellulose* **2016,** *23* (1), 505-518.
279. Zeinali, E.; Haddadi-Asl, V.; Roghani-Mamaqani, H., Nanocrystalline cellulose grafted random copolymers of N-isopropylacrylamide and acrylic acid synthesized by RAFT polymerization: effect of different acrylic acid contents on LCST behavior. *RSC Adv.* **2014,** *4* (59), 31428-31442.
280. Zeinali, E.; Haddadi-Asl, V.; Roghani-Mamaqani, H., Synthesis of dual thermo- and pH-sensitive poly(N-isopropylacrylamide-co-acrylic acid)-grafted cellulose nanocrystals by reversible addition-fragmentation chain transfer polymerization. *J. Biomed. Mater. Res. A* **2018,** *106* (1), 231-243.
281. Haqani, M.; Roghani-Mamaqani, H.; Salami-Kalajahi, M., Synthesis of dual-sensitive nanocrystalline cellulose-grafted block copolymers of N-isopropylacrylamide and acrylic acid by reversible addition-fragmentation chain transfer polymerization. *Cellulose* **2017,** *24* (5), 2241-2254.
282. Liu, T.; Xue, F.; Ding, E., Cellulose nanocrystals grafted with polyacrylamide assisted by macromolecular RAFT agents. *Cellulose* **2016,** *23* (6), 3717-3735.

283. Liu, T.; Ding, E.; Xue, F., Polyacrylamide and poly(N,N-dimethylacrylamide) grafted cellulose nanocrystals as efficient flocculants for kaolin suspension. *Int. J. Biol. Macromol.* **2017,** *103*, 1107-1112.
284. Hu, H.; Hou, X.-J.; Wang, X.-C.; Nie, J.-J.; Cai, Q.; Xu, F.-J., Gold nanoparticle-conjugated heterogeneous polymer brush-wrapped cellulose nanocrystals prepared by combining different controllable polymerization techniques for theranostic applications. *Polym. Chem.* **2016,** *7* (18), 3107-3116.
285. Hatton, F. L.; Kedzior, S. A.; Cranston, E. D.; Carlmark, A., Grafting-from cellulose nanocrystals via photoinduced Cu-mediated reversible-deactivation radical polymerization. *Carbohydr. Polym.* **2017,** *157*, 1033-1040.
286. Matyjaszewski, K., Atom transfer radical polymerization: from mechanisms to applications. *Israel J. Chem.* **2012,** *52* (3-4), 206-220.
287. Pintauer, T.; Matyjaszewski, K., Atom transfer radical addition and polymerization reactions catalyzed by ppm amounts of copper complexes. *Chem. Soc. Rev.* **2008,** *37* (6), 1087-1097.
288. Yin, Y.; Tian, X.; Jiang, X.; Wang, H.; Gao, W., Modification of cellulose nanocrystal via SI-ATRP of styrene and the mechanism of its reinforcement of polymethylmethacrylate. *Carbohydr. Polym.* **2016,** *142*, 206-212.
289. Zhang, J.; Wu, Q.; Li, M.-C.; Song, K.; Sun, X.; Lee, S.-Y.; Lei, T., Thermoresponsive copolymer poly (N-Vinylcaprolactam) grafted cellulose nanocrystals: synthesis, structure, and properties. *ACS Sustain. Chem. Eng.* **2017,** *5* (8), 7439-7447.
290. Zoppe, J. O.; Dupire, A. V. M.; Lachat, T. G. G.; Lemal, P.; Rodriguez-Lorenzo, L.; Petri-Fink, A.; Weder, C.; Klok, H.-A., Cellulose nanocrystals with tethered polymer chains: chemically patchy versus uniform decoration. *ACS Macro Lett.* **2017,** *6* (9), 892-897.
291. Yi, J.; Xu, Q.; Zhang, X.; Zhang, H., Temperature-induced chiral nematic phase changes of suspensions of poly(N,N-dimethylaminoethyl methacrylate)-grafted cellulose nanocrystals. *Cellulose* **2009,** *16* (6), 989-997.
292. Zoppe, J. O.; Habibi, Y.; Rojas, O. J.; Venditti, R. A.; Johansson, L.-S.; Efimenko, K.; Österberg, M.; Laine, J., Poly(N-isopropylacrylamide) Brushes Grafted from Cellulose Nanocrystals via Surface-Initiated Single-Electron Transfer Living Radical Polymerization. *Biomacromolecules* **2010,** *11* (10), 2683-2691.
293. Wu, W.; Huang, F.; Pan, S.; Mu, W.; Meng, X.; Yang, H.; Xu, Z.; Ragauskas, A. J.; Deng, Y., Thermo-responsive and fluorescent cellulose nanocrystals grafted with polymer brushes. *J. Mater. Chem. A* **2015,** *3* (5), 1995-2005.
294. Zoppe, J. O.; Xu, X.; Känel, C.; Orsolini, P.; Siqueira, G.; Tingaut, P.; Zimmermann, T.; Klok, H.-A., Effect of Surface Charge on Surface-Initiated Atom Transfer Radical Polymerization from Cellulose Nanocrystals in Aqueous Media. *Biomacromolecules* **2016,** *17* (4), 1404-1413.
295. Ribelli, T. G.; Lorandi, F.; Fantin, M.; Matyjaszewski, K., Atom Transfer Radical Polymerization: Billion Times More Active Catalysts and New Initiation Systems. *Macromol. Rapid Commun.* **2019,** *40* (1), 1800616.
296. Yi, J.; Xu, Q.; Zhang, X.; Zhang, H., Chiral-nematic self-ordering of rodlike cellulose nanocrystals grafted with poly(styrene) in both thermotropic and lyotropic states. *Polymer* **2008,** *49* (20), 4406-4412.
297. Morandi, G.; Heath, L.; Thielemans, W., Cellulose Nanocrystals Grafted with Polystyrene Chains through Surface-Initiated Atom Transfer Radical Polymerization (SI-ATRP). *Langmuir* **2009,** *25* (14), 8280-8286.

298. Yu, J.; Wang, C.; Wang, J.; Chu, F., In situ development of self-reinforced cellulose nanocrystals based thermoplastic elastomers by atom transfer radical polymerization. *Carbohydr. Polym.* **2016,** *141*, 143-150.
299. Wang, H.-D.; Roeder, R. D.; Whitney, R. A.; Champagne, P.; Cunningham, M. F., Graft modification of crystalline nanocellulose by Cu(0)-mediated SET living radical polymerization. *J. Polym. Sci. Part A: Polym. Chem.* **2015,** *53* (24), 2800-2808.
300. Xu, Q.; Yi, J.; Zhang, X.; Zhang, H., A novel amphotropic polymer based on cellulose nanocrystals grafted with azo polymers. *Eur. Polym. J.* **2008,** *44* (9), 2830-2837.
301. Wang, Z.; Zhang, Y.; Yuan, L.; Hayat, J.; Trenor, N. M.; Lamm, M. E.; Vlaminck, L.; Billiet, S.; Du Prez, F. E.; Wang, Z.; Tang, C., Biomass Approach toward Robust, Sustainable, Multiple-Shape-Memory Materials. *ACS Macro Lett.* **2016,** *5* (5), 602-606.
302. Hemraz, U. D.; Lu, A.; Sunasee, R.; Boluk, Y., Structure of poly(N-isopropylacrylamide) brushes and steric stability of their grafted cellulose nanocrystal dispersions. *J. Coll. Interface Sci.* **2014,** *430*, 157-165.
303. Chen, X.; Huang, L.; Sun, H.-J.; Cheng, S. Z. D.; Zhu, M.; Yang, G., Stimuli-Responsive Nanocomposite: Potential Injectable Embolization Agent. *Macromol. Rapid Commun.* **2014,** *35* (5), 579-584.
304. Grishkewich, N.; Akhlaghi, S. P.; Zhaoling, Y.; Berry, R.; Tam, K. C., Cellulose nanocrystal-poly(oligo(ethylene glycol) methacrylate) brushes with tunable LCSTs. *Carbohydr. Polym.* **2016,** *144*, 215-22.
305. Zhang, X.; Zhang, J.; Dong, L.; Ren, S.; Wu, Q.; Lei, T., Thermoresponsive poly(poly(ethylene glycol) methylacrylate)s grafted cellulose nanocrystals through SI-ATRP polymerization. *Cellulose* **2017,** *24* (10), 4189-4203.
306. Zhang, J.; Wu, Q.; Li, M.-C.; Song, K.; Sun, X.; Lee, S.-Y.; Lei, T., Thermoresponsive Copolymer Poly(N-Vinylcaprolactam) Grafted Cellulose Nanocrystals: Synthesis, Structure, and Properties. *ACS Sustainable Chemistry & Engineering* **2017,** *5* (8), 7439-7447.
307. Majoinen, J.; Walther, A.; McKee, J. R.; Kontturi, E.; Aseyev, V.; Malho, J. M.; Ruokolainen, J.; Ikkala, O., Polyelectrolyte Brushes Grafted from Cellulose Nanocrystals Using Cu-Mediated Surface-Initiated Controlled Radical Polymerization. *Biomacromolecules* **2011,** *12* (8), 2997-3006.
308. McKee, J. R.; Appel, E. A.; Seitsonen, J.; Kontturi, E.; Scherman, O. A.; Ikkala, O., Healable, Stable and Stiff Hydrogels: Combining Conflicting Properties Using Dynamic and Selective Three-Component Recognition with Reinforcing Cellulose Nanorods. *Adv. Funct. Mater.* **2014,** *24* (18), 2706-2713.
309. Rosilo, H.; McKee, J. R.; Kontturi, E.; Koho, T.; Hytönen, V. P.; Ikkala, O.; Kostiainen, M. A., Cationic polymer brush-modified cellulose nanocrystals for high-affinity virus binding. *Nanoscale* **2014,** *6* (20), 11871-11881.
310. Malho, J.-M.; Morits, M.; Löbling, T. I.; Nonappa; Majoinen, J.; Schacher, F. H.; Ikkala, O.; Gröschel, A. H., Rod-Like Nanoparticles with Striped and Helical Topography. *ACS Macro Lett.* **2016,** *5* (10), 1185-1190.
311. Morits, M.; Hynninen, V.; Nonappa; Niederberger, A.; Ikkala, O.; Gröschel, A. H.; Müllner, M., Polymer brush guided templating on well-defined rod-like cellulose nanocrystals. *Polym. Chem.* **2018,** *9* (13), 1650-1657.
312. Hemraz, U. D.; Campbell, K. A.; Burdick, J. S.; Ckless, K.; Boluk, Y.; Sunasee, R., Cationic Poly(2-aminoethylmethacrylate) and Poly(N-(2-

aminoethylmethacrylamide) Modified Cellulose Nanocrystals: Synthesis, Characterization, and Cytotoxicity. *Biomacromolecules* **2015,** *16* (1), 319-325.
313. Arredondo, J.; Jessop, P. G.; Champagne, P.; Bouchard, J.; Cunningham, M. F., Synthesis of CO2-responsive cellulose nanocrystals by surface-initiated Cu(0)-mediated polymerisation. *Green Chem.* **2017,** *19* (17), 4141-4152.
314. Li, Y.; Zhu, L.; Grishkewich, N.; Tam, K. C.; Yuan, J.; Mao, Z.; Sui, X., CO2-Responsive Cellulose Nanofibers Aerogels for Switchable Oil–Water Separation. *ACS Appl. Mater. Interfaces* **2019,** *11* (9), 9367-9373.
315. Kaldéus, T.; Telaretti Leggieri, M. R.; Cobo Sanchez, C.; Malmström, E., All-Aqueous SI-ARGET ATRP from Cellulose Nanofibrils Using Hydrophilic and Hydrophobic Monomers. *Biomacromolecules* **2019,** *20* (5), 1937-1943.
316. Roeder, R. D.; Garcia-Valdez, O.; Whitney, R. A.; Champagne, P.; Cunningham, M. F., Graft modification of cellulose nanocrystals via nitroxide-mediated polymerisation. *Polym. Chem.* **2016,** *7* (41), 6383-6390.
317. Garcia-Valdez, O.; Brescacin, T.; Arredondo, J.; Bouchard, J.; Jessop, P. G.; Champagne, P.; Cunningham, M. F., Grafting CO2-responsive polymers from cellulose nanocrystals via nitroxide-mediated polymerisation. *Polym. Chem.* **2017,** *8* (28), 4124-4131.
318. Zoppe, J. O.; Dupire, A. V. M.; Lachat, T. G. G.; Lemal, P.; Rodriguez-Lorenzo, L.; Petri-Fink, A.; Weder, C.; Klok, H.-A., Cellulose Nanocrystals with Tethered Polymer Chains: Chemically Patchy versus Uniform Decoration. *ACS Macro Letters* **2017,** *6* (9), 892-897.
319. Lin, F.; Cousin, F.; Putaux, J.-L.; Jean, B., Temperature-Controlled Star-Shaped Cellulose Nanocrystal Assemblies Resulting from Asymmetric Polymer Grafting. *ACS Macro Lett.* **2019,** *8* (4), 345-351.
320. Pötzinger, Y.; Rabel, M.; Ahrem, H.; Thamm, J.; Klemm, D.; Fischer, D., Polyelectrolyte layer assembly of bacterial nanocellulose whiskers with plasmid DNA as biocompatible non-viral gene delivery system. *Cellulose* **2018,** *25* (3), 1939-1960.
321. Hu, H.; Yuan, W.; Liu, F.-S.; Cheng, G.; Xu, F.-J.; Ma, J., Redox-Responsive Polycation-Functionalized Cotton Cellulose Nanocrystals for Effective Cancer Treatment. *ACS Appl. Mater. Interfaces* **2015,** *7* (16), 8942-8951.
322. Hou, L.; Fang, J.; Wang, W.; Xie, Z.; Dong, D.; Zhang, N., Indocyanine green-functionalized bottle brushes of poly(2-oxazoline) on cellulose nanocrystals for photothermal cancer therapy. *J. Mater. Chem. B* **2017,** *5* (18), 3348-3354.
323. Sunasee, R.; Araoye, E.; Pyram, D.; Hemraz, U. D.; Boluk, Y.; Ckless, K., Cellulose nanocrystal cationic derivative induces NLRP3 inflammasome-dependent IL-1β secretion associated with mitochondrial ROS production. *Biochem. Biophys. Rep.* **2015,** *4*, 1-9.
324. Taheri, A.; Mohammadi, M., The use of cellulose nanocrystals for potential application in topical delivery of hydroquinone. *Chem. Biology Drug Design* **2015,** *86* (1), 102-106.
325. Nurani, M.; Akbari, V.; Taheri, A., Preparation and characterization of metformin surface modified cellulose nanofiber gel and evaluation of its anti-metastatic potentials. *Carbohydr. Polym.* **2017,** *165*, 322-333.
326. Jackson, J. K.; Letchford, K.; Wasserman, B. Z.; Ye, L.; Hamad, W. Y.; Burt, H. M., The use of nanocrystalline cellulose for the binding and controlled release of drugs. *Int. J. Nanomed.* **2011,** *6*, 321.

327. Ma, Q.; Cao, L.; Liang, T.; Li, J.; Lucia, L. A.; Wang, L., Active Tara Gum/PVA Blend Films with Curcumin-Loaded CTAC Brush-TEMPO-Oxidized Cellulose Nanocrystals. *ACS Sustain. Chem. Eng.* **2018,** *6* (7), 8926-8934.
328. Qing, W.; Wang, Y.; Wang, Y.; Zhao, D.; Liu, X.; Zhu, J., The modified nanocrystalline cellulose for hydrophobic drug delivery. *Appl. Surf. Sci.* **2016,** *366*, 404-409.
329. Zainuddin, N.; Ahmad, I.; Kargarzadeh, H.; Ramli, S., Hydrophobic kenaf nanocrystalline cellulose for the binding of curcumin. *Carbohydr. Polym.* **2017,** *163*, 261-269.
330. Foo, M. L.; Tan, C. R.; Lim, P. D.; Ooi, C. W.; Tan, K. W.; Chew, I. M. L., Surface-modified nanocrystalline cellulose from oil palm empty fruit bunch for effective binding of curcumin. *Int. J. Biol. Macromol.* **2019,** *138*, 1064-1071.
331. Cellante, L.; Costa, R.; Monaco, I.; Cenacchi, G.; Locatelli, E., One-step esterification of nanocellulose in a Brønsted acid ionic liquid for delivery to glioblastoma cancer cells. *New J. Chem.* **2018,** *42* (7), 5237-5242.
332. Tang, L.; Lin, F.; Li, T.; Cai, Z.; Hong, B.; Huang, B., Design and synthesis of functionalized cellulose nanocrystals-based drug conjugates for colon-targeted drug delivery. *Cellulose* **2018,** *25* (8), 4525-4536.
333. Singla, R.; Soni, S.; Padwad, Y. S.; Acharya, A.; Yadav, S. K., Sustained delivery of BSA/HSA from biocompatible plant cellulose nanocrystals for in vitro cholesterol release from endothelial cells. *Int. J. Biol. Macromol.* **2017,** *104*, 748-757.
334. Ndong Ntoutoume, G. M. A.; Granet, R.; Mbakidi, J. P.; Brégier, F.; Léger, D. Y.; Fidanzi-Dugas, C.; Lequart, V.; Joly, N.; Liagre, B.; Chaleix, V.; Sol, V., Development of curcumin–cyclodextrin/cellulose nanocrystals complexes: New anticancer drug delivery systems. *Bioorg. Med. Chem. Lett.* **2016,** *26* (3), 941-945.
335. Rioux, B.; Pouget, C.; Ndong-Ntoutoume, G. M.; Granet, R.; Gamond, A.; Laurent, A.; Pinon, A.; Champavier, Y.; Liagre, B.; Fagnère, C., Enhancement of hydrosolubility and in vitro antiproliferative properties of chalcones following encapsulation into β-cyclodextrin/cellulose-nanocrystal complexes. *Bioorg. Med. Chem. Lett.* **2019**.
336. Khattab, M. M.; Dahman, Y., Functionalized Bacterial Cellulose Nanowhiskers as Long-Lasting Drug Nanocarrier for Antibiotics and Anticancer Drugs. *Can. J. Chem. Eng.* **2019,** *0* (ja).
337. Foo, M.; Tan, C.; Lim, P.; Ooi, E. C.; Tan, K.; Chew, I. M., Surface-modified nanocrystalline cellulose from oil palm empty fruit bunch for effective binding of curcumin. *Int. J. Biol. Macromol.* **2019**.
338. Xia, Y.; Wan, J., Preparation and adsorption of novel cellulosic fibers modified by β-cyclodextrin. *Polym. Adv. Tech.* **2008,** *19* (4), 270-275.
339. Lee, M. H.; Yoon, K. J.; Ko, S.-W., Grafting onto cotton fiber with acrylamidomethylated β-cyclodextrin and its application. *J. Appl. Polym. Sci.* **2000,** *78* (11), 1986-1991.
340. Dong, S.; Cho, H. J.; Lee, Y. W.; Roman, M., Synthesis and cellular uptake of folic acid-conjugated cellulose nanocrystals for cancer targeting. *Biomacromolecules* **2014,** *15* (5), 1560-7.
341. Bittleman, K. R.; Dong, S.; Roman, M.; Lee, Y. W., Folic Acid-Conjugated Cellulose Nanocrystals Show High Folate-Receptor Binding Affinity and Uptake by KB and Breast Cancer Cells. *ACS Omega* **2018,** *3* (10), 13952-13959.

342. Hujaya, S. D.; Manninen, A.; Kling, K.; Wagner, J. B.; Vainio, S. J.; Liimatainen, H., Self-assembled nanofibrils from RGD-functionalized cellulose nanocrystals to improve the performance of PEI/DNA polyplexes. *J. Coll. Interface Sci.* **2019,** *553*, 71-82.
343. Hou, L.; Fang, J.; Wang, W.; Xie, Z.; Dong, D.; Zhang, N., Indocyanine green-functionalized bottle brushes of poly (2-oxazoline) on cellulose nanocrystals for photothermal cancer therapy. *J. Mater. Chem. B* **2017,** *5* (18), 3348-3354.
344. Hu, H.; Hou, X.-J.; Wang, X.-C.; Nie, J.-J.; Cai, Q.; Xu, F.-J., Gold nanoparticle-conjugated heterogeneous polymer brush-wrapped cellulose nanocrystals prepared by combining different controllable polymerization techniques for theranostic applications. *Polym. Chem.* **2016,** *7* (18), 3107-3116.
345. Li, N.; Zhang, H.; Xiao, Y.; Huang, Y.; Xu, M.; You, D.; Lu, W.; Yu, J., Fabrication of Cellulose-Nanocrystal-Based Folate Targeted Nanomedicine via Layer-by-Layer Assembly with Lysosomal pH-Controlled Drug Release into the Nucleus. *Biomacromolecules* **2019,** *20* (2), 937-948.
346. Ndong Ntoutoume, G. M. A.; Grassot, V.; Brégier, F.; Chabanais, J.; Petit, J.-M.; Granet, R.; Sol, V., PEI-cellulose nanocrystal hybrids as efficient siRNA delivery agents—Synthesis, physicochemical characterization and in vitro evaluation. *Carbohydr. Polym.* **2017,** *164*, 258-267.
347. Lin, N.; Bruzzese, C.; Dufresne, A., TEMPO-Oxidized Nanocellulose Participating as Crosslinking Aid for Alginate-Based Sponges. *ACS Appl. Mater. Interfaces* **2012,** *4* (9), 4948-4959.
348. Faradilla, R. H. F.; Lee, G.; Rawal, A.; Hutomo, T.; Stenzel, M. H.; Arcot, J., Nanocellulose characteristics from the inner and outer layer of banana pseudo-stem prepared by TEMPO-mediated oxidation. *Cellulose* **2016,** *23* (5), 3023-3037.
349. Lin, N.; Dufresne, A., Surface chemistry, morphological analysis and properties of cellulose nanocrystals with gradiented sulfation degrees. *Nanoscale* **2014,** *6* (10), 5384-5393.
350. Park, S.; Baker, J. O.; Himmel, M. E.; Parilla, P. A.; Johnson, D. K., Cellulose crystallinity index: measurement techniques and their impact on interpreting cellulase performance. *Biotechnol. Biofuels* **2010,** *3* (1), 10.
351. Usov, I.; Nyström, G.; Adamcik, J.; Handschin, S.; Schütz, C.; Fall, A.; Bergström, L.; Mezzenga, R., Understanding nanocellulose chirality and structure–properties relationship at the single fibril level. *Nat. Commun.* **2015,** *6*, 7564.
352. Isogai, A., *Determination of length and width of nanocelluloses from their dilute dispersions*. Trans. of the XVIth Fund. Res. Symp. Oxford, 2017: Manchester, 2017.
353. Mukherjee, A.; Hackley, V. A., Separation and characterization of cellulose nanocrystals by multi-detector asymmetrical-flow field-flow fractionation. *Analyst* **2018,** *143* (3), 731-740.
354. Mao, Y.; Liu, K.; Zhan, C.; Geng, L.; Chu, B.; Hsiao, B. S., Characterization of Nanocellulose Using Small-Angle Neutron, X-ray, and Dynamic Light Scattering Techniques. *J. Physi. Chem. B* **2017,** *121* (6), 1340-1351.
355. Shimizu, M.; Saito, T.; Nishiyama, Y.; Iwamoto, S.; Yano, H.; Isogai, A.; Endo, T., Fast and Robust Nanocellulose Width Estimation Using Turbidimetry. *Macromol. Rapid Commun.* **2016,** *37* (19), 1581-1586.

356. Tanaka, R.; Saito, T.; Hondo, H.; Isogai, A., Influence of Flexibility and Dimensions of Nanocelluloses on the Flow Properties of Their Aqueous Dispersions. *Biomacromolecules* **2015,** *16* (7), 2127-2131.
357. Zergane, H.; Abdi, S.; Xu, H.; Hemming, J.; Wang, X.; Willför, S.; Habibi, Y., Ampelodesmos mauritanicus a new sustainable source for nanocellulose substrates. *Ind. Crops. Prod.* **2020,** *144*, 112044.
358. Fröhlich, E., The role of surface charge in cellular uptake and cytotoxicity of medical nanoparticles. *Int. J. Nanomed.* **2012,** *7*, 5577.
359. Alexis, F.; Pridgen, E.; Molnar, L. K.; Farokhzad, O. C., Factors Affecting the Clearance and Biodistribution of Polymeric Nanoparticles. *Mol. Pharm.* **2008,** *5* (4), 505-515.
360. Choi, H. S.; Liu, W.; Misra, P.; Tanaka, E.; Zimmer, J. P.; Ipe, B. I.; Bawendi, M. G.; Frangioni, J. V., Renal clearance of nanoparticles. *Nat. Biotech.* **2007,** *25* (10), 1165.
361. Blanco, E.; Shen, H.; Ferrari, M., Principles of nanoparticle design for overcoming biological barriers to drug delivery. *Nat. Biotech.* **2015,** *33*, 941.
362. Tenzer, S.; Docter, D.; Kuharev, J.; Musyanovych, A.; Fetz, V.; Hecht, R.; Schlenk, F.; Fischer, D.; Kiouptsi, K.; Reinhardt, C.; Landfester, K.; Schild, H.; Maskos, M.; Knauer, S. K.; Stauber, R. H., Rapid formation of plasma protein corona critically affects nanoparticle pathophysiology. *Nat. Nanotech.* **2013,** *8*, 772.
363. Sim, R. B.; Wallis, R., Immune attack on nanoparticles. *Nat. Nanotech.* **2011,** *6*, 80.
364. Moad, G.; Chen, M.; Häussler, M.; Postma, A.; Rizzardo, E.; Thang, S. H., Functional polymers for optoelectronic applications by RAFT polymerization. *Polym. Chem.* **2011,** *2* (3), 492-519.
365. Chiefari, J.; Chong, Y.; Ercole, F.; Krstina, J.; Jeffery, J.; Le, T. P.; Mayadunne, R. T.; Meijs, G. F.; Moad, C. L.; Moad, G., Living free-radical polymerization by reversible addition− fragmentation chain transfer: the RAFT process. *Macromolecules* **1998,** *31* (16), 5559-5562.
366. Perrier, S. b., 50th Anniversary Perspective: RAFT Polymerization□ A User Guide. *Macromolecules* **2017,** *50* (19), 7433-7447.
367. Moad, G.; Rizzardo, E.; Thang, S. H., Living radical polymerization by the RAFT process–a third update. *Aust. J. Chem.* **2012,** *65* (8), 985-1076.
368. Moad, G., RAFT polymerization to form stimuli-responsive polymers. *Polym. Chem.* **2017,** *8* (1), 177-219.
369. Moad, G.; Mayadunne, R. T.; Rizzardo, E.; Skidmore, M.; Thang, S. H., Kinetics and mechanism of RAFT polymerization. *ACS Publications*: **2003**.
370. Liu, J.; Duong, H.; Whittaker, M. R.; Davis, T. P.; Boyer, C., Synthesis of functional core, star polymers via RAFT polymerization for drug delivery applications. *Macromol. Rapid Comm.* **2012,** *33* (9), 760-766.
371. Stenzel, M. H., RAFT polymerization: an avenue to functional polymeric micelles for drug delivery. *Chem. Commun.* **2008,** (30), 3486-3503.
372. Liu, C.; Li, B.; Du, H.; Lv, D.; Zhang, Y.; Yu, G.; Mu, X.; Peng, H., Properties of nanocellulose isolated from corncob residue using sulfuric acid, formic acid, oxidative and mechanical methods. *Carbohyd. Polym.* **2016,** *151*, 716-724.
373. Isogai, A.; Saito, T.; Fukuzumi, H., TEMPO-oxidized cellulose nanofibers. *Nanoscale* **2011,** *3* (1), 71-85.

374. Khine, Y. Y.; Stenzel, M. H., Surface modified cellulose nanomaterials: a source of non-spherical nanoparticles for drug delivery. *Mater. Horiz.* **2020**.
375. Jiang, F.; Hsieh, Y.-L., Chemically and mechanically isolated nanocellulose and their self-assembled structures. *Carbohyd. Polym.* **2013,** *95* (1), 32-40.
376. Wang, H.; Chen, C.; Fang, L.; Li, S.; Chen, N.; Pang, J.; Li, D., Effect of delignification technique on the ease of fibrillation of cellulose II nanofibers from wood. *Cellulose* **2018,** *25* (12), 7003-7015.
377. Tang, Z.; Li, W.; Lin, X.; Xiao, H.; Miao, Q.; Huang, L.; Chen, L.; Wu, H., TEMPO-oxidized cellulose with high degree of oxidation. *Polymers* **2017,** *9* (9), 421.
378. Isogai, A.; Zhou, Y., Diverse nanocelluloses prepared from TEMPO-oxidized wood cellulose fibers: Nanonetworks, nanofibers, and nanocrystals. *Curr. Opin. Solid State Mater. Sci.* **2019,** *23* (2), 101-106.
379. Fukuzumi, H.; Saito, T.; Iwata, T.; Kumamoto, Y.; Isogai, A., Transparent and High Gas Barrier Films of Cellulose Nanofibers Prepared by TEMPO-Mediated Oxidation. *Biomacromolecules* **2009,** *10* (1), 162-165.
380. Jiao, L.; Bian, H.; Gao, Y.; Lin, X.; Zhu, W.; Dai, H., Highly Dispersible Cellulose Nanofibrils Produced via Mechanical Pretreatment and TEMPO-mediated Oxidation. *Fiber. Polym.* **2018,** *19* (11), 2237-2244.
381. Moberg, T.; Sahlin, K.; Yao, K.; Geng, S.; Westman, G.; Zhou, Q.; Oksman, K.; Rigdahl, M., Rheological properties of nanocellulose suspensions: effects of fibril/particle dimensions and surface characteristics. *Cellulose* **2017,** *24* (6), 2499-2510.
382. Phanthong, P.; Reubroycharoen, P.; Hao, X.; Xu, G.; Abudula, A.; Guan, G., Nanocellulose: Extraction and application. *Carbon Resources Conversion* **2018,** *1* (1), 32-43.
383. Mao, Y.; Liu, K.; Zhan, C.; Geng, L.; Chu, B.; Hsiao, B. S., Characterization of nanocellulose using small-angle neutron, X-ray, and dynamic light scattering techniques. *J. Phys. Chem. B* **2017,** *121* (6), 1340-1351.
384. Morán, J. I.; Alvarez, V. A.; Cyras, V. P.; Vázquez, A., Extraction of cellulose and preparation of nanocellulose from sisal fibers. *Cellulose* **2008,** *15* (1), 149-159.
385. Khine, Y. Y.; Ganda, S.; Stenzel, M. H., Covalent Tethering of Temperature Responsive pNIPAm onto TEMPO-Oxidized Cellulose Nanofibrils via Three-Component Passerini Reaction. *ACS Macro Lett.* **2018,** *7* (4), 412-418.
386. Habibi, Y., Key advances in the chemical modification of nanocelluloses. *Chem. Soc. Rev.* **2014,** *43* (5), 1519-1542.
387. Yao, C.; Wang, F.; Cai, Z.; Wang, X., Aldehyde-functionalized porous nanocellulose for effective removal of heavy metal ions from aqueous solutions. *RSC advances* **2016,** *6* (95), 92648-92654.
388. Park, S.; Baker, J. O.; Himmel, M. E.; Parilla, P. A.; Johnson, D. K. J. B. f. b., Cellulose crystallinity index: measurement techniques and their impact on interpreting cellulase performance. **2010,** *3* (1), 10.
389. Ye, C.; Malak, S. T.; Hu, K.; Wu, W.; Tsukruk, V. V., Cellulose Nanocrystal Microcapsules as Tunable Cages for Nano- and Microparticles. *ACS Nano* **2015,** *9* (11), 10887-10895.
390. Roman, M.; Dong, S.; Hirani, A.; Lee, Y. W., Cellulose Nanocrystals for Drug Delivery. In Polysaccharide Materials: Performance by Design, *Am. Chem. Soc*. **2009**; 1017, 81-91.

391. Jackson, J. K.; Letchford, K.; Wasserman, B. Z.; Ye, L.; Hamad, W. Y.; Burt, H. M., The use of nanocrystalline cellulose for the binding and controlled release of drugs. *Inter. J. Nanomed.* **2011,** *6*, 321.
392. Kaldéus, T.; Nordenström, M.; Carlmark, A.; Wågberg, L.; Malmström, E., Insights into the EDC-mediated PEGylation of cellulose nanofibrils and their colloidal stability. *Carbohyd. Polym.* **2018,** *181*, 871-878.
393. Habibi, Y., Key advances in the chemical modification of nanocelluloses. *Chem. Soc. Rev.* **2014,** *43* (5), 1519-1542.
394. Ramil, C. P.; Lin, Q., Photoclick chemistry: a fluorogenic light-triggered in vivo ligation reaction. *J Current Opinion Chem. Biol.* **2014,** *21*, 89-95.
395. Mueller, J. O.; Voll, D.; Schmidt, F. G.; Delaittre, G.; Barner-Kowollik, C., Fluorescent polymers from non-fluorescent photoreactive monomers. *Chem. Commun.* **2014,** *50* (99), 15681-15684.
396. Mueller, J. O.; Guimard, N. K.; Oehlenschlaeger, K. K.; Schmidt, F. G.; Barner-Kowollik, C., Sunlight-induced crosslinking of 1,2-polybutadienes: access to fluorescent polymer networks. *Polym. Chem.* **2014,** *5* (4), 1447-1456.
397. Dietrich, M.; Delaittre, G.; Blinco, J. P.; Inglis, A. J.; Bruns, M.; Barner-Kowollik, C., Photoclickable Surfaces for Profluorescent Covalent Polymer Coatings. *Adv. Funct. Mater.* **2012,** *22* (2), 304-312.
398. Li, Z.; Qian, L.; Li, L.; Bernhammer, J. C.; Huynh, H. V.; Lee, J.-S.; Yao, S. Q., Tetrazole Photoclick Chemistry: Reinvestigating Its Suitability as a Bioorthogonal Reaction and Potential Applications. *Angew. Chem. Inter. Ed.* **2016,** *55* (6), 2002-2006.
399. Shang, X.; Lai, R.; Song, X.; Li, H.; Niu, W.; Guo, J., Improved Photoinduced Fluorogenic Alkene-Tetrazole Reaction for Protein Labeling. *Bioconjugate Chem.* **2017,** *28* (11), 2859-2864.
400. Zhao, S.; Dai, J.; Hu, M.; Liu, C.; Meng, R.; Liu, X.; Wang, C.; Luo, T., Photo-induced coupling reactions of tetrazoles with carboxylic acids in aqueous solution: application in protein labelling. *Chem. Commun.* **2016,** *52* (25), 4702-4705.
401. Heiler, C.; Offenloch, J. T.; Blasco, E.; Barner-Kowollik, C., Photochemically Induced Folding of Single Chain Polymer Nanoparticles in Water. *ACS Macro Lett.* **2017,** *6* (1), 56-61.
402. Cserép, G. B.; Herner, A.; Kele, P., Bioorthogonal fluorescent labels: a review on combined forces. *Methods Appl. Fluoresc.* **2015,** *3* (4), 042001.
403. Abe, M.; Bégué, D.; Silva, H. S.; Dargelos, A.; Wentrup, C., Triplet States of Tetrazoles, Nitrenes, and Carbenes from Matrix Photolysis of Tetrazoles, and Phenylcyanamide as a Source of Phenylnitrene. *J. Phys. Chem. A* **2018,** *122* (37), 7276-7283.
404. Song, W.; Wang, Y.; Qu, J.; Madden, M. M.; Lin, Q., A Photoinducible 1,3-Dipolar Cycloaddition Reaction for Rapid, Selective Modification of Tetrazole-Containing Proteins. *Angew. Chem. Inter. Ed.* **2008,** *47* (15), 2832-2835.
405. Zhang, Y.; Liu, W.; Zhao, Z. K., Nucleophilic Trapping Nitrilimine Generated by Photolysis of Diaryltetrazole in Aqueous Phase. *Molecules* **2014,** *19* (1), 306-315.
406. Scheiner, P.; Dinda, J. F., Product Formation in Tetrazole Photolysis. *Tetrahedron* **1970,** *26* (11), 2619-&.

407. Qu, J.-B.; Chapman, R.; Chen, F.; Lu, H.; Stenzel, M. H., Swollen Micelles for the Preparation of Gated, Squeezable, pH-Responsive Drug Carriers. *ACS Appl. Mater. Interfaces* **2017,** *9* (16), 13865-13874.
408. Tewes, F.; Munnier, E.; Antoon, B.; Ngaboni Okassa, L.; Cohen-Jonathan, S.; Marchais, H.; Douziech-Eyrolles, L.; Souce, M.; Dubois, P.; Chourpa, I., Comparative study of doxorubicin-loaded poly(lactide-co-glycolide) nanoparticles prepared by single and double emulsion methods. *Eur. J. Pharm. Biopharm. : official journal of Arbeitsgemeinschaft fur Pharmazeutische Verfahrenstechnik e.V* **2007,** *66* (3), 488-92.
409. Cacicedo, M. L.; León, I. E.; Gonzalez, J. S.; Porto, L. M.; Alvarez, V. A.; Castro, G. R., Modified bacterial cellulose scaffolds for localized doxorubicin release in human colorectal HT-29 cells. *J Coll. Surf. B: Biointerfaces* **2016,** *140*, 421-429.
410. Islan, G. A.; de Verti, I. P.; Marchetti, S. G.; Castro, G. R., Studies of ciprofloxacin encapsulation on alginate/pectin matrixes and its relationship with biodisponibility. *J Appl. Biochem. Biotech.* **2012,** *167* (5), 1408-1420.
411. Shi, Y.; Lammers, T.; Storm, G.; Hennink, W. E., Physico-Chemical Strategies to Enhance Stability and Drug Retention of Polymeric Micelles for Tumor-Targeted Drug Delivery. *Macromol. Biosci.* **2017,** *17* (1), 1600160.
412. Chu, K. S.; Schorzman, A. N.; Finniss, M. C.; Bowerman, C. J.; Peng, L.; Luft, J. C.; Madden, A. J.; Wang, A. Z.; Zamboni, W. C.; DeSimone, J. M., Nanoparticle drug loading as a design parameter to improve docetaxel pharmacokinetics and efficacy. *Biomaterials* **2013,** *34* (33), 8424-8429.
413. Callari, M.; De Souza, P. L.; Rawal, A.; Stenzel, M. H., The Effect of Drug Loading on Micelle Properties: Solid-State NMR as a Tool to Gain Structural Insight. *Angew. Chem. Inter. Ed.* **2017,** *56* (29), 8441-8445.
414. Cao, C.; Zhao, J.; Chen, F.; Lu, M.; Khine, Y. Y.; Macmillan, A.; Garvey, C. J.; Stenzel, M. H., Drug-induced morphology transition of self-assembled glycopolymers: Insight into the drug-polymer interaction. *Chem. Mater.* **2018**.
415. Khan, R. A.; Salmieri, S.; Dussault, D.; Uribe-Calderon, J.; Kamal, M. R.; Safrany, A.; Lacroix, M., Production and Properties of Nanocellulose-Reinforced Methylcellulose-Based Biodegradable Films. *J. Agric. Food. Chem.* **2010,** *58* (13), 7878-7885.
416. Lin, N.; Dufresne, A., Nanocellulose in biomedicine: Current status and future prospect. *Eur. Polym. J.* **2014,** *59* (Supplement C), 302-325.
417. Lee, K.-Y.; Aitomäki, Y.; Berglund, L. A.; Oksman, K.; Bismarck, A., On the use of nanocellulose as reinforcement in polymer matrix composites. *Compos. Sci. Technol.* **2014,** *105* (Supplement C), 15-27.
418. Qi, W.; Xu, H.-N.; Zhang, L., The aggregation behavior of cellulose micro/nanoparticles in aqueous media. *RSC Advances* **2015,** *5* (12), 8770-8777.
419. Cudjoe, E.; Khani, S.; Way, A. E.; Hore, M. J. A.; Maia, J.; Rowan, S. J., Biomimetic Reversible Heat-Stiffening Polymer Nanocomposites. *ACS Central Science* **2017,** *3* (8), 886-894.
420. Kaldéus, T.; Nordenström, M.; Carlmark, A.; Wågberg, L.; Malmström, E., Insights into the EDC-mediated PEGylation of cellulose nanofibrils and their colloidal stability. *Carbohydr. Polym.* **2018,** *181*, 871-878.
421. Barsbay, M.; Güven, O.; Davis, T. P.; Barner-Kowollik, C.; Barner, L., RAFT-mediated polymerization and grafting of sodium 4-styrenesulfonate from cellulose initiated via γ-radiation. *Polymer* **2009,** *50* (4), 973-982.

422. Wang, S. X.; Wang, M. X.; Wang, D. X.; Zhu, J., Catalytic Enantioselective Passerini Three-Component Reaction. *Angew. Chem.* **2008,** *120* (2), 394-397.
423. Ramozzi, R.; Morokuma, K., Revisiting the Passerini Reaction Mechanism: Existence of the Nitrilium, Organocatalysis of Its Formation, and Solvent Effect. *J. Org. Chem.* **2015,** *80* (11), 5652-5657.
424. Sehlinger, A.; Kreye, O.; Meier, M. A. R., Tunable Polymers Obtained from Passerini Multicomponent Reaction Derived Acrylate Monomers. *Macromolecules* **2013,** *46* (15), 6031-6037.
425. Sehlinger, A.; Schneider, R.; Meier, M. A. R., Passerini addition polymerization of an AB-type monomer – A convenient route to versatile polyesters. *Eur. Polym. J.* **2014,** *50* (Supplement C), 150-157.
426. Sehlinger, A.; de Espinosa, L. M.; Meier, M. A. R., Synthesis of Diverse Asymmetric α,ω-Dienes Via the Passerini Three-Component Reaction for Head-to-Tail ADMET Polymerization. *Macromol. Chem. Phys.* **2013,** *214* (24), 2821-2828.
427. Solleder, S. C.; Meier, M. A. R., Sequence Control in Polymer Chemistry through the Passerini Three-Component Reaction. *Angew. Chem. Int. Ed.* **2014,** *53* (3), 711-714.
428. Kreye, O.; Kugele, D.; Faust, L.; Meier, M. A. R., Divergent Dendrimer Synthesis via the Passerini Three-Component Reaction and Olefin Cross-Metathesis. *Macromol. Rapid Commun.* **2014,** *35* (3), 317-322.
429. Jee, J.-A.; Spagnuolo, L. A.; Rudick, J. G., Convergent Synthesis of Dendrimers via the Passerini Three-Component Reaction. *Org. Lett.* **2012,** *14* (13), 3292-3295.
430. Soyler, Z.; Onwukamike, K. N.; Grelier, S.; Grau, E.; Cramail, H.; Meier, M. A. R., Sustainable succinylation of cellulose in a CO2-based switchable solvent and subsequent Passerini 3-CR and Ugi 4-CR modification. *Green Chem.* **2018,** *20* (1), 214-224.
431. Kim, H.; Kim, K.; Lee, S. J., Nature-inspired thermo-responsive multifunctional membrane adaptively hybridized with PNIPAm and PPy. *Npg Asia Materials* **2017,** *9*, e445.
432. Khine, Y. Y.; Jiang, Y.; Dag, A.; Lu, H.; Stenzel, M. H., Dual-Responsive pH and Temperature Sensitive Nanoparticles Based on Methacrylic Acid and Di(ethylene glycol) Methyl Ether Methacrylate for the Triggered Release of Drugs. *Macromol. Biosci.* **2015,** *15* (8), 1091-1104.
433. Park, B. R.; Nabae, Y.; Surapati, M.; Hayakawa, T.; Kakimoto, M.-a., Poly(N-isopropylacrylamide)-modified silica beads with hyperbranched polysiloxysilane for three-dimensional cell cultivation. *Polym. J.* **2012,** *45*, 210.
434. Jones, M. W.; Gibson, M. I.; Mantovani, G.; Haddleton, D. M., Tunable thermo-responsive polymer–protein conjugates via a combination of nucleophilic thiol–ene "click" and SET-LRP. *Polymer Chemistry* **2011,** *2* (3), 572-574.
435. Zhang, X.-Z.; Zhuo, R.-X.; Cui, J.-Z.; Zhang, J.-T., A novel thermo-responsive drug delivery system with positive controlled release. *Int. J. Pharm.* **2002,** *235* (1), 43-50.
436. Porsch, C.; Hansson, S.; Nordgren, N.; Malmstrom, E., Thermo-responsive cellulose-based architectures: tailoring LCST using poly(ethylene glycol) methacrylates. *Polym. Chem.* **2011,** *2* (5), 1114-1123.

437. Hufendiek, A.; Barner-Kowollik, C.; Meier, M. A. R., Renewable, fluorescent, and thermoresponsive: cellulose copolymers via light-induced ligation in solution. *Polym. Chem.* **2015,** *6* (12), 2188-2191.
438. Skey, J.; O'Reilly, R. K., Facile one pot synthesis of a range of reversible addition–fragmentation chain transfer (RAFT) agents. *Chem. Commun.* **2008,** (35), 4183-4185.
439. McKenzie, T.; Costa, L. d. M.; Fu, Q.; Dunstan, D.; Qiao, G., Investigation into the photolytic stability of RAFT agents and the implications for photopolymerization reactions. *Polym. Chem.* **2016,** *7* (25), 4246-4253.
440. Biswal, D. R.; Singh, R. P., Characterisation of carboxymethyl cellulose and polyacrylamide graft copolymer. *Carbohyd. Polym.* **2004,** *57* (4), 379-387.
441. Ieong, N. S.; Hasan, M.; Phillips, D. J.; Saaka, Y.; O'Reilly, R. K.; Gibson, M. I., Polymers with molecular weight dependent LCSTs are essential for cooperative behaviour. *Polym. Chem.* **2012,** *3* (3), 794-799.
442. Pardoll, D. M., Immunology beats cancer: a blueprint for successful translation. *Nat. Immunol.* **2012,** *13* (12), 1129-1132.
443. Waldmann, T. A., Immunotherapy: past, present and future. *Nat. Med.* **2003,** *9* (3), 269-277.
444. Dunn, G. P.; Bruce, A. T.; Ikeda, H.; Old, L. J.; Schreiber, R. D., Cancer immunoediting: from immunosurveillance to tumor escape. *Nat. Immunol.* **2002,** *3* (11), 991-998.
445. Mittal, D.; Gubin, M. M.; Schreiber, R. D.; Smyth, M. J., New insights into cancer immunoediting and its three component phases—elimination, equilibrium and escape. *Curr. Opin. Immunol.* **2014,** *27*, 16-25.
446. Vesely, M. D.; Schreiber, R. D., Cancer Immunoediting: antigens, mechanisms and implications to cancer immunotherapy. *Ann. NY Acad. Sci.* **2013,** *1284* (1), 1.
447. Romero, J.; Aptsiauri, N.; Vazquez, F.; Cozar, J.; Canton, J.; Cabrera, T.; Tallada, M.; Garrido, F.; Ruiz-Cabello, F., Analysis of the expression of HLA class I, proinflammatory cytokines and chemokines in primary tumors from patients with localized and metastatic renal cell carcinoma. *Tissue antigens* **2006,** *68* (4), 303-310.
448. Dunn, G. P.; Koebel, C. M.; Schreiber, R. D., Interferons, immunity and cancer immunoediting. *Nat. Rev. Immunol.* **2006,** *6* (11), 836-848.
449. Reiman, J. M.; Kmieciak, M.; Manjili, M. H.; Knutson, K. L. In Tumor immunoediting and immunosculpting pathways to cancer progression, Seminars in cancer biology, Elsevier: 2007; pp 275-287.
450. Borden, E. C.; Sondel, P. M., Lymphokines and cytokines as cancer treatment. Immunotherapy realized. *Cancer* **1990,** *65* (S3), 800-814.
451. Dranoff, G., Cytokines in cancer pathogenesis and cancer therapy. *Nat. Rev. Cancer* **2004,** *4* (1), 11-22.
452. Lee, S.; Margolin, K., Cytokines in cancer immunotherapy. *Cancers* **2011,** *3* (4), 3856-3893.
453. Lode, H. N.; Reisfeld, R. A., Targeted cytokines for cancer immunotherapy. *Immunol. Res.* **2000,** *21* (2-3), 279-288.
454. Smyth, M. J.; Cretney, E.; Kershaw, M. H.; Hayakawa, Y., Cytokines in cancer immunity and immunotherapy. *Immunol. Rev.* **2004,** *202* (1), 275-293.
455. Wolf, S. F.; Lee, K.; Swiniarski, H.; O'toole, M.; Sturmhoefel, K., Cytokines and cancer immunotherapy. *Immunol. Invest.* **2000,** *29* (2), 143-146.

456. Dinarello, C. A., The proinflammatory cytokines interleukin-l and tumor necrosis factor and treatment of the septic shock syndrome. *J. Infectious Diseases* **1991,** *163* (6), 1177-1184.
457. Chemokines. In *Encyclopedia of Cancer*, Schwab, M., Ed. Springer Berlin Heidelberg: Berlin, Heidelberg, 2011; pp 772-774.
458. Bobanga, I. D.; Petrosiute, A.; Huang, A. Y., Chemokines as cancer vaccine adjuvants. *Vaccines* **2013,** *1* (4), 444-462.
459. Nagarsheth, N.; Wicha, M. S.; Zou, W., Chemokines in the cancer microenvironment and their relevance in cancer immunotherapy. *Nat. Rev. Immunol.* **2017,** *17* (9), 559.
460. Vicari, A. P.; Caux, C., Chemokines in cancer. *Cytokine Growth F. R.* **2002,** *13* (2), 143-154.
461. Ren, M.; Guo, Q.; Guo, L.; Lenz, M.; Qian, F.; Koenen, R. R.; Xu, H.; Schilling, A. B.; Weber, C.; Richard, D. Y., Polymerization of MIP-1 chemokine (CCL3 and CCL4) and clearance of MIP-1 by insulin-degrading enzyme. *EMBO J.* **2010,** *29* (23), 3952-3966.
462. Vallet, S.; Anderson, K. C., CCR1 as a target for multiple myeloma. *Expert Opin Ther. Tar.* **2011,** *15* (9), 1037-1047.
463. Zeng, X.; Moore, T. A.; Newstead, M. W.; Hernandez-Alcoceba, R.; Tsai, W. C.; Standiford, T. J., Intrapulmonary expression of macrophage inflammatory protein 1α (CCL3) induces neutrophil and NK cell accumulation and stimulates innate immunity in murine bacterial pneumonia. *Infect. Immun.* **2003,** *71* (3), 1306-1315.
464. Zibert, A.; Balzer, S.; Souquet, M.; Quang, T. H.; Paris-Scholz, C.; Roskrow, M.; Dilloo, D., CCL3/MIP-1 α Is a Potent Immunostimulator When Coexpressed with Interleukin-2 or Granulocyte-Macrophage Colony-Stimulating Factor in a Leukemia/Lymphoma Vaccine. *Hum. Gene Ther.* **2004,** *15* (1), 21-34.
465. Smith, D. M.; Simon, J. K.; Baker Jr, J. R., Applications of nanotechnology for immunology. *Nat. Rev. Immunol.* **2013,** *13* (8), 592-605.
466. Irvine, D. J.; Swartz, M. A.; Szeto, G. L., Engineering synthetic vaccines using cues from natural immunity. *Nat. Mater.* **2013,** *12* (11), 978-990.
467. Du, A. W.; Stenzel, M. H., Drug carriers for the delivery of therapeutic peptides. *Biomacromolecules* **2014,** *15* (4), 1097-1114.
468. Swaminathan, J.; Ehrhardt, C., Liposomal delivery of proteins and peptides. *Expert Opin Drug Del.* **2012,** *9* (12), 1489-1503.
469. Chen, F.; Stenzel, M. H., Polyion complex micelles for protein delivery. *Aust. J. Chem.* **2018,** *71* (10), 768-780.
470. Truong, N. P.; Jia, Z.; Burges, M.; McMillan, N. A.; Monteiro, M. J., Self-catalyzed degradation of linear cationic poly (2-dimethylaminoethyl acrylate) in water. *Biomacromolecules* **2011,** *12* (5), 1876-1882.
471. Insua, I.; Wilkinson, A.; Fernandez-Trillo, F., Polyion complex (PIC) particles: Preparation and biomedical applications. *Eur. Polym. J.* **2016,** *81*, 198-215.
472. Hie, L.; Nathel, N. F. F.; Shah, T. K.; Baker, E. L.; Hong, X.; Yang, Y.-F.; Liu, P.; Houk, K.; Garg, N. K., Conversion of amides to esters by the nickel-catalysed activation of amide C–N bonds. *Nature* **2015,** *524* (7563), 79-83.
473. Kvach, M. V.; Ustinov, A. V.; Stepanova, I. A.; Malakhov, A. D.; Skorobogatyi, M. V.; Shmanai, V. V.; Korshun, V. A., A convenient synthesis of cyanine dyes: Reagents for the labeling of biomolecules. *Eur. J. Org. Chem.* **2008,** *2008* (12), 2107-2117.

474. Harrison, R. H.; Steele, J. A.; Chapman, R.; Gormley, A. J.; Chow, L. W.; Mahat, M. M.; Podhorska, L.; Palgrave, R. G.; Payne, D. J.; Hettiaratchy, S. P., Modular and Versatile Spatial Functionalization of Tissue Engineering Scaffolds through Fiber-Initiated Controlled Radical Polymerization. *Adv. Funct. Mater.* **2015,** *25* (36), 5748-5757.
475. Sun, F.; Feng, C.; Liu, H.; Huang, X., PHEA-g-PDMAEA well-defined graft copolymers: SET-LRP synthesis, self-catalyzed hydrolysis, and quaternization. *Polym. Chem.* **2016,** *7* (45), 6973-6979.
476. Skrabania, K.; Miasnikova, A.; Bivigou-Koumba, A. M.; Zehm, D.; Laschewsky, A., Examining the UV-vis absorption of RAFT chain transfer agents and their use for polymer analysis. *Polym. Chem.* **2011,** *2* (9), 2074-2083.
477. Del Pino, P.; Pelaz, B.; Zhang, Q.; Maffre, P.; Nienhaus, G. U.; Parak, W. J., Protein corona formation around nanoparticles–from the past to the future. *Mater. Horiz.* **2014,** *1* (3), 301-313.
478. Tenzer, S.; Docter, D.; Kuharev, J.; Musyanovych, A.; Fetz, V.; Hecht, R.; Schlenk, F.; Fischer, D.; Kiouptsi, K.; Reinhardt, C., Rapid formation of plasma protein corona critically affects nanoparticle pathophysiology. *Nat. Nanotechnol.* **2013,** *8* (10), 772.
479. Liu, N.; Tang, M.; Ding, J., The interaction between nanoparticles-protein corona complex and cells and its toxic effect on cells. *Chemosphere* **2019**, 125624.
480. Kou, L.; Sun, J.; Zhai, Y.; He, Z., The endocytosis and intracellular fate of nanomedicines: Implication for rational design. *Asian J. Pharm. Sci.* **2013,** *8* (1), 1-10.
481. Wang, J.; Byrne, J. D.; Napier, M. E.; DeSimone, J. M., More effective nanomedicines through particle design. *Small* **2011,** *7* (14), 1919-1931.
482. Mao, Z.; Zhou, X.; Gao, C., Influence of structure and properties of colloidal biomaterials on cellular uptake and cell functions. *Biomater. Sci.* **2013,** *1* (9), 896-911.
483. Huang, X.; Teng, X.; Chen, D.; Tang, F.; He, J., The effect of the shape of mesoporous silica nanoparticles on cellular uptake and cell function. *Biomaterials* **2010,** *31* (3), 438-448.
484. Chithrani, B. D.; Ghazani, A. A.; Chan, W. C., Determining the size and shape dependence of gold nanoparticle uptake into mammalian cells. *Nano Lett.* **2006,** *6* (4), 662-668.
485. Qiu, Y.; Liu, Y.; Wang, L.; Xu, L.; Bai, R.; Ji, Y.; Wu, X.; Zhao, Y.; Li, Y.; Chen, C., Surface chemistry and aspect ratio mediated cellular uptake of Au nanorods. *Biomaterials* **2010,** *31* (30), 7606-7619.
486. Alemdaroglu, F. E.; Alemdaroglu, N. C.; Langguth, P.; Herrmann, A., Cellular uptake of DNA block copolymer micelles with different shapes. *Macromol. Rapid Comm.* **2008,** *29* (4), 326-329.
487. Salatin, S.; Maleki Dizaj, S.; Yari Khosroushahi, A., Effect of the surface modification, size, and shape on cellular uptake of nanoparticles. *Cell Biol. Int.* **2015,** *39* (8), 881-890.
488. Walkey, C. D.; Olsen, J. B.; Guo, H.; Emili, A.; Chan, W. C., Nanoparticle size and surface chemistry determine serum protein adsorption and macrophage uptake. *J. Am. Chem. Soc.* **2012,** *134* (4), 2139-2147.

489. Barbalinardo, M.; Caicci, F.; Cavallini, M.; Gentili, D., Protein corona mediated uptake and cytotoxicity of silver nanoparticles in mouse embryonic fibroblast. *Small* **2018,** *14* (34), 1801219.
490. Anderson, C. R.; Gnopo, Y. D.; Gambinossi, F.; Mylon, S. E.; Ferri, J. K., Modulation of cell responses to Ag-(MeO2MA-co-OEGMA): Effects of nanoparticle surface hydrophobicity and serum proteins on cellular uptake and toxicity. *J. Biomed. Mater. Res. A* **2018,** *106* (4), 1061-1071.
491. Anderson, C. R.; Abecunas, C.; Warrener, M.; Laschewsky, A.; Wischerhoff, E., Effects of methacrylate-based thermoresponsive polymer brush composition on fibroblast adhesion and morphology. *Cell. Mol. Bioeng.* **2017,** *10* (1), 75-88.
492. Lázaro, I. A.; Haddad, S.; Sacca, S.; Orellana-Tavra, C.; Fairen-Jimenez, D.; Forgan, R. S., Selective surface PEGylation of UiO-66 nanoparticles for enhanced stability, cell uptake, and pH-responsive drug delivery. *Chem* **2017,** *2* (4), 561-578.
493. Lee, H.; Sung, D.; Veerapandian, M.; Yun, K.; Seo, S.-W., PEGylated polyethyleneimine grafted silica nanoparticles: enhanced cellular uptake and efficient siRNA delivery. *Anal. Bioanal. Chem.* **2011,** *400* (2), 535-545.
494. Yu, J.; Li, X.; Luo, Y.; Lu, W.; Huang, J.; Liu, S., Poly (ethylene glycol) shell-sheddable magnetic nanomicelle as the carrier of doxorubicin with enhanced cellular uptake. *Colloids and Surfaces B: Biointerfaces* **2013,** *107*, 213-219.
495. Zeng, L.; Gao, J.; Liu, Y.; Gao, J.; Yao, L.; Yang, X.; Liu, X.; He, B.; Hu, L.; Shi, J., Role of protein corona in the biological effect of nanomaterials: Investigating methods. *TrAC Trends in Analytical Chemistry* **2019**.
496. Pelaz, B.; del Pino, P.; Maffre, P.; Hartmann, R.; Gallego, M.; Rivera-Fernandez, S.; de la Fuente, J. M.; Nienhaus, G. U.; Parak, W. J., Surface functionalization of nanoparticles with polyethylene glycol: effects on protein adsorption and cellular uptake. *ACS nano* **2015,** *9* (7), 6996-7008.
497. Lesniak, A.; Salvati, A.; Santos-Martinez, M. J.; Radomski, M. W.; Dawson, K. A.; Åberg, C., Nanoparticle adhesion to the cell membrane and its effect on nanoparticle uptake efficiency. *J. Am. Chem. Soc.* **2013,** *135* (4), 1438-1444.
498. Lesniak, A.; Fenaroli, F.; Monopoli, M. P.; Åberg, C.; Dawson, K. A.; Salvati, A., Effects of the presence or absence of a protein corona on silica nanoparticle uptake and impact on cells. *ACS nano* **2012,** *6* (7), 5845-5857.
499. Huang, K.; Boerhan, R.; Liu, C.; Jiang, G., Nanoparticles penetrate into the multicellular spheroid-on-chip: effect of surface charge, protein corona, and exterior flow. *Mol. Pharm.* **2017,** *14* (12), 4618-4627.
500. Lee, Y. K.; Choi, E.-J.; Webster, T. J.; Kim, S.-H.; Khang, D., Effect of the protein corona on nanoparticles for modulating cytotoxicity and immunotoxicity. *Int. J. Nanomed.* **2015,** *10*, 97.
501. Lehmann, J. S.; Zhao, A.; Sun, B.; Jiang, W.; Ji, S., Multiplex Cytokine Profiling of Stimulated Mouse Splenocytes Using a Cytometric Bead-based Immunoassay Platform. *JoVE (J. Vis. Exp.)* **2017,** (129), e56440.
502. Lehmann, J. S.; Rughwani, P.; Kolenovic, M.; Ji, S.; Sun, B., LEGENDplex™: Bead-assisted multiplex cytokine profiling by flow cytometry. *Method Enzymol.* **2019,** *629*, 151-176.
503. Liu, X.; Wu, F.; Tian, Y.; Wu, M.; Zhou, Q.; Jiang, S.; Niu, Z., Size dependent cellular uptake of rod-like bionanoparticles with different aspect ratios. *Sci. Rep.* **2016,** *6*, 24567.

504. Daud, J. B.; Lee, K. Y., Surface modification of nanocellulose. *Handbook of Nanocellulose and Cellulose Nanocomposites* **2017,** *1*, 101-122.